

1-1-2013

Simulations And Experiments Of Fuel Injection, Mixing And Combustion In Di Gasoline Engines

Yi Zheng
Wayne State University,

Follow this and additional works at: http://digitalcommons.wayne.edu/oa_dissertations

 Part of the [Other Mechanical Engineering Commons](#)

Recommended Citation

Zheng, Yi, "Simulations And Experiments Of Fuel Injection, Mixing And Combustion In Di Gasoline Engines" (2013). *Wayne State University Dissertations*. Paper 722.

This Open Access Dissertation is brought to you for free and open access by DigitalCommons@WayneState. It has been accepted for inclusion in Wayne State University Dissertations by an authorized administrator of DigitalCommons@WayneState.

**SIMULATIONS AND EXPERIMENTS OF FUEL INJECTION, MIXING AND
COMBUSTION IN DI GASOLINE ENGINES**

by

YI ZHENG

DISSERTATION

Submitted to the Graduate School

of Wayne State University,

Detroit, Michigan

in partial fulfillment for the requirements

for the degree of

DOCTOR OF PHILOSOPHY

2013

MAJOR: MECHANICAL ENGINEERING

Approved by:

Advisor

Date

ACKNOWLEDGEMENTS

I want first to thank my advisor, Dr. Ming-Chia Lai, for his invaluable guidance and constant encouragement throughout the years of my PhD study. He has been a source of inspiration and motivation for my research. Without his guidance and support, this research would not be completed. I am also grateful to my other committee members, Dr. Trilochan Singh, Dr. Marcis Jansons, Dr. Wen Li, and Dr. Fatih Celiker for their time in reviewing my thesis.

I would like to specially thank Dr. Xingbin Xie for his dedicated supports, insightful comments and guidance. I offer my regards to the lab colleagues who worked together throughout the research, especially to Mr. Atsushi Matsumoto and Mr. Po-I Lee who assisted me with their knowledge and experience in the field of study.

Finally, I would like to thank my family, for being supportive and patient throughout the years. I owe special thanks to my wife, Dr. Xin Guo, for her love and encouragement.

TABLE OF CONTENTS

Acknowledgements.....	ii
List of Tables	vi
List of Figures	vii
CHAPTER 1 INTRODUCTION	1
1.1 Background.....	1
1.2 Scopes of Thesis Work and Thesis Outline.....	6
CHAPTER 2 LITERATURE REVIEW	8
2.1 Gasoline Direct Injection (GDI) Engine	8
2.2 Direct Injection Injector and Spray	11
2.2.1 Internal Nozzle flow of DI injectors	12
2.2.2 Spray Characteristics of DI injectors.....	16
2.3 Wall Impingements and fuel film formation.....	18
2.4 In-Cylinder Spray/Mixing Characterizations in GDI engines.....	20
CHAPTER 3 STUDY METHODOLOGY	23
3.1 Experimental Setup.....	23
3.1.1 Direct-injection injectors	23
3.1.2 Spray Visualization Setup.....	27
3.1.3 Spray Impingement and RIM Setup.....	30
3.1.4 Optical Accessible Engine	44
3.2 Numerical Simulation Setup.....	47

3.2.1 Internal Nozzle Flow	47
3.2.2 Spray and Wall Impingement.....	51
3.2.3 Interaction between Spray and Charge Motion.....	60
CHAPTER 4 RESULTS AND DISCUSSIONS	65
4.1 Internal Nozzle Flow	65
4.1.1 Internal nozzle flow of injector for DI diesel engine	65
4.1.2 Internal nozzle flow of GDI injector	78
4.2 Spray and Wall Impingement.....	85
4.2.1 Sprays in Quiescent Spray Chamber.....	85
4.2.2 CFD Techniques and Spray Simulation	90
4.2.3 Wall Impingement and RIM test for PDI injector	104
4.2.4 Wall Impingement and RIM test for multi-hole injectors	110
4.3 Interaction between Spray and Charge Motion.....	131
4.3.1 Effects of Spray pattern and Injection Timing for Baseline case	132
4.3.2 Effects of Valve Actuation for Low-Speed Low-Load Case.....	139
4.3.3 Effect of Variable Valve Actuation for Medium and High-Load Case	148
CHAPTER 5 CONCLUSION	168
5.1 Summary of the Work.....	168
5.2 Recommendation and Future Work.....	172
References.....	174
Abstract.....	189

Autobiographical Statement..... 191

LIST OF TABLES

Table 3.1 Specifications of tested injectors for internal nozzle flow.....	26
Table 3.2 Fuel properties	26
Table 3.3 Specifications of tested injectors for spray	29
Table 3.4 Specifications of tested injectors for wall impingement	30
Table 3.5 Specifications of the engines.....	45
Table 3.6 Operation conditions of the metal engines.	46
Table 3.7 Numerical conditions of injector A	57
Table 4.1 Operating conditions	116

LIST OF FIGURES

Figure 1.1 CFD images of key physical processes in DISI gasoline engines: (a) Internal nozzle flow of multi-hole gasoline injector. Vapor phase is colored by volume fraction. (b) Fuel injection and vaporization from a multi-hole fuel injector, color-coded with injector nozzle numbers. (c) The side- and bottom- view of the wall wetting footprints on the piston. (d) The velocity streamlines of intake-air in cylinder through the intake valves. (e) Mixture preparation and spark ignition. (f) Homogeneous flame propagation.	3
Figure 2.1 An illustration of the gasoline engines categorized by fuel-injector location and mixture-formation duration. (a) Port-fuel injection (PFI) engine. (b) Homogeneous charge direct-injection spark-ignition engine. (c) Stratified charge direct-injection spark-ignition engine.	9
Figure 2.2 An illustration of the configurations in stratified charge direct-injection spark-ignition engine: (a) Wall guide direct-injection spark-ignition engine. (b) Air guide direct-injection spark-ignition engine. (c) Spray guide direct-injection spark-ignition engine.	10
Figure 2.3 Nozzle geometry. (a) Diesel injector, (b) GDI injector.....	13
Figure 2.4 Spray parameters	16
Figure 3.1 Internal nozzle structure of diesel injectors: two-hole nozzle (a) and single-hole nozzle (b) nozzles captured using phase-contrast imaging technique; (c) the close-up view of three-hole GDI injector nozzle tip.....	24
Figure 3.2 Experimental setup of spray visualization. (a) Back-lighting, (b) Schlieren.	28
Figure 3.3 Experimental setup of RIM visualization for PDI injector.....	32
Figure 3.4 Experimental setup of RIM visualization for multi-hole injector C.	33
Figure 3.5 Experimental setup of RIM visualization for multi-hole injector D: (a) schematic image, (b) photograph.....	35
Figure 3.6 Calibration curve for the rough window between liquid film thickness and reduction	37

Figure 3.7 Computation regions of (a) PDI injector and (b) multi-hole injector C	38
Figure 3.8 Evolution of the mean intensity in the wetted surface on the window and calibration point of multi-hole injector D configuration: (a) Evolution of averaged reduction ΔI on the window, (b) Evolution of deposit wetting area	41
Figure 3.9 Calibration curves for multi-hole injector D	42
Figure 3.10 Image processing of the RIM images, (a) Raw image, (b) Background removed image, (c) Binary image, (d) Time filtered image, and (e) Time and space filtered image.	43
Figure 3.11 Schematic and photograph of the Optical Engine.	44
Figure 3.12 Cam profiles of (a) Optical Engine and (b) Metal Engine. Early Intake Valve Closing (EIVC) and Late Intake Valve Closing (LIVC).	46
Figure 3.13 (a) Geometry for single-hole, (b) two-hole nozzles, (c) mesh strategy of two-hole nozzles. Inj. Pressure: 100 MPa.	48
Figure 3.14 The geometry and computation grid of three hole injector (a) Geometry, (b) mesh strategy (hexahedron).....	51
Figure 3.15 LISA breakup model.....	52
Figure 3.16 KH-RT breakup model.	53
Figure 3.17 Collision regimes of an impinging droplet on a wet wall.	54
Figure 3.18 Spray targeting of Injector A.....	56
Figure 3.19 Computation Grid for the numerical analysis and comprehensive mesh in value region – both Grid embedding (a) and AMR (b) and used.....	57
Figure 3.20 Computational grid of the PDI injector (top) and spray targeting for the multi-hole injector C (bottom).....	59
Figure 3.21 Computational grid of the multi-hole injector D.....	60

Figure 3.22 Geometry modeled for CFD evaluation.....	61
Figure 3.23 Geometry and mesh strategy.....	63
Figure 3.24 1-D GT-Power model of homogeneous charge DISI engine without EGR.	63
Figure 4.1 Computed mean pressure contours of single-hole (a) and two-hole (b) nozzles. (Inj. Pressure: 100 MPa.)	66
Figure 4.2 Near-nozzle jet morphology of two-hole nozzle and single-hole nozzle (Fuel: Biodiesel, injection pressure: 30 MPa, injection duration: 4.0 ms, Images taken at 2.0 ms ASOI).	66
Figure 4.3 The 2D and 3D streamline Flow characteristic in the sac and nozzle inlet for SHN (left) and THN (right) as computed using RANS.	68
Figure 4.4 The normalized streamwise velocity profiles of the axisymmetric SHN compared to those of the THN on the major axes at the exit plane.....	69
Figure 4.5 The turbulence intensity profiles of the axisymmetric SHN compared to those of the THN on the symmetry line on the major axes at the exit plane.	69
Figure 4.6 The effect of hole number on the streamlines of multi-hole nozzles.	70
Figure 4.7 The effect of hole number on the normalized exit velocity profiles (vertical) of the multi-hole nozzle.....	72
Figure 4.8 The Effect of hole number on the normalized streamwise vorticity profiles of the multi-hole nozzle.....	72
Figure 4.9 The streamlines inside the THN hole as viewed from the entrance, showing rotational curvatures and acceleration as the flow moves through the converging tapered hole. From left to right: RANS with Realizable k-turbulence model, URANS with SST turbulence model, and Scale Adaptive Simulation (SAS) model.	75
Figure 4.10 The vortex envelopes denoted by iso-surface of Q-criterion inside the THN at 30MPa and 100MPa injection pressure, as computed by URANS with SST turbulence model.....	76

Figure 4.11 The cavitation contour (vapor volume concentration as marked) inside the THN at 30MPa and 100MPa injection pressures, as computed by URANS with SST turbulence model.....	77
Figure 4.12 The cavitation contour (green, 1% vapor concentration) and the vortex envelopes denoted by iso-surface of Q-criterion (orange, $1E13/sec^2$) inside the THN at 100MPa injection pressure, as computed by URANS with SST turbulence model.	77
Figure 4.13 URANS simulation of the (a) the constant 50%-vapor fraction contours, (b) $Q=0.5E13$ iso-surface contours, and (c) the interactions of streamlines on the symmetry plane with 80%-vapor fraction contours inside the nozzle hole and sac volume, using n-Decane properties, 100-bar injection pressure,, and 15 μ m needle stroke.....	80
Figure 4.14 Early view of GDI spray. Injection pressure is 800 psi; imaging interval timing is 50 μ s.....	81
Figure 4.15 URANS simulation of the (a) the constant 50%-vapor fraction contours, (b) $Q=0.5E13$ iso-surface contours, and (c) the interactions of streamlines on the symmetry plane with 80%-vapor fraction contours inside the nozzle hole and sac volume, using n-Decane properties, 100-bar injection pressure, and 50 μ m needle stroke.....	83
Figure 4.16 RANS simulation using k- ϵ model for similar conditions as Fig. 4.14(a). The constant 50%-vapor fraction contours are shown with 75% transparency, with the cut-plane profiles shown at $L/D = 0, 0.7, 1.4$	84
Figure 4.17 Comparison of different Visualization Techniques, 1.5ms ASOI, E100, injector A: (a) $T_{cell} = 150^{\circ}C$, $P_{inj} = 5MPa$. (b) $T_{cell} = 200^{\circ}C$, $P_{inj} = 10MPa$	86
Figure 4.18 Effect of chamber temperature, pressure, and fuel temperature, $P_{inj} = 10MPa$, Energy content is equivalent of 10mg of gasoline. 1ms ASOI, E100, injector B.	87
Figure 4.19 Effect of fuel composition. $T_{ch} = 200^{\circ}C$, $P_{ch} = 1bar$, $T_{fuel} = 60^{\circ}C$, Energy content is equivalent of 5mg of gasoline.	88
Figure 4.20 Schlieren spray images for PDI injector under variant chamber pressure and temperature.	89

Figure 4.21 Measured and computed Spray Images; $T_{ch} = 200^{\circ}\text{C}$, $P_{ch} = 1\text{bar}$	90
Figure 4.22 Comparison of spray images from the experiment (top) with the numerical simulation (bottom), After SOI: 0.2ms, 0.7ms, 1.2ms, 1.7ms, Injector A, 25C 1bar.	91
Figure 4.23 Comparison of spray images from the experiment (top) with the numerical simulation (bottom), After SOI: 0.2ms, 0.7ms, 1.2ms, 1.7ms, Injector A, 200C 1bar.	92
Figure 4.24 Comparison of spray images from the experiment (top) with the numerical simulation (bottom), After SOI: 0.2ms, 0.7ms, 1.2ms, 1.7ms, Injector A, 25C 3bar.	92
Figure 4.25 Comparison of spray images from the experiment (top) with the numerical simulation (bottom), After SOI: 0.2ms, 0.7ms, 1.2ms, 1.7ms, Injector A, 200C 3bar	93
Figure 4.26 Comparison of experiment and numerical results of vapor phase penetration.	95
Figure 4.27 Liquid and vapor mass change in time.....	96
Figure 4.28 Comparison of Schlieren images and CFD-simulation (3D parcel representation) for multi-hole injector ($T_{ch} = 200^{\circ}\text{C}$, $P_{ch} = 1\text{bar}$, Injection duration = 0.5ms).	97
Figure 4.29 Comparison of experiment and numerical results (velocity vector field) of multi-hole injector at 0.75ms after start of injection.	97
Figure 4.30 Comparison of binary Schlieren images and CFD-simulation for PDI injector.	102
Figure 4.31 Comparison of experiment and numerical results of PDI injector spray penetration.	103
Figure 4.32 CFD-simulation of piston impingement, PDI injector (3D parcel representation) ($T_{ch} = 100^{\circ}\text{C}$, $P_{ch} = 1\text{bar}$, Injection duration = 0.5ms).....	104
Figure 4.33 Evolution of fuel film thickness ($T_{ch} = 150^{\circ}\text{C}$, $P_{ch} = 3\text{bar}$, Injection duration = 0.5ms).	105

Figure 4.34 Instantaneous images of the fuel film thickness. PDI injector, $T_{ch} = 100^{\circ}\text{C}$	106
Figure 4.35 Averaged film thickness of PDI injection, (a) $T_{ch} = 100^{\circ}\text{C}$, Injection duration = 0.2ms, (b) $T_{ch} = 100^{\circ}\text{C}$, Injection duration = 0.5ms.....	107
Figure 4.36 Instantaneous images of the fuel film thickness. PDI injector, $T_{ch} = 150^{\circ}\text{C}$	108
Figure 4.37 Averaged film thickness of PDI injection, (a) $T_{ch} = 150^{\circ}\text{C}$, Injection duration = 0.2ms, (b) $T_{ch} = 150^{\circ}\text{C}$, Injection duration = 0.5ms.....	109
Figure 4.38 Comparison of experimental spray evolution and CFD-simulation for multi-hole injector (a) Schlieren images; (b) 3D parcel representation; (c) 2D velocity vector field; (d) 2D equivalence ratio ($T_{ch} = 150^{\circ}\text{C}$, $P_{ch} = 1\text{bar}$, Injection duration = 0.5ms)	111
Figure 4.39 Instantaneous images of the fuel film thickness. Multi-hole injector, Injection duration = 0.5ms.	112
Figure 4.40 Averaged film thickness of multi-hole injection, and injection duration = 0.5ms, (a) $T_{ch} = 100^{\circ}\text{C}$, (b) $T_{ch} = 150^{\circ}\text{C}$	113
Figure 4.41 Computed evolution of liquid film thickness and iso-surfaces (equivalence ratio = 1, opaqueness = 30%) for PDI injector (left) and multi-hole injector (right) ($T_{ch} = 100^{\circ}\text{C}$, $P_{ch} = 1\text{bar}$, Injection duration = 0.5ms)	115
Figure 4.42 Wall wetting images (Case#1~4) after fuel droplet deposit on window surface.....	117
Figure 4.43 Wall wetting images (Case#5~10) after fuel droplet deposit on window surface.....	118
Figure 4.44 Evolution of fuel film thickness and spatial distribution (Case#1~4) after fuel droplet deposit on window	120
Figure 4.45 Averaged film thickness and film mass after fuel droplet deposit on window (Case#1~4).....	121

Figure 4.46 Evolution of fuel film thickness and spatial distribution (Case#5~10) after fuel droplet deposit on window.....	123
Figure 4.47 Averaged film thickness and film mass after fuel droplet deposit on window (Case#5~10).	124
Figure 4.48 Comparison of experimental free spray evolution and CFD-simulation (3D parcel representation).....	127
Figure 4.49 Comparison of experimental impinging spray and CFD-simulation (3D parcel representation). (a) case 5, (b) case 6.....	128
Figure 4.50 Comparison of experimental fuel film thickness and spatial distribution (left) and CFD-simulation (right), 2.6ms after start of injection (Case#6).	130
Figure 4.51 Comparison of experimental fuel film mass and CFD-simulation. Top: case1 and 2, Bottom: case 5 and 6.....	131
Figure 4.52 Comparison between CFD and OAE results of the in-cylinder spray processes, 1000 rpm, Injector B, 100MPa, 16mg (0.88ms duration). (a) SOI = 60 deg CA aTDC, (b) SOI = 120 deg CA aTDC, (c) SOI = 180 deg CA aTDC,	133
Figure 4.53 The effects of SOI on the (a) Tumble and Swirl ratios and (b) integrated turbulent kinetic energy, Late Intake Valve Closing (LIVC), injector B, optical engine.	135
Figure 4.54 (a) Total liquid film mass evolution, and (b) wall wetting footprints at 12 deg CA ASOI (Right), Late Intake Valve Closing (LIVC), injector B, optical engine.	136
Figure 4.55 Effect of injection timing on engine combustion: 1500 rpm, 4.7 BMEP, Low-Lift EIVC, Injector B, E85 [112].....	138
Figure 4.56 CFD validation with injection at 270 deg CA with LIVC deactivation configuration, 1000 rpm, Injector A.	140
Figure 4.57 Superimposed false-color in-cylinder spray image sequences showing the effects of valve deactivation on mixing, various SOI (vertical) from (a) 310 deg CA and (b) 290 deg CA bTDC: 2-Valve (Red) vs. 1-Valve (Green), EIVC, 1000 rpm, 1 bar BMEP equivalent.	141

Figure 4.58 The effects of valve deactivation on spray vaporization.	142
Figure 4.59 Computed Charge motion Dynamic ratios of VVA, SOI=60° aTDC, 1000 rpm, 1 bar BMEP equivalent. (a) Tumble ratio Y, (b) Tumble ratio X, (c) Swirl ratio.	145
Figure 4.60 Averaged turbulent kinetic energy, SOI= 60° aTDC, 1000 rpm, 1 bar BMEP equivalent.	145
Figure 4.61 Total liquid film mass, SOI= 60° aTDC, 1000 rpm, 1 bar BMEP equivalent.	146
Figure 4.62 Metal engine test results at 1000RPM, 1bar BMEP with EIVC.....	148
Figure 4.63 EIVC @2000 RPM, 2 Bar BMEP, LLC. (a) 2-valve vs. (b) 1-valve....	149
Figure 4.64 LIVC @1500 RPM, 8 Bar BMEP, HLC. (a) 2-valve vs. (b) 1-valve.....	150
Figure 4.65 The Streamlines of EIVC cases at 2000 rpm: (a) 2-valve vs. (b) 1- valve; LIVC cases at 1500 rpm: (c) 2-valve (d) vs. 1-valve.....	153
Figure 4.66 The side view of fuel droplet distributions of EIVC cases at 2000 rpm, 2 Bar BMEP:(a) 2-valve vs. (b) 1-valve.	154
Figure 4.67 The bottom view of fuel droplet distributions of EIVC cases at 2000 rpm, 2 Bar BMEP: (a) 2-valve vs. (b) 1-valve.	155
Figure 4.68 Interaction between spray and intake charge motion.	156
Figure 4.69 The effects of valve deactivations on computed charge motions dynamic ratios. (a) EIVC case:2000 rpm 2 bar BMEP, (b) LIVC case:1500 rpm 8 Bar BMEP.	158
Figure 4.70 In-cylinder flow streamlines and wall wetting. (a) EIVC case:2000 rpm 2 bar BMEP, (b) LIVC case:1500 rpm 8 Bar BMEP.	160
Figure 4.71 Total liquid film mass.....	161
Figure 4.72 In-cylinder air-fuel distributions before combustion. (a) 2-valve, (b) 1- valve (EIVC, 2000 rpm), (c) 2-valve, (d) 1-valve (LIVC, 1500 rpm).	162

Figure 4.73 Equivalence ratio distributions at spark timing	163
Figure 4.74 In-cylinder velocity vector field and temperature iso-surface (2000 K). 1-valve (EIVC, 2000 rpm).....	164
Figure 4.75 Comparison between computed and experimental profiles of in- cylinder pressure. EIVC Metal Engine 2000 rpm, 2 bar BMEP (2 valves).....	165
Figure 4.76 Evolution of ignition kernel and flame front. (a) EIVC Metal Engine 2000 rpm, 2 bar BMEP, (b) LIVC Metal Engine 1500 rpm, 8 bar BMEP. Temperature iso-surface (2000 K).	166
Figure 4.77 Evolution of CH ₂ O mass and concentration. EIVC Metal Engine 2000 rpm, 2 bar BMEP (2 valves).	167

CHAPTER 1 INTRODUCTION

1.1 Background

Worldwide, the number of vehicles in operation (cars; light, medium and heavy duty trucks; and buses) exceeded the 1 billion-unit mark in 2010 for the first time ever [1]. And it is estimated that the world's fleet will reach 2 billion motor vehicles by 2020, with passenger-cars representing at least half of all vehicles [2]. Internal combustion engines (ICE) are the predominant energy conversion technology in transportation and individual mobility. The combustion of hydrocarbons (whether fossil fuels today or biofuels in the future) leads to the formation of pollutant emissions and greenhouse gases, such as soot, nitrogen oxides (NO_x), carbon monoxide (CO) or carbon dioxide (CO_2). In United States, 97.5% of transportation CO_2 emissions come from petroleum-derived fuels in 2010. The gasoline powered vehicles has been responsible for 63.8% U.S. CO_2 emissions over the last twenty years. The transportation accounts for the majority of CO (61.8%) and NO_x (50.9%) emissions. Highway vehicles are responsible for the largest [3].

The major challenge in the research and development of internal combustion engines is to optimize the engine combustion system to simultaneously enhance power output, improve fuel efficiency and lower pollutant emissions. To achieve these goals, some of the engine technologies, such as direct fuel injection (DI), turbocharger application, and variable valve timing/actuation (VVT/VVA), work together to make big-engine power with downsizing engine (reduction of the engine size) fuel economy [4].

Modern direct-injection gasoline engines have been in series production and increasingly marketed worldwide by many manufacturers since 1996, and it is believed that advanced gasoline engines will remain competitive in vehicle applications for many years to come. In gasoline direct injection engines (GDI) the fuel is injected directly into the cylinder. Compared to a spark-ignition engine equipped with the port fuel injection (PFI) system, the direct-injection spark-ignition (DISI) combustion has many advantages, such as improvement of fuel consumption, better transient response during load variations, more precise control of air-fuel ratio, enhanced system optimization, and lower pollutant emission. Direct Fuel Injection is the key technology to control fuel metering, fuel-air mixing formation, combustion, and emissions of advanced internal combustion engines. These engines will command multiple combustion modes, such as high-power and low-temperature combustion, for more efficient and cleaner propulsion or power applications. Combined with advanced valve-train, variable compression-ratio, variable air-charging down-sized engine architecture, DI will pave the way for the engine of the future. The key physical processes in gasoline direct injection engines include fuel-spray injection and vaporization, intake-air flow, wall wetting, homogeneous or stratified mixture formation, spark ignition and flame formation, flame propagation, and exhaust flow with engine-out emissions and catalytic aftertreatment. Some of the physical processes are shown in Fig. 1.1.

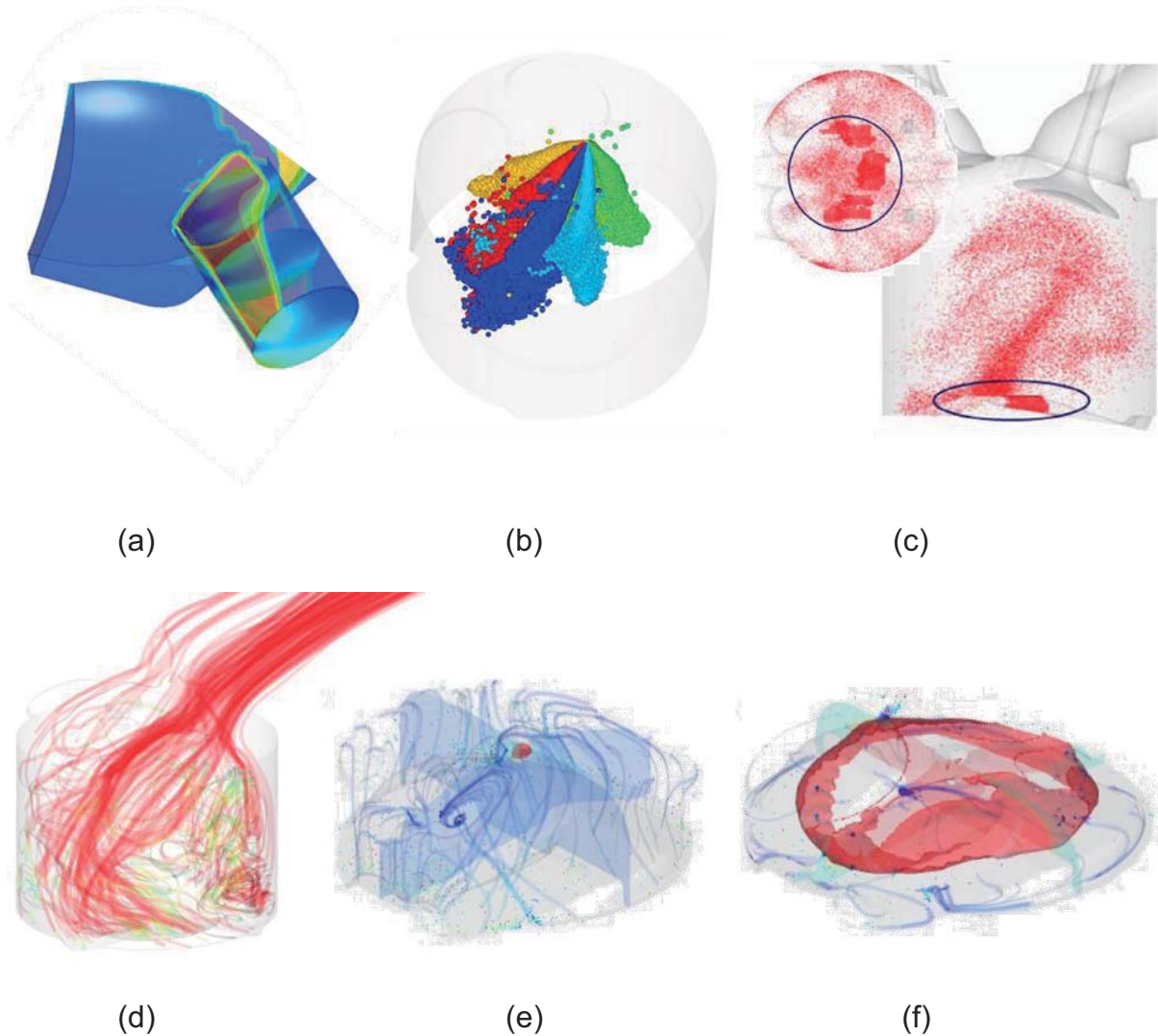


Figure 1.1 CFD images of key physical processes in DISI gasoline engines: (a) Internal nozzle flow of multi-hole gasoline injector. Vapor phase is colored by volume fraction. (b) Fuel injection and vaporization from a multi-hole fuel injector, color-coded with injector nozzle numbers. (c) The side- and bottom- view of the wall wetting footprints on the piston. (d) The velocity streamlines of intake-air in cylinder through the intake valves. (e) Mixture preparation and spark ignition. (f) Homogeneous flame propagation.

In direct injection internal combustion engines applications, the multi-hole nozzle, with its robust features and cost-effectiveness, are being used currently for side-mounted or central mounted applications, with primarily stoichiometric homogeneous applications. However, higher performance demands greater

improvements in the injection technology. These requirements have brought even greater impetus to the understanding of fluid dynamics of the flow inside the nozzle orifice and the fuel sprays immediately outside the nozzle exit, and their dependence on the nozzle geometry and internal flow features as shown in Fig. 1.1a. Near-nozzle fuel jet development dominated by internal nozzle flow and related fluid-dynamic instability governs the primary break-up process of the injected fuel. The momentum of the fuel spray and spray atomization control the mixing of the injected fuel with surrounding oxidant gas, which is crucial to achieve highly-efficient and clean combustion for direct injection diesel and gasoline engines.

It is well known that the combustion and emission characteristics of the DI engine are strongly influenced by the rate of vaporization of the liquid fuel, which is dependent on the spray atomization (Fig. 1.1b). Therefore, the fuel deliver system, nozzle geometry, and spray patterns should be designed to deliver fuel amounts more precise and accurate, with a good spray axisymmetric distribution over the entire operation range, and must produce a fuel spray that is well atomized during the time between injection and ignition. The impingement of liquid fuel by a strongly penetrating fuel spray on the combustion chamber wall and piston head in small-bore direct injection engine (Fig. 1.1c) is inevitable and undesirable, because it delays the gas-phase fuel-air mixture preparation processes prior to combustion and a possible source for exhaust particulate matter and unburnt hydrocarbon (UHC) emissions [5] and should be considered to meet future particle-number-based emission standards.

Advanced valvetrain can provide independent control of the intake valve lift, profile and duration. The ability to deactivate one of the valves or have different lift profiles provides additional control of in-cylinder flow (Fig. 1.1d). The air and fuel are supplied separately and the interaction between intake air and spray can affect combustion performance in DI engines (Fig. 1.1e). Therefore an advanced valvetrain coupled with side-mounted GDI multiple-hole sprays is expected to pave the way for better combustion quality and simultaneous reduction of pollutant emissions and fuel consumption. In addition, ethanol and ethanol-gasoline blends are being used in the down-sized, down-spiced and variable-valve-train engine architecture, because of their synergy in improving the turbo-charged DI gasoline performance.

Homogenized combustion processes (Fig. 1.1f) avoid peak temperatures by mixture homogenization and exhaust gas recirculation, and thus lower the emission of NO_x and soot significantly, which are formed in the presence of peak temperatures and fuel overconcentration only. In the combustion process development modern methods such as optical spray diagnostics and CFD-based engine modeling are applied in order to make pre-selections of relevant injection and engine parameters in the early design period and to gain a detailed knowledge about the acting physical mechanisms. With these methods important impulses can be derived for the combustion system development.

1.2 Scopes of Thesis Work and Thesis Outline

The objective of this study is to understand the internal nozzle flow of DI injectors, sprays and vaporization, wall wetting, and interaction between fuel spray and in-cylinder gas motion through CFD modeling.

The measurement of the wall film thickness and mass was carried out by experimentally using the RIM technique. The characterization of DI spray and fuel-air mixing was investigated through the application of optical diagnostics.

Chapter 2 reviews the engine technologies: direct-injection engines, direct-injection injectors, DI spray and wall impingements. The applications for advanced engine development, such as optical diagnostics and multidimensional modeling simulation methods, are discussed.

Chapter 3 will address the study methodology. The research work has been accomplished by optical engine experiments and 3D-CFD based engine modeling. The experimental setup for the observation of spray, wall impingement, and in-cylinder flow is first illustrated. To measure the fuel film thickness resulting from fuel spray impingement, the high-speed spray visualization and Refractive Index Matching technique is highlighted. Second, the computational models are demonstrated including mesh management, turbulence models for quasi-steady near-nozzle jet morphology of direct-injection diesel and gasoline injectors; spray model, wall impingement model, and liquid film model.

Chapter 4 first presents the internal flow predictions using with multi-dimensional multi-phase CFD simulations. Second, the spray characteristics and simulations without charge motion are discussed. The formation and evolution of the

fuel spray emerging from multi-hole injector and outward opening piezo-driven injector were investigated under various surrounding conditions. Then, the interactions between spray and cylinder/piston walls are discussed. Fuel film thickness resulting from fuel spray impingement will be measured using the RIM technique. Numerical study is conducted for the same experiment conditions to understand the spray behavior and impingement. Finally, the interactions with charge motions inside optical engine are presented. The benefits and tradeoffs of valve deactivation and its effect on efficiency, combustion stability and emissions will be discussed. The implications to the engine combustion and emission performance are summarized.

Chapter 5 summarizes the work in this thesis and recommends future paths for research based on the findings here.

CHAPTER 2 LITERATURE REVIEW

This chapter presents a literature review covers published experimental and computational direct-injection spray research. The purpose of this review is to understand the effects of fuel-spray injection on air-fuel mixing, surface wetting, and turbulence intensity in GDI engines, and to set up experimental and computational investigation guideline.

2.1 Gasoline Direct Injection (GDI) Engine

With increasing pressure to reduce both fuel consumption and pollutant emissions, engine researchers have been looking to a way to combine the two current combustion systems: homogeneous-charge spark-ignition for gasoline-fueled engines (low pollutant emissions) and direct-injection compression-ignition for diesel-fueled engines (high fuel efficiency) [6]. The direct-injection spark-ignition (DISI) combustion represents one promising solution to improve fuel economy and meet increasingly stringent emissions standards.

Fig. 2.1 provides an overview of gasoline engine combustion modes. These include Port-fuel injection (PFI) engine, homogeneous charge direct-injection spark-ignition engine, and stratified charge direct-injection spark-ignition engine. The fuel-air mixture in the gasoline engines is prepared in-cylinder and out-cylinder. PFI engines (external mixture formation, Fig. 2.1a) are equipped with the fuel injectors at the intake port and the air-fuel mixture is created outside of the combustion chamber. Fuel is injected in the port with relatively low fuel pressure in the range of 300-

500kPa. In PFI engine, a liquid fuel film is formed in the intake port and valve area, which results in delayed fuel vaporization.

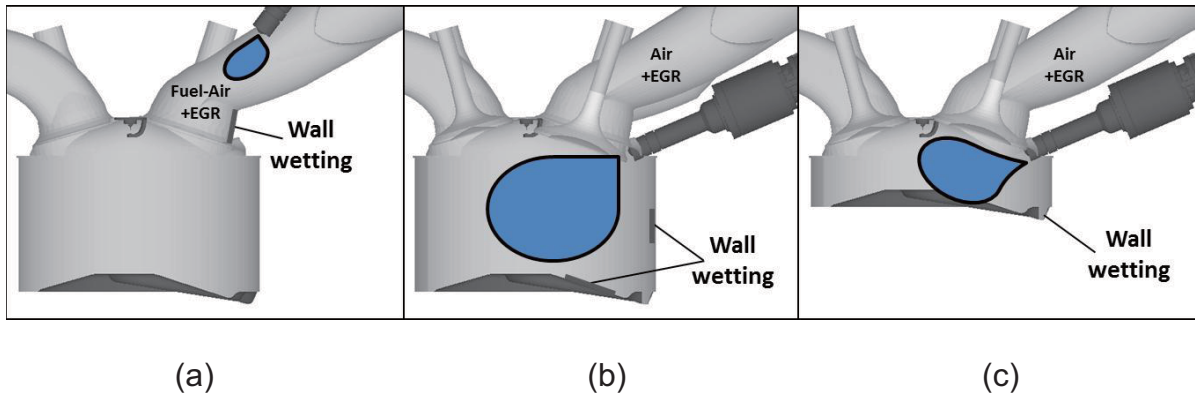


Figure 2.1 An illustration of the gasoline engines categorized by fuel-injector location and mixture-formation duration. (a) Port-fuel injection (PFI) engine. (b) Homogeneous charge direct-injection spark-ignition engine. (c) Stratified charge direct-injection spark-ignition engine.

However, like carburetors have been supplanted by PFI injection, DISI engines (internal mixture formation) have the potential to replace the PFI engine by producing significant improvements in fuel economy, transient response, performance, and emissions over PFI engines [7, 8]. There are two variants of DISI engine corresponds to injection timing – the homogeneous charge direct-injection spark-ignition engine (Fig. 2.1b) and Stratified charge direct-injection spark-ignition engine (Fig. 2.1c). For stratified charge DISI engine, there are three main approaches to the combustion process as shown in Fig. 2.2, depending on the relative position of the injector with respect to the spark plug and the way the mixture is transported inside the cylinder. The injector is side mounted and the injected fuel is guided either by the bowl shaped piston (wall guided, Fig. 2.2a) or by the cylinder internal airflow (air guided, Fig. 2.2b) toward the spark plug. In the spray guided the

injector is placed in a central position in the cylinder head with the spark plug nearby (Fig. 2.2c).

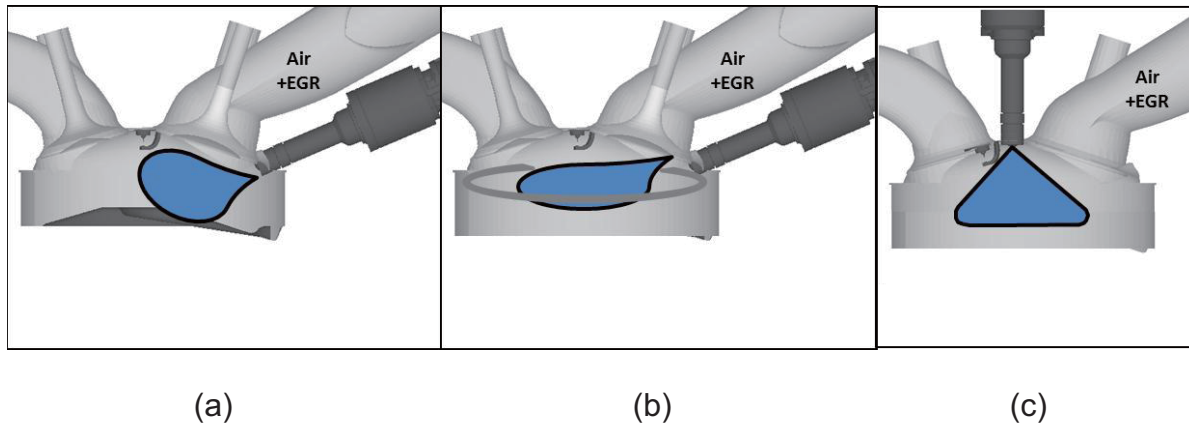


Figure 2.2 An illustration of the configurations in stratified charge direct-injection spark-ignition engine: (a) Wall guide direct-injection spark-ignition engine. (b) Air guide direct-injection spark-ignition engine. (c) Spray guide direct-injection spark-ignition engine.

Homogeneous charge DISI engine (often supplemented with turbocharging or supercharging, or both) has the potential to simultaneously improve power (up to ~15%), increase fuel economy (3%~5%), and reduce unburned hydrocarbon (UBHC) emissions, while taking advantage of the same highly effective catalytic aftertreatment systems as PFI engines [9]. With lean combustion, the Stratified charge DISI engine has the highest benefit potential of fuel economy for the reduction of pumping losses and heat transfer losses during low load and speed operation, while at the higher load and speed the engine is operated in the “homogeneous” mode [10]. Besides, DISI engines also improve the transient response, cold startability, and control of air/fuel ratio.

2.2 Direct Injection Injector and Spray

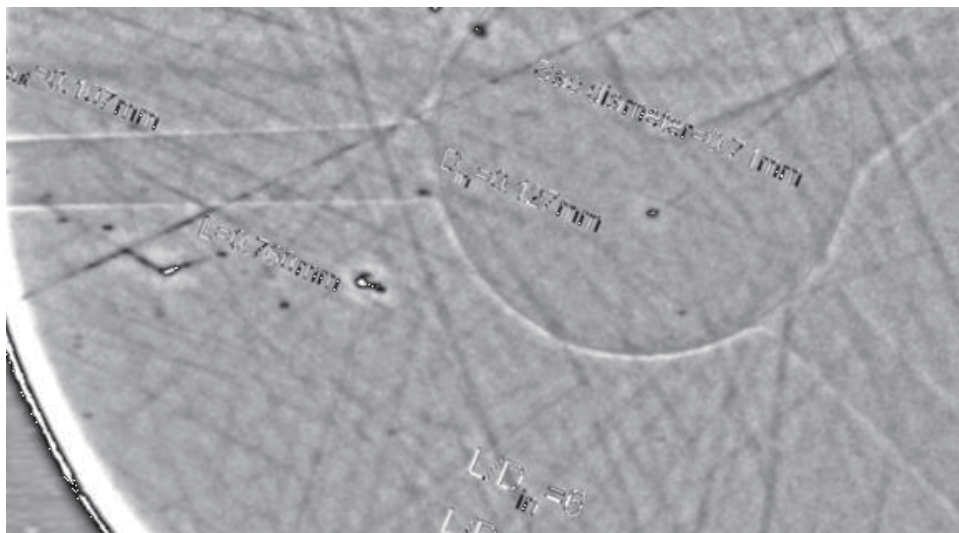
Advanced fuel-injector technology has been applied in the development of DI engines, and four types of injectors: high-pressure swirl injector, fan injector, solenoid-controlled single-hole or multi-hole injector, and outwardly opening piezo-driven injector (PDI), have been used successfully in DI engines [11]. The momentum of the fuel spray and spray atomization control the mixing of the injected fuel with surrounding oxidant gas, which is crucial to achieve highly-efficient and clean combustion for direct injection (DI) diesel and gasoline engines. Recent trend of the diesel engine is to use smaller and more orifices, and higher injection pressure. The advantages of smaller nozzle holes have been reported [12], such as lower particulate matter (PM) and carbon monoxide (CO) emission and possibly better fuel economy. To place multiple orifices in an injector nozzle, the orifices are located off-axis to the nozzle axis and symmetrically aligned around the nozzle axis, which is most preferred DI diesel nozzle configuration.

The GDI engines converge to the multi-hole injector geometry because of its robustness, flexibility and cost-performance. The gasoline DI multi-hole injectors sometimes use both symmetric and asymmetric hole patterns, with or without a center hole. In homogenous charge DISI engine, spray trajectory and fuel atomization characteristics of the multi-hole injectors significantly is crucial to the fuel-air mixing and wall wetting. The multi-hole injectors can reduce smoke emissions because of enhanced evaporation, resulting in a shorter liquid length [13]. Outwardly opening PDI injector has low penetration to reduce wall wetting and a spray A-shape cone that is relatively insensitive to in-cylinder pressure or

temperature changes, and a stable recirculation zone near the spray tip. With fast and precise injection, outwardly opening PDI injector provides excellent stable spray for stratified spray guided DISI combustion systems [9, 14]. Diesel injector is used in a gasoline direct injection compression-ignition (GDCI) combustion system and delivering gasoline fuel using multiple injections [15]. However, higher performance demands greater improvements in the injection technology. These requirements have brought even greater impetus to the understanding of fluid dynamics of the flow inside the nozzle orifice and the fuel sprays immediately outside the nozzle exit, and their dependence on the nozzle geometry and internal flow features.

2.2.1 Internal Nozzle flow of DI injectors

Spray penetration, mixing and combustion is sensitive to spray orifice exit conditions. Fig. 2.3 illustrates the nozzle geometry of two-hole diesel injector and gasoline DI injector.



(a)

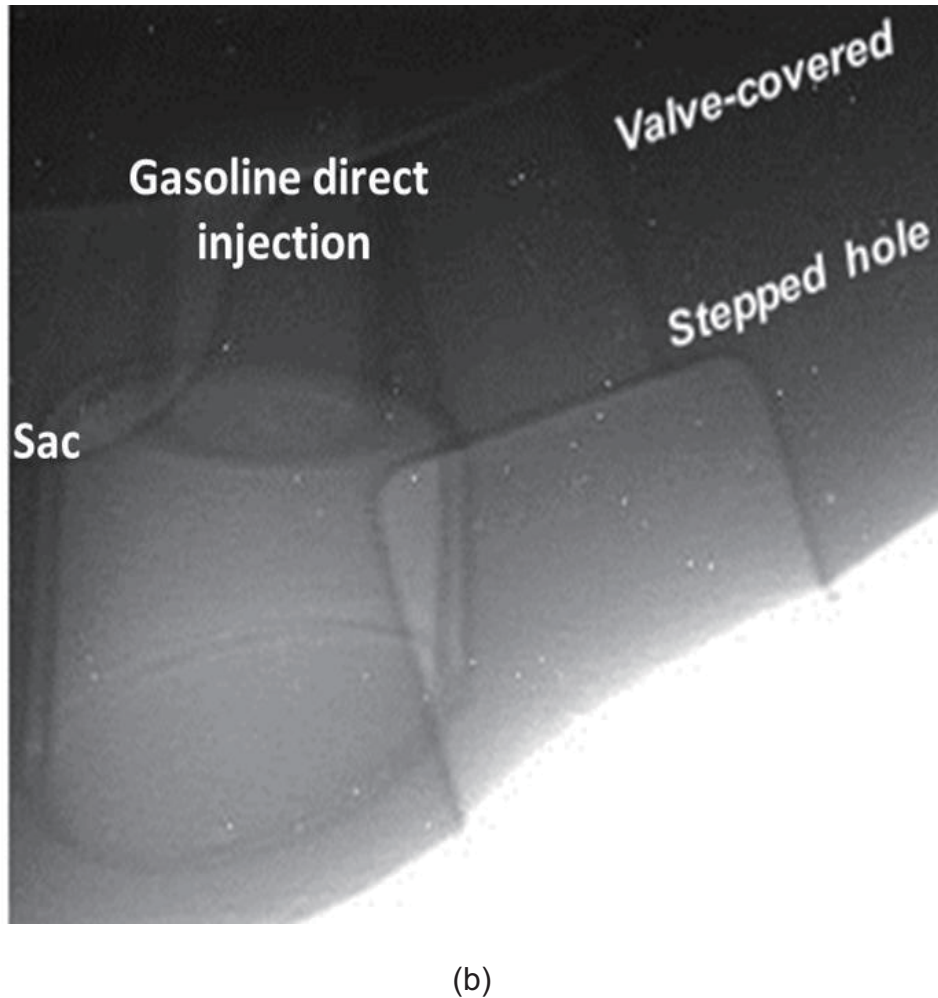


Figure 2.3 Nozzle geometry. (a) Diesel injector, (b) GDI injector

The internal nozzle flow and near-field primary atomization has been receiving attention as a tool to enable analysis of the influence of nozzle design on the key spray parameters and reduce reliance on hardware trial-and-tests for multi-objective spray optimizations [16]. Visible-light imaging techniques have been dominantly used to visualize the internal and near-nozzle fuel flow and led to

remarkable progress in analysis of near-nozzle spray geometry [17-23]. However, these techniques have their limitation in the visualization of near-nozzle jet morphology especially for dense and high-speed fuel sprays. To overcome this, single-shot ultrafast x-ray phase-contrast imaging technique has been introduced recently for dense high-speed fuel sprays [24-27]. X-ray phase-contrast imaging technique records phase variations of the emerging radiation from liquid/gas interfaces rather than absorption-induced intensity variations when the x-ray beam passes through an object [27]. Near-nozzle fuel jet morphology during diesel and gasoline injection has been unveiled from recent studies using X-Ray. However, such study has not been extended to more realistic and practical multi-hole injectors until now.

This off-axis location of the orifices makes the near-nozzle spray to be strongly affected by the vortex flow inside the nozzle sac other than axial laminar-like flow. The structure of the vortex flow and cavitation inside the multi-hole Diesel nozzles has been unveiled from quite a few simulation studies [17-19, 28, 29] and large scale-up hydraulic (water analog) model experiments. These results showed that vortical flow is formed inside the nozzle orifice and it strongly affects the near-nozzle spray development [17, 18, 29]. Some previous study focused on the near-nozzle jet morphology of high-pressure Diesel spray injected by a single-hole nozzle which center of hole is located on the nozzle axis [23-25]. Previous test results revealed the laminar-like jet features formed very near the nozzle exit, which becomes unstable mostly due to turbulence and cavitation inside the nozzle and aerodynamic effect much later on outside the nozzle. In the case of smooth orifice

inlet, where vena contracta and cavitation effects are less significant, mono-dispersed planar wave is formed on the jet surface, while totally turbulent jet morphology rather than wavy structure was observed for sharp orifice inlet. However, such a study had not extended to more realistic and practical multi-hole nozzles which jets are strongly affected by the vortex flow inside the nozzle.

It is now generally accepted in the fuel injection community that for high-speed jet or pressure-driven single-phase atomizer [30, 31], such as DI diesel or gasoline multi-hole injectors, there are different factors affecting the primary breakup, including turbulence [32-35], cavitation [36-40], and vortices [41-43]. Turbulent flows inevitably are three-dimensional and therefore are accompanied by vortices or vertical flow structure. While cavitation is not always desirable, they are sometimes inevitable, especially for the more volatile fuels such as gasoline and higher fuel temperature. For transient highly dynamic fuel injection processes, to resolve the dynamic interactions of these complicated flow structures covering a wide range of length scales and phases, within the short transient injection duration is indeed quite a challenge. The CFD simulations using more complicated Eulerian and Lagrangian cavitation models have been shown to correlate the rotational flow structure observed at the scale-up hydraulic nozzle model [17, 18, 29]. Specifically, there seems to be the existence of counter-vortex flows inside the scaled-up hydraulic model as visualized by the cavitation bubbles. Depending on the source of locations, these cavitation streaks are termed "geometric cavitation" from flow separation, and "streak cavitation," which connects between the orifices via the sac.

2.2.2 Spray Characteristics of DI injectors

In Fig. 2.4, the most commonly used qualities of spray are size distribution of droplets, spray tip penetration and plume angle.

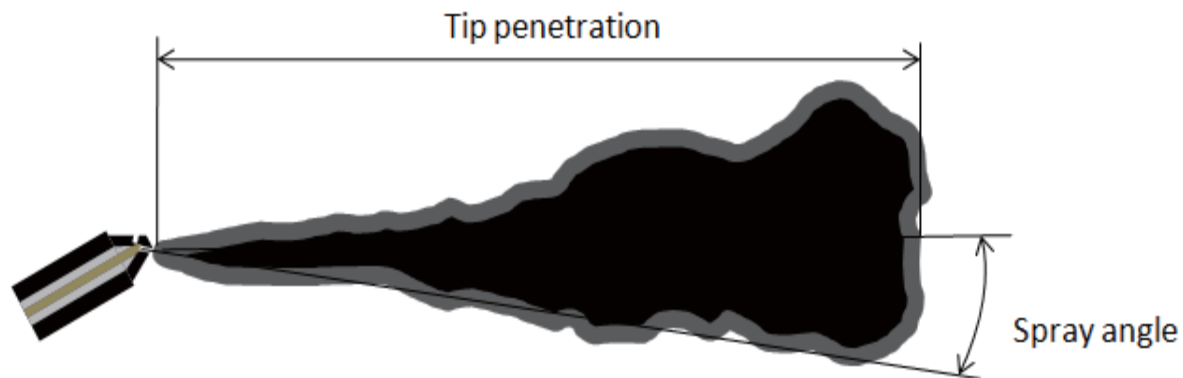


Figure 2.4 Spray parameters

Spray angle is influenced by the nozzle design, fuel properties and ambient conditions. Spray tip penetration as a function of nozzle geometry, injection pressure, and ambient conditions is a key factor in the design of diesel and gasoline direct injection engines.

The spray droplets undergo a number of subroutines: breakup, collision, vaporization and drop drag. If the fuel spray impact the piston, the formation and evaporation of liquid fuel films should be considered. Among these physical processes, the breakup process is most important to droplet predict velocity and droplet size. Numerical study is conducted using Kelvin-Helmholtz / Rayleigh-Taylor (KH-RT) breakup model based on the competition between KH and RT instabilities

and shows good agreement with experimental results in spray behavior, Sauter mean diameter (SMD) and velocity [44].

Schmidt et al. [45] developed a Linearized Instability Sheet Atomization (LISA) model (Fig. 2.3b) and was applied to pressure-swirl injectors first. It also shows that the LISA model is applicable to outwardly opening nozzles as well. The Taylor Analogy Breakup (TAB) model proposed by O'Rourke and Amsden [46] is a classic method for calculating drop distortion and breakup by analogously to a spring-mass system.

In order to model sprays, Lagrangian droplet "parcels" represent a number of identical drops and is used to statistically represent the entire spray field. In other relevant study, the coupled Eulerian-Lagrangian method has been used to correlate the injector internal flow and near-field primary atomization [16] without the limitation of aerodynamic breakup. There are mainly three turbulence transport models for Lagrangian spray modeling: Reynolds Averaged Navier-Stokes (RANS), Large Eddy Simulation (LES) and Direct Numerical Simulation (DNS) [44-50]. Accounting for the variations in the drop shape (sphere or disk), the drop drag coefficients can be obtained by the dynamic drag model [51]. No Time Counter (NTC) method is developed to model the collision and coalescence of droplets [52]. The NTC method is based on techniques used in gas dynamics for Direct Simulation Monte Carlo (DSMC) calculations. This model has been shown to be faster and more accurate than O'Rourke's model under certain conditions [53, 54]. The standard vaporization model was used to calculate the time rate of change of droplet radius due to vaporization [55].

In spray optical analysis, Mie-scattering, Back-lit, and Schlieren are three main techniques to visualize spray behavior. Unlike Mie-scattering technique is for liquid phase visualization only, Back-lit is a simple method, which can obtain both vapor phase and liquid phase as a shadow. Schlieren method is another effective technique to visualize nonhomogeneous transparent flow fields, such as the vapor phase of sprays. Using the Schlieren technique, it is able to visualize the change of the refraction indexes and density gradient in the object caused by material and temperature difference [56, 57]. The details of back-lit method and Schlieren visualization technique will be discussed in Chapter 3.

2.3 Wall Impingements and fuel film formation

Spray impingement on solid surface occurs in many industrial and technical processes [58]. The impingement of liquid fuel on the combustion chamber wall and piston head in the direct injection engine is mostly undesirable although difficult to avoid, because it affects mixture preparation prior to combustion and is a possible source for unburned hydrocarbon (UHC) and particulate matter emissions [59], which is the focus of future particle-number-based emission standards.

Unthrottled stratified charge DISI engines provide high fuel efficiency at part load, but have challenge to create the proper stratified-charge fuel distribution to ensure reliable ignition, proper combustion phasing, and minimum engine emissions. Most current designs use a high-pressure hollow-cone PDI injector or multi-hole injector to deliver fuel sprays into chamber in spray-guide or wall-guide DISI engines as shown in Fig. 2.2. During this process, the fuel sprays impact the piston and form

a film of liquid fuel [61]. The fuel film formation and evaporation, which result in in-cylinder pool fires and unburned hydrocarbon and smoke emissions, have been studied extensively experimentally and computationally, but many questions remain [11]. For homogeneous charge DISI engines, an optimization of injector spray pattern can reduce liner and piston wetting which leads to a reduction in oil dilution (Fig. 1.1c). It also reduces soot emissions over a wide window of fuel injection timing [62].

The problem of wall impingement has been studied quite extensively experimentally and computationally for DI diesel, port-injection and DI gasoline [63-70]. For gasoline-fueled engines, port fuel injection generally produces a thicker fuel film than DI because of the lower injection pressure and ambient temperature compared to DI cases. It has also been suggested that the level of soot emissions is more strongly dependent on the wall film thickness than the total amount of fuel on the piston head [71].

Recent studies addressed the measurements of adhered liquid fuel film. The fuel film formed on the piston head in direct-injection engines was measured quantitatively by Refractive Index Matching technique (RIM) by Drake et al. [61, 72]. This relatively simple optical method can be used for quantitative temporal and spatial measurements of fuel film under vaporizing conditions. The results showed that the area-average film thickness is around $1\mu\text{m}$ and the maximum film is about $3\mu\text{m}$ [72], [73]. Liquid film formation and precise thickness measurement have also been analyzed by RIM measurements and qualitative LIF visualizations for direct injection SI engines [74] using piezo outward opening nozzles. The maximum peak

film thicknesses is found to be in the range of 0.9-1.0 μm , and that faster evaporation rates occur at the outer edges of the film with smaller thickness.

Multi-dimensional CFD offers a promising alternative to experiments for its capability to offer much more detailed information on mixture formation and spray impingement. Numerical methods are still a challenge today, mainly because the sub-models used to simulate the physical phenomena of injection spray and droplet impingement are not sufficiently validated. Thus there is a need for more accurate models and experimental parameters influencing the spray-wall interaction [75]. The wall film thickness for diesel spray impingement has been simulated by considering and evaluating the heat transfer between the temperature-controlled wall and impinging spray [76]. The effects of injection pressure and wall inclination angle on the macroscopic behavior of a multi-hole GDI spray were investigated experimentally and numerically [77]. The behavior of the spray impingement was observed using an optical access engine, however the amount of liquid film remaining on the piston crown appears under-predicted after compared with simulation results [78].

2.4 In-Cylinder Spray/Mixing Characterizations in GDI engines

Advanced valvetrain coupled with Direct Injection (DI) provides an opportunity to simultaneously reduce fuel consumption and emissions [4]. In GDI engines, fuel is delivered during intake or compression strokes directly through a multi-hole, mini-sac injector with pressures ranging from 1 to 20 MPa [79]. Imperfect mixing and wall wetting result in HC and soot, thus the intake ports and combustion chamber are designed to achieve a moderate or high tumble motion depending on the engine

operating conditions [80-82]. Physical processes in engines can be visualized, quantified, and optimized through optical engine diagnostics and CFD-based engine modeling. Optical Accessible Engine (OAE) provides the direct imaging capability to dynamic and realistic in-cylinder charge motion, and it is widely used for engine spray and combustion research [83, 84]. Most common type of OAE is equipped with a hollow piston with an optical window on the top of it to provide an optical path to the bottom of the piston, which is named Bowditch piston. An optical engine may have windows on the side of the cylinder.

Because of their robustness and cost performance, multi-hole nozzles are currently being adopted as the gasoline DI fuel injector of choice, mostly in the side-mount configuration. The effects of spray patterns on air-fuel mixing, in-cylinder flow development, surface wetting, and turbulence intensity, are discussed for GDI engine under different speed/load conditions [62]. In addition, ethanol and ethanol-gasoline blends are being used in the down-sized, down-speed and variable-valve-train engine architecture, because of their synergy in improving the turbo-charged DI gasoline performance. There has been much research in the literature carried out with interactions of DI gasoline sprays and the in-cylinder flow fields [85-93], but very little study on the side-mounted multi-hole nozzle with the interaction of charge motions.

Multi-dimensional computational fluid dynamics (CFD) offers a promising alternative to experiments for its capability to offer much more detailed information on in-cylinder mixture formation. Numerical method has been used to analyze the injector nozzle flow, near-field primary spray evolution, and wall impingement of

gasoline and diesel engine, and compare with experimental observation [94, 95]. In order to get a better understanding of in-cylinder process, new ideas may arise to improve ICE design. It is well-known that turbulence modeling is one of the key factors which limit accuracy and predictive ability. The charge motion and its interaction with spray were studied computationally and experimentally, and showed that the mixture preparation prior to combustion is important for predicting combustion characteristics and emissions [96, 97, 98]. These research works also show that the significant influence of turbulence modeling on in-cylinder flow predicting and Reynolds-averaged Navier-Stokes (RANS) turbulence method is probably still the best compromise between reliability and computationally expensive. The ignition process and combustion regimes of gasoline DI engine were investigated by using CFD method [99].

CHAPTER 3 STUDY METHODOLOGY

The fuel-air mixing and distribution in DI gasoline engines is the result of complex interactions between the sprays/vaporization, turbulent in-cylinder flow, wall wetting and the combustion chamber geometry. In this chapter, the use of optical diagnostics and numerical methods in the internal nozzle flow, spray evolution, the interaction between spray and walls, and the interaction between spray and charge motion is discussed.

3.1 Experimental Setup

In this section, the structure and specification of two DI diesel injectors and one DI gasoline injector are first presented. Then the instrument setup and data processing method in optical visualization experiments and RIM technique are presented.

3.1.1 Direct-injection injectors

Two diesel injectors (single-hole nozzle, SHN and two-hole nozzle, THN) and one gasoline injector (three-hole nozzle) are presented to investigate the in-nozzle flow characteristics. The internal structures of SHN and THN visualized with higher energy x-ray beam and longer exposure time are shown in Fig. 3.1a and Fig. 3.1b [100]. These two nozzles SHN and THN have identical sac diameter (0.71 mm) and similar hydro-grinding level. The difference in the hole diameter of both nozzle inlet and nozzle exit is around 4%. Also a close-up image of the nozzle tip of the three-hole GDI injector is shown in Fig. 3.1 c, with the counter bore of the nozzle hole near

the exit slightly visible. There is a rim about 1 mm high on the edge of the injector; therefore, the closest point of visualization starts at about 1mm downstream of the director-plate surface.

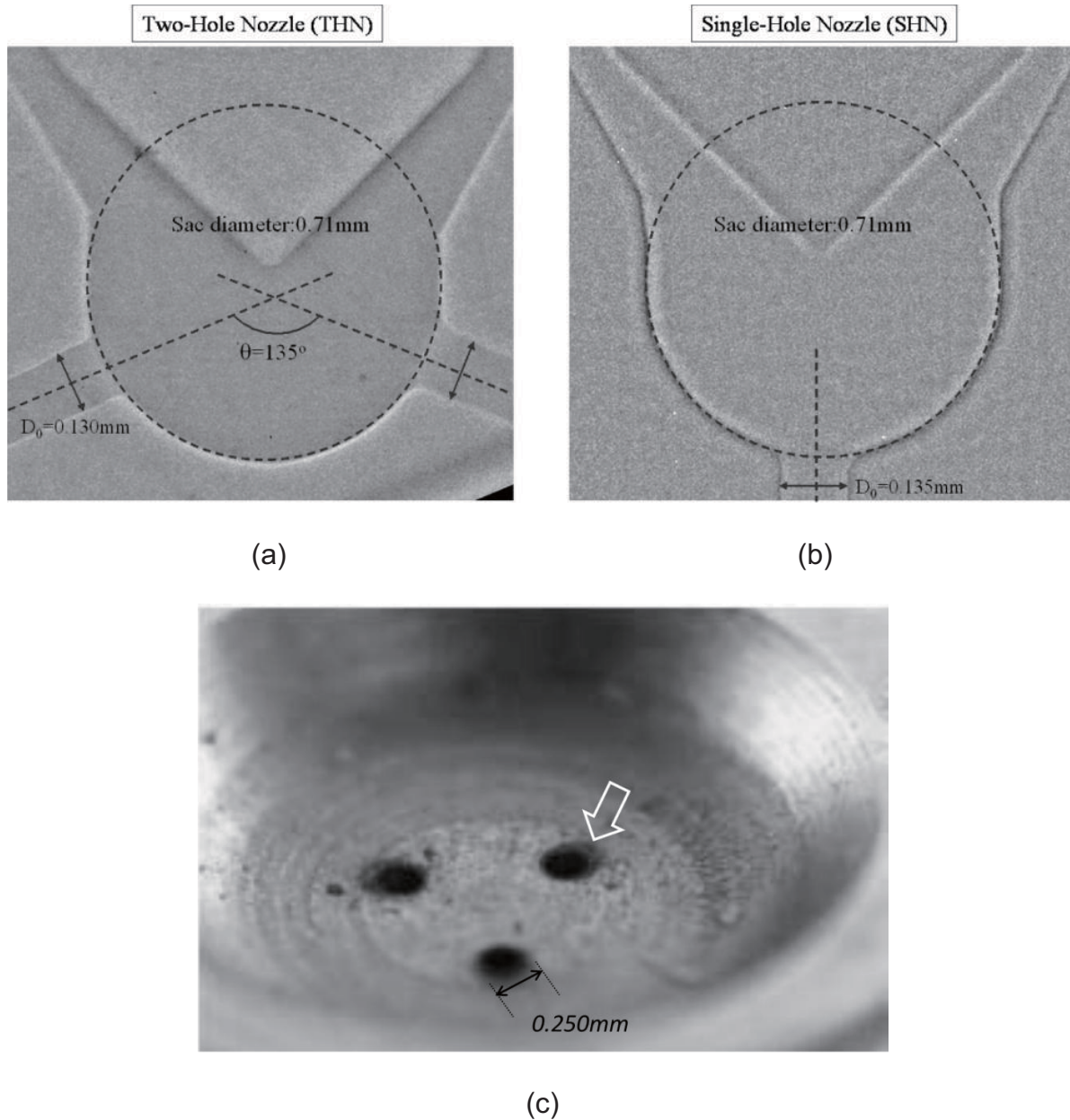


Figure 3.1 Internal nozzle structure of diesel injectors: two-hole nozzle (a) and single-hole nozzle (b) nozzles captured using phase-contrast imaging technique; (c) the close-up view of three-hole GDI injector nozzle tip

Table 3.1 shows the specifications of the DI diesel and gasoline injectors. A single-hole nozzle (SHN) with the orifice diameter (D_o) of 0.135 mm was used in this study as a reference nozzle. A two-hole nozzle (THN) with the nozzle angle between two-orifices of 135° was used as the test nozzle and compared with the single-hole nozzle. The nozzles of THN injector are tapered holes, with the diameter at the nozzle inlet 130 μm and 110 μm at the nozzle outlet. The injection pressure range applied for these two injectors varied from 30 MPa to 100 MPa. To investigate the near-nozzle flow characteristics in the quasi-steady injection stage, relatively longer injection pulse duration (3.0 ms) than that of real Diesel engines was applied. Experiments were performed under room pressure and temperature conditions. The injector design and spray of gasoline DI injector resembles those of DI diesel injectors. A three-hole nozzle GDI injector is used because it represents the basic nozzle geometry of the current multi-hole nozzle GDI injector but without too many spray plumes to complicate the field of view. The injector nozzle has the orifice diameter of 250 μm , the L/D aspect ratio of 1.4, and the inclination angle with the injector axis of 20° .

The fuel properties for the DI diesel injectors and gasoline injector are shown in Table 3.2. Diesel was used as the test fuel for single-hole nozzle injector and two-hole nozzle injector. To conduct CFD simulations for GDI three-hole injector, the n-Decane properties were used to better approximate the X-ray spray experiment conditions.

Table 3.1 Specifications of tested injectors for internal nozzle flow

	Diesel injector		Gasoline DI injector
Number of nozzles	Single-hole	Two-hole	Three-hole
Nozzle diameter, mm	0.135	0.130	0.25
L/D aspect ratio	6	6	1.4
Injection pressure, MPa	30, 100	30, 100	10
Injection duration, ms	3.0	3.0	1.3
Fuel	Diesel	Diesel	n-Decane

Table 3.2 Fuel properties

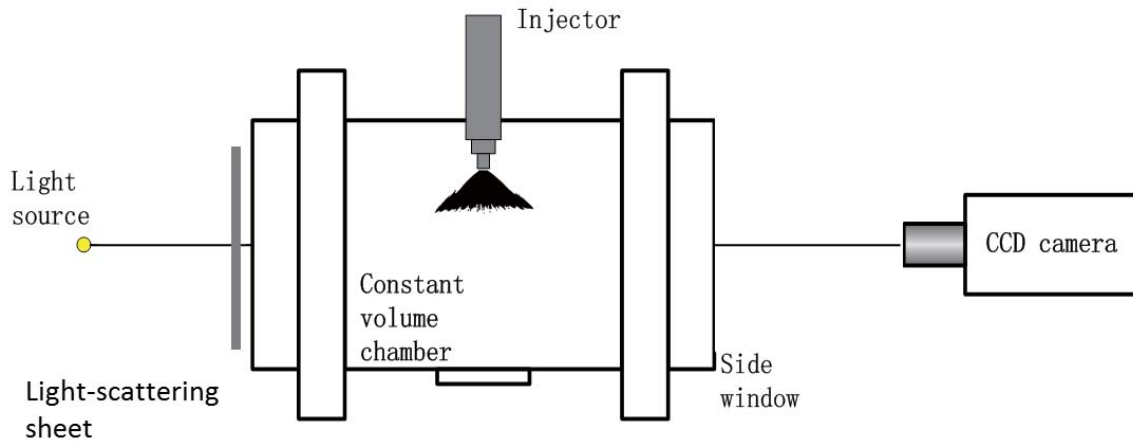
	Diesel	n-Decane	Ethanol	Gasoline	Iso-octane
Density [kg/m ³]	856	726	785	737	692
Viscosity [10^{-6} m ² /s]	3.18	1.223	1.52	0.46	0.65
Surface Tension [10^3 N/m]	28	23	21.9	22	18.2
Latent Heat of Vaporization [kJ/kg]	865	263	865	380-500	298

3.1.2 Spray Visualization Setup

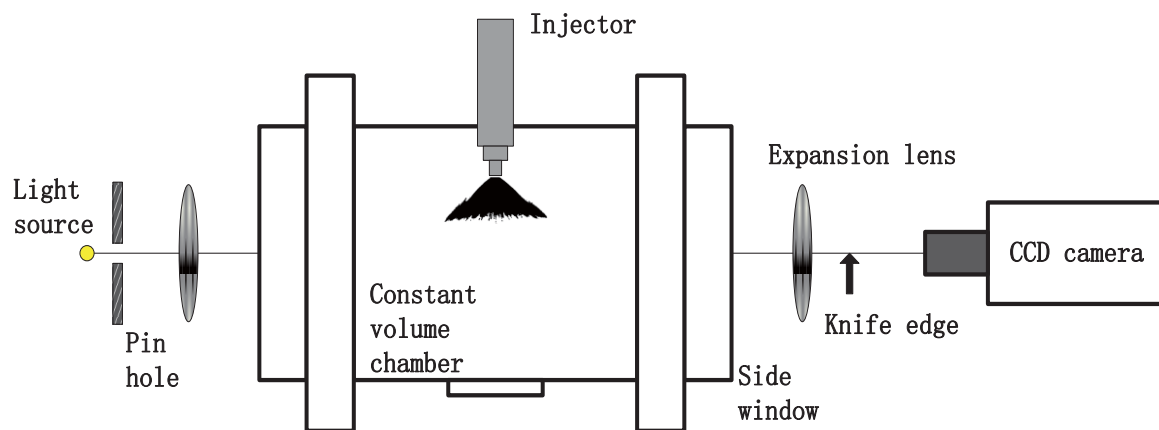
The spray and wall impingement visualization experiments are conducted using a spray constant volume vessel chamber without charge motion. The spray vessel testing is suitable for detail study of the spray and vaporization, wall impingement and surface wetting.

Back-lighting visualization (Fig. 3.2a) is a simple method, which can obtain both vapor phase and liquid phase as a shadow. Schlieren visualization technique (Fig. 3.2b) was carried out to characterize the sprays of both side-mounted multi-hole nozzle injector and outwardly opening piezo-driven direct injector in a conditioned pressure chamber. Then the experiment apparatus were setup for the calibration and measurement of liquid fuel film thickness for the same injectors using the Refractive Index Matching technique.

The experiment apparatus and optical setup for the Schlieren spray visualization method is schematically presented in Fig. 3.2b. The chamber is made of carbon steel and has a cylindrical shape which inner diameter and length are $\Phi 150 \text{ mm} \times 180 \text{ mm}$. The light from a projection lamp formed parallel rays after travelling the tiny pinhole and the expansion lens. The collimated light then passed through the chamber and focused by another lens. A knife edge is placed on this focal point to block half of the refracted light. Finally, the beam came into the high speed digital camera with a resolution of 512×512 pixels. The CCD camera was synchronized with injector driver by a signal generator.



(a)





(b)

Figure 3.2 Experimental setup of spray visualization. (a) Back-lighting, (b) Schlieren.

The spray visualization experiments were performed using a high-speed digital camera to image the spray structures under typical DI engine fuel injection conditions. Both 100% pure ethanol (E100) and RON-91 (Research Octane Number 91) gasoline were tested as shown in Table 3.2. The results for two multi-hole GDI injectors, with specifications listed in Table 3.3, are presented. Injector A is a

production injector which is designed for the production metal engine used in this research and injector B is a prototype injector for optical engine experiments. Injector B has larger orifice diameter and thus higher flow rate compared to Injector A because it is designed for E85 compatible engines which requires more fuel delivered during operation with high concentration of ethanol fuel. The Injector A with pure ethanol, injected at 10 MPa, is the default baseline in this research, and the spray images are taken at 1 ms after start of injection (ASOI), unless otherwise specified.

Table 3.3 Specifications of tested injectors for spray


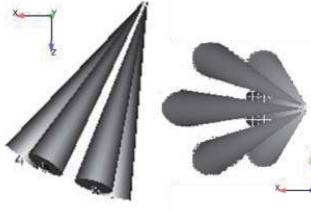
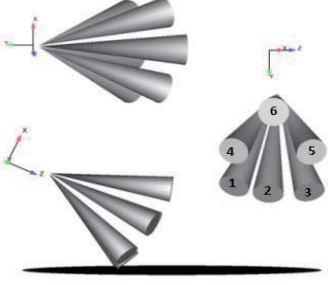
	Multi-holes injector A	Multi-holes injector B
Nozzle diameter (mm)	0.230	0.263
Nozzle length (mm)	0.31	0.30
Averaged L/D ratio	1.36	1.14
Number of holes	6	6
Static mass flow with N-Heptane (g/s)	15.9	20.5
Example of spray image		

3.1.3 Spray Impingement and RIM Setup

Table 3.4 shows the injector specifications and conditions of the outwardly opening piezo-driven injector and the two side-mounted multi-hole GDI injectors (MHN) for wall impingement and RIM tests. The spray angle of the outward opening PDI injector is 92.28° . Both multi-hole injectors have 6 nozzles and the spray targeting is shown in Table 3.4. The injection pressure was set at 10MPa which can be changed by regulating the nitrogen pressure at the fuel tank. Injector C has much smaller orifice diameter with the spray pattern more accumulated. The spray chamber can be heated up to 250°C by circulation air heater and pressured up to 4 bar through controlling the valves.

Table 3.4 Specifications of tested injectors for wall impingement

	piezo-driven direct injector	Multi-holes injector C	Multi-holes injector D
Nozzle Diameter [mm]	4	0.104	0.225
Nozzle Length [mm]	-	0.23	0.285
Averaged L/D	-	2.21	1.25
Number of holes	Hollow cone	6	6

Static mass flow with N-Heptane [g/s]	35	4.00	15.4
Example of spray image (side view)			

The wall impingement experiments for outwardly opening PDI injector and multi-hole injector C were performed using the pure ethanol. In the tests of liquid film thickness calibration and measurements using RIM technique, pure iso-octane was used as the fuel. The fuel properties of ethanol and iso-octane are shown in Table 3.2.

The thickness of the liquid fuel film was measured using the Refractive Index Matching (RIM) technique. The experiment setup for calibration and PDI injector film measurement is displayed in Fig. 3.3. Two 140 mm diameter 50 mm thick quartz windows were mounted on the sides of the chamber and one 60 mm diameter 20 mm thick quartz window was on the bottom. A ground glass diffuser, 50 mm in diameter and 2 mm thick, was maintained under the injector with a distance of 10 mm from the injector tip. The top surface of this commercial quality BK7 quartz was polished by grits. Polished diffusers have the advantageous of surface uniformity

and 1500 grits level provides very fine scattering. Lighting from a continuous 65 Volte projection lamp was provided from the side window with an incident angle of about 10° . The images were captured with the high speed digital CCD camera through a mirror placed directly beneath the impingement surface and outside the spray chamber.

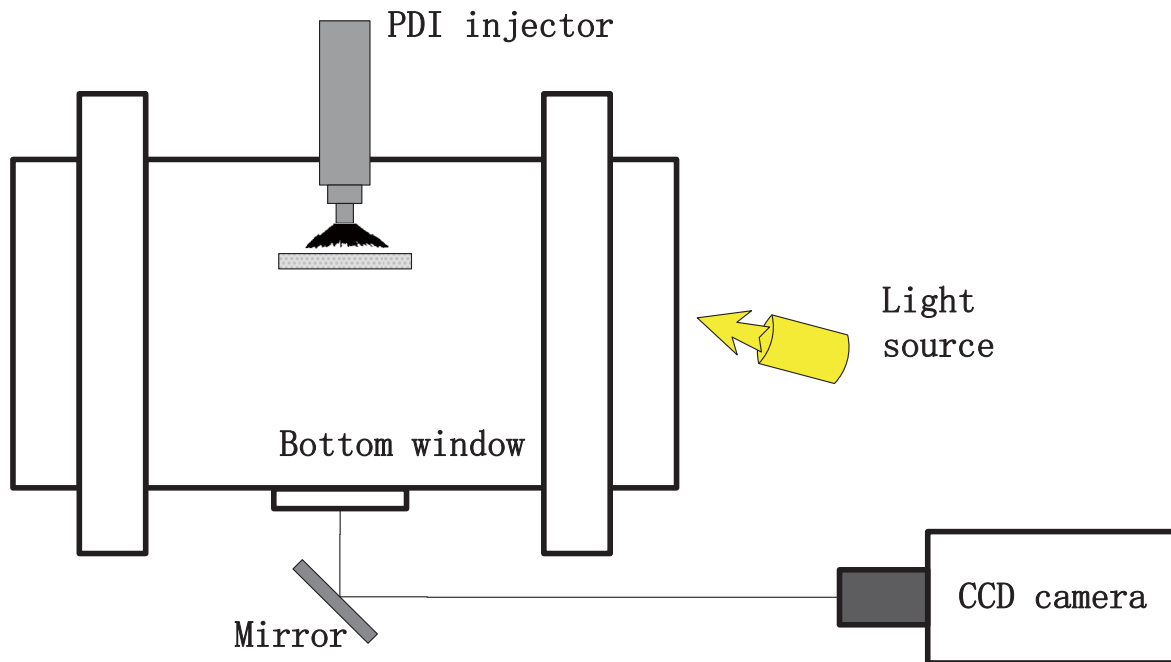


Figure 3.3 Experimental setup of RIM visualization for PDI injector.

The RIM measurement setup for the multi-hole injector C is shown in Fig. 3.4. The impingement window was placed in the camber with angle of 23° to replicate the piston injector orientation of a side-mounted GDI Engine. The window plate used for multi-hole injector has the same specifications with the one used for PDI injector except the shape is square (100 mm \times 100 mm). The perpendicular distance between the top surface and the injector tip was set at 20 mm. A continuous 65Volte lighting through a mirror placed beneath and outside the chamber to the

impingement surface. The images were captured through side window of the spray chamber with the high speed digital CCD camera.

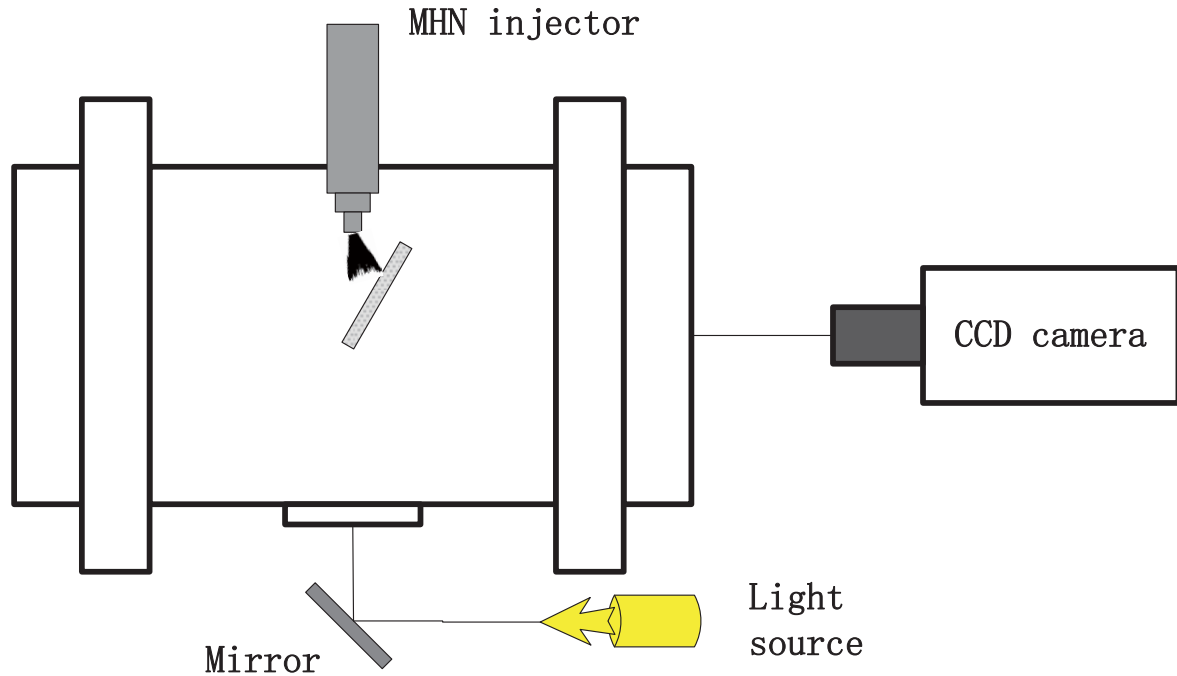
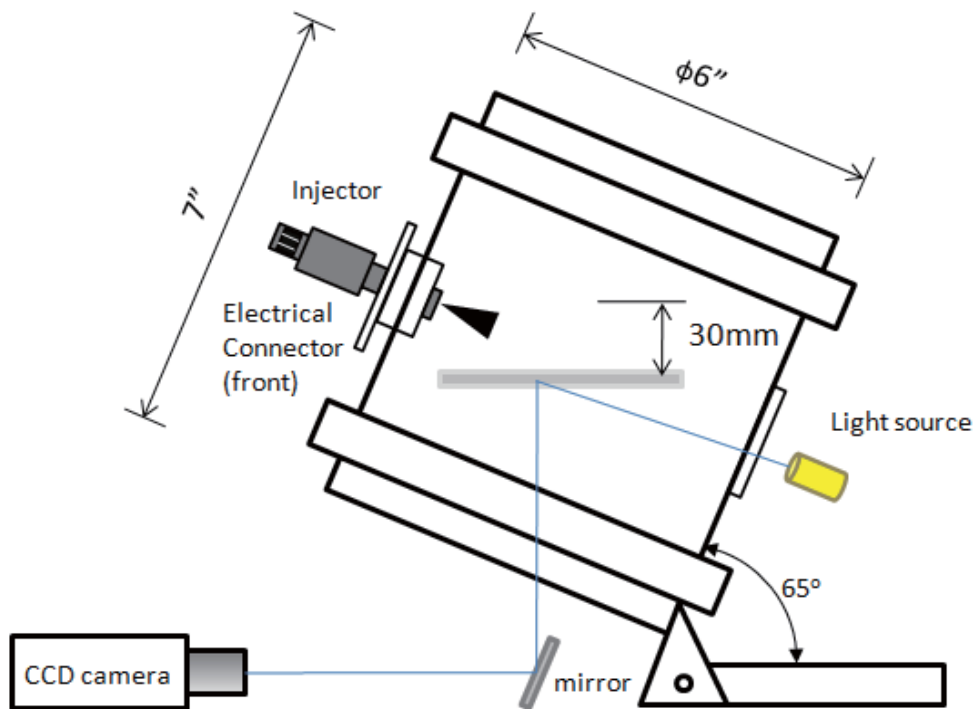


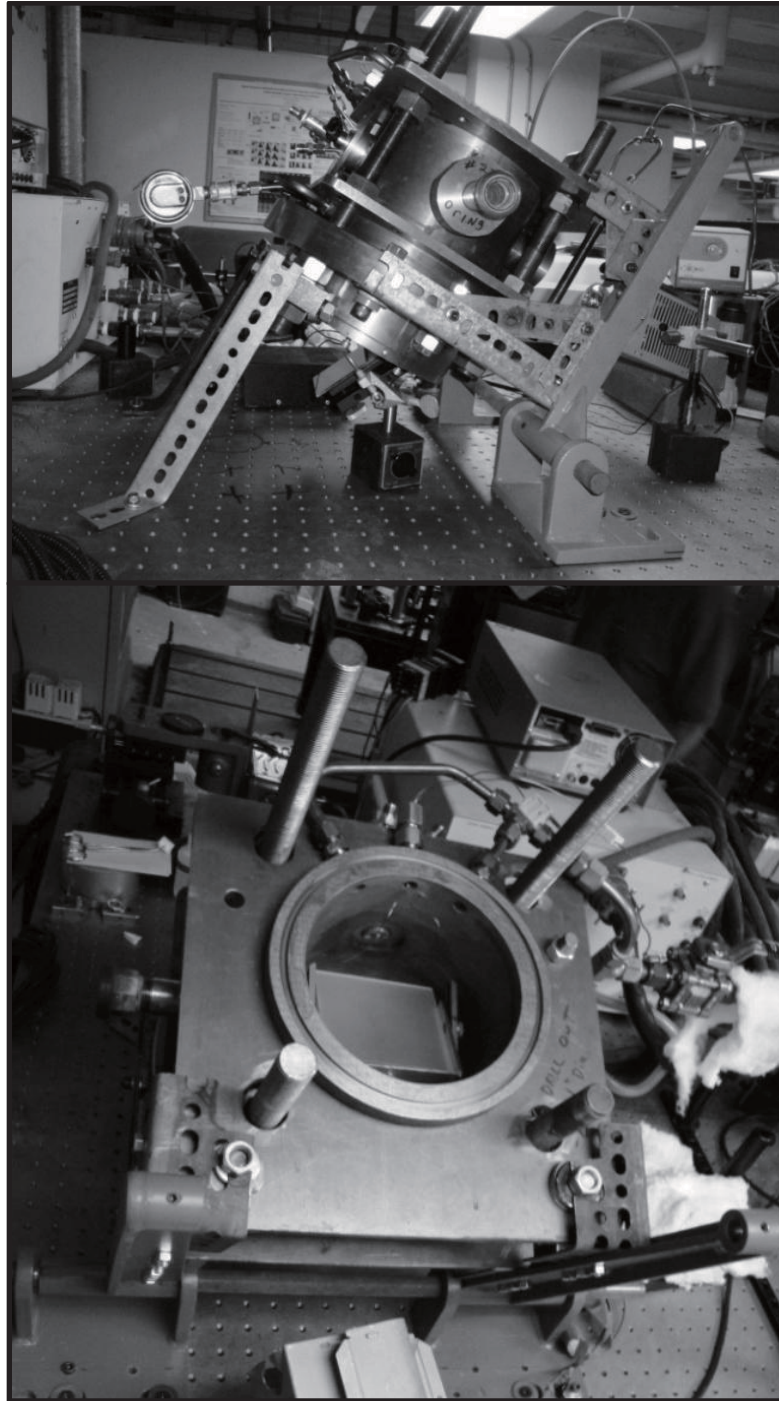
Figure 3.4 Experimental setup of RIM visualization for multi-hole injector C.

One hypothesis in RIM method is that the thickness of film is uniform. To avoid the nonuniform film caused by gravity effect in Fig 3.4, the RIM measurement test for multi-hole injector D use the setup as shown in Figure 3.5. The six-hole GDI injector D was mounted on the cylinder wall of the chamber with angle of 25 deg. The injection specifications are shown in Table 3.4. Two 140mm diameter 50mm thick quartz windows were mounted on the sides of the inclined pressurized chamber (the inclination angle of the chamber is 65 deg) and one 60mm diameter 20mm thick quartz window was on the bottom. The pressurized chamber can be heated up to 250°C by a circulation air heater and pressured up to 4bar. A flat

optical ground glass diffuser (N-BK7, Thorlabs), 100mm × 100mm, 2mm thick was placed in the pressurized chamber horizontally. Various grit polishes on the diffuser were tested, but the results presented of this paper were obtained using the 220 grit polish, which shows the best sensitivity to the range of film thickness of interest, which is around 1 micron. Lighting was provided by a continuous projection lamp from the side window with an incident angle of about 10°. The images were captured with the high speed digital CCD camera through a mirror placed directly beneath the impingement surface and outside the spray chamber.



(a)



(b)

Figure 3.5 Experimental setup of RIM visualization for multi-hole injector D: (a) schematic image, (b) photograph.

The RIM technique measures the spatial distribution of the fuel film thickness, from which the adhered puddle mass can be calculated. In this method, the difference in index of refraction between the impinging surface and air results in the scattering of light off the roughened surface, which is modified by the presence of a liquid that closely match the index of refraction of the impingement window [73]. Drake et al. [61, 72] showed that the relation between the fuel film thickness and the variation of intensity in the scattered light. The reflection variation (reduction) through the window was written as:

$$\Delta I(x, y) = 1 - \frac{I_{wet}(x, y)}{I_{dry}(x, y)}$$

where I_{dry} is the intensity of the scattered light in reference image at the location of (x, y) and I_{wet} is the intensity with liquid deposit.

After the calibration procedure was performed, a function f can be built between the liquid film thicknesses $h(x, y)$ and the reflection variation in the scattered light ΔI :

$$h(x, y) = f(\Delta I)$$

The calibration was carried out at ambient condition for PDI injector and multi-hole injector C. The experiment setup was shown in Fig. 3.3 without the injection system. By an AccuPet Pro precision digital syringe, a known volume liquid was dropped on the roughened window surface. The minimum volume that can be

delivered was 0.1 μ L. The averaged reference dry image was obtained before the liquid being deposited on the window. The liquid droplet rapidly expansions after it deposits on the roughened window surface. Once the liquid film has reached the maximum surface, the image was used as a calibration point. The threshold value of the deposit wet area in the image was calculated using Otsu's method in MATLAB software and then the number of black pixels was counted to obtain the area size. The reduction in the scattered light ΔI can be calculated similarly. After repeating a range of liquid volumes, the calibration relation curve was found as shown in Figure 3.6.

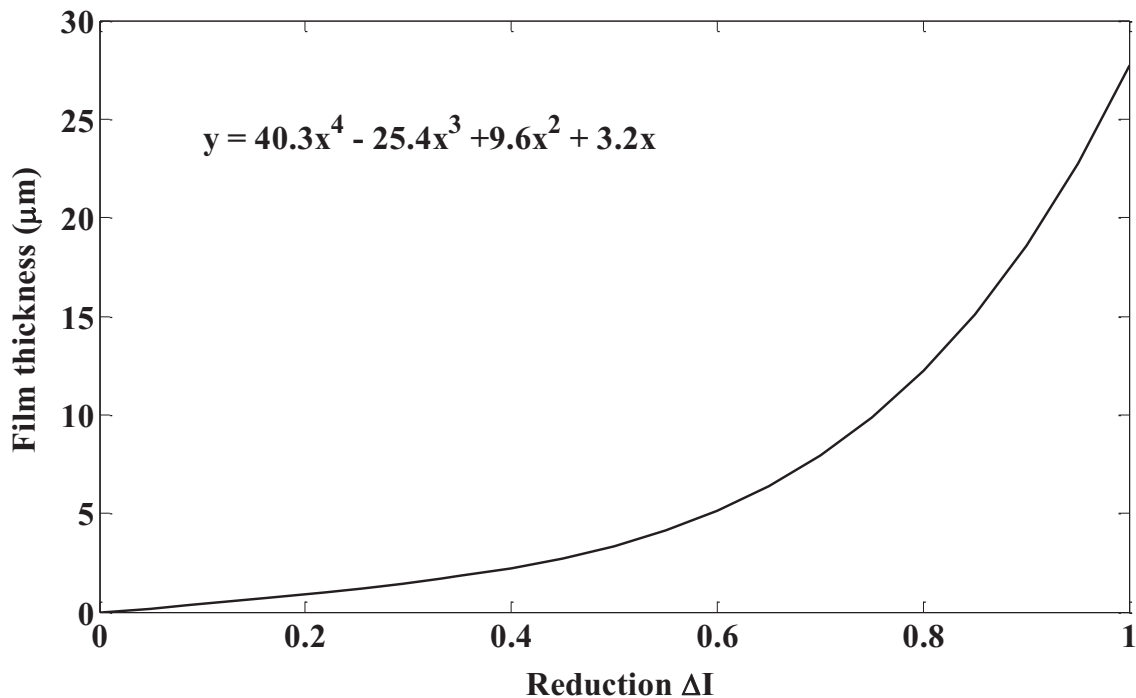
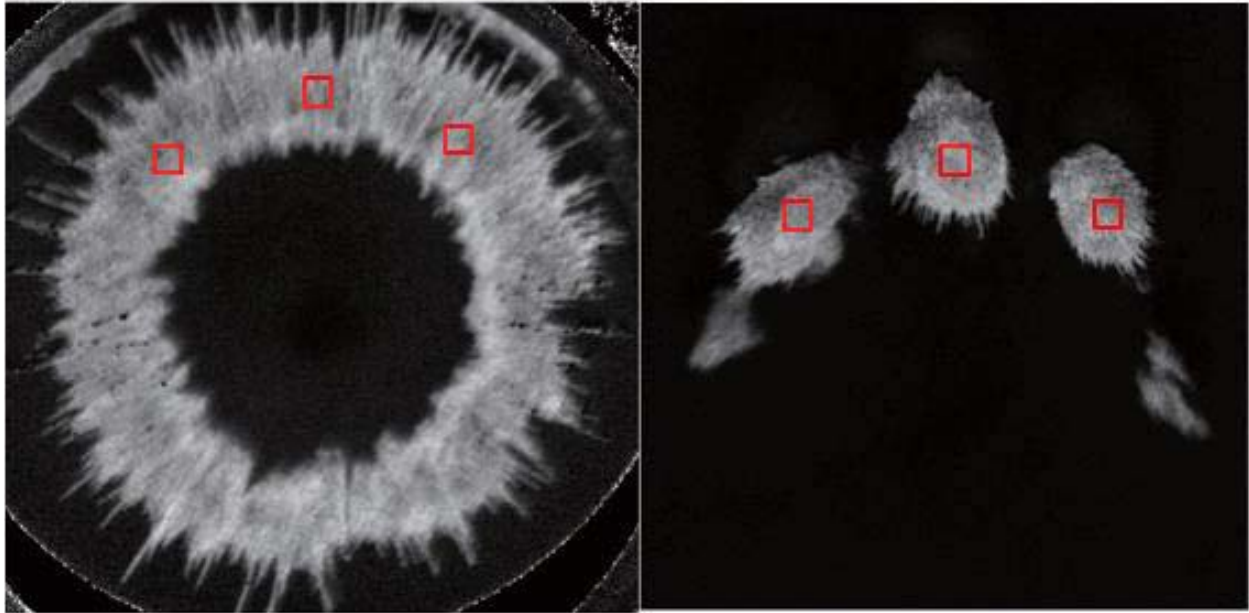


Figure 3.6 Calibration curve for the rough window between liquid film thickness and reduction

Three square regions were selected in the central part of the annular deposit for the PDI injector and on each plume point for the multi-hole injector as shown in Fig. 3.7 respectively. The reduction in the scattered light ΔI was calculated for each

rectangular area. The liquid film thickness was obtained by averaging for these 3 square regions.



(a)

(b)

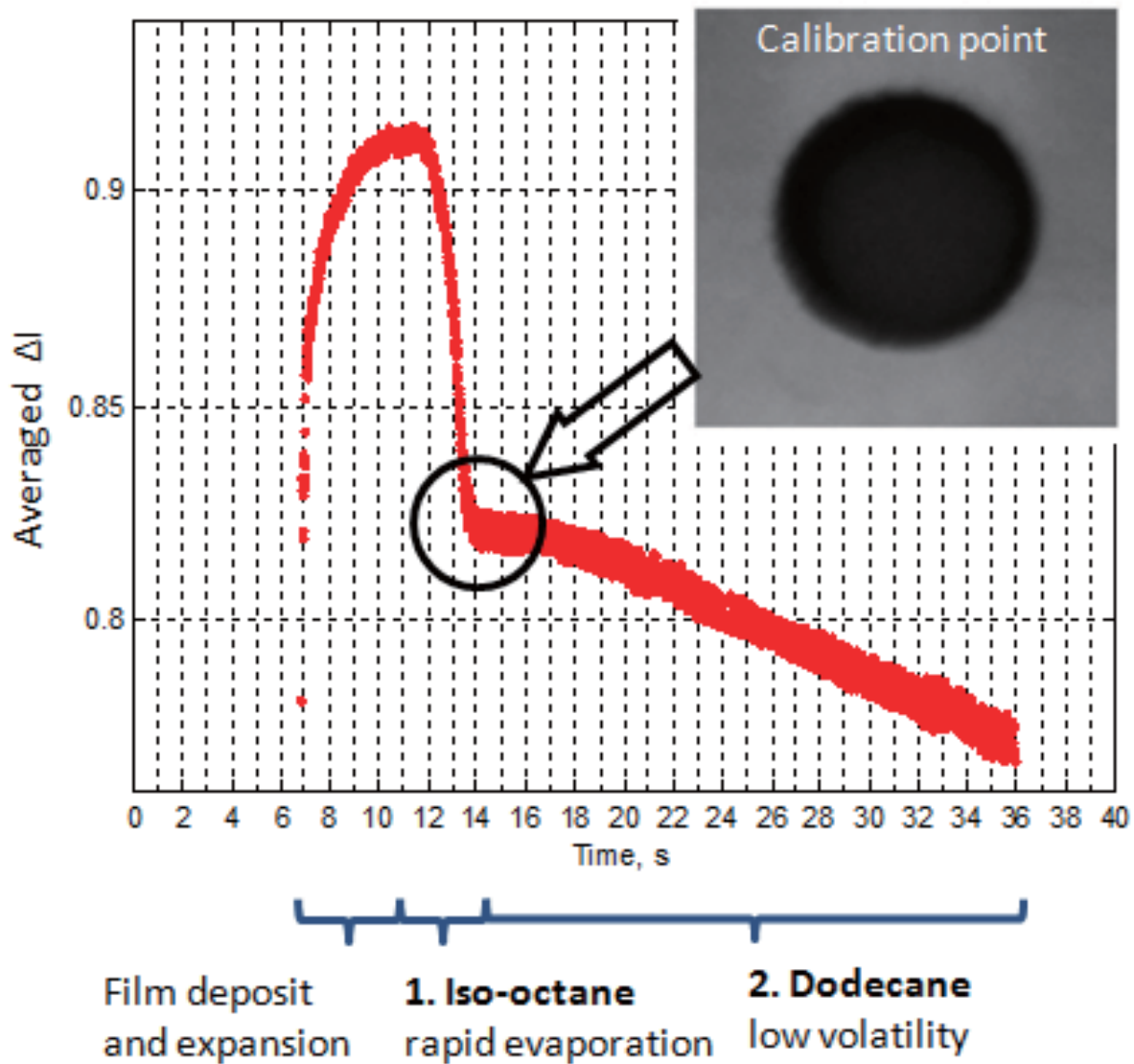
Figure 3.7 Computation regions of (a) PDI injector and (b) multi-hole injector C

In the RIM test of side-mounted multi-hole injector D, A liquid mixture of a high volatility component (iso-octane) and a low volatility component (dodecane) with known deposit volume was used for calibration procedure similar to a recent study by Maligne and Bruneaux [74]. Spray impingement and liquid film thickness measurements were performed using iso-octane as fuel. The index of refraction of Iso-octane and dodecane is 1.40 and 1.42 respectively, which is close to the index of refraction of the window material, 1.46. The calibration experiment was carried out at ambient condition to obtain the correlation between fuel film thickness and variation of reflection. The experiment setup is the same as shown in Fig. 3.5, but without the injection system.

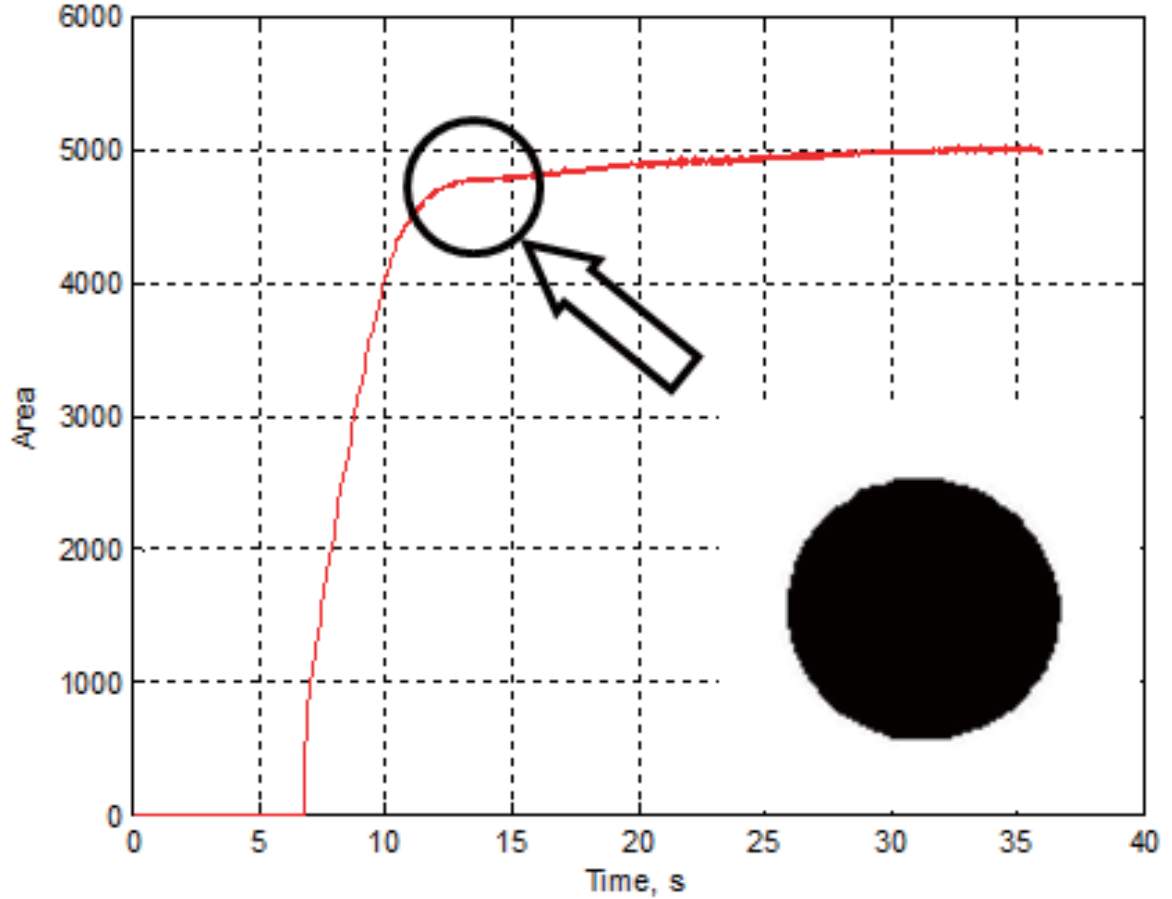
To improve the measurement of liquid fuel film thickness, a liquid mixture of 10% by volume of dodecane and 90% by volume of iso-octane was used for calibration procedure instead of single component calibration fuel. Fig. 3.8 shows the time evolution of the averaged reduction in the scattered light and deposit area. The liquid mixture was dripped on the dry window by syringe and the scattering reduction value increased from 0 to maximum. After the deposited film expanded, the mixture rapidly evaporated as noted in stage 1 in Fig. 3.8a. The corresponding reduction dropped in less than 3 second to the calibration point. It is assumed that the high volatility component (iso-octane) in the mixture was completely evaporated before this calibration point and only the low volatility component (dodecane) remained on the window surface [74]. The dodecane then evaporated relatively slowly and the scattering reduction decreased to the value of dry window in around 24 seconds after the calibration point.

At the calibration point, the dodecane volume and the corresponding deposit area, as shown in Fig. 3.8b, were used to obtain the fuel film thickness. The minimum volume delivered by the syringe was $0.1\mu\text{L}$ in this study. Therefore, the dodecane volume was calculated as 10% of the initial volume of mixture droplet, which provided a very thin film thickness. Fig.3.8b shows the film wetted area at calibration point. The threshold value of this deposit area in the binary image was found using Otsu's method in MATLAB software and the number of pixels below the threshold was counted to obtain the size of area. It is assumed that the film thickness is uniform. Therefore, the fuel film thickness could be obtained at the calibration point from the dodecane volume and the wetted area. The averaged

reference dry image was obtained before the liquid was deposited on the window surface. The mean reduction in the scattered light can be calculated from the reflection variation equation. The calibration technique used in the current system is not sensitive enough to resolve thickness below 0.5 microns and thicknesses less than that are extrapolated to zero point by default. After repeating a range of liquid volumes, the calibration relation curve is shown in Fig. 3.9.



(a)



(b)

Figure 3.8 Evolution of the mean intensity in the wetted surface on the window and calibration point of multi-hole injector D configuration: (a) Evolution of averaged reduction ΔI on the window, (b) Evolution of deposit wetting area

After the calibration procedure, the six-hole injector was mounted on the cylinder wall of the chamber with angle of 25 deg as shown in Fig. 3.5. Fuel was injected on the rough flat window surface at various ambient conditions, injection conditions and distance between the injector tip and window, using the same optical setup.

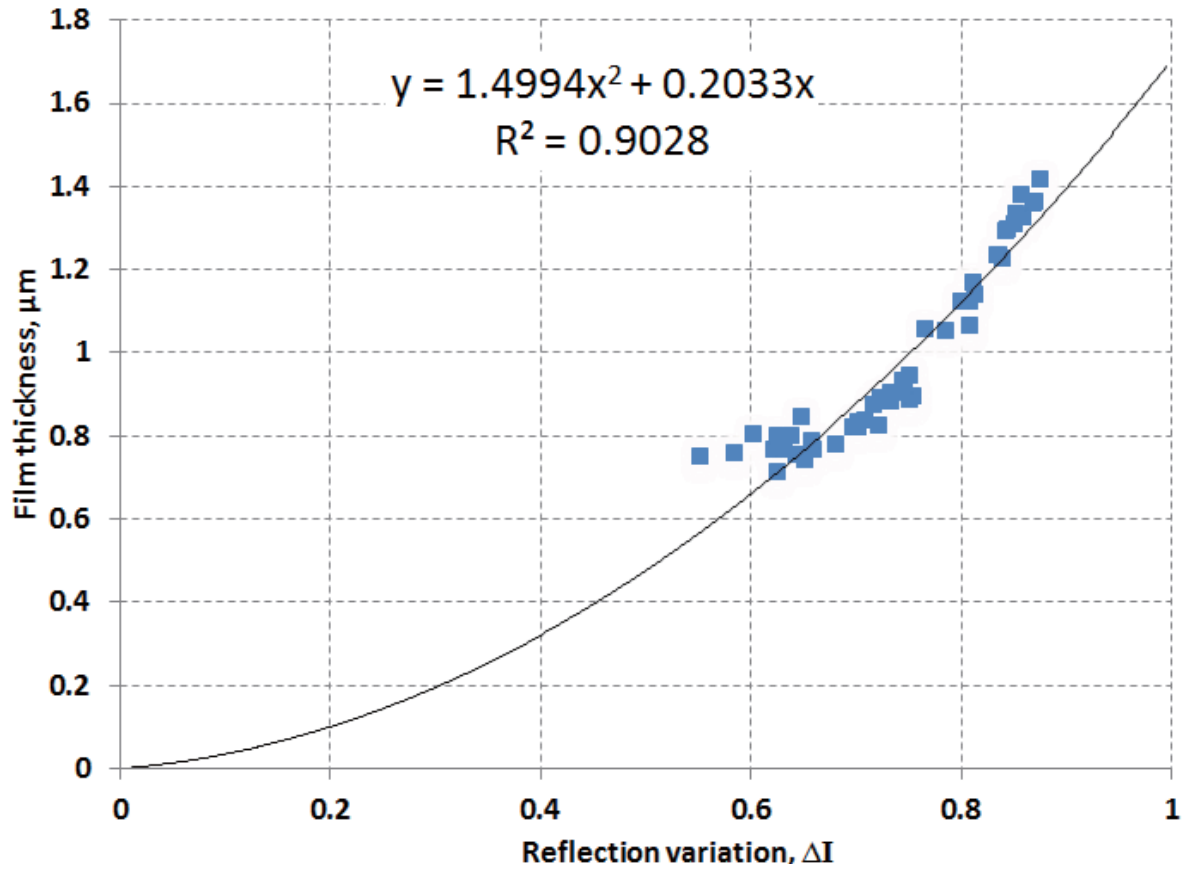


Figure 3.9 Calibration curves for multi-hole injector D

The processing of RIM experiment images was shown in Fig. 3.10. First, the averaged reference image was subtracted from the wetting images to calculate the reduction in scattered light ΔI . This was then converted to a binary image that was used to obtain the instantaneous area of deposit film. The threshold that converts the intensity image into the binary image was calculated by Otsu's method, which minimizes the intraclass variance of the black and white pixels. To eliminate the noise on the background image, time and space filtering were carried out to improve the image quality. For the time filter, a fixed-point filter is used to average a

sequence of images with window size of 10. For the space filter, a mean filter is adapted to 4x4 blocks. Fig. 3.10d and Fig. 3.10e show the filled contour of images that applied the time filter and space filters, respectively. Color coded image is used to accentuate the intensity, with the red region representing a high intensity, and blue region, low intensity.

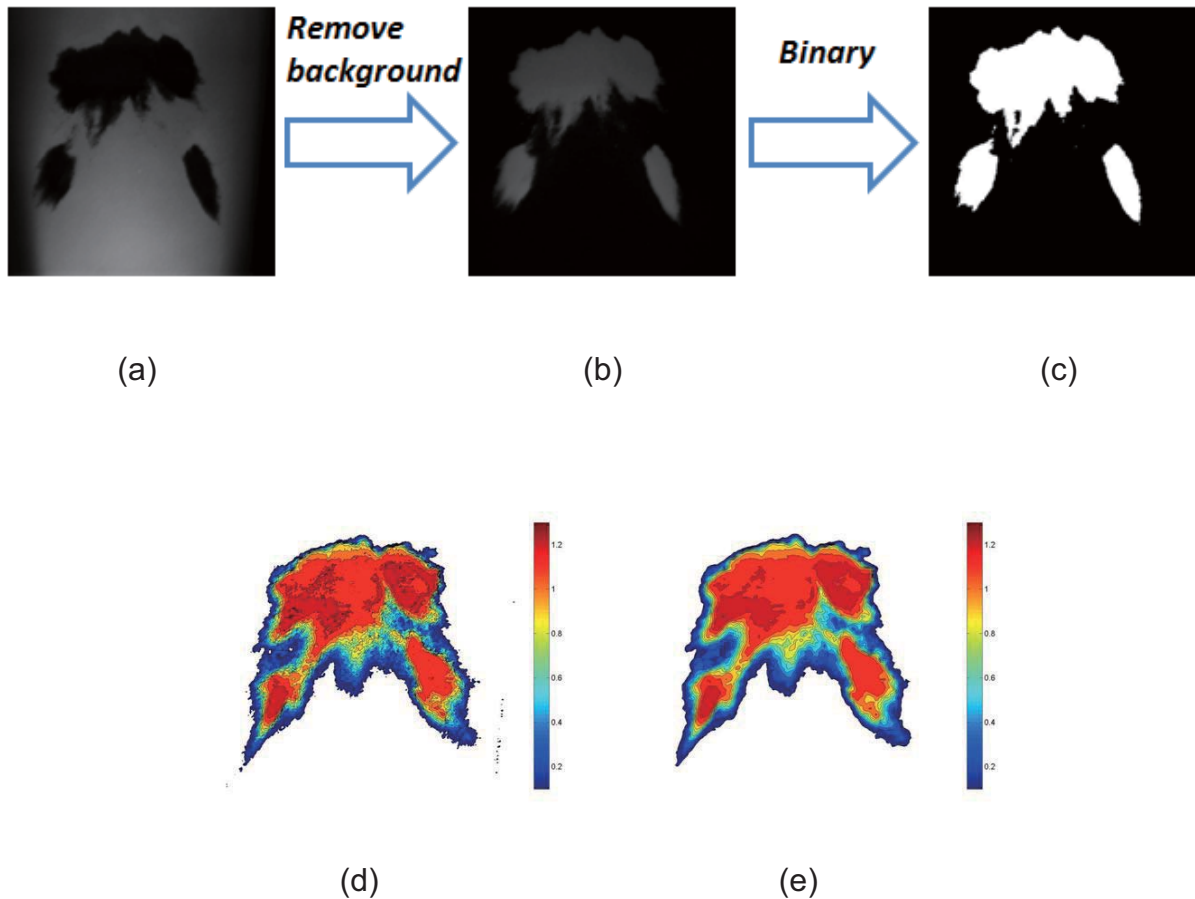


Figure 3.10 Image processing of the RIM images, (a) Raw image, (b) Background removed image, (c) Binary image, (d) Time filtered image, and (e) Time and space filtered image.

3.1.4 Optical Accessible Engine

An optical accessible engine (OAE) which utilizes the same cylinder head, injector, cams, and shares the same 86-mm bore as a production 2-litre engine, is used for the spray mixing investigation and compared with CFD simulations. The optical engine has quartz liner and Bowditch quartz to provide side- and bottom-view spray visualizations inside the cylinder (Fig. 3.11). A Phantom 7.1 CMOS high-speed digital camera is used for the imaging with solid lighting provided by continuous projector light source for both the Mie and Schlieren imaging techniques.

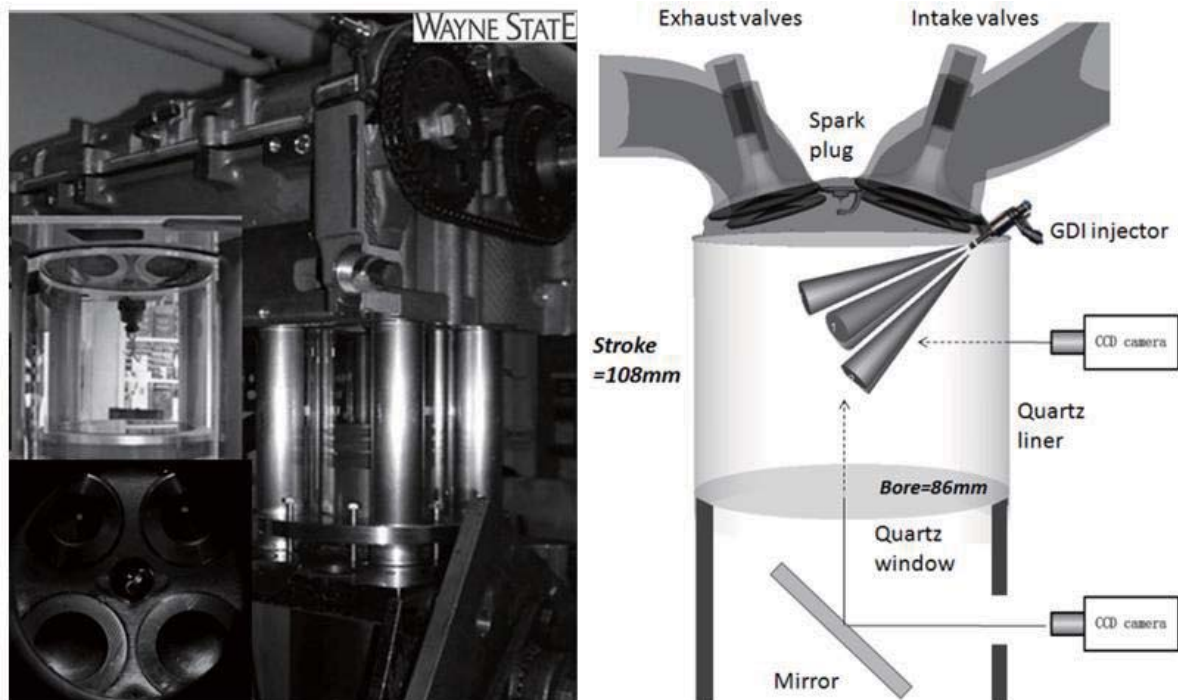


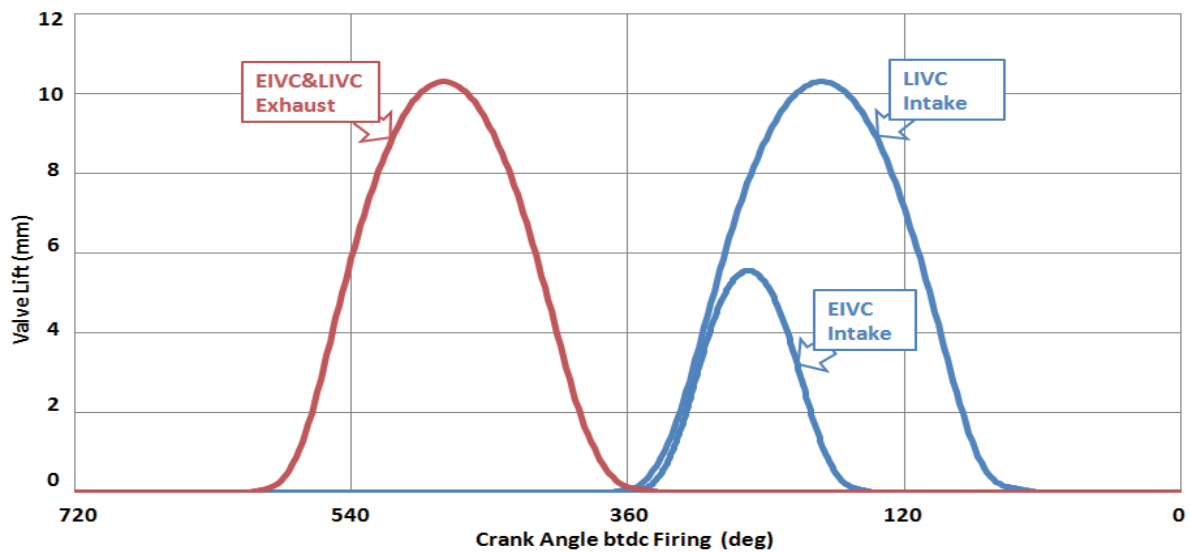
Figure 3.11 Schematic and photograph of the Optical Engine.

Optical engine piston has a flat top while the piston head of metal engine has a bowl and valve recesses as shown in Fig. 3.11. Major specifications of engines are

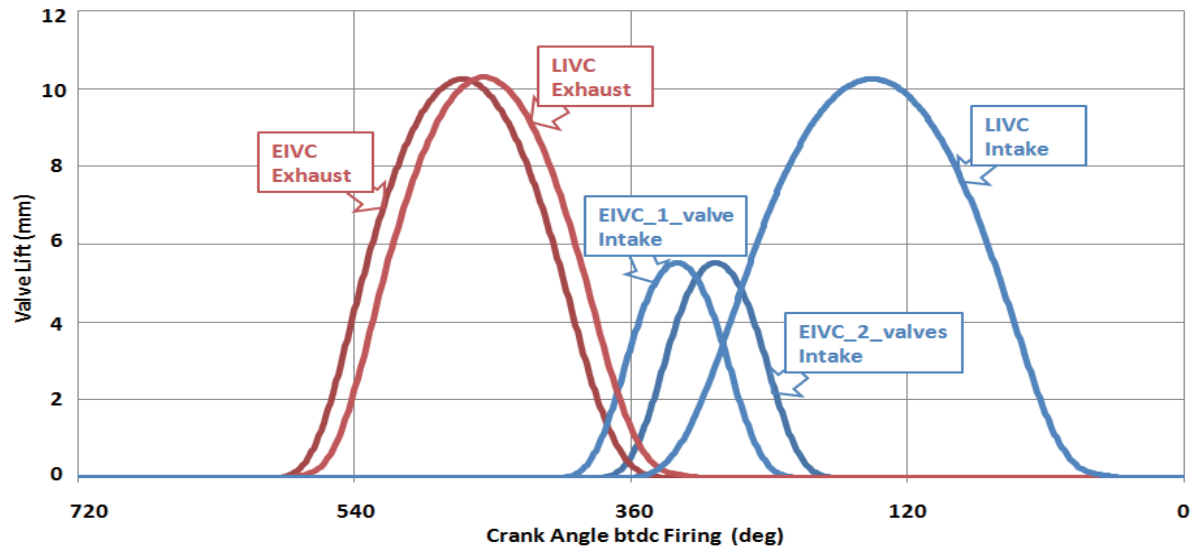
listed in Table 3.5 and the cam profiles are illustrated in Fig. 3.12 for optical engine and metal engine respectively. Table 3.6 shows the operation conditions of the metal engine cases.

Table 3.5 Specifications of the engines.

	Optical Engine	Metal Engine
Piston Head	Flat	Bowl
Injector Type	Injector A, B	Injector A
Bore, mm	86	86
Stroke, mm	108	86
Compression Ratio	10.9	11.9
Engine Speed, rpm	1000	1500, 2000



(a)



(b)

Figure 3.12 Cam profiles of (a) Optical Engine and (b) Metal Engine. Early Intake Valve Closing (EIVC) and Late Intake Valve Closing (LIVC).

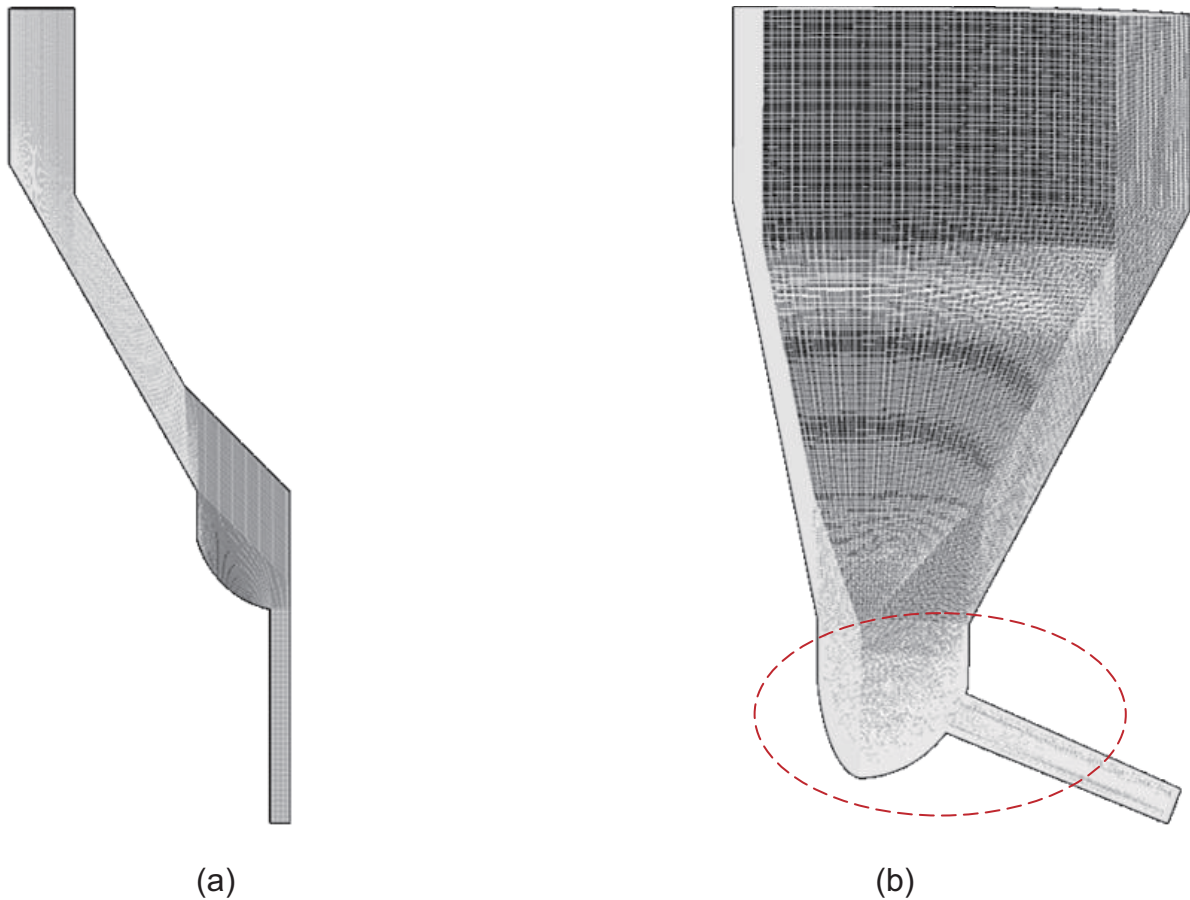
Table 3.6 Operation conditions of the metal engines.

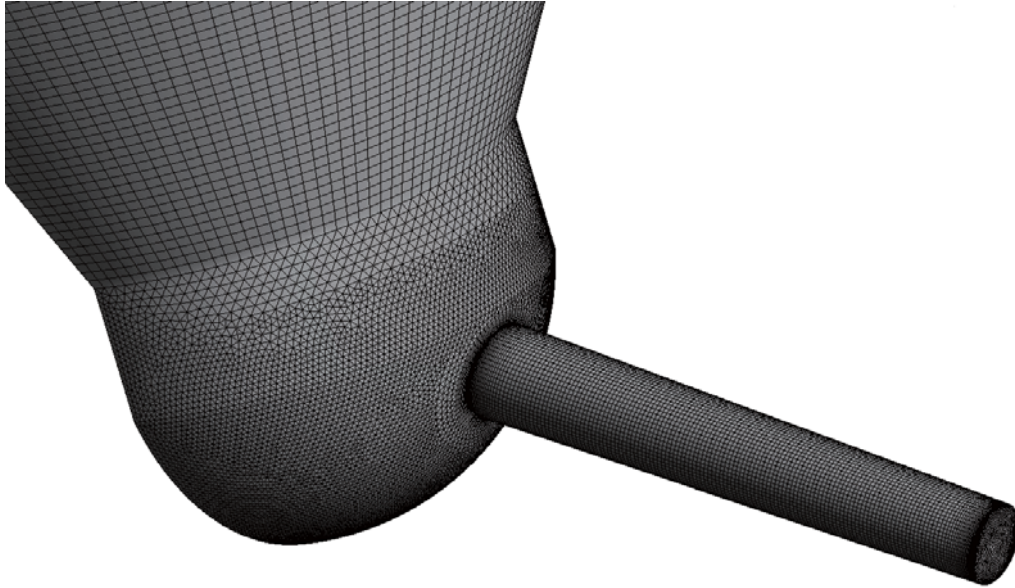
	EIVC		LIVC	
Intake valve(s)	2 valve	1 valve	2 valve	1 valve
Engine Speed, rpm	2000	2000	1500	1500
BMEP, bar	2	2	8	8
MAP, kPa	53	95	unthrottled	unthrottled
SOI, CA deg, aTDC	410	410	440	420

3.2 Numerical Simulation Setup

3.2.1 Internal Nozzle Flow

CFD Simulation has been shown to correlate the injector design to spray performances [19, 20, 101]. To simplify, the axisymmetric, two-dimensional geometry meshing with a total of 30,000 cells is used for single-hole nozzle, and symmetric geometry with 550,000 cells hybrid mesh is used for two-hole nozzle to begin with, as shown in Fig.3.13. These symmetry assumptions rule out needle eccentricity, surface roughness, and any initial swirl component along the injector axis. The working fluid is a mixture of diesel fuel and vapor. And non-condensable gas is considered.





(c)

Figure 3.13 (a) Geometry for single-hole, (b) two-hole nozzles, (c) mesh strategy of two-hole nozzles. Inj. Pressure: 100 MPa.

To aid the interpretation of the results, steady-state CFD simulation is carried out at full needle lift for both the single-hole and two-hole nozzles using Fluent. As a first step, the Reynolds-Averaged Navier-Stokes (RANS) with standard $k-\epsilon$ turbulence model, and Eulerian full-cavitation model, which is based on the assumption of a continuous mixture of liquid and vapor bubbles having the same velocity, is used.

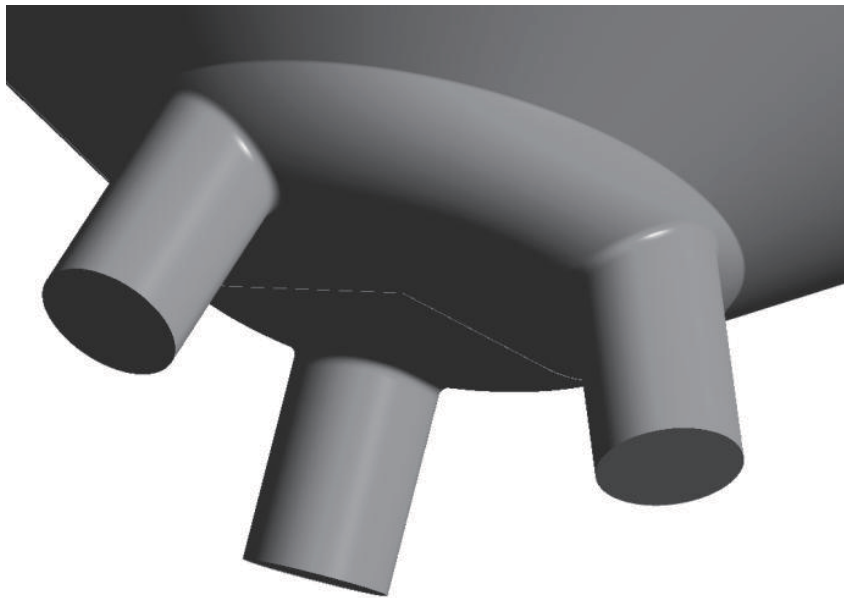
The diagnostics and resolution of cavitation bubbles, which can be sub-micron in size, inside real-size nozzle is much more difficult for visible light techniques and even the current X-ray techniques [102, 103], especially for sac-type nozzles. The simultaneous matching of Reynolds, Cavitation, and Weber numbers of the scale-up model to real-size nozzle also makes it difficult to assess and the effect of scaling on cavitation models from scale-up model to real size nozzle.

However, the hydro-ground hole inlets of both SHN and THN, and the converging nozzle configuration of the THN are known to suppress cavitation and increase discharge coefficients. CFD simulations based on RANS and URANS turbulence models were applied to study the vortex structure and cavitation in injection holes. According to a comparative study of URANS approach with SST turbulence model and Scale Adaptive Simulation (SAS) [43], the current numerical approach, although may be overdamped with numerical dissipation, should be sufficient to compare the mean flow structure of the ideal nozzles tested. Finally, the full nozzle geometry results for both the RANS with standard $k-\epsilon$ turbulence model and the URANS with SST turbulence model were compared.

Fig 3.14 shows the geometry and computation grid (pure hexahedron mesh) of three hole GDI injector. Instead of the well-validated Reynolds-Averaged Navier-Stokes (RANS) with $k-\epsilon$ turbulence model which has been used extensively to show the mean flow features inside the nozzle before (e.g., [104]). It has now been shown that the Unsteady Reynolds-Averaged Navier-Stokes (URANS) with shear stress transport (SST) turbulence model [43] or turbulence scale resolved approaches like Scale Adaptive Simulation (SAS) [43] and Large Eddy Simulation (LES) [16] are needed to better simulate the dynamics of turbulent, vortical and usually cavitation flow and prove a better optimization and design tool.

The SST approach uses a $k-\omega$ formulation in the inner parts of the boundary layer makes the model directly usable all the way down to the wall through the viscous sub-layer, hence the SST $k-\omega$ model can be used as a Low-Re turbulence model without any extra damping functions. The SST formulation also switches to a

k- ϵ behavior in the free-stream and thereby avoids the common k- ω problem that the model is too sensitive to the inlet free-stream turbulence properties. Because of its computational efficiency over LES, this approach as implemented in ANSYS-CFX12.1, with the Eulerian-Eulerian Rayleigh-Plesset cavitation model, is used for this study. The second-order discretization scheme in both spatial and time was used. The boundary conditions are set to be static pressure at the step hole exit, zero gradient for liquid and vapor VOF, zero gradient for other quantities. The computation grid is sufficiently fine with less than 1 micron near the wall and most of y^+ is less than 2, and usually more than 15 nodes inside the boundary layer. The computed flow rate is within 1% deviation to the measurement, in excellent agreement.



(a)



(b)

Figure 3.14 The geometry and computation grid of three hole injector (a) Geometry, (b) mesh strategy (hexahedron).

3.2.2 Spray and Wall Impingement

BREAKUP MODEL

Simulations of multi-hole spray and impingement were carried out using CONVERGE [54], a commercial three dimensional CFD software. The spray droplets undergo a number of subroutines: breakup, collision, vaporization and drop drag. If the fuel spray impact the piston, the formation and evaporation of liquid fuel films should be considered. Among these physical processes, the breakup process is critical to droplet predict velocity and size. In this study, spray characteristics of PDI hollow-cone spray were simulated using LISA-TAB. Once the sheet parcels travel a distance from the injector, the parcels are undergoing collision, drag,

evaporation, and turbulent dispersion. This sheet break up length of LISA model (Fig 3.15) is given by

$$L = \frac{V}{\Omega_s} \ln\left(\frac{\eta_b}{\eta_0}\right)$$

where V the absolute velocity of the liquid sheet, Ω_s is the maximum growth rate, and LISA length quantity $\ln\left(\frac{\eta_b}{\eta_0}\right)$ is set to 12 in this study. The TAB model is used with LISA model to predict secondary drop breakup.

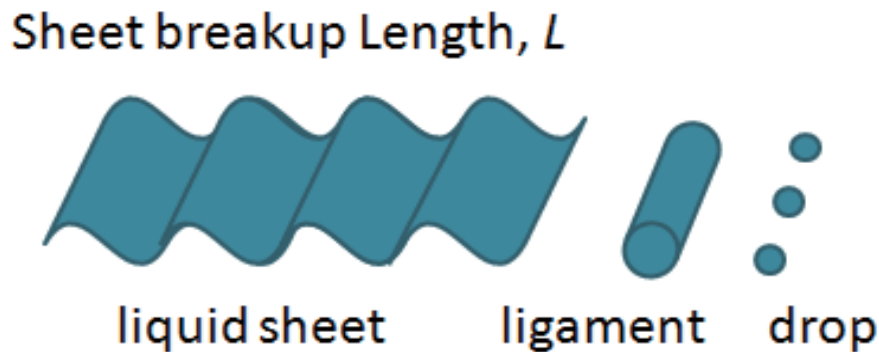


Figure 3.15 LISA breakup model.

Kelvin-Helmholtz/Rayleigh-Taylor (KH-RT) breakup model (Fig. 3.16) was used to predict the spray behavior of multi-hole injector. The KH model simulated the primary aerodynamic instabilities breakup and the RT model calculated the secondary breakup due to decelerative instabilities. For KH-RT breakup model, the breakup length was written as

$$L_b = C_{bl} \sqrt{\frac{\rho_l}{\rho_g}} d_0$$

Where ρ_l and ρ_g are the density of the fuel liquid and the ambient gas, d_0 is the diameter of the orifice, C_{bl} is the breakup length constant and set to 4 and the KH breakup time constant which is determined to be 8 in this study after the comparison with the experimental results. Only KH instabilities are responsible for drop breakup inside of the breakup length, while both KH and RT mechanisms are activated beyond the breakup length.

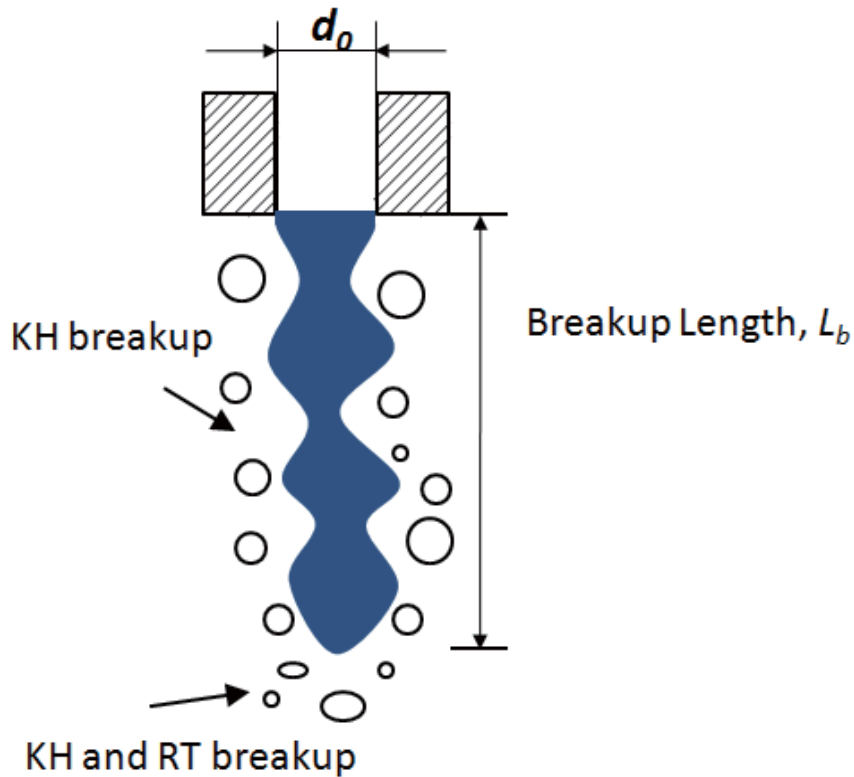


Figure 3.16 KH-RT breakup model.

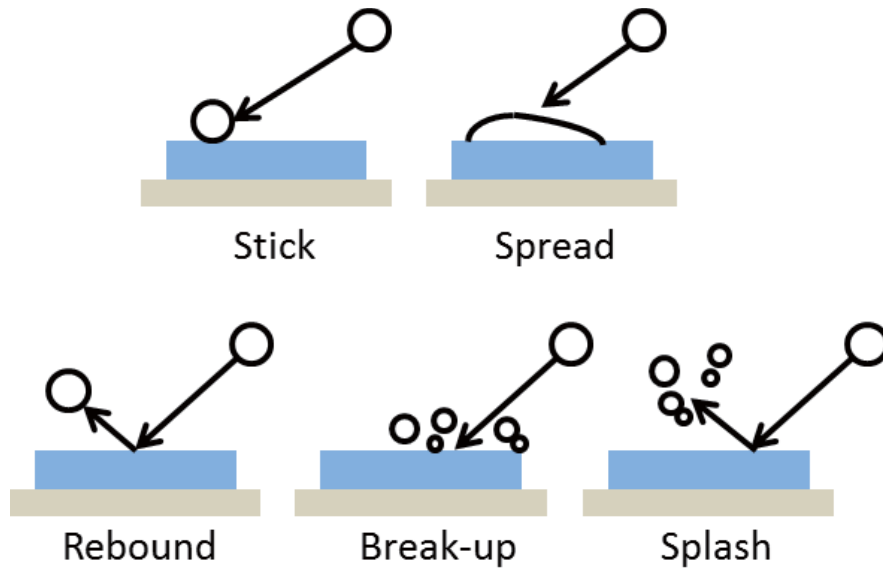


Figure 3.17 Collision regimes of an impinging droplet on a wet wall.

WALL IMPINGEMENT MODEL

Generally, the collision between an impinging drop and a wet surface may result in five different regimes: sticking, spreading, rebounding, breakup and splash [57].

The interaction of liquid drips and solid surfaces is modeled using a wall film model, which is a hybrid model that assumes individual particle-based quantities and film-based quantities [45]. The liquid film transport is modeled by the film momentum equation [46]. The drop Weber number is defined as

$$We = \frac{\rho_l V_n^2 d}{\sigma}$$

where ρ_l is the liquid density, V_n is the drop velocity component normal to the surface, d is the drop diameter, and σ is the liquid surface tension. The criterion for splash [46] is given by

$$E^2 = \frac{We}{\min\left(\frac{h}{d}, 1\right) + \frac{\delta}{d}} > E_{\text{criterion}}^2$$

where h is the local film thickness and δ is the boundary layer thickness calculated from the drop diameter and Reynolds number.

The spray targeting and the numerical conditions are shown in Fig. 3.18 and Table 3.7 respectively. The computational domain was a cylinder of $\Phi 150\text{mm}$ x 180mm , which represented a constant volume vessel. The number of cells was in the range of 75,000 and 270,000, and the cell size was: 2mm for the central region, 1mm for the each nozzle direction area, and 8mm for the other area. The numerical grid used in this research is show in Fig. 3.19a. In addition to the embedded grid control, CONVERGE is able to use Adaptive Mesh Refinement (AMR) automatically to enhance the mesh around the spray edge as shown in Fig. 3.19b. The level of embedding for velocity, temperature, and mass fraction in this study was set to 3, which made the mesh size 1mm where AMR was turned on. The maximum number of droplet parcels is ensuring the precise resolution of relevant droplet processes. over 1 million to The calculation was performed only for Injector A.

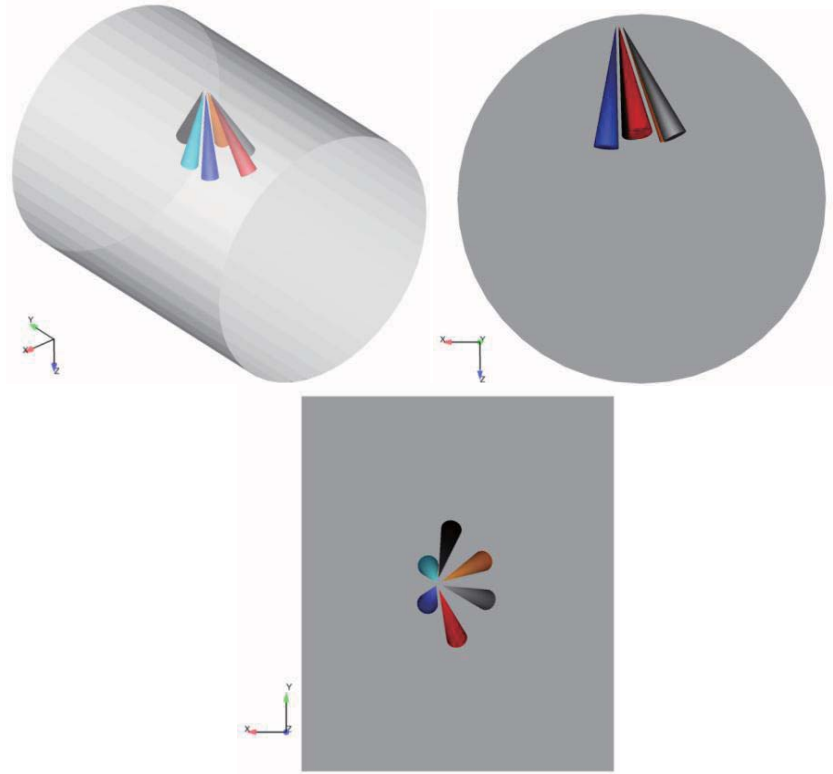
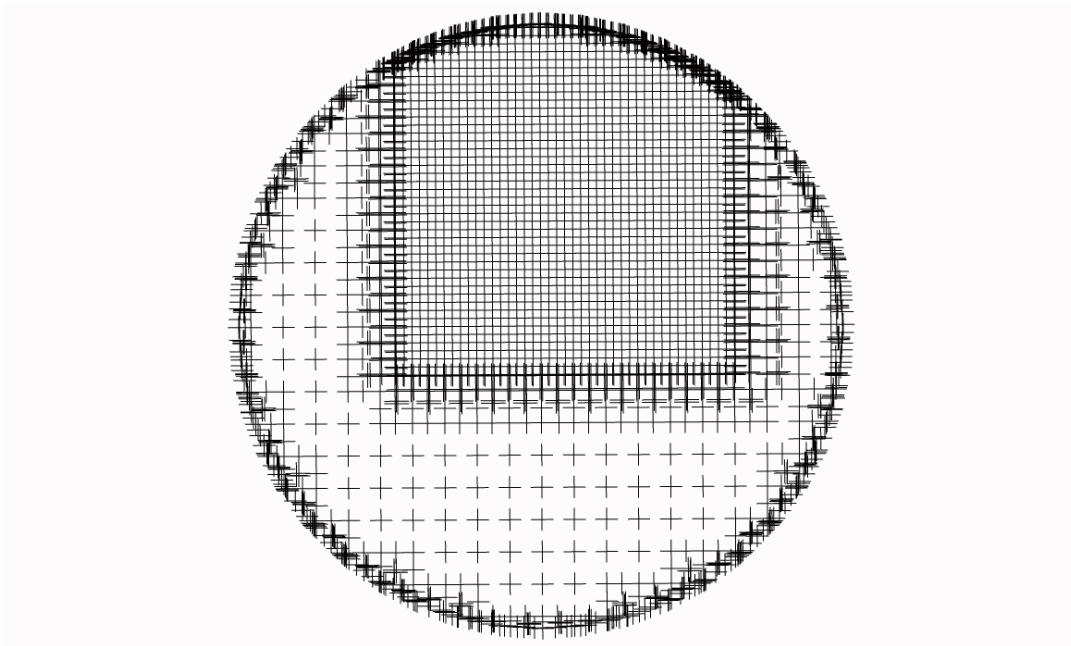
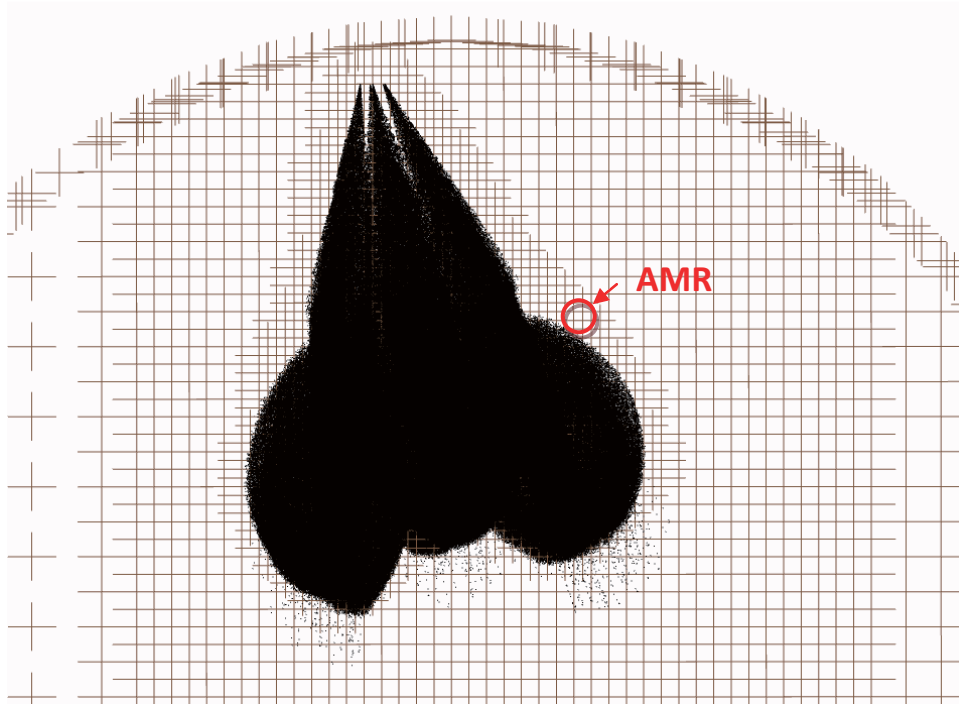


Figure 3.18 Spray targeting of Injector A.



(a)



(b)

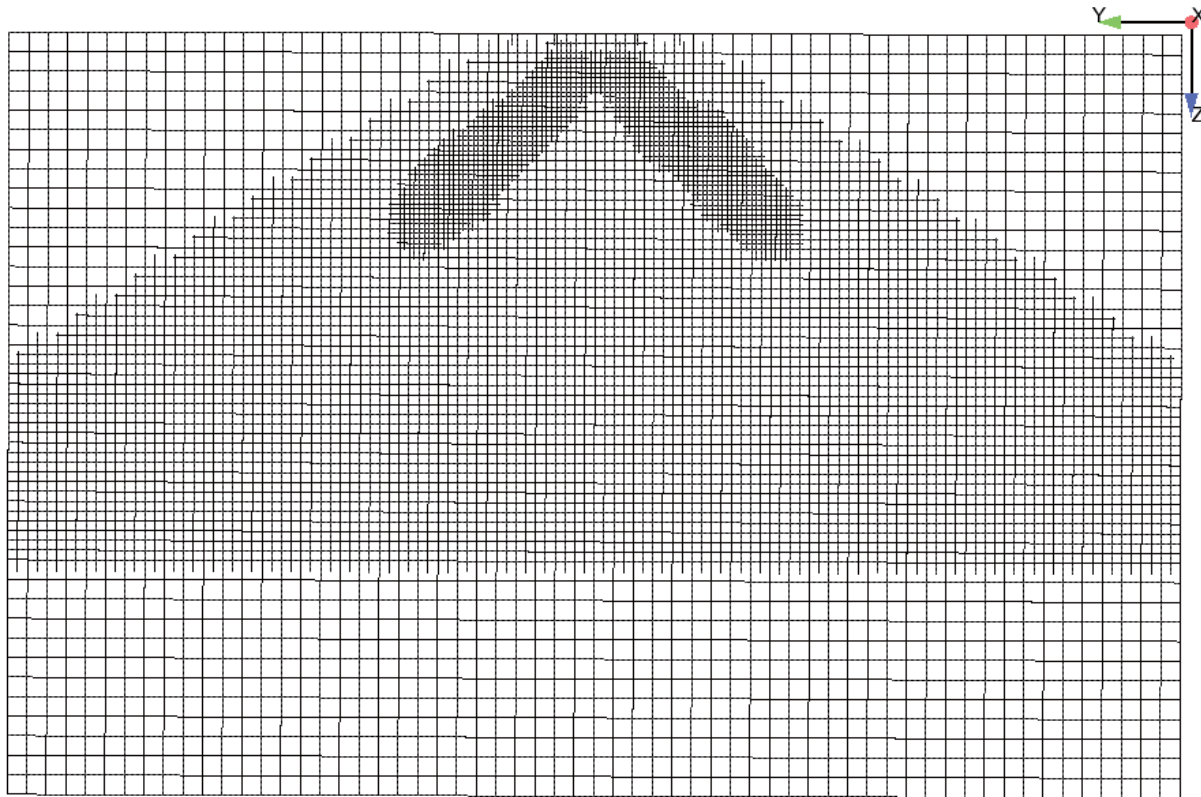
Figure 3.19 Computation Grid for the numerical analysis and comprehensive mesh in value region – both Grid embedding (a) and AMR (b) and used.

Table 3.7 Numerical conditions of injector A

CFD code	CONVERGE	
Coordinate system	Cartesian	
Numerical space (mm)	$\Phi 150 \times 180$	
Number of cell	300,000	
Cell size (mm)	Basic Region:	8.0mm
	Embedded Region:	2.0mm
	Embedded Nozzles Direction:	1.0mm
	Adaptive Mesh Refinement (AMR):	1.0mm

The numerical grids used in this study for PDI injector and multi-hole injector C is displayed in Fig. 3.20. The computational domain for the simulation of the PDI injection was a cylinder of $\Phi 240 \text{ mm} \times 120 \text{ mm}$. The number of cells was about 500,000. The mesh size was: 2 mm for the central region, 1mm for the injector nozzle area. Adaptive Mesh Refinement (AMR) was used in CONVERGE to automatically enhance the mesh resolution based upon gradients in field variables, such as velocity, temperature and species. The spray plume shape area shows the refined mesh around the fuel spray.

Similar mesh strategy was used in multi-hole injection simulation as shown in Fig. 3.20. Embedded mesh was used in the spray area and along each nozzle. AMR refinement method was activated for velocity, temperature and fuel species. Table 3.4 also shows the spray targeting of the 6 holes DI injector C.



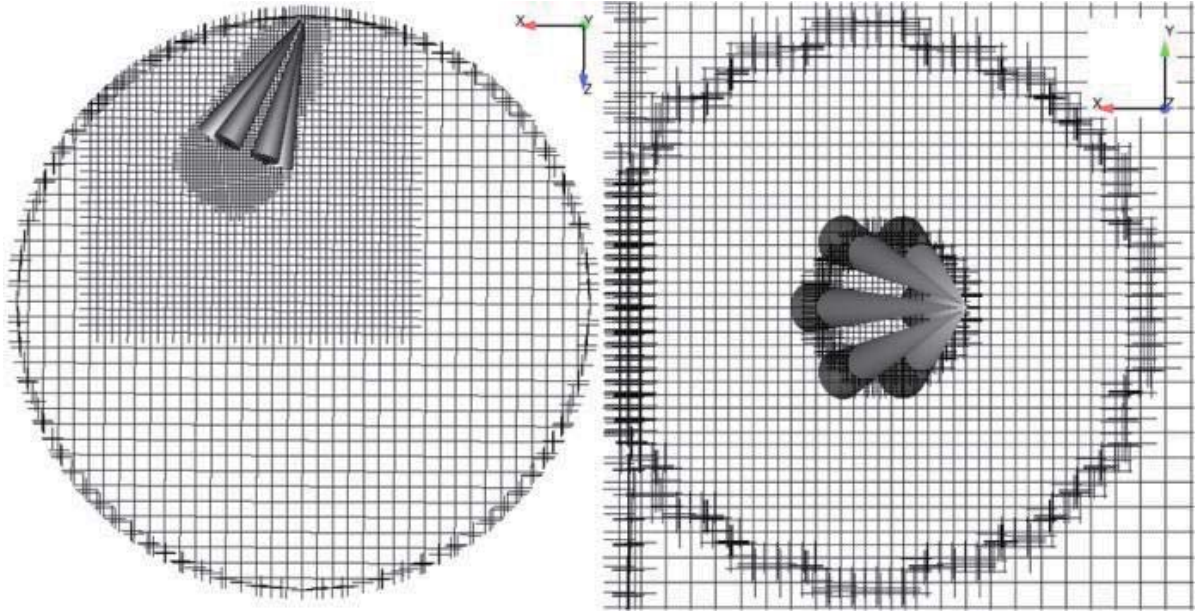


Figure 3.20 Computational grid of the PDI injector (top) and spray targeting for the multi-hole injector C (bottom)

The computational grids of multi-hole injector D for wall impingement simulation are shown in Fig. 3.21. The computational domain is a cylinder of $\Phi 120\text{mm} \times 40\text{mm}$. The number of cells was about 150,000. The mesh size was: 2mm for the central region, 0.5 mm for the injector nozzle area, and 1mm for the impinging boundary. Adaptive Mesh Refinement (AMR) was used in CONVERGE to automatically enhance the mesh resolution based upon gradients in field variables, such as velocity, temperature and species.

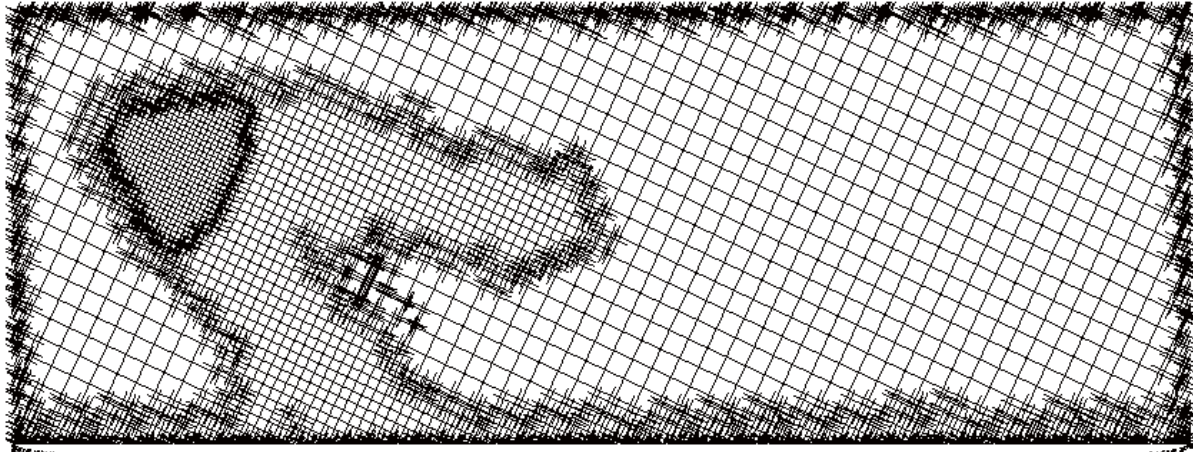


Figure 3.21 Computational grid of the multi-hole injector D.

3.2.3 Interaction between Spray and Charge Motion

Optical engine piston has a flat top while the piston head of metal engine has a bowl and valve recesses as shown in Fig. 3.11, and Fig. 3.22. Simulation of the engine was carried out using commercial CFD software CONVERGE.

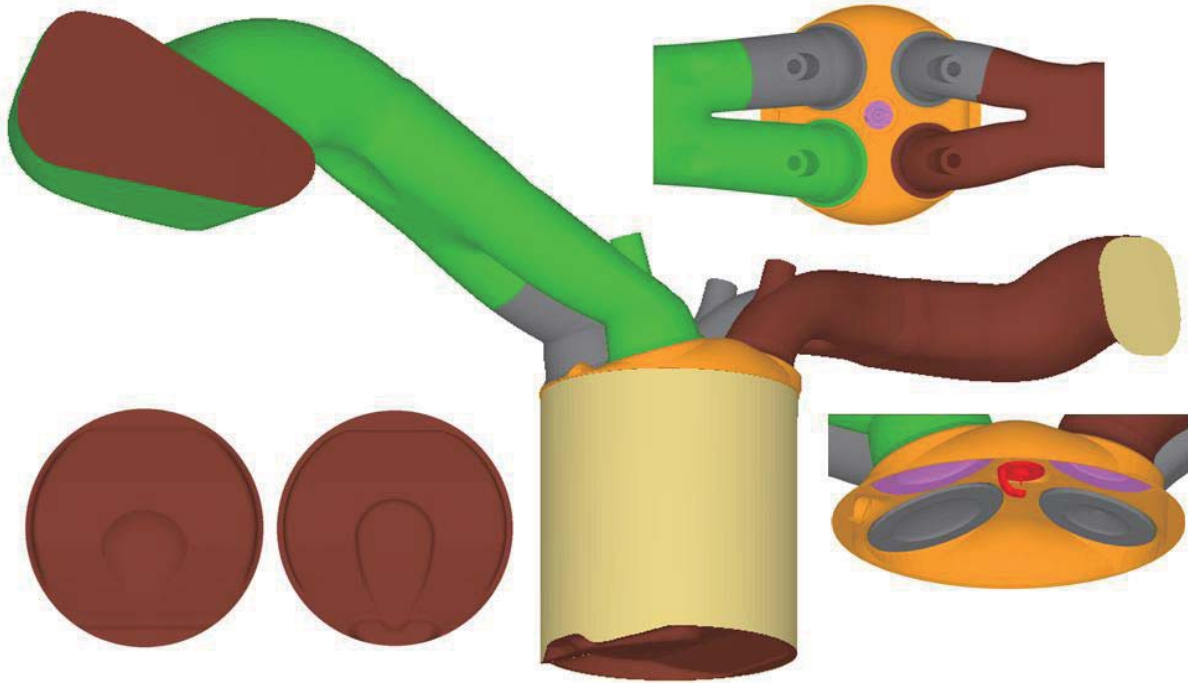
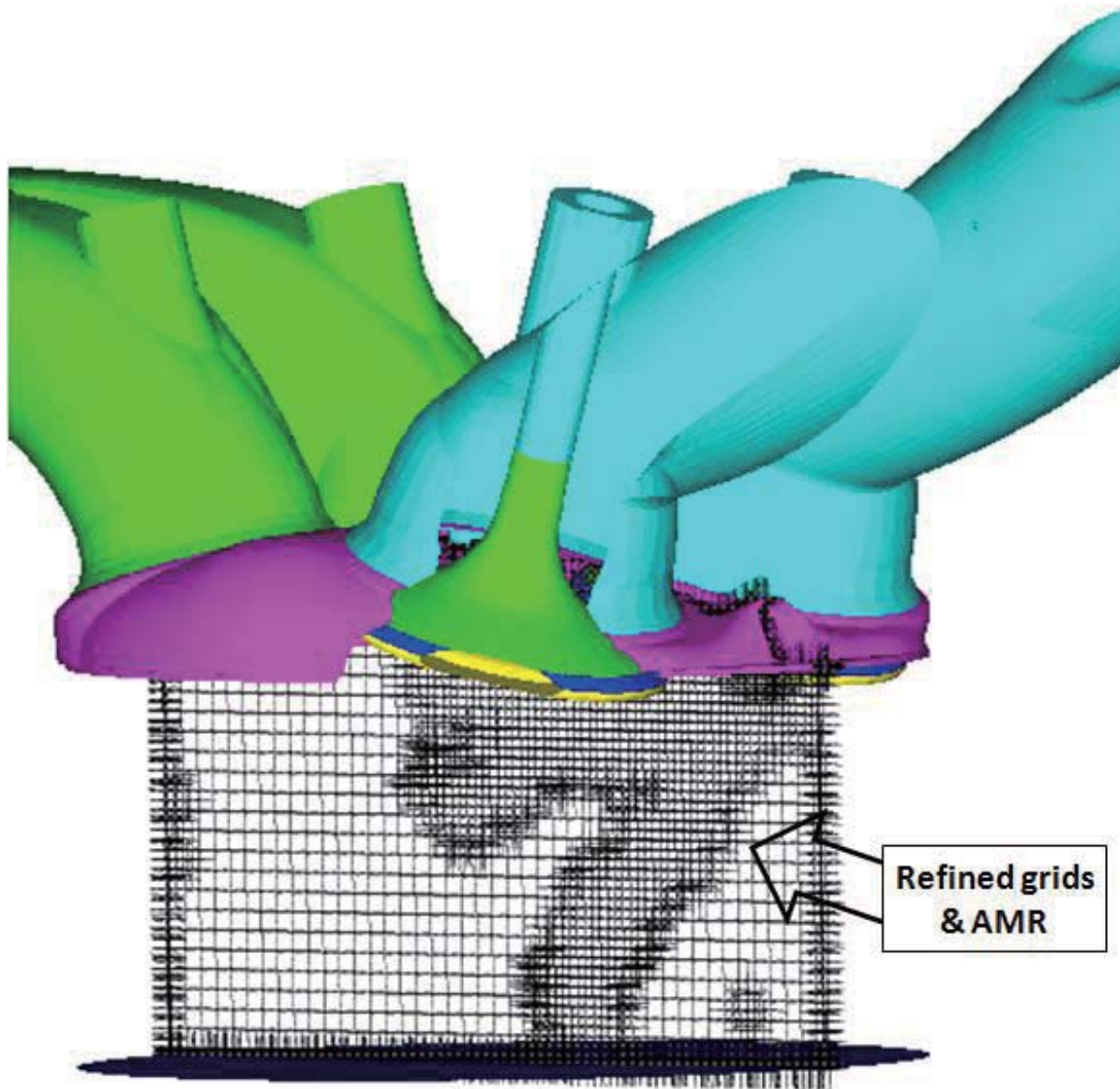


Figure 3.22 Geometry modeled for CFD evaluation.

The calculation domain included the intake and exhaust ports as shown in Fig. 3.23. Optical engine piston has a flat top while the piston head of metal engine has a bowl and valve recesses. The base grid size was 4 mm with built-in mesh refinements, namely embedded refine and Adaptive Mesh Refine (AMR), to make the mesh finer at critical areas near the injector and intake valve. The mesh size was 0.25mm at the injector tip area, 0.125 mm around spark plug for combustion simulation, 0.5 mm for the mesh refined by the AMR, and 1 mm for the other area. The calculation time step was set to 1 μ s.

The combination of Kelvin-Helmholtz and Rayleigh-Taylor models, known as the KH-RT model, and the No Time Counter (NTC) method were chosen for the

break-up and collision model respectively. The model parameters of spray atomization are based on the spray characteristics analysis in the constant volume vessel without out charge motion. The turbulence model for modeling the turbulent flow and mixing is the renormalization group (RNG) $k-\epsilon$ model, which is one of the Reynolds-averaged Navier-Stokes equation models.



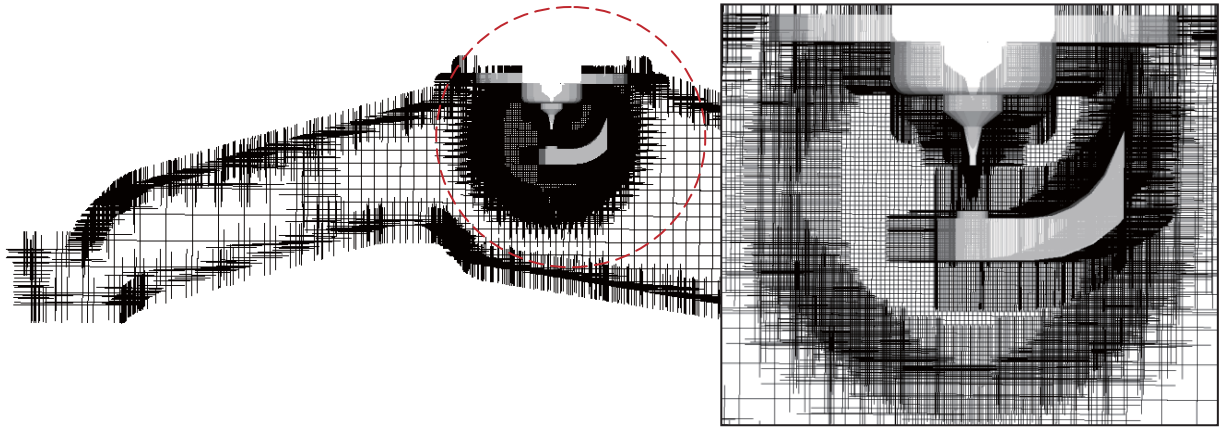


Figure 3.23 Geometry and mesh strategy.

1-dimensional simulation was carried out to generate the boundary and initial conditions for the 3-D CFD simulations. The GT-Power model is showed in Fig. 3.24.

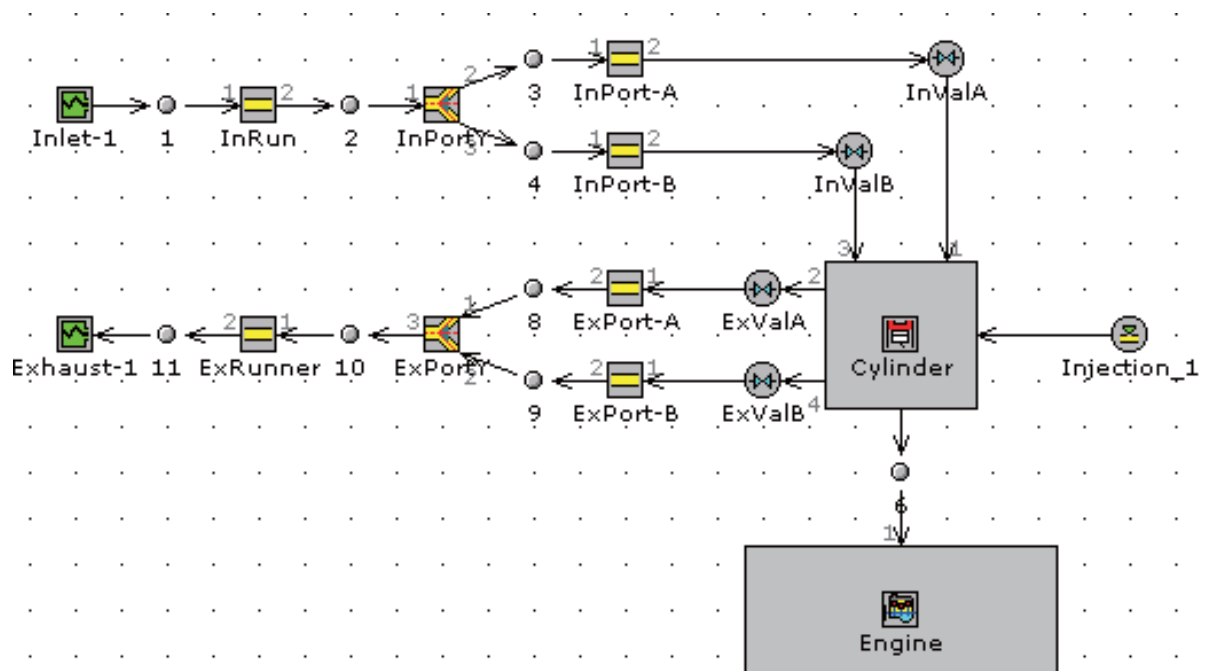


Figure 3.24 1-D GT-Power model of homogeneous charge DISI engine without EGR.

SAGE detailed chemical kinetics model is used to include the effects of detailed chemistry in combustion applications [110]. The SAGE model uses the CVODE solver which is part of the SUNDIALS package. This approach allows the user to introduce a chemical kinetics mechanism into the simulation with a set of CHEMKIN-formatted input files, which here become the standard format for defining chemical mechanisms. In this study, a reduced dual component chemistry mechanism [54] for RON 91 (iso-octane 91%, n-heptane 9%) is used. To speed up the solution of detailed chemical kinetics, the multi-zone model solves detailed chemistry (SAGE) in zones where group of cells that have similar thermodynamic state [111].

CHAPTER 4 RESULTS AND DISCUSSIONS

This chapter presents results from experiments and simulations for direct-injection spray's in-nozzle flow, vaporization, interaction with wall and in-cylinder flow. The first section discusses the internal nozzle flow field of diesel injector and gasoline DI injector through the numerical methods. The next section present results obtained for an optical constant volume vessel including spray vaporization, fuel film formation with experimental measurements and simulation works. The third section summarizes the fuel injection, wall wetting, and air-fuel mixing in both optical engine and real engine.

4.1 Internal Nozzle Flow

The fuel spray momentum controls the mixture process of the injected fuel with surrounding oxidant gas, which is crucial to achieve highly-efficient and clean combustion for direct injection (DI) diesel and gasoline engines. Near-nozzle fuel jet development dominated by internal nozzle flow and related fluid-dynamic instability governs the primary break-up process of the injected fuel. In this section, the in-nozzle flow of the diesel injector for DI diesel engine is first discussed. Then the internal flow predictions of a multi-hole gasoline DI injector are presented.

4.1.1 Internal nozzle flow of injector for DI diesel engine

Fig. 4.1 shows the computed pressure contours using the geometrical dimension measurement taken from the phase contrast images (Fig. 3.1). As

described in Chapter 3.2, the standard $k-\epsilon$ turbulence model and Eulerian full-cavitation model are used.

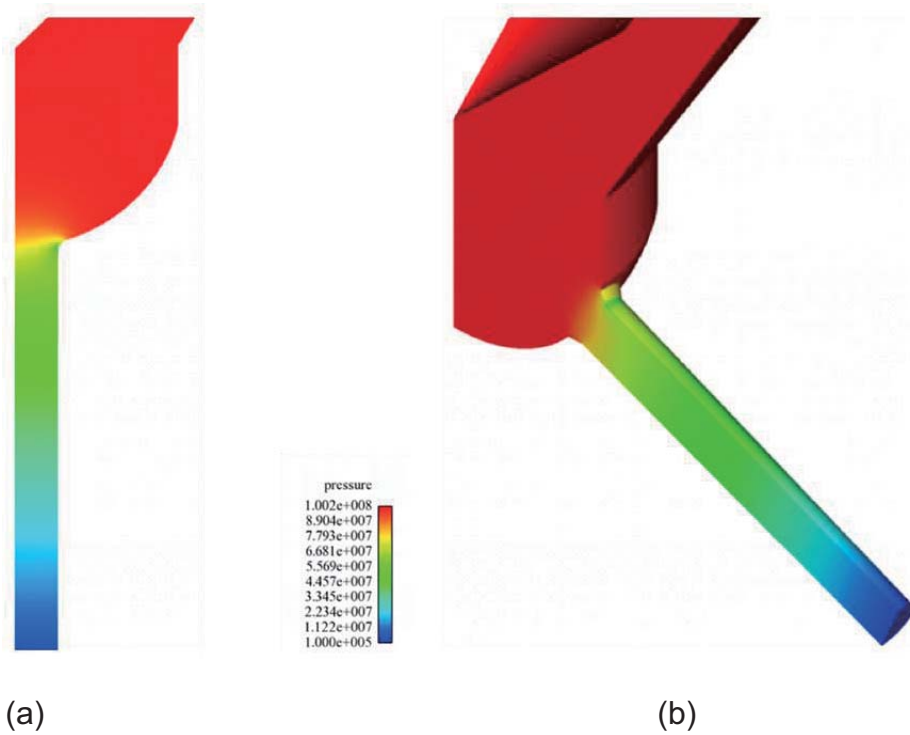


Figure 4.1 Computed mean pressure contours of single-hole (a) and two-hole (b) nozzles. (Inj. Pressure: 100 MPa.)

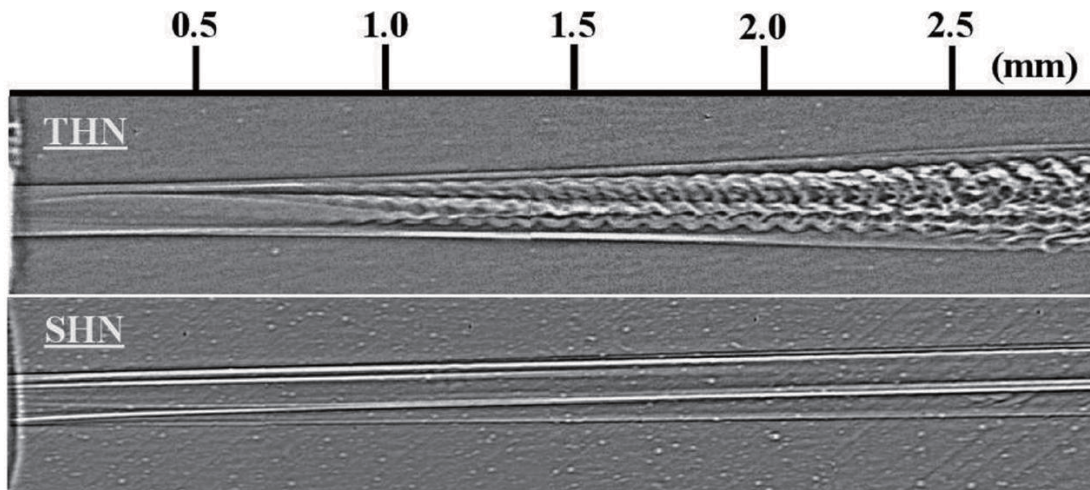


Figure 4.2 Near-nozzle jet morphology of two-hole nozzle and single-hole nozzle (Fuel: Biodiesel, injection pressure: 30 MPa, injection duration: 4.0 ms, Images taken at 2.0 ms ASOI).

The dramatic difference between the SHN and THN is shown in Fig. 4.2 at the low injection pressure of 30MPa, using more viscous Biodiesel fuels between the SHN and the THN cases. This near-field jet morphology of the injector nozzle was obtained by the single-shot ultrafast x-ray phase-contrast imaging technique, implemented by the high-intensity and high-brilliance x-ray beam available at the Advanced Photon Source (APS) in Argonne National Laboratory. Very distinct wavy structure was clearly observed near the hole exit of THN and the lateral jet boundary began to spread, as early as 1 mm downstream. In contrast, the jet coming out of SHN is very stable, almost laminar-like, and spread much less slowly as far as 3mm downstream, although there seems to be some disturbances propagating downstream without developing into aerodynamic wave features. As a result, the SHN sprays showed more stable spray morphology and smaller near nozzle spray angle compared to the THN sprays. Due to relatively stable flow characteristics, the break-up of the SHN spray occurred at farther downstream of the nozzle exit compared to the THN spray. The Reynolds numbers of these conditions are not very high, and the flow is in the transitional regime and not yet highly turbulent. Due to the internal flow difference, however, the THN jet already manifests more instability.

The different in-nozzle flow structure between the two nozzle configurations can be readily illustrated using CFD simulations. The streamlines computed for the SHN and THN using RANS are shown in Fig. 4.3. The three-dimensional fluid flow entering the two-hole nozzle creates much more complicated streamlines with stronger curvatures.

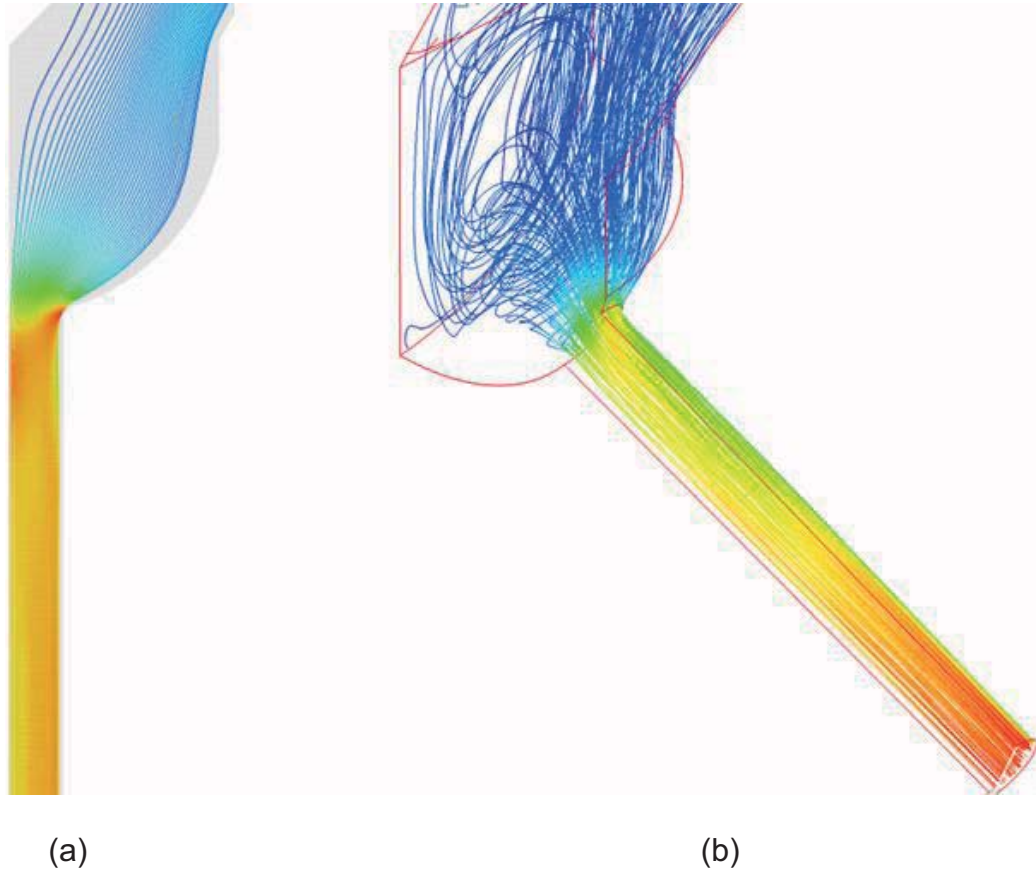


Figure 4.3 The 2D and 3D streamline Flow characteristic in the sac and nozzle inlet for SHN (left) and THN (right) as computed using RANS.

First we examine the velocity and turbulence intensity distributions at the exit plane of THN in Fig. 4.4 and 4.5. For illustration purpose, only the THN profiles on the major symmetry (vertical and horizontal) axes are shown. As a result, the velocity profile of the THN is much more complicated than SHN. The computed mean flow structure shows that THN has a less uniform mean velocity profile, with a downwash feature in the vertical plane along the injector axis, and a thicker shear layer near the wall, as shown in Fig. 4.4, as well as a higher turbulence intensity, which is normalized with the mean velocity, as shown in Fig. 4.5.

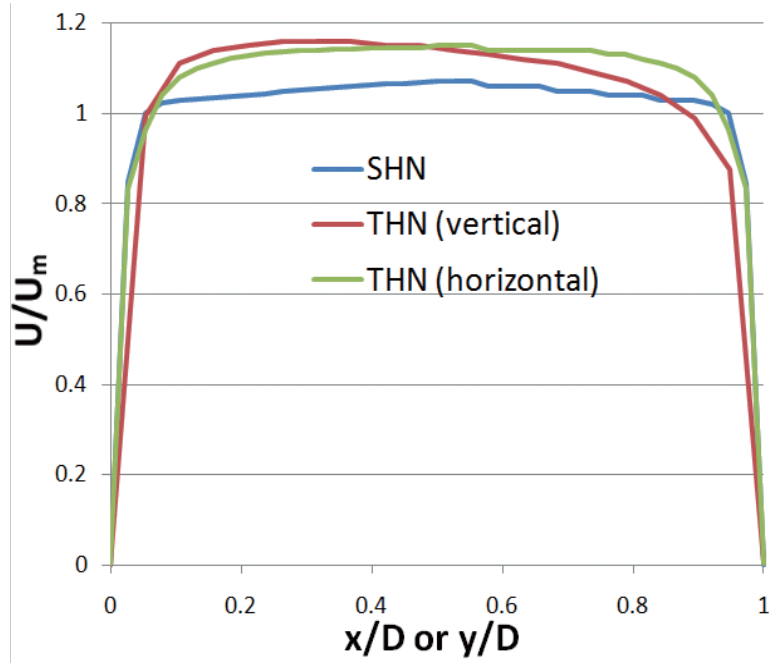


Figure 4.4 The normalized streamwise velocity profiles of the axisymmetric SHN compared to those of the THN on the major axes at the exit plane.

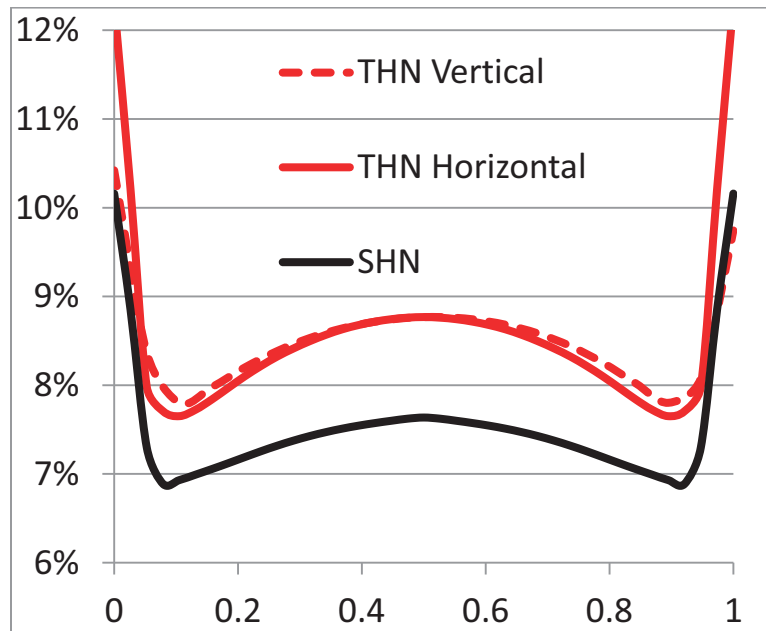


Figure 4.5 The turbulence intensity profiles of the axisymmetric SHN compared to those of the THN on the symmetry line on the major axes at the exit plane.

The interaction of the downwash with its accompanied higher mass and momentum fluxes on the lower side, and the two counter-rotating vortices in precession could explain the shorter wavelength on the lower (down flow) side. The divergence angles, which are the angle formed by the velocity vectors with orifice axis, are also much larger for THN cases compared with SHN one, c.a. up to be about an order of magnitude larger. These fundamental flow features are consistent with the stronger flow instability and wider cone angle observed for the THN sprays compared to those of SHN, although any geometric or operational asymmetry due to even surface roughness or valve eccentricity will only enhance the instability.

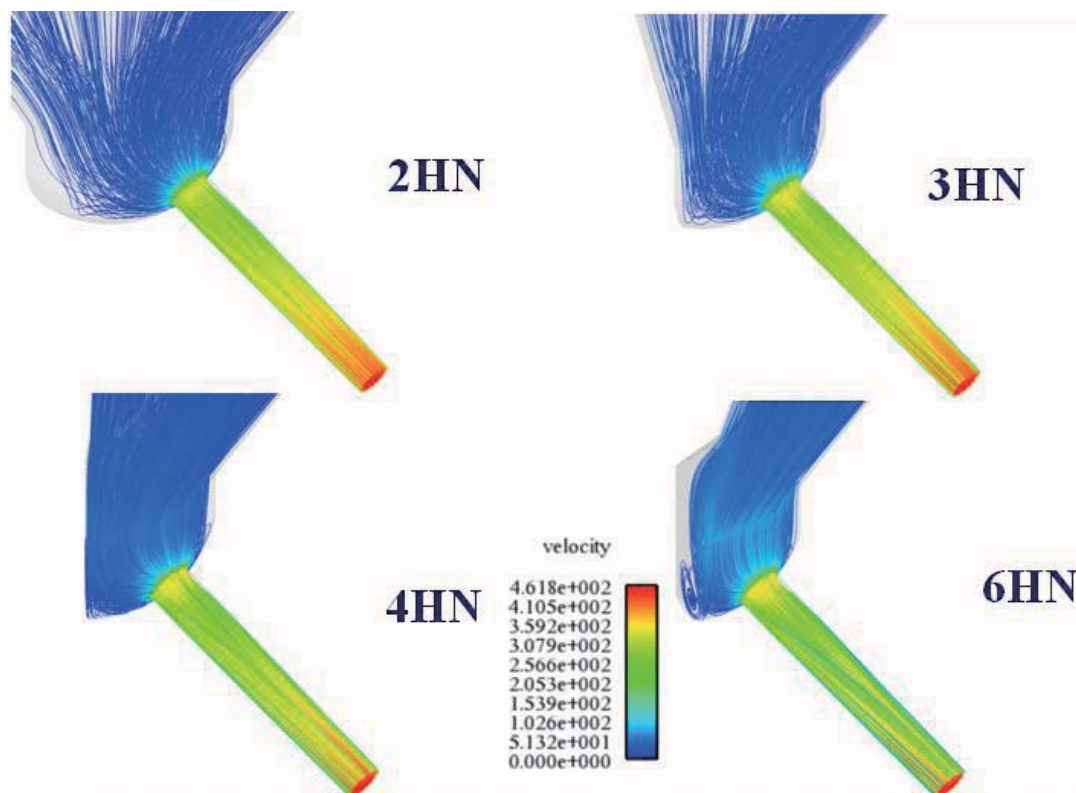


Figure 4.6 The effect of hole number on the streamlines of multi-hole nozzles.

The effects of number of holes can be more readily investigated using RANS. The computed streamlines are shown in Fig. 4.6 which shown similar behavior with a slight difference. Fig. 4.7 shows that the number of hole tends to increase the flow asymmetry. As a result of the downwash, multi-hole nozzles also produce stronger divergent velocity vector angles at the exit, consistent with experimental observation.

Another perspective can be gleaned by examining the vorticity profiles at the exit plane. The counter-rotating vortices are symmetric by default if the symmetry boundary conditions are imposed geometrically. They are formed by the flow negotiating the valve and sac geometry into the orifice and not directly from cavitation, although cavitation model is included in the analysis. They grow in intensity as they progress through the orifice due to the taper-hole geometry, and become quite homogenous when they exit the hole. The counter-rotational vortices are actually bound or clad by a thin shear layer near the orifice wall, which imposes the no-slip boundary condition. This thin annular shear layer serves to constrict the streamwise vortices and to generate turbulence, but upon the flow exiting the orifice, it will be relaxed immediately and allow the vortices to freely interact, subject to strong turbulent vortex dynamics and much weaker aerodynamic shear stress at the interface, at least initially. These rotational internal flow features due to the multi-hole nozzle geometry have not been considered in almost all spray calculations or multiphase breakup simulations.

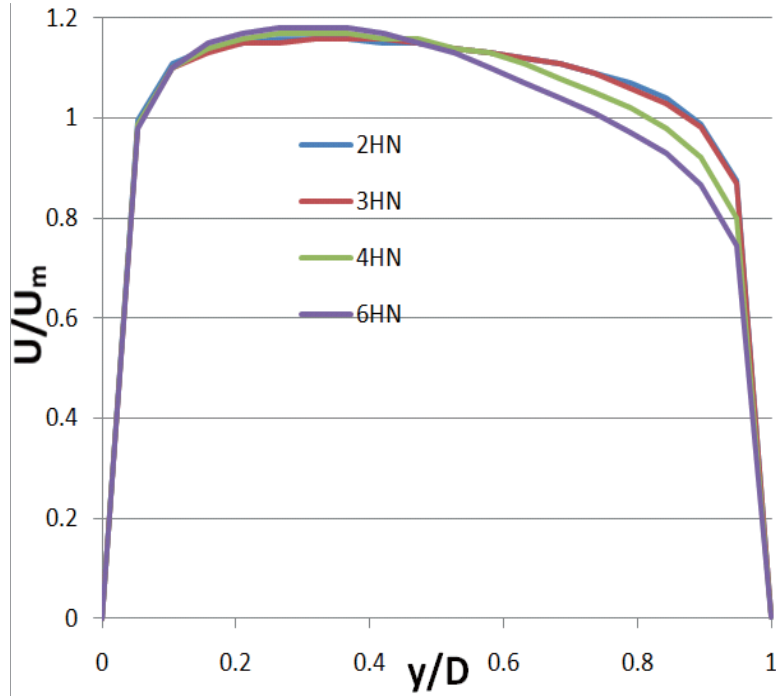


Figure 4.7 The effect of hole number on the normalized exit velocity profiles (vertical) of the multi-hole nozzle.

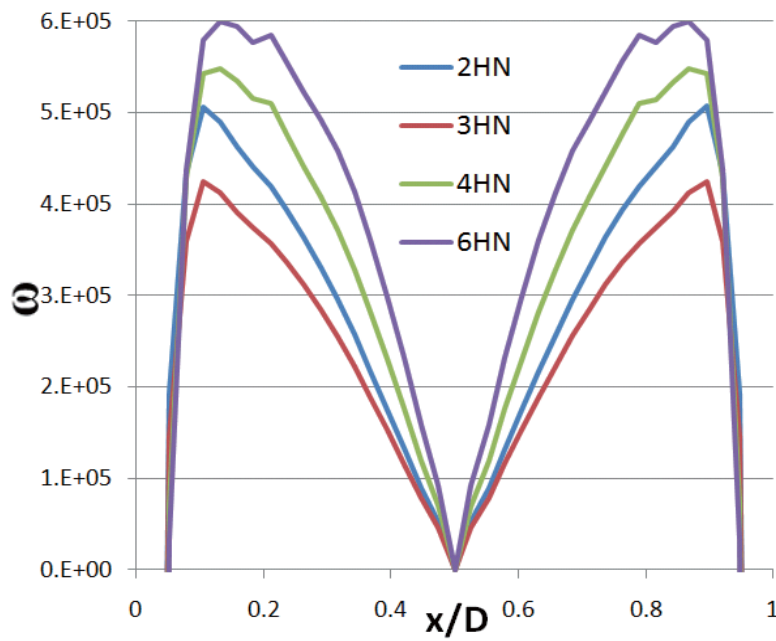
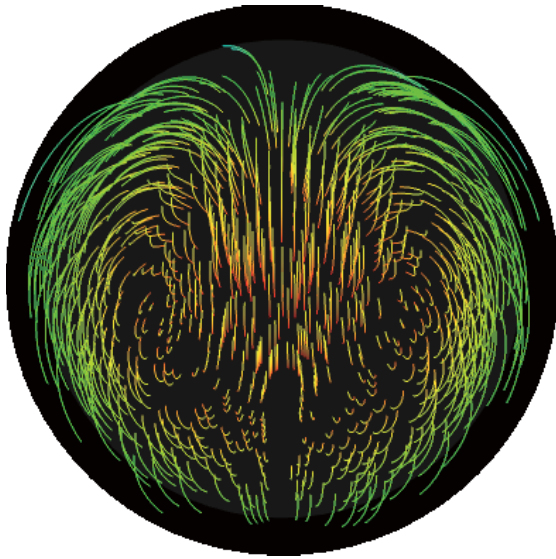


Figure 4.8 The Effect of hole number on the normalized streamwise vorticity profiles of the multi-hole nozzle.

Fig. 4.8 shows that there is a pair of dominant counter-rotating core vortices at the exit plane, and that the vorticity strength in general increases with the number of hole. In comparison to SHN which does not develop streamwise vortices by default under ideal symmetry condition. The vorticity strength of the multi-hole nozzle is surprisingly strong, on the order of a million inverse sec, given the relatively low Reynolds number turbulent flow conditions.

A better visualization can be achieved by plotting the streamlines inside the THN hole as viewed from the orifice entrance. Fig. 4.9 shows such a view, using results from a full nozzle model to relax the forced symmetry condition imposed by the half-hole computation domain. By default, the same streamline view for SHN is radial and devoid of any rotation, but the streamlines inside the THN is rotational, even enhanced as they accelerate through the converging tapered orifice. The interaction of the downwash behavior with the two counter-rotating vortices in precession could explain the shorter wavelength on the lower (down flow) side, observed in Fig. 4.9. Also shown for comparison is the results using URANS with shear stress transport (SST) turbulence model [105], which is a two-equation eddy-viscosity model which has become very popular. The use of a $k-\omega$ formulation in the inner parts of the boundary layer makes the model directly usable all the way down to the wall through the viscous sub-layer; hence the SST $k-\omega$ model can be used as a Low-Re turbulence model without any extra damping functions. The SST formulation also switches to a $k-\epsilon$ behavior in the free-stream and thereby avoids the common $k-\omega$ problem that the model is too sensitive to the inlet free-stream turbulence properties. The newly available in Fluent Scale-Adaptive Simulation

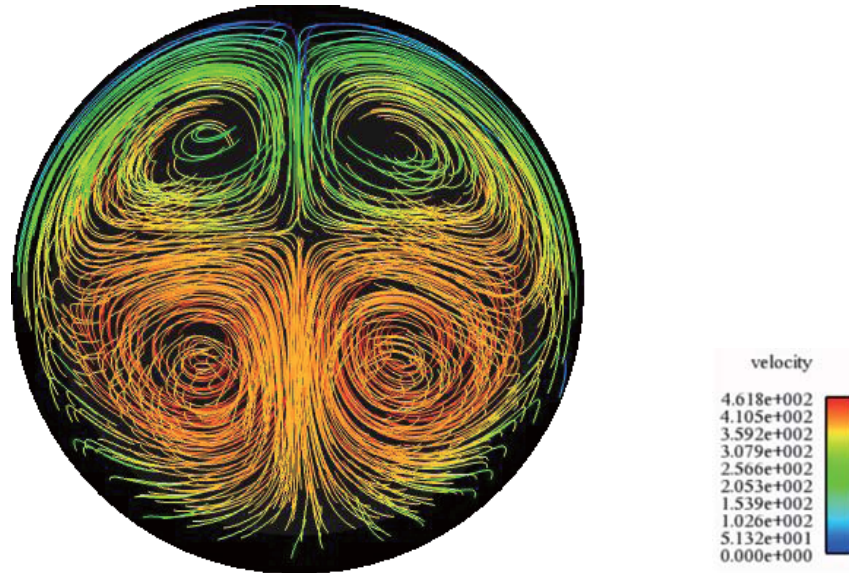
(SAS) model introduce the von Karman length-scale into the turbulence scale equation which provides a LES-like behavior in unsteady regions and standard RANS capabilities in stable flow regions [106]. Instead of two vortices observed using the more dissipative RANS simulation, the URANS simulation with SST and SAS shows four vortices, or two pairs of counter-rotating vortices.



(a)



(b)



(c)

Figure 4.9 The streamlines inside the THN hole as viewed from the entrance, showing rotational curvatures and acceleration as the flow moves through the converging tapered hole. From left to right: RANS with Realizable k-turbulence model, URANS with SST turbulence model, and Scale Adaptive Simulation (SAS) model.

However, the use of vorticity could be misleading when rotation due to pure shear and rotation due to actual swirling motion become comparable, e.g. wall-bounded flows within the nozzle hole. Therefore, the Q-criterion [43, 107, 108], which is the second invariant of velocity gradient tensor ∇u , is a better indication. Positive Q iso-surfaces isolate areas where the strength of rotation overcomes the strain, thus making those surfaces eligible as vortex envelopes. The computed URANS iso-surface results of the Q, cavitation, and simultaneously are shown in Fig. 4.10, 4.11, and 4.12 respectively. At the injection entrance, the upper vortex pair is stronger than the lower pair due to stronger streamline curvature. However, the swirl intensity of the upper vortex pair loses intensity along the injection hole due to the downwash effect, whereas the decay of the lower vortex pair is much slower. As a

result, the lower vortex pair turns out to have stronger intensity than the upper one at the nozzle exit. This also explains the observation in the spray that the lower waves have consistently shorter length scales than the upper ones mentioned above.

The oscillation frequency of the URANS simulation is on the order of 5 to 10 MHz depending on the injection pressure from 30 to 100 MPa using diesel fuel properties, which is consistent to the wavelength observed experimentally. These results are very encouraging in light of the phase-contrast X-ray imaging, however, more research is needed in both the experiment and simulation sides to improve and validate the accuracy of the numerical schemes, and physical submodels, including turbulence and cavitation and their interactions.

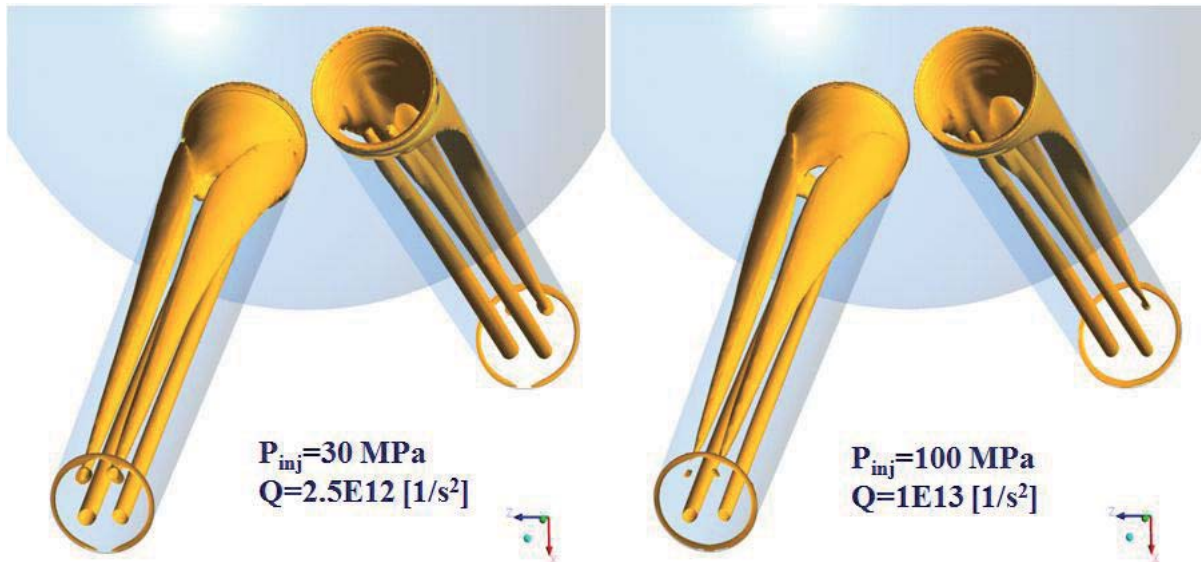


Figure 4.10 The vortex envelopes denoted by iso-surface of Q-criterion inside the THN at 30MPa and 100MPa injection pressure, as computed by URANS with SST turbulence model.

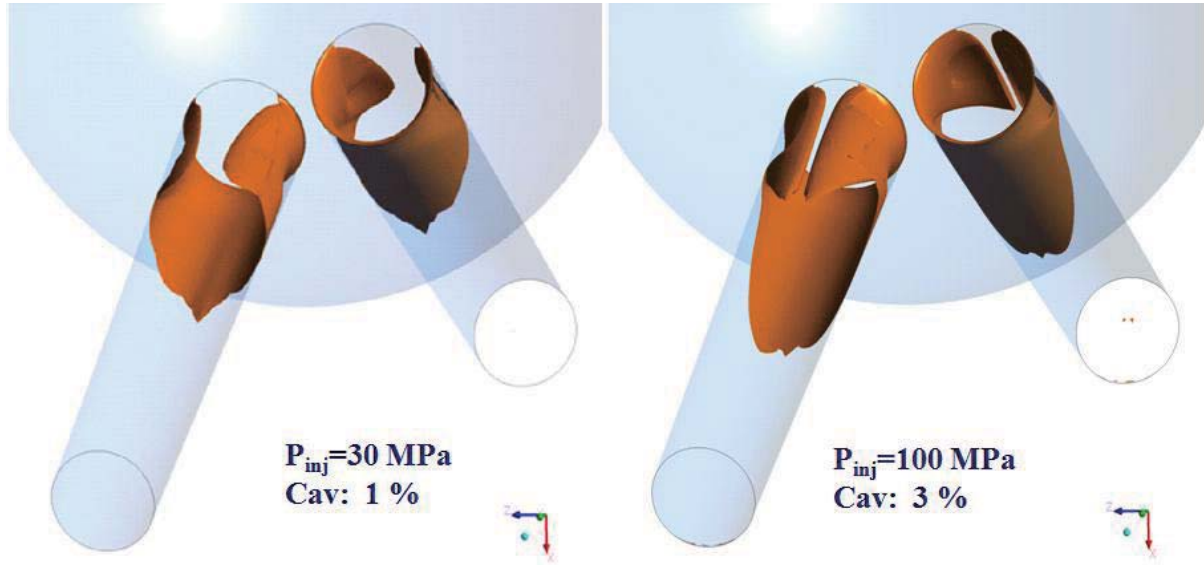


Figure 4.11 The cavitation contour (vapor volume concentration as marked) inside the THN at 30MPa and 100MPa injection pressures, as computed by URANS with SST turbulence model.

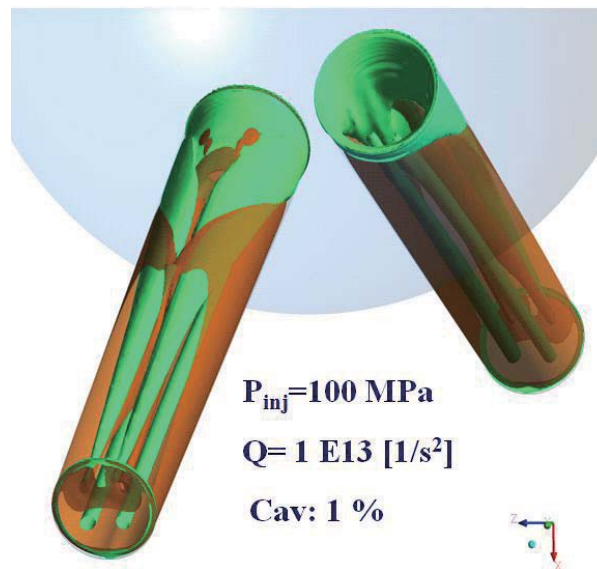


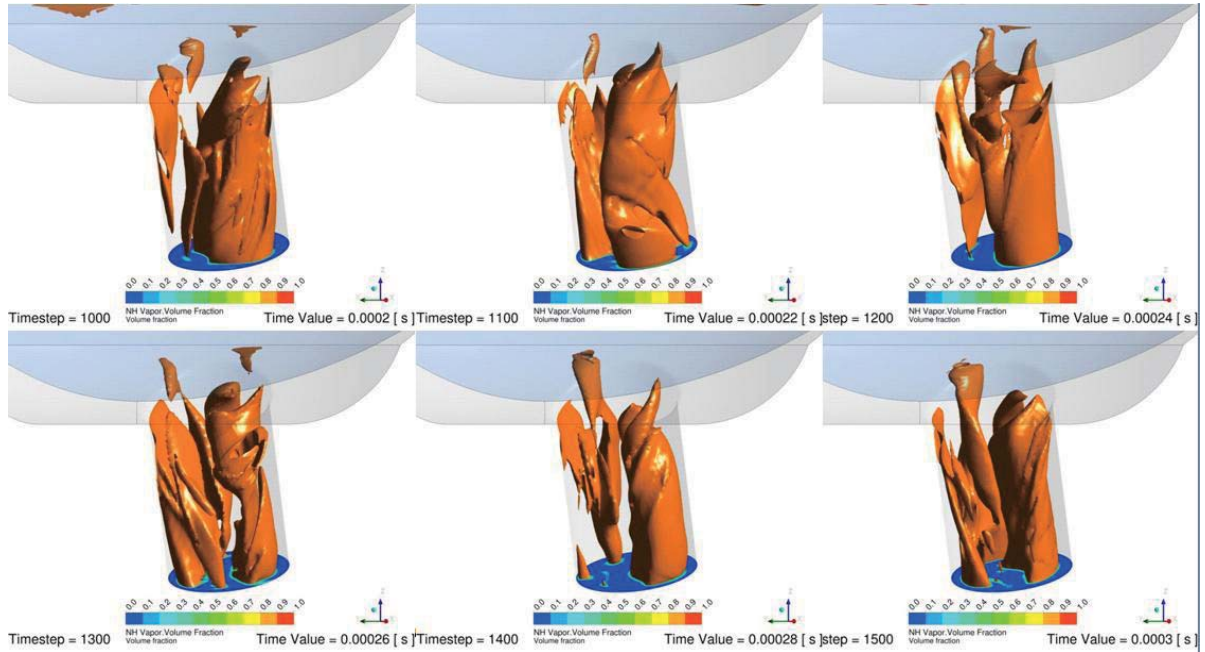
Figure 4.12 The cavitation contour (green, 1% vapor concentration) and the vortex envelopes denoted by iso-surface of Q-criterion (orange, $1\text{E}13/\text{sec}^2$) inside the THN at 100MPa injection pressure, as computed by URANS with SST turbulence model.

4.1.2 Internal nozzle flow of GDI injector

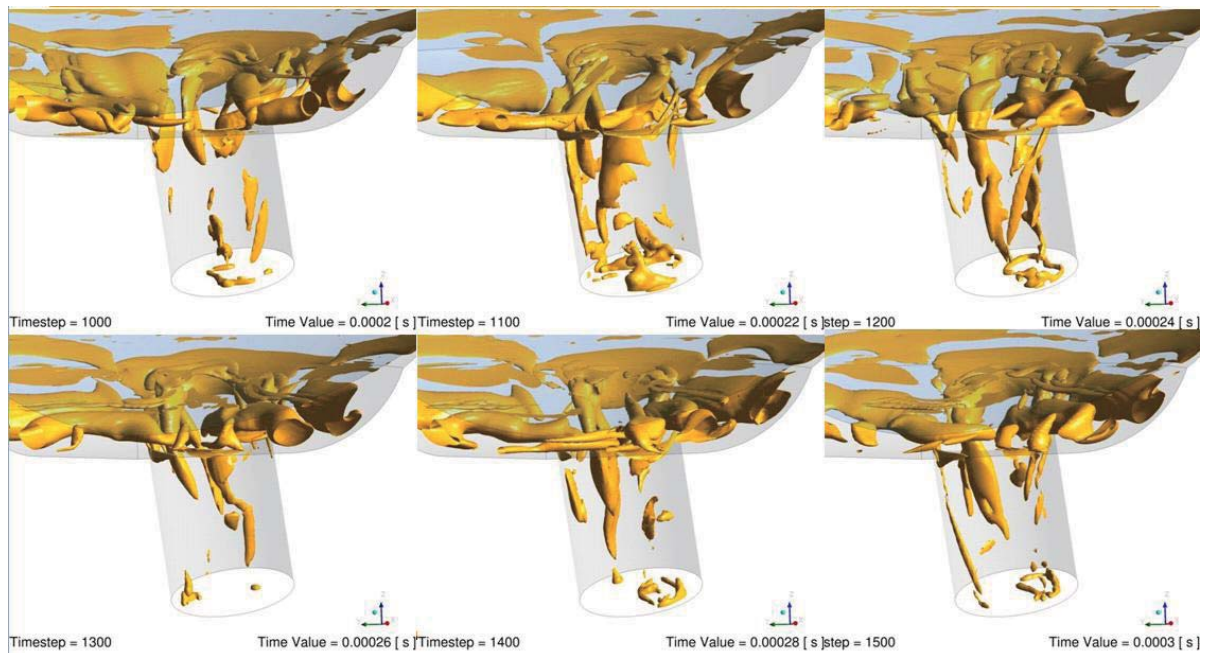
Multi-hole DI injectors are being adopted in the advanced downsized DISI ICE powertrain in the automotive industry worldwide because of their robustness and cost-performance. Although their injector design and spray resembles those of DI diesel injectors, there are many basic but distinct differences due to different injection pressure and fuel properties, the sac design, lower L/D aspect ratios in the nozzle hole, closer spray-to-spray angle and hence interactions.

The interface structure as shown by the X-ray phase contrast is characterized by ligaments and possibly membranes, indicative of turbulence/vorticities and cavitation or two-phase breakup mechanisms. Further insight can be obtained by carrying out the Unsteady Reynolds-Averaged Navier-Stokes (URANS) simulation with shear stress transport (SST) turbulence model to quantify the interactions of turbulence and cavitation [43]. The injection pressure of 100 bars is kept constant and the n-Decane properties were used to approximate the test fluid. The result of two constant needle stokes of 13 μm and 50 μm , representing the early and quasi-steady state of the spray development are presented in Fig. 4.13 and 4.15 respectively. Only six visualizations within 100 μs of the stable URANS simulation are shown to depict the major features of the non-stationary flow field. For wall-bounded flows within the nozzle hole, the use of vorticity could be misleading since rotation due to pure shear and rotation due to actual swirling motion may become comparable. Therefore, the second invariant of velocity gradient tensor ∇u , or the Q-criterion, is a better indication. Positive Q iso-surfaces isolate areas where the

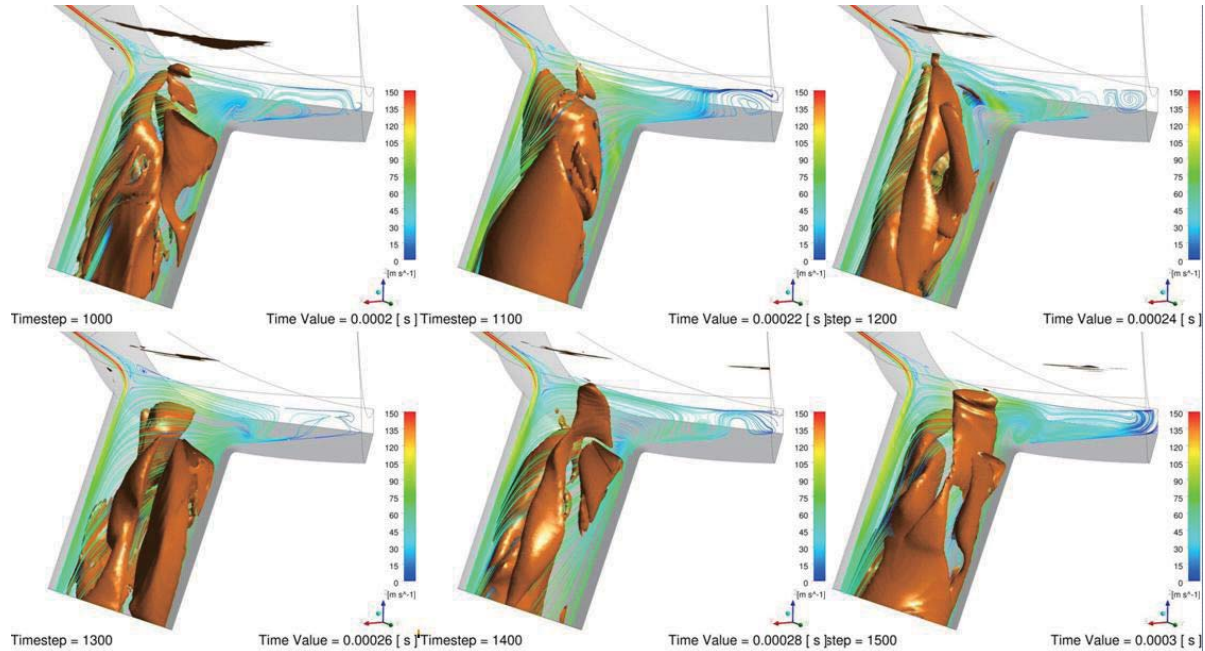
strength of rotation overcomes the strain, thus making those surfaces eligible as vortex envelopes.



(a)



(b)



(c)

Figure 4.13 URANS simulation of the (a) the constant 50%-vapor fraction contours, (b) $Q=0.5E13$ iso-surface contours, and (c) the interactions of streamlines on the symmetry plane with 80%-vapor fraction contours inside the nozzle hole and sac volume, using n-Decane properties, 100-bar injection pressure, and $15\mu\text{m}$ needle stroke.

The SST model has been shown to be less dissipative than the k-epsilon model and should produce more accurate results. The first notable features of the flow are the large extent of cavitation region, as depicted by the constant 50%-vapor fraction contours in Fig. 4.13 (a), in these short aspect ratio holes. Since low-volatility n-Decane fuel properties are used, the cavitation is not primarily due to the low vapor pressure but vortices and air ingestion into the nozzle hole. Therefore, the cavitation streaks are limited inside the hole and not much into the sac; they are anchored on the sharp hole entrance wall and sometimes directly upstream to the ball valve surface, and it. As a result, these nozzles have quite low discharge

coefficients, ca. less than 50% (Fig. 4.14). The high $Q = 0.5E13$ iso-surface contours shown in Fig. 4.13 (b), however, extend well into the sac and around the ball valve. The maximum value is similar to those in diesel orifice using the same techniques, but are much more complicated in structure and originated well upstream, around the valve and inside the sac volume. The Reynolds numbers under this condition is not very high, just falling inside the transitional low turbulent flow regimes, but the unsteady nature of the transitional flow field coupled with the cavitation, similar to those in compound nozzle [104] can break up the fluid quite efficiently. The interactions of streamlines on the symmetry plane with 80%-vapor fraction contours inside the nozzle hole and sac volume are plotted in Fig. 4.13 (c) which shows the flow wraps around the cavitation streaks inside the nozzle hole in a highly unsteady and complicated manner.

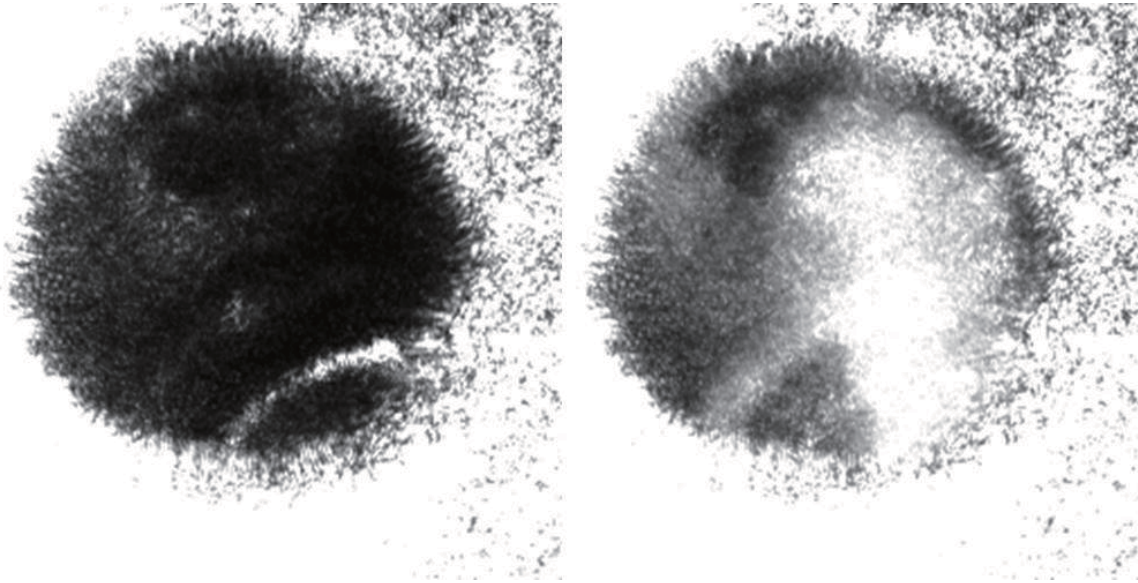
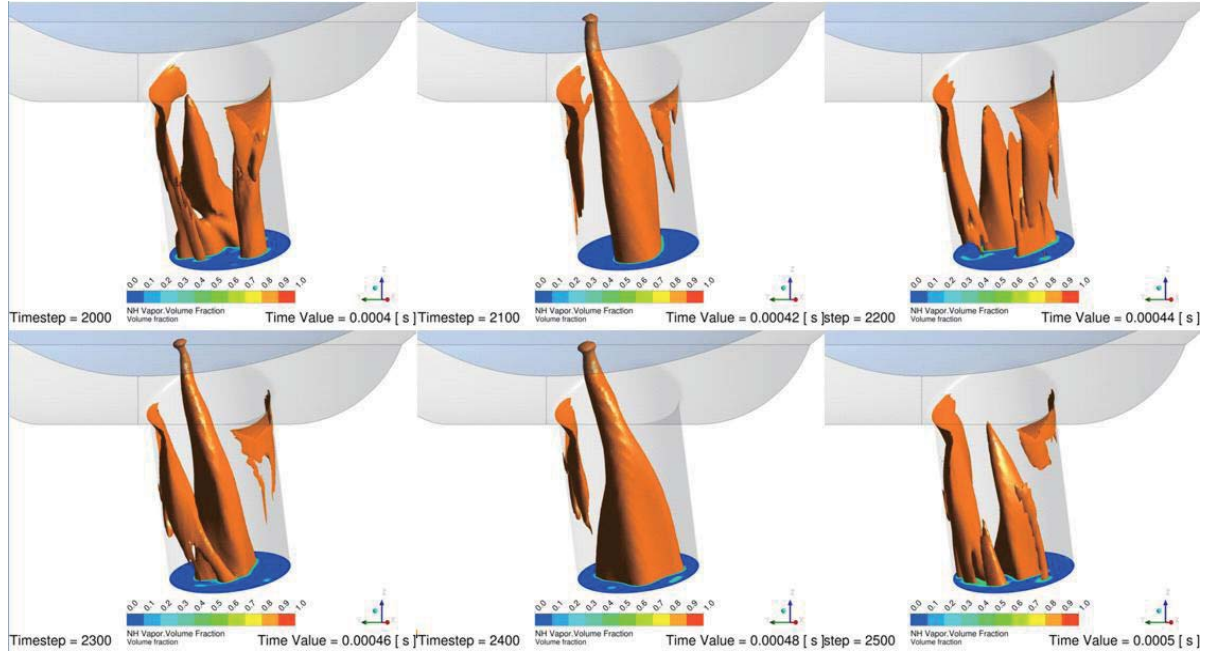
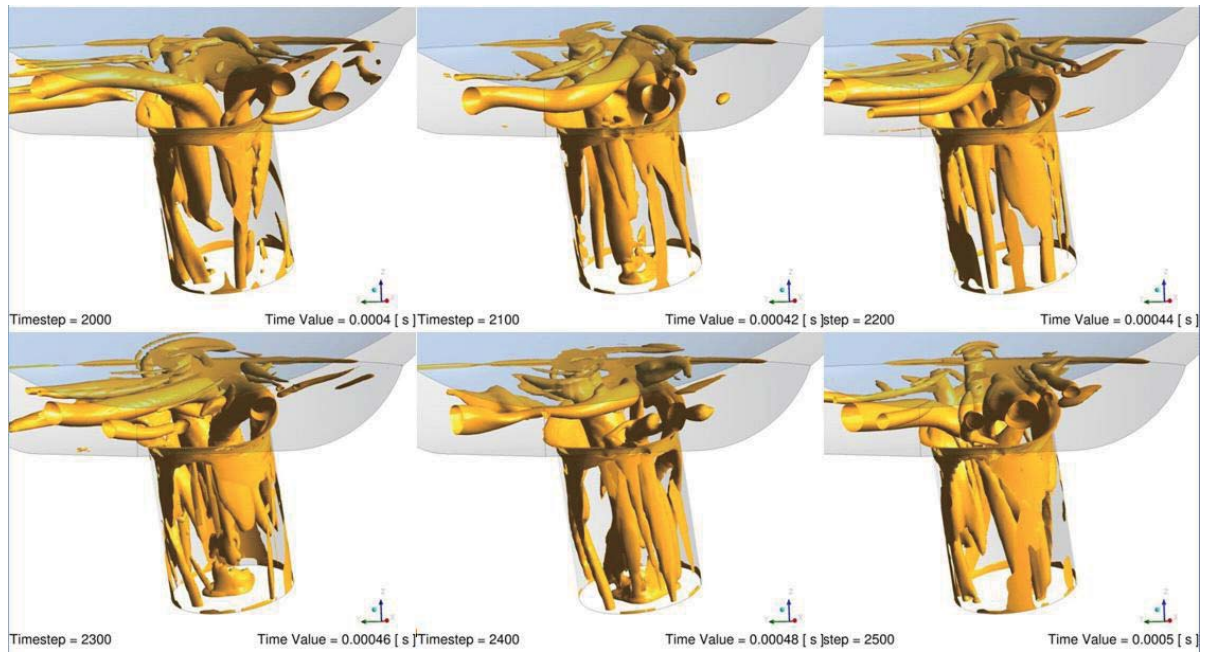


Figure 4.14 Early view of GDI spray. Injection pressure is 800 psi; imaging interval timing is 50 μ s.



(a)



(b)

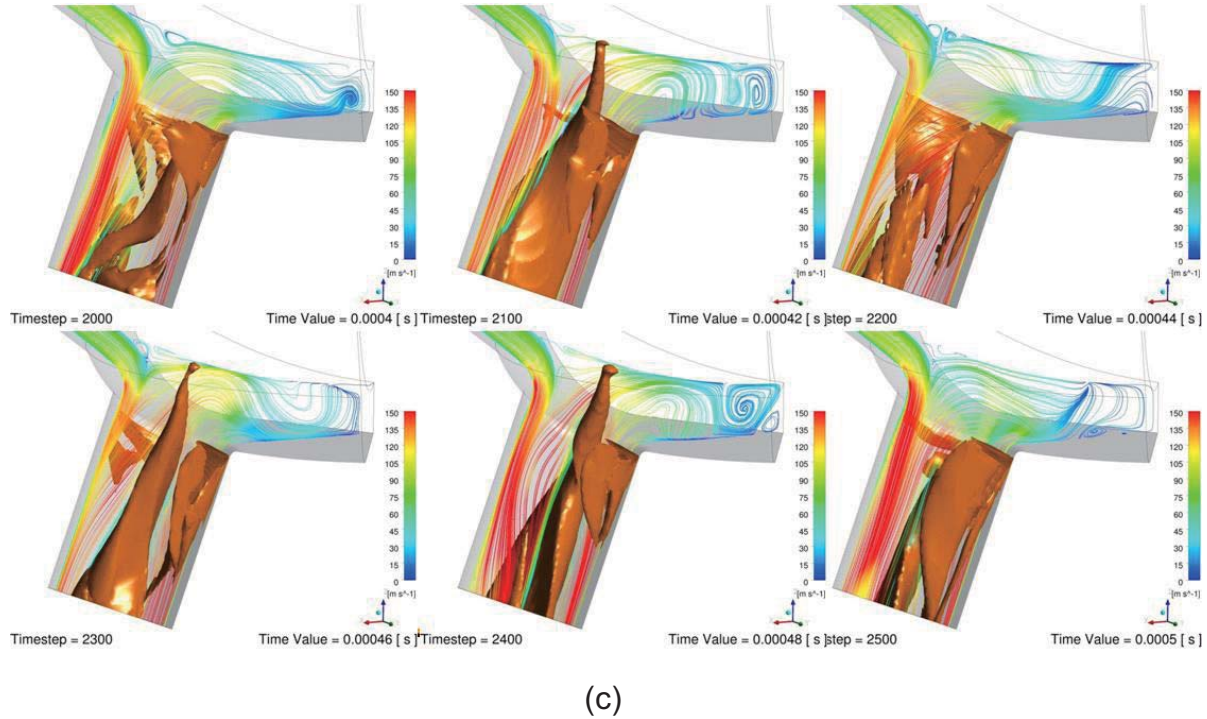


Figure 4.15 URANS simulation of the (a) the constant 50%-vapor fraction contours, (b) $Q=0.5E13$ iso-surface contours, and (c) the interactions of streamlines on the symmetry plane with 80%-vapor fraction contours inside the nozzle hole and sac volume, using n-Decane properties, 100-bar injection pressure, and $50\mu\text{m}$ needle stroke.

The effects of needle stroke on the quasi-steady nozzle flow structure were also compared using URANS simulation and shown in Fig. 4.15 at the higher needle stroke of $64\mu\text{m}$. The flow rate is much higher, and so is the Reynolds number under this condition, but are still not higher 10,000 for the test cases shown. The cavitation intensity is less and smaller in size than the low-lift case, and the fuel is able to fill the hole more. Further validation and statistical analysis are warranted to quantitatively correlate the internal flow inside the nozzle to the breakup mechanism.

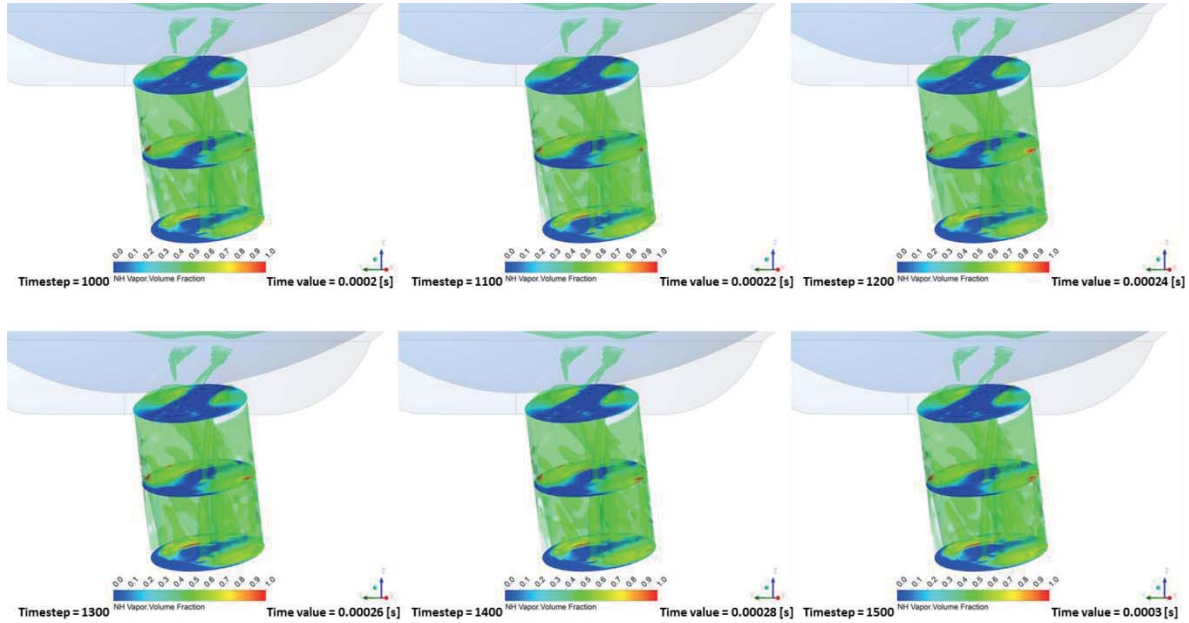


Figure 4.16 RANS simulation using $k-\epsilon$ model for similar conditions as Fig. 4.14(a). The constant 50%-vapor fraction contours are shown with 75% transparency, with the cut-plane profiles shown at $L/D = 0, 0.7, 1.4$.

Comparing results of the LES simulation [16] at the exit of the nozzle, the current results have similar low discharge coefficients, which means that about half of the hole area is not effectively used or occupied with liquid. The liquid phase distributions, however, were quite different. It is not clear whether the different injector design, computational techniques or boundary conditions contribute most to the difference. More experiments and simulations are clearly needed to resolve this interesting research topic. However, the effects of turbulence models are significant as shown in Fig. 4.16, where the phase distributions of the same geometry computed using $k-\epsilon$ model, which is used also in earlier papers [16]. The more dissipative nature of $k-\epsilon$ model predicts more stable two-phase distributions inside the hole, with the liquid on the inside (toward the centerline of the injector axis) and

center of the hole, whereas the SST predicts a much more unsteady distribution for the same low-lift case as shown in Fig. 4.10a.

The simulation results (Q-criterion and vapor fraction) of GDI injector show that the complicated unsteady flow features dominate the near-nozzle breakup mechanisms which are quite unlike those of diesel.

4.2 Spray and Wall Impingement

In order to obtain a better understanding of the fuel-air mixing in DISI engine, the DI spray injection and spray-wall interaction are studied in a quiescent spray chamber experimentally and numerically. The first two sections discuss the optical visualizations and numerical results of the spray without wall impingement and charge motion respectively. The last section presents the experimental results and CFD simulations of wall impingement and fuel wetting measurement.

4.2.1 Sprays in Quiescent Spray Chamber

Spray and its vaporization are one of the key processes in DI engines, because of the spray-wall interaction and fuel-charge motion interaction. Mie scattering, back-lighting, and Schlieren visualization have been widely adopted for spray visualization [11, 63, 87~91]. Some typical spray images of the GDI injector A and B are shown in Fig. 4.17, where the collapsed spray due to flash boiling are imaged using different lighting and optical techniques. Schlieren imaging is able to visualize the vapor clouds around the spray, which are invisible in the Mie scattering images, or very vague in the back-lit images; therefore is the preferred technique to

visualize vaporizing sprays, as shown in Fig. 4.18 and Fig. 4.19. (grid size is 5mm × 5mm).

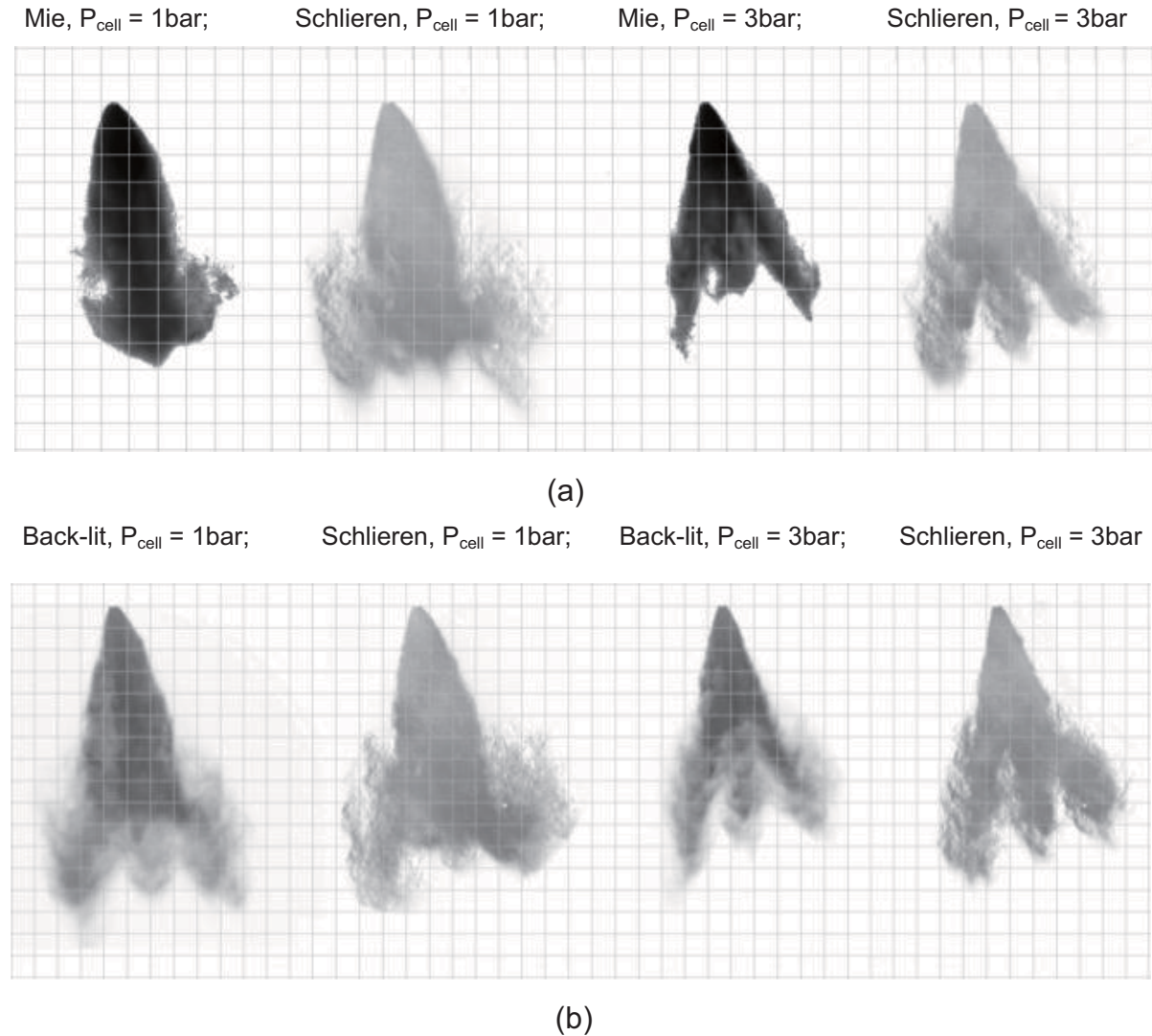


Figure 4.17 Comparison of different Visualization Techniques, 1.5ms ASOI, E100, injector A: (a) $T_{\text{cell}} = 150^{\circ}\text{C}$, $P_{\text{inj}} = 5\text{MPa}$. (b) $T_{\text{cell}} = 200^{\circ}\text{C}$, $P_{\text{inj}} = 10\text{MPa}$.

It should be noted that only slightly slower vaporization and faster spray penetration is observed when replacing E0 with E100 with the same injected volume or pulse width [109]; however, when equivalent fuel energy are compared, the spray

are significantly different toward the end of injection because of the larger fuel mass injected and the higher latent heat needed for vaporization, as shown in Fig. 4.19.

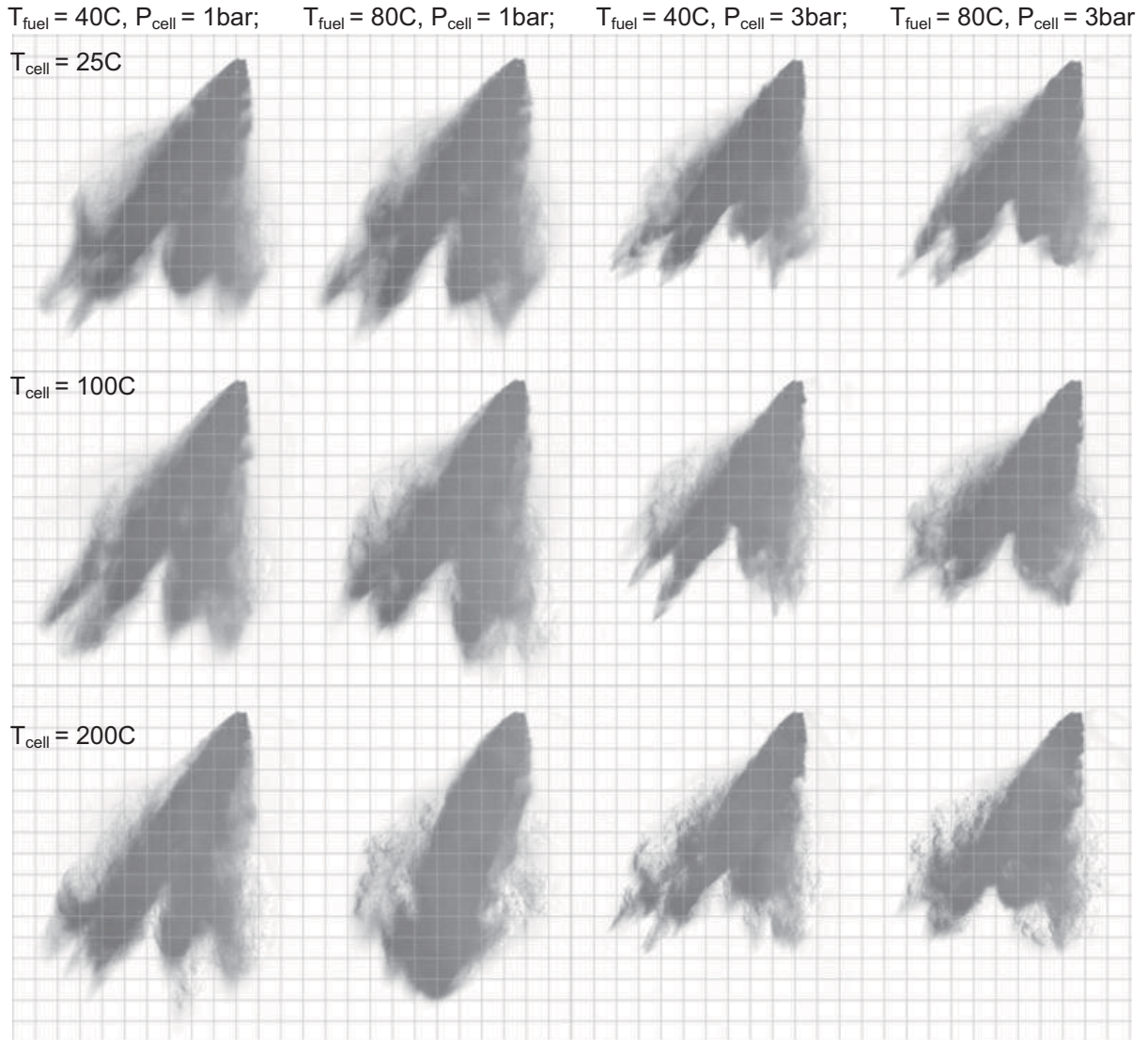


Figure 4.18 Effect of chamber temperature, pressure, and fuel temperature, $P_{\text{inj}} = 10\text{MPa}$, Energy content is equivalent of 10mg of gasoline. 1ms ASOI, E100, injector B.

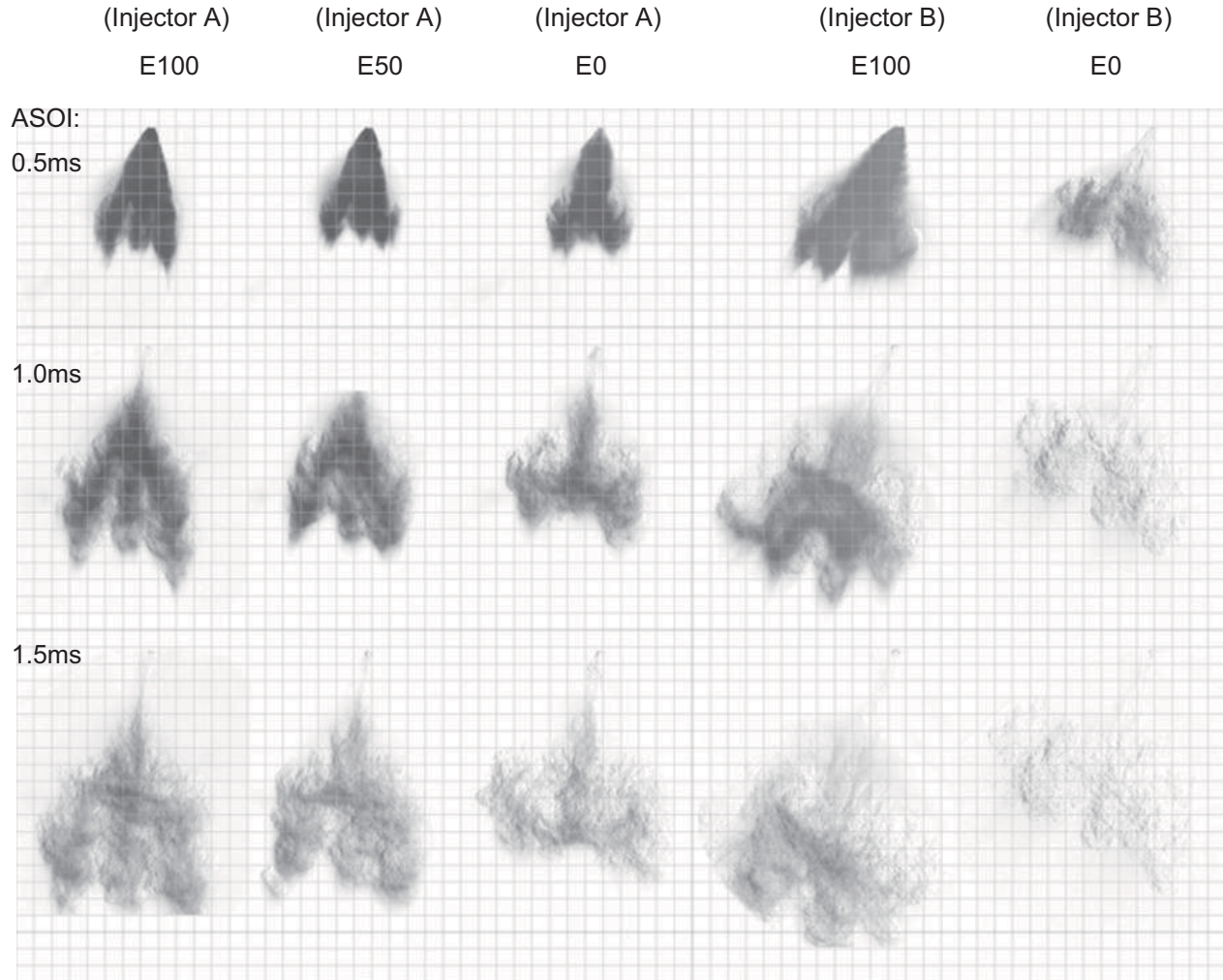
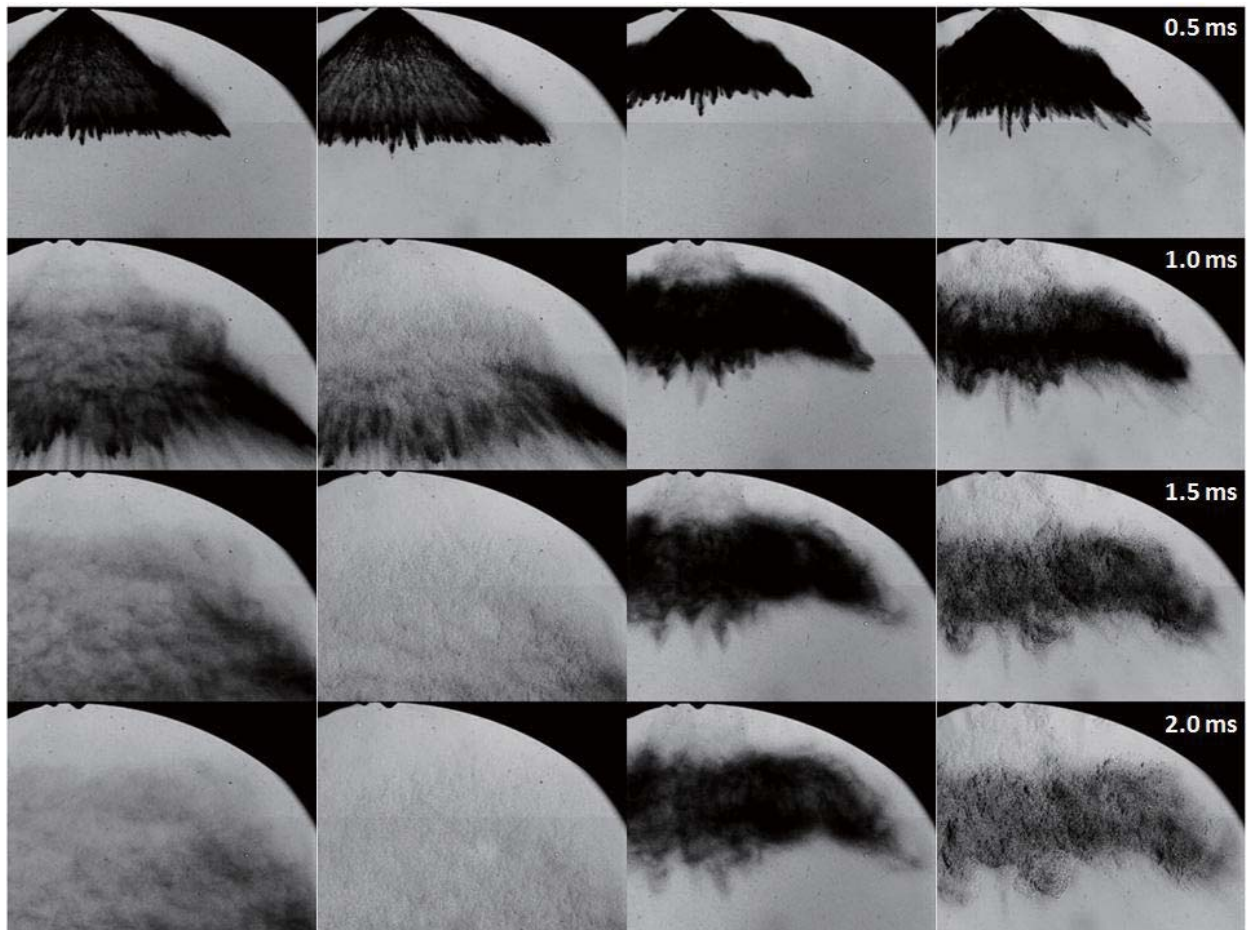


Figure 4.19 Effect of fuel composition. $T_{ch} = 200^{\circ}\text{C}$, $P_{ch} = 1\text{bar}$, $T_{fuel} = 60^{\circ}\text{C}$, Energy content is equivalent of 5mg of gasoline.

The spray of a PDI outwardly opening injector is characterized by a hollow cone spray. Figure 4.20 illustrates the hollow-cone spray propagation from an outward opening piezo-driven injector at time 0.5, 1, 1.5 and 2 ms after the start of injection. The process of vaporization was evaluated by the Schlieren images. During the injection process, the ambient gas in the chamber was displaced by the

high momentum liquid droplet and was accelerated with the dispersed droplets by the drag forces. The liquid droplet vaporization start at the spray atomization occurred, the vapor envelop was decelerated and overtaken by the following liquid droplets. High compact spray was observed where the chamber pressure is 4bar. The wall impingements and 3D-CFD simulation for the PDI injector and Multi-hole GDI injector will be discussed in next sections.



(a) $T_{ch}= 25^{\circ}\text{C}$, $P_{ch}= 1\text{bar}$; (b) $T_{ch}= 200^{\circ}\text{C}$, $P_{ch}= 1\text{bar}$; (c) $T_{ch}= 25^{\circ}\text{C}$, $P_{ch}= 4\text{bar}$; (d) $T_{ch}= 200^{\circ}\text{C}$, $P_{ch}= 4\text{bar}$

Figure 4.20 Schlieren spray images for PDI injector under variant chamber pressure and temperature.

4.2.2 CFD Techniques and Spray Simulation

Compared to Diesel sprays, the DISI sprays have smaller enclosed cone angle, more volatile fuels, shorter aspect-ratio nozzle holes and consequently more unstable vortices. As a result, more interactions among the various spray plumes are expected. Therefore, in addition to the embedded grid control used to reduce the grid size at sensitive areas such as the injector tip, Adaptive Mesh Refinement (AMR) is also used to automatically enhance mesh resolution in critical areas of spray development within the spray or combustion chamber. The Kelvin-Helmholtz and Rayleigh-Taylor (KH-RT) breakup model, the No Time Counter (NTC) collision model, and the renormalization group (RNG) $k-\epsilon$ model are used, in conjunction with the RANS solver. The uncertainty in the liquid fractions of the multi-phase jets and the interactions among different spray plumes, as well as and the potential of flash boiling [5, 15, 20~23] make it difficult to simulate the dynamic spray plumes using RANS simulation, although reasonable agreement in spray plume penetration could be achieved, as shown in Fig. 4.21.

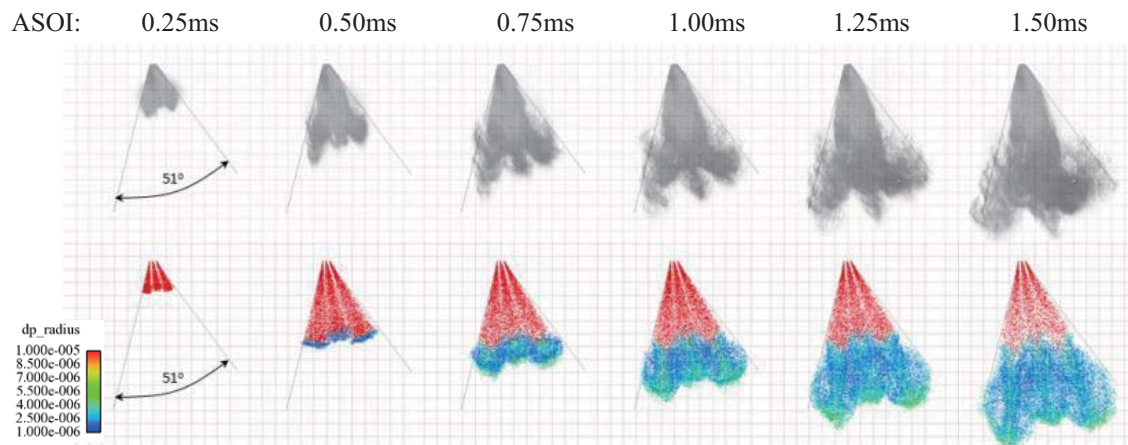


Figure 4.21 Measured and computed Spray Images; $T_{ch} = 200^{\circ}\text{C}$, $P_{ch} = 1\text{bar}$.

The simulation images show the mass fraction of ethanol vapor. The overall shapes of sprays were comparable. Since the simulation outputs are vapor fraction, it is reasonable not to have the upstream portion of the spray at 25C conditions. And the center of the plumes had lower fraction because of the liquid core. As the temperature increased, the liquid core evaporated and dense vapor appeared instead.

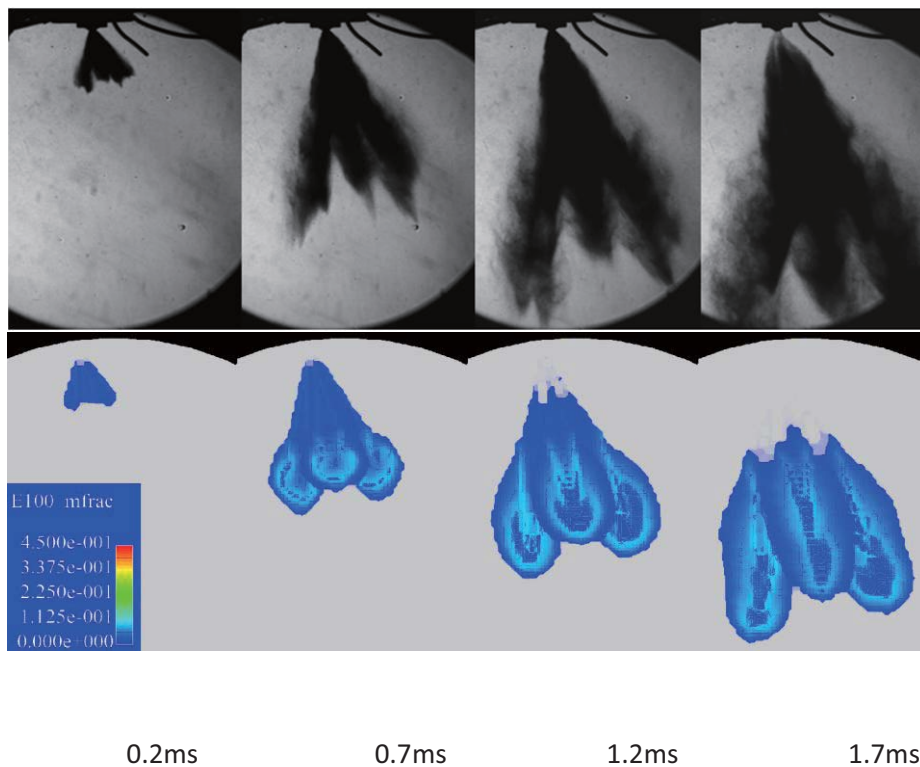


Figure 4.22 Comparison of spray images from the experiment (top) with the numerical simulation (bottom), After SOI: 0.2ms, 0.7ms, 1.2ms, 1.7ms, Injector A, 25C 1bar.

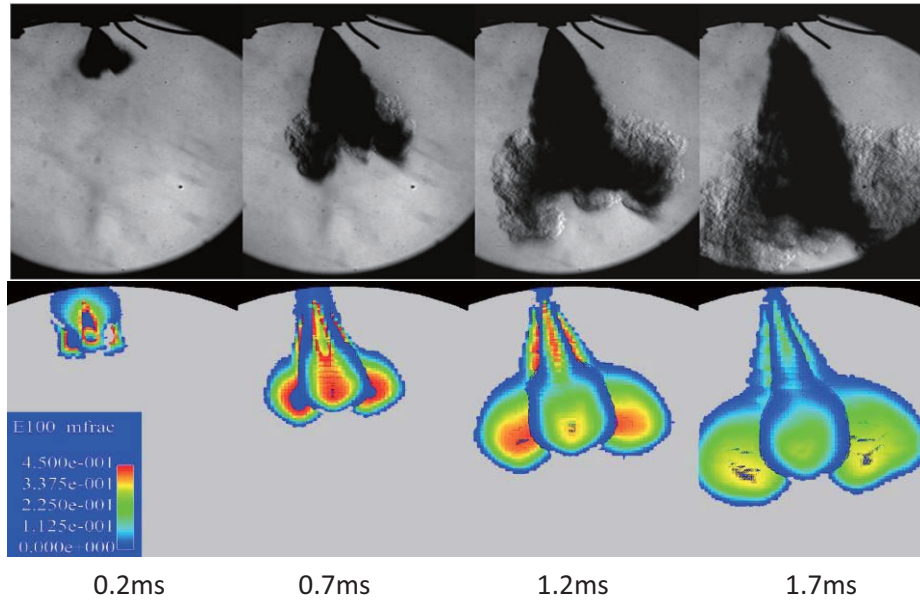


Figure 4.23 Comparison of spray images from the experiment (top) with the numerical simulation (bottom), After SOI: 0.2ms, 0.7ms, 1.2ms, 1.7ms, Injector A, 200C 1bar.

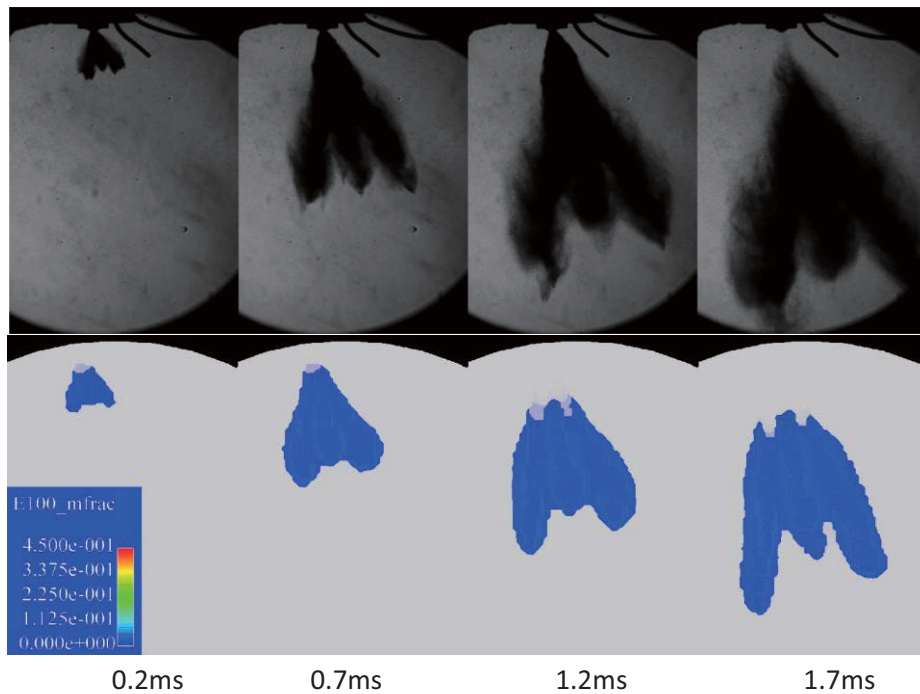


Figure 4.24 Comparison of spray images from the experiment (top) with the numerical simulation (bottom), After SOI: 0.2ms, 0.7ms, 1.2ms, 1.7ms, Injector A, 25C 3bar.

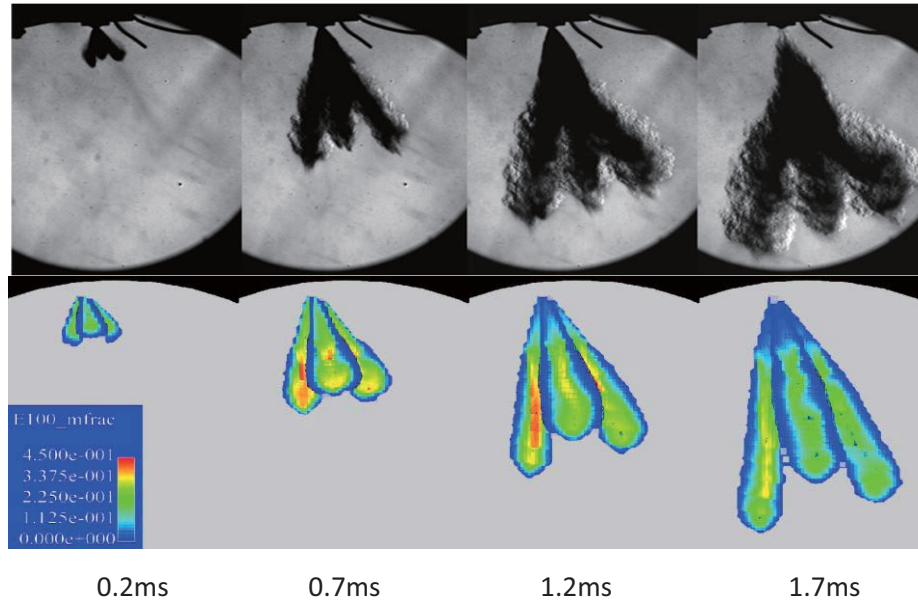
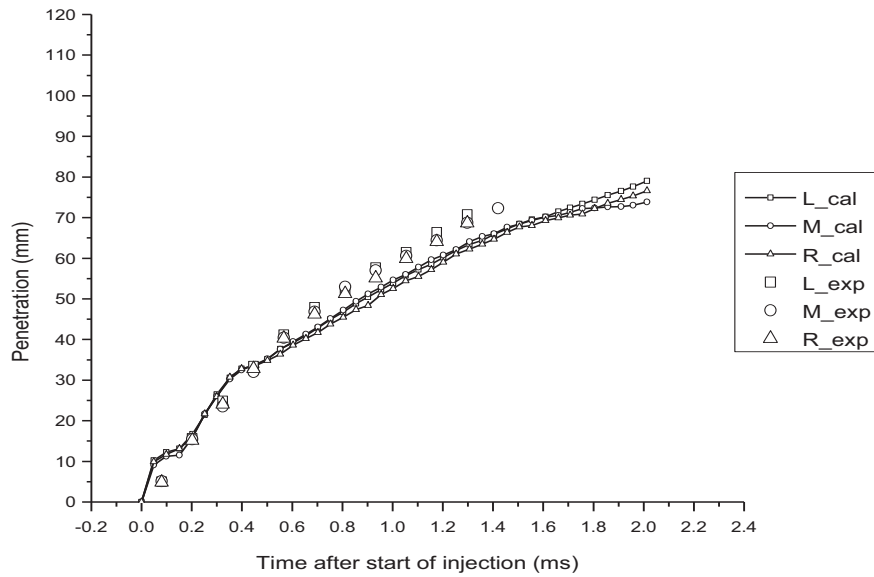
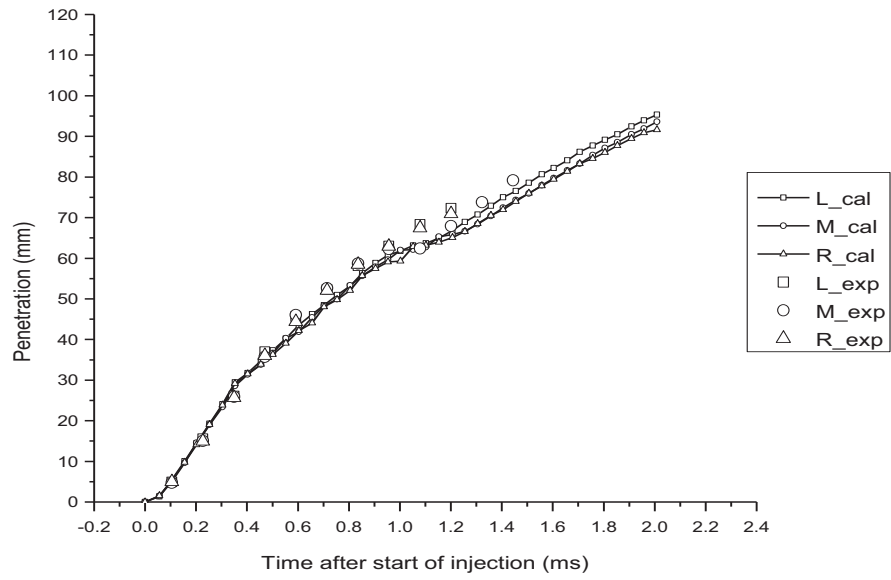
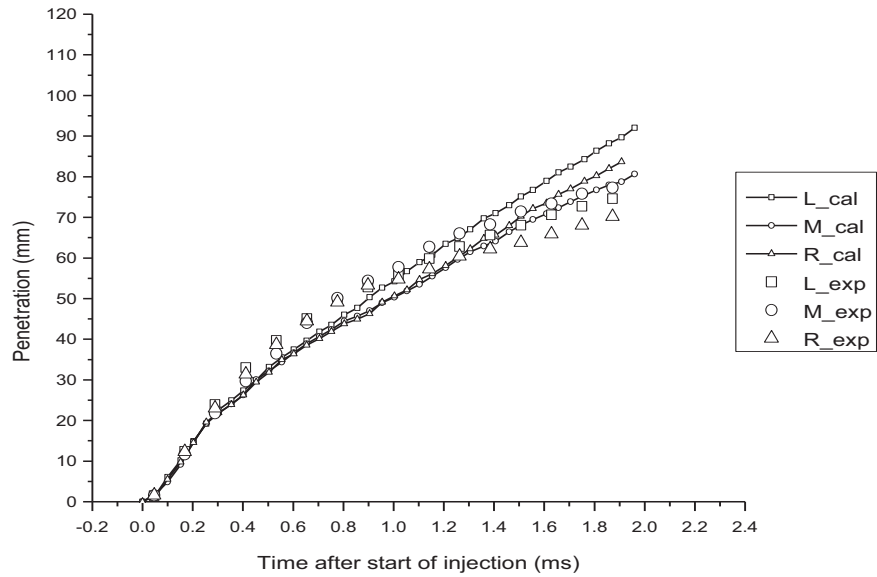
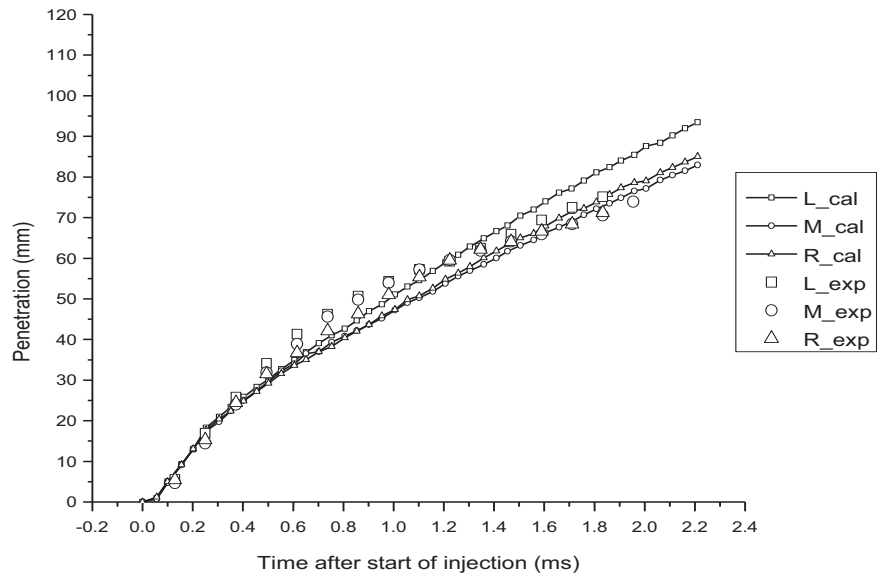


Figure 4.25 Comparison of spray images from the experiment (top) with the numerical simulation (bottom), After SOI: 0.2ms, 0.7ms, 1.2ms, 1.7ms, Injector A, 200C 3bar

The comparison of penetrations with the experimental data is plotted in Fig.4.26. L, M, and R in the figure indicated Left, Middle, and Right plume of the spray. The simulation fairly agreed with the empirical data, especially at the early stage of injection. However, it slightly under-predicted the penetration at middle stage of injection and eventually became longer than the experimental data at the end. This indicates that the RT model did not work well and further modification is required. The mass of liquid and vapor ethanol in the domain is plotted with time in Fig.4.27.

(a) $T_{ch}=25C$, $P_{ch}=1bar$ (b) $T_{ch}=200C$, $P_{ch}=1bar$



(c) Tch=25C, Pch=3bar

(d) Tch=200C, Pch=3bar

Figure 4.26 Comparison of experiment and numerical results of vapor phase penetration.

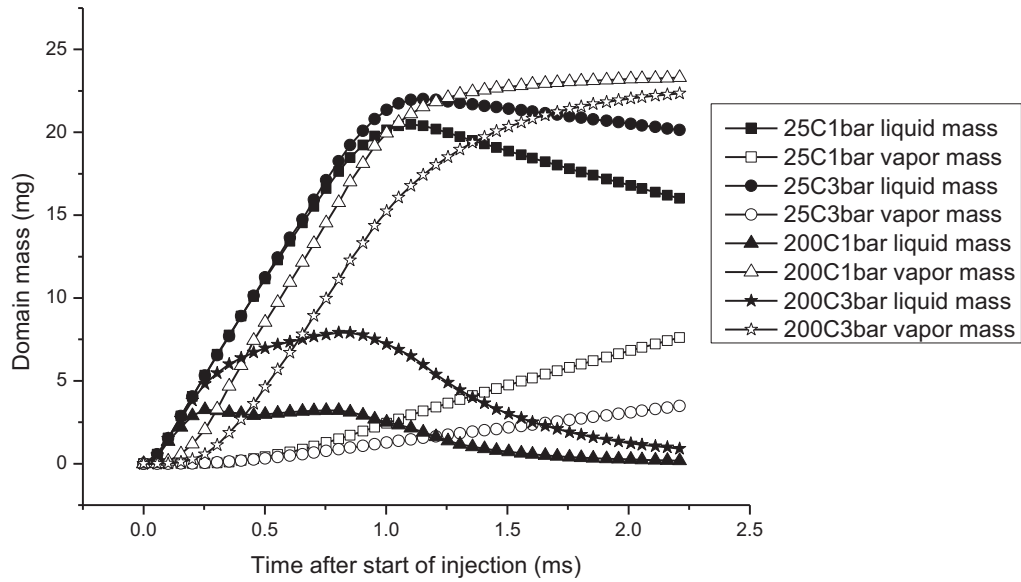


Figure 4.27 Liquid and vapor mass change in time.

In Figure 4.28, the images of spray propagation of GDI injector C were obtained experimentally and numerically. The chamber temperature is 200°C and chamber pressure is 1bar. It is clearly seen that the lost momentum of the vapor phase envelop and overtaken by the following liquid spray. This process can be evaluated in Fig. 4.29.

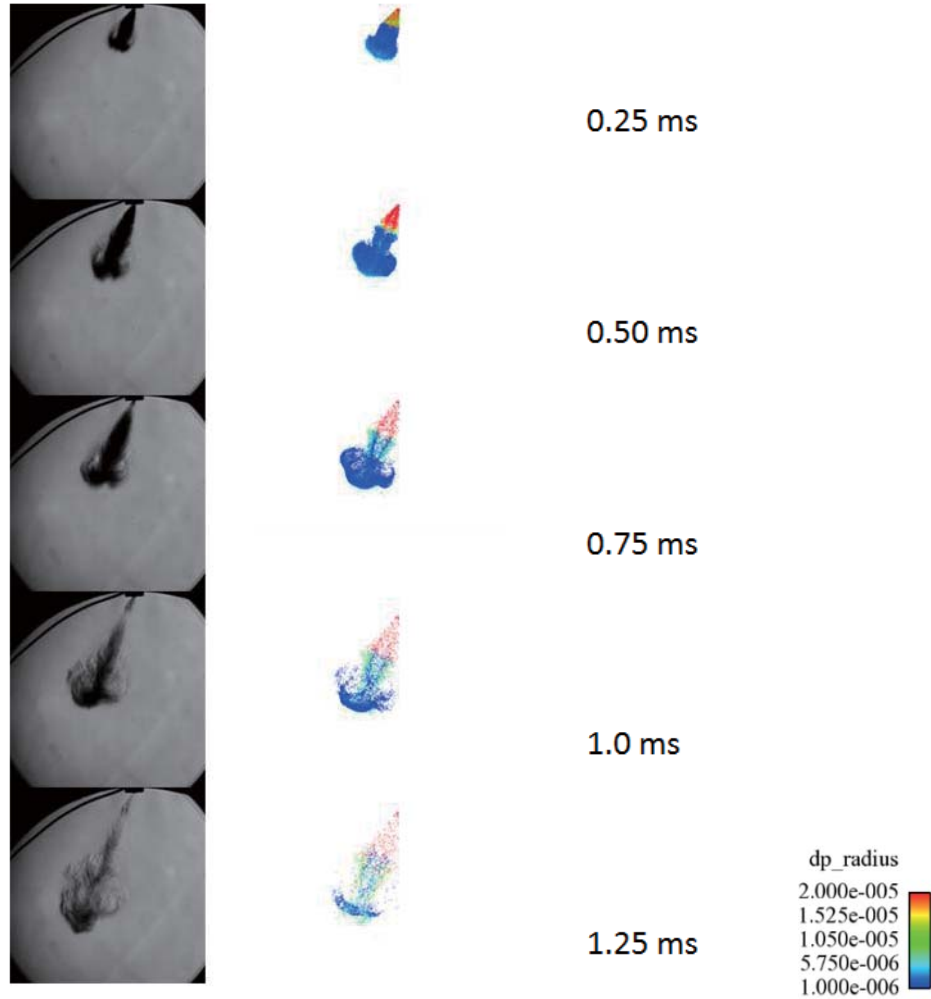


Figure 4.28 Comparison of Schlieren images and CFD-simulation (3D parcel representation) for multi-hole injector ($T_{ch} = 200^{\circ}\text{C}$, $P_{ch} = 1\text{bar}$, Injection duration = 0.5ms).

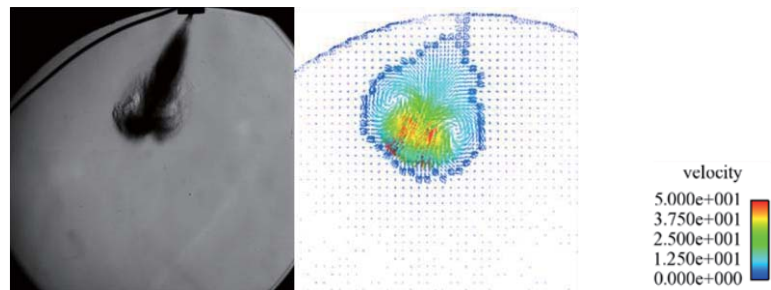
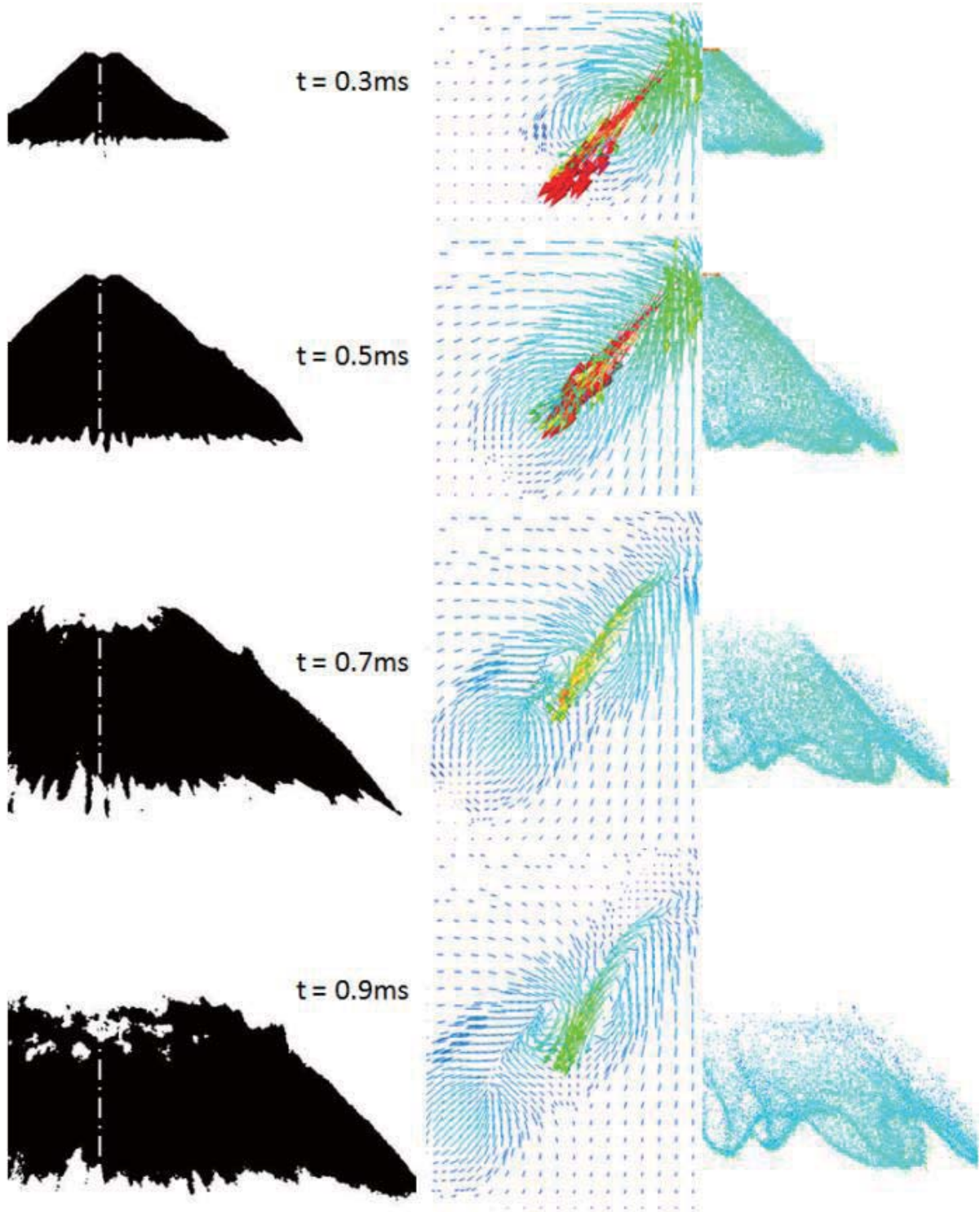
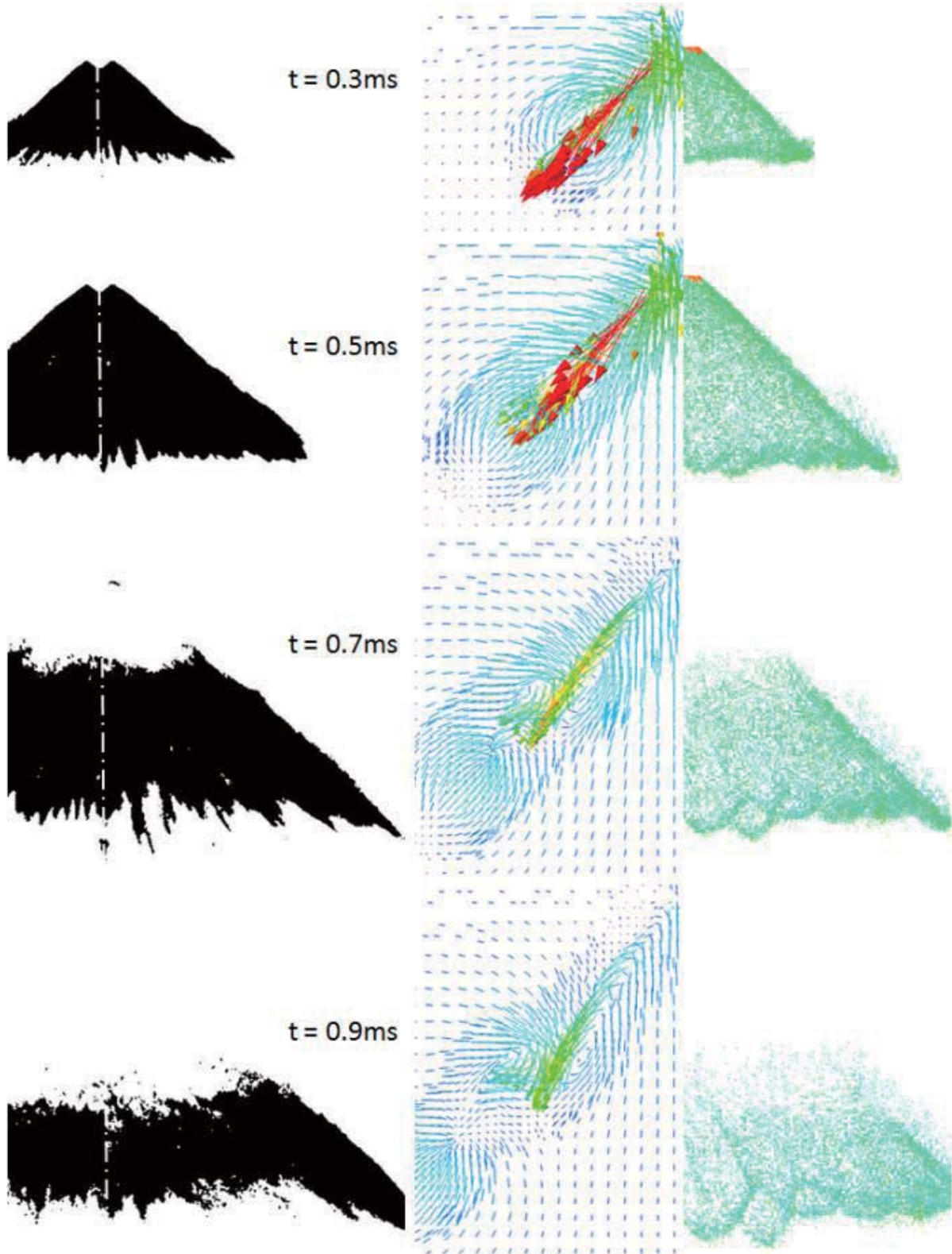


Figure 4.29 Comparison of experiment and numerical results (velocity vector field) of multi-hole injector at 0.75ms after start of injection.

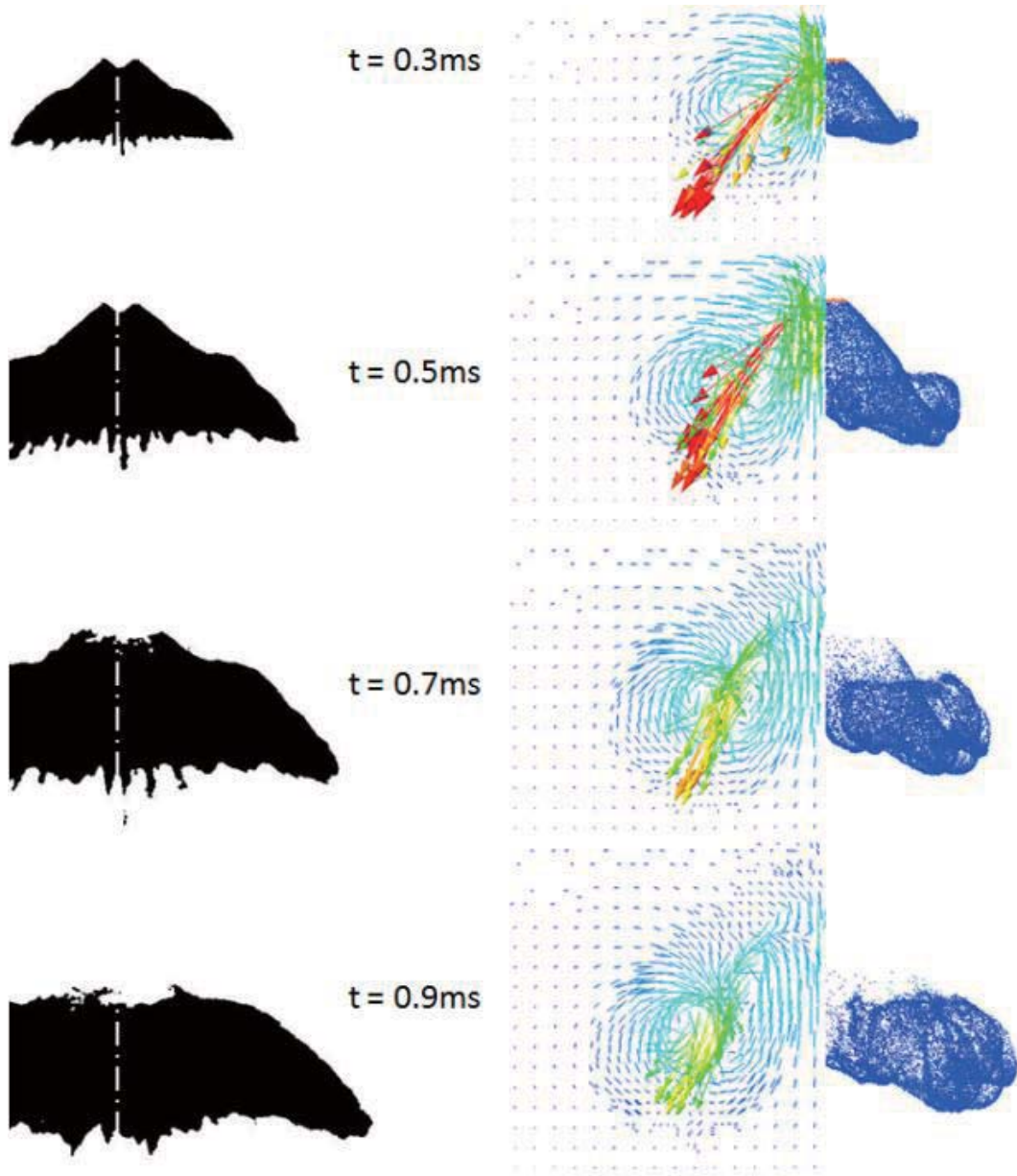
The numerical analysis of the PDI injection was carried out using CONVERGE 3D-CFD codes. In each simulation case, about 30,000 parcels were tracked for sufficiently precise statistical resolution. The binary Schlieren images were used for general spray shape comparison of the developing processes of hollow-cone sprays with two chamber temperatures and pressures as shown in Figure 30. The 3D parcel representation and the binary Schlieren images have shown a reasonable agreement in spray shapes spray cone angle and spray penetration. As the velocity vector field of the gas phase in Figure 4.30 indicated, the velocity of gas phase increases due to the high momentum liquid phase, which result in the recirculation zones. Strong vortex has been found in the inner and outer region of the hollow spray with chamber pressure 4bar. It is believed that the density of the ambient gas in the chamber strongly effect the spray structure, spray propagation and vortex formation. As shown in Figure 4.31, the predicted value of spray penetration using the dynamic drag model shows good agreement with the experiment results.



(a) $T_{\text{ch}} = 25^\circ\text{C}$, $P_{\text{ch}} = 1\text{bar}$;



(b) $T_{\text{ch}} = 200^\circ\text{C}$, $P_{\text{ch}} = 1\text{bar}$;



(c) $T_{\text{ch}} = 25^\circ\text{C}$, $P_{\text{ch}} = 4\text{bar}$;

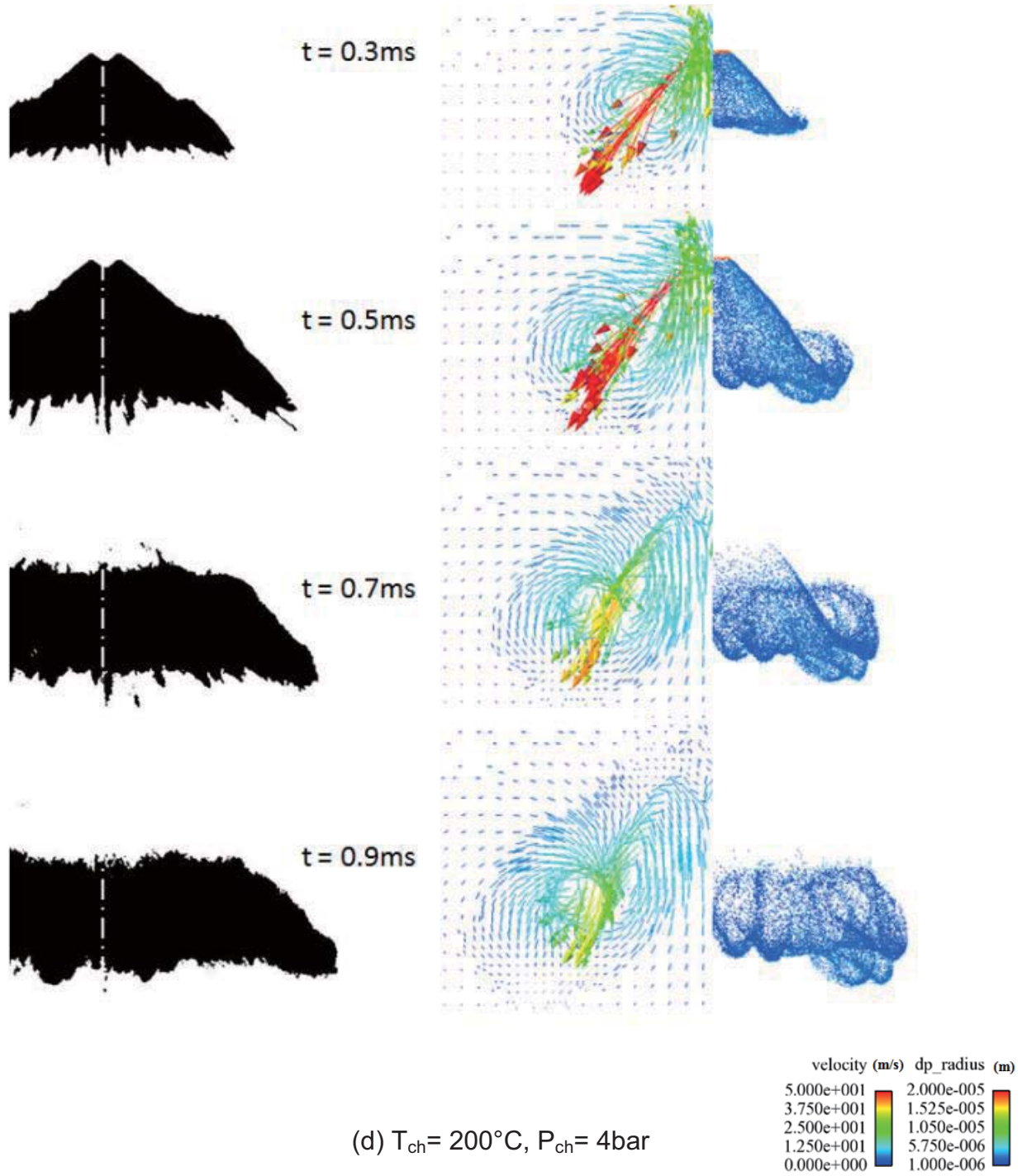
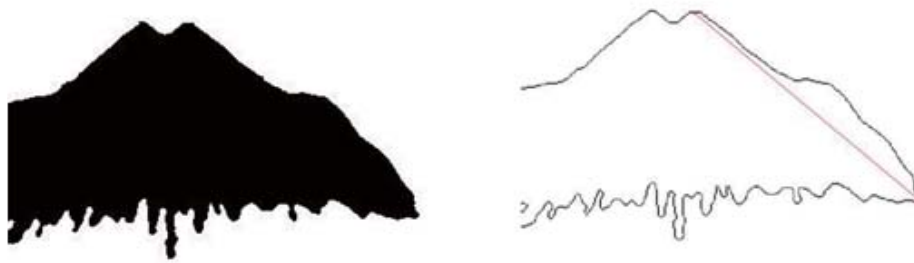


Figure 4.30 Comparison of binary Schlieren images and CFD-simulation for PDI injector.

In this study, the spray penetration is defined as the maximum distance between the PDI injector nozzle and the tip of the spray. Figure 3.21 display the process of automatically calculating the spray penetration using MATLAB. It is believed that the injection pressure, the drag, the fuel properties, spray cone angle and ambient pressure govern the spray penetration [44]. Among these factors, the drop drag coefficients are critical for accurate spray modeling.



(a)

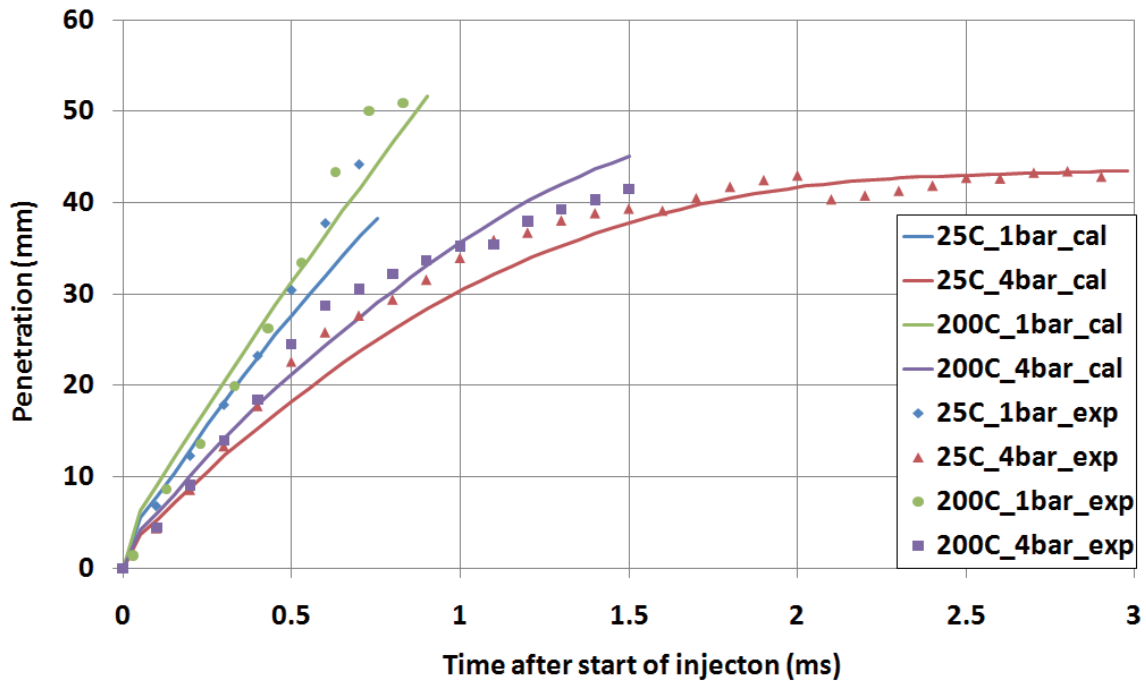


Figure 4.31 Comparison of experiment and numerical results of PDI injector spray penetration.

4.2.3 Wall Impingement and RIM test for PDI injector

In section 4.2.1 and 4.2.1, the formation and evolution of the fuel spray emerging from multi-hole injector and outward opening piezo-driven injector were investigated. In this section, the spray-wall interaction is discussed experimentally and numerically. Then the measurement and simulation of wall wetting are carried out using RIM technique.

The wetting of piston surface by a strongly penetrating fuel spray is believed to be a major source of soot emissions. This section first presents the wall impingement numerical and experimental results of DI injectors. In Figure 4.32, the impingement for a PDI injector spray is computed using same drop/wall interaction model. The flat piston surface is 10mm down from the injector tip. The vortex structure formed by the impingement is similar with the multi-hole injector. Experiments are required to verify the propagation of spray and the height of the impinged spray.

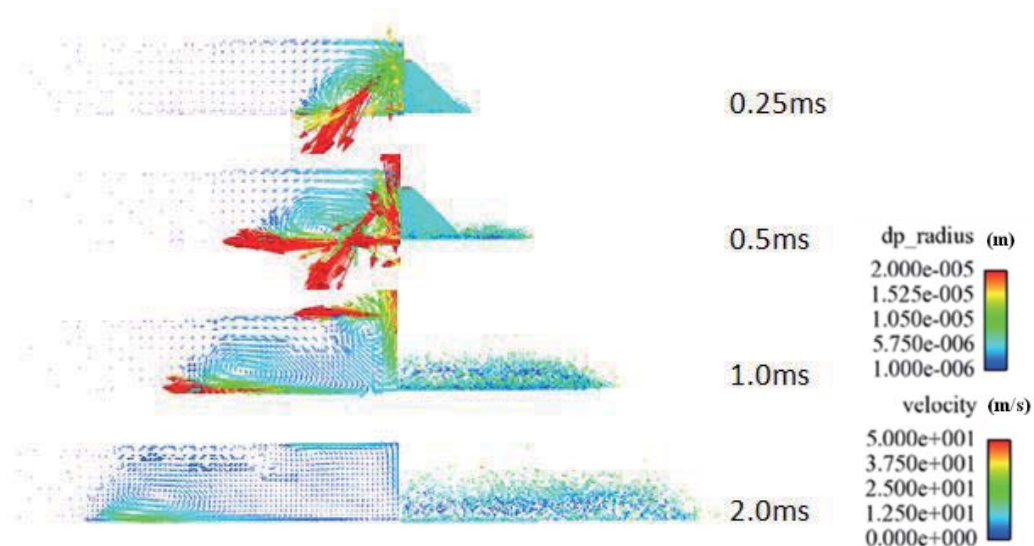


Figure 4.32 CFD-simulation of piston impingement, PDI injector (3D parcel representation) ($T_{ch} = 100^{\circ}\text{C}$, $P_{ch} = 1\text{bar}$, Injection duration = 0.5ms).

Fig. 4.33 shows the time evolution of reduction in the scattered light of the PDI spray at $T_{ch} = 150\text{ }^{\circ}\text{C}$, $P_{ch} = 3\text{ bar}$ and Injection duration = 0.5 ms, which displays the process of liquid film evaporation. The instantaneous liquid fuel film structure was observed by both visualization and quantitative analysis. The instantaneous images of the fuel film thickness is obtained at 1.25 ms (0.75 ms for the case of $T_{ch} = 150\text{ }^{\circ}\text{C}$, $P_{ch} = 1\text{ bar}$, Injection duration = 0.2 ms) for the spray PDI injector as shown in Fig. 4.34 and Fig. 4.36. Also the resulting time evolution of liquid film thickness of PDI spray for the different conditions is presented in Fig. 4.35 and Fig. 4.37.

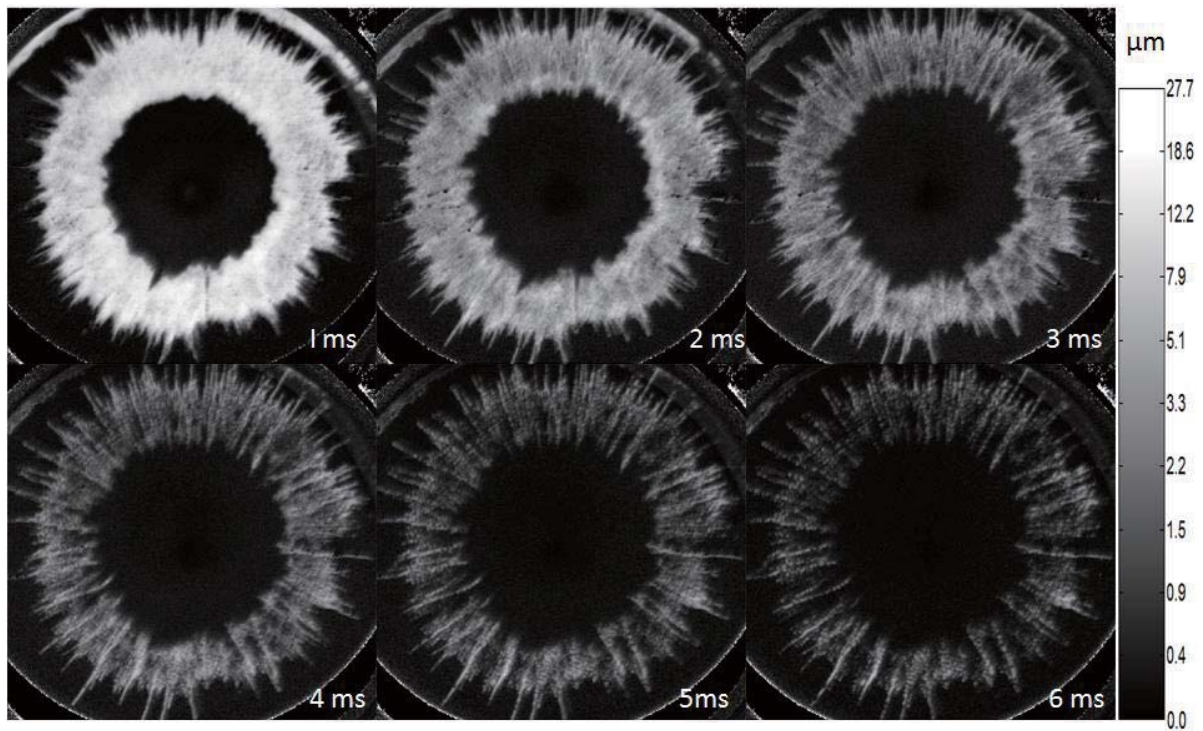


Figure 4.33 Evolution of fuel film thickness ($T_{ch} = 150\text{ }^{\circ}\text{C}$, $P_{ch} = 3\text{ bar}$, Injection duration = 0.5ms).

The annular form area on the wall surface is much larger and reduction level is higher for longer injection duration, which can be proofed from time evolution of liquid thickness as shown in Fig. 4.35 and Fig. 4.37. The chamber temperature strongly effect the film thickness after the comparison between $T_{ch} = 100\text{ }^{\circ}\text{C}$ and $T_{ch} = 150\text{ }^{\circ}\text{C}$, the film thickness decreases much faster for the case of $T_{ch} = 150\text{ }^{\circ}\text{C}$.

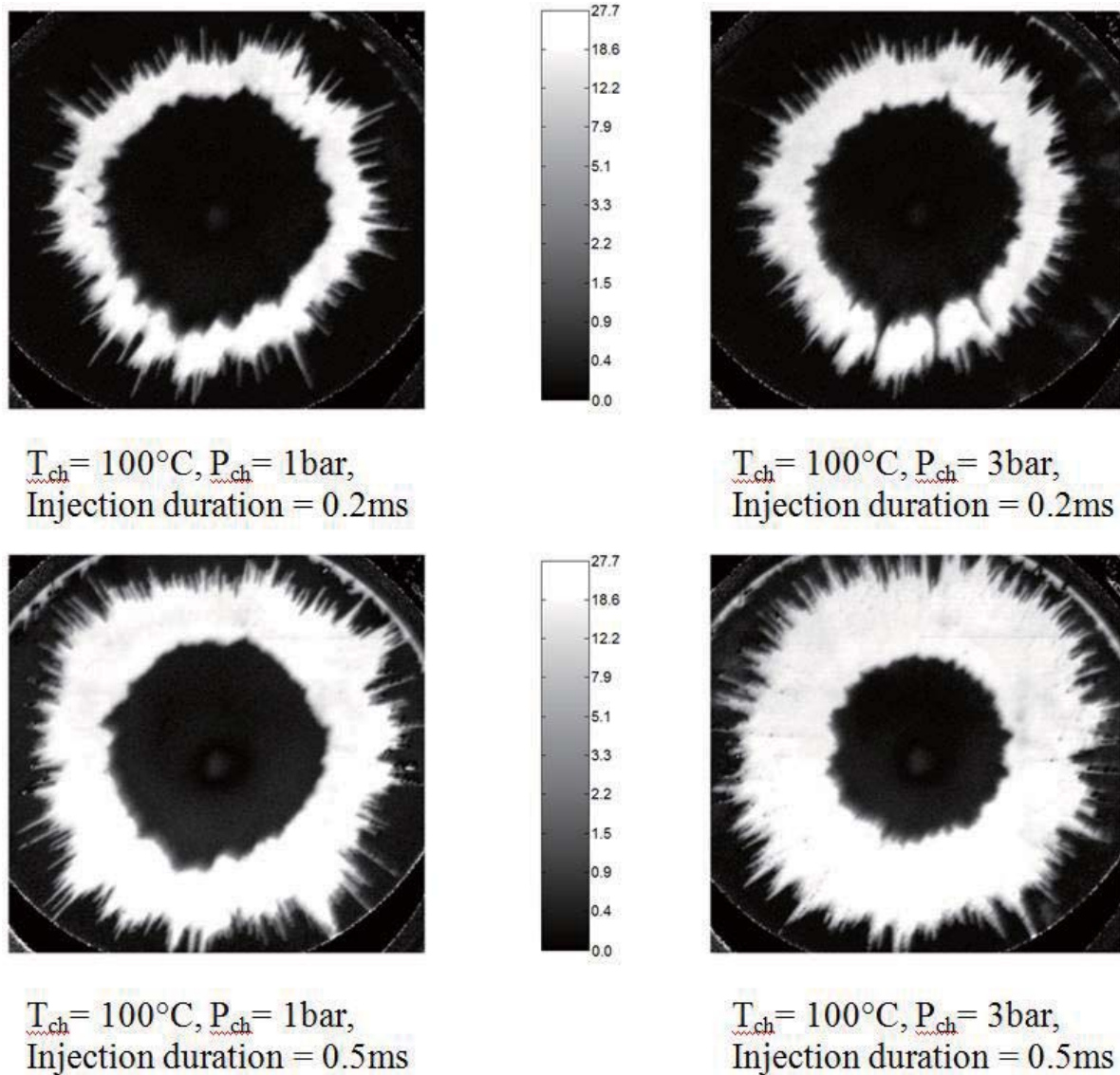
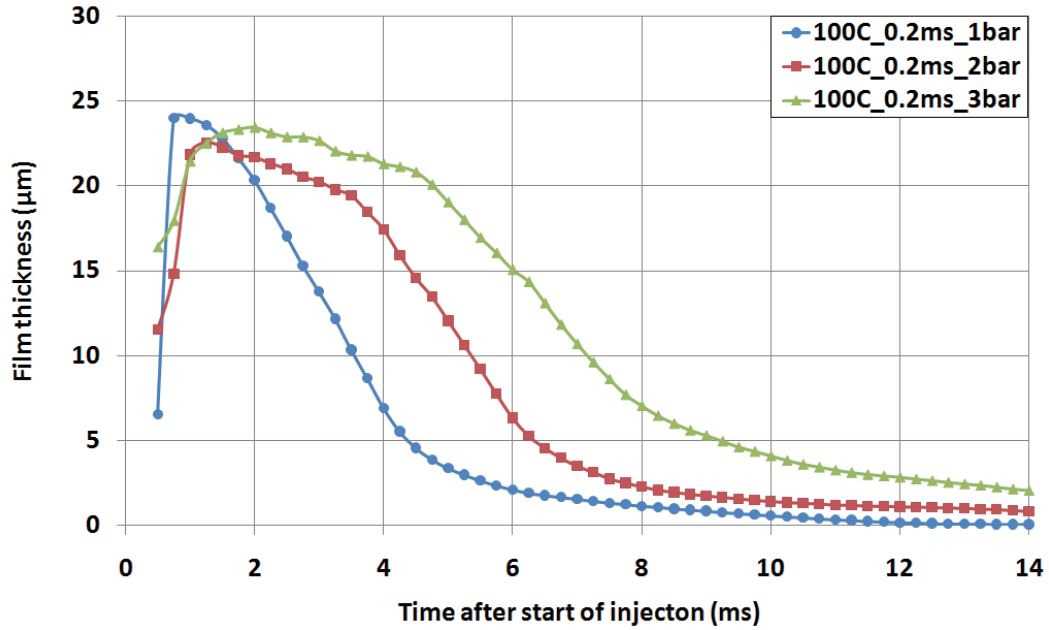
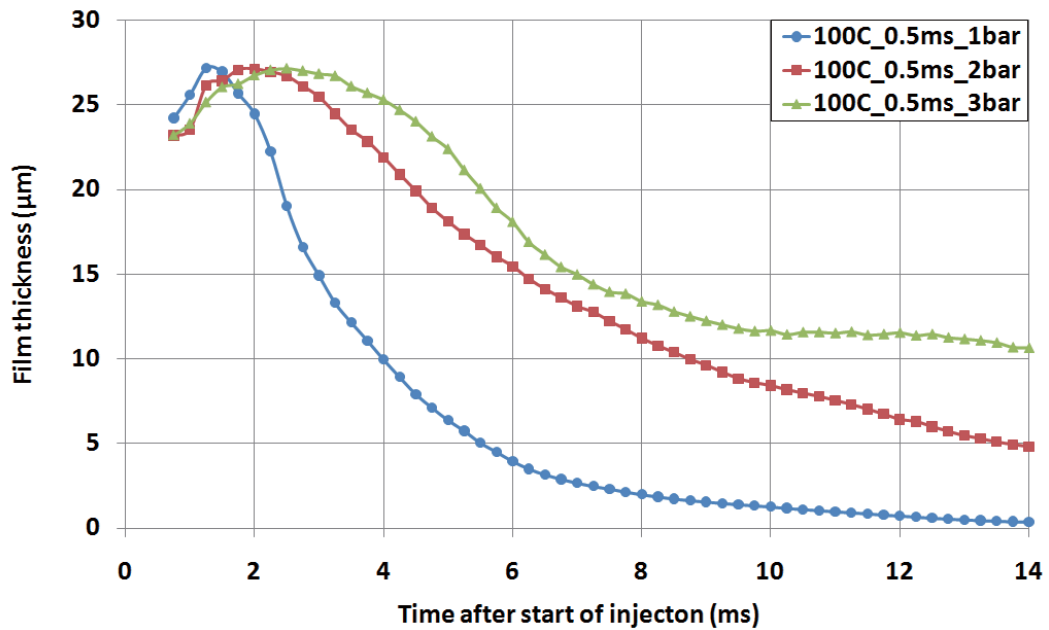


Figure 4.34 Instantaneous images of the fuel film thickness. PDI injector, $T_{ch} = 100^{\circ}\text{C}$.

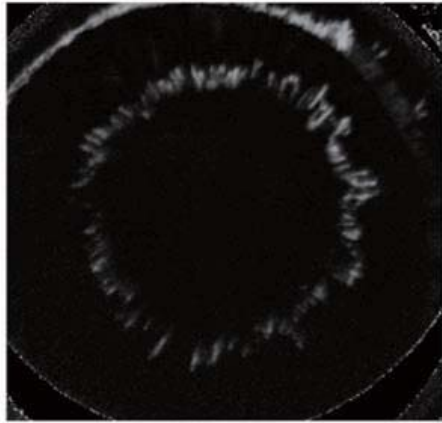


(a)

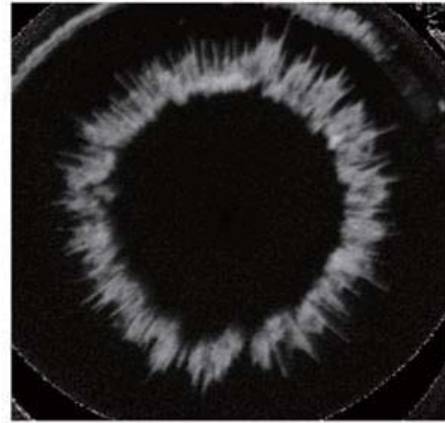
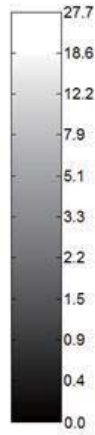


(b)

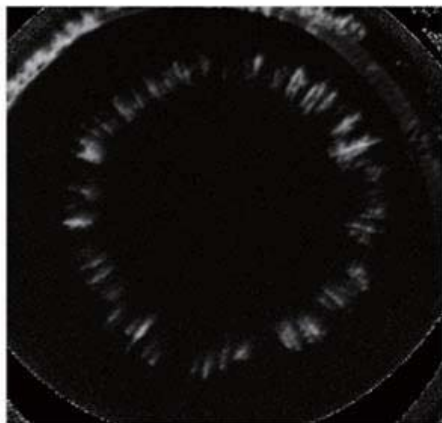
Figure 4.35 Averaged film thickness of PDI injection, (a) $T_{ch} = 100^{\circ}\text{C}$, Injection duration = 0.2ms, (b) $T_{ch} = 100^{\circ}\text{C}$, Injection duration = 0.5ms.



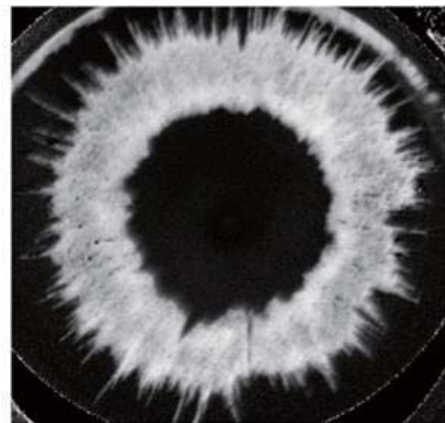
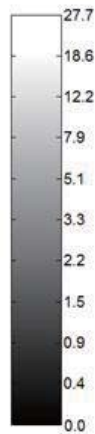
$T_{ch} = 150^{\circ}\text{C}$, $P_{ch} = 1\text{bar}$,
Injection duration = 0.2ms



$T_{ch} = 150^{\circ}\text{C}$, $P_{ch} = 3\text{bar}$,
Injection duration = 0.2ms

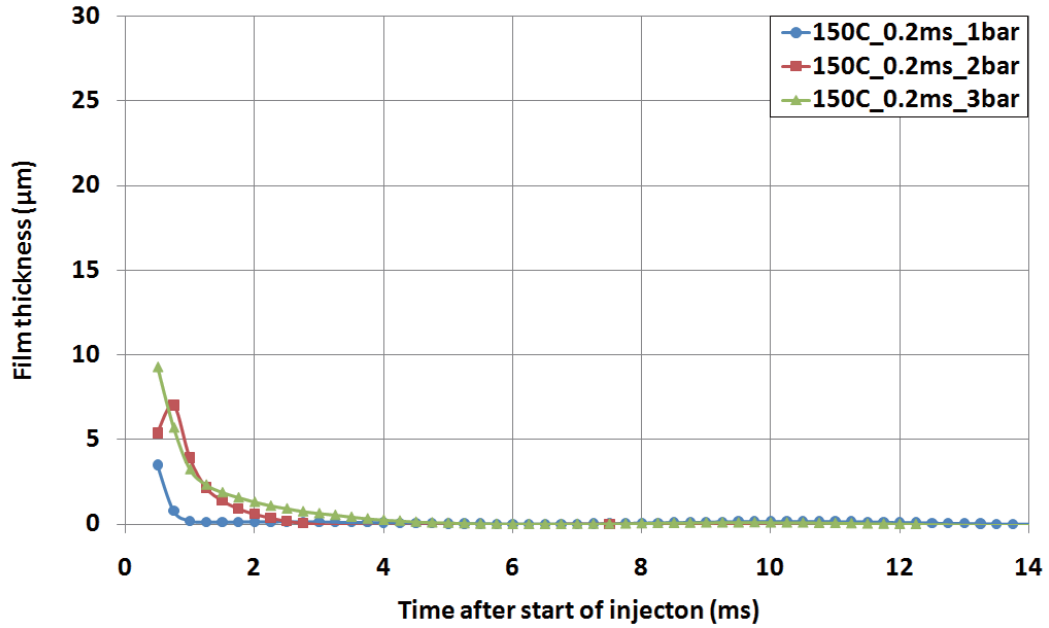


$T_{ch} = 150^{\circ}\text{C}$, $P_{ch} = 1\text{bar}$,
Injection duration = 0.5ms

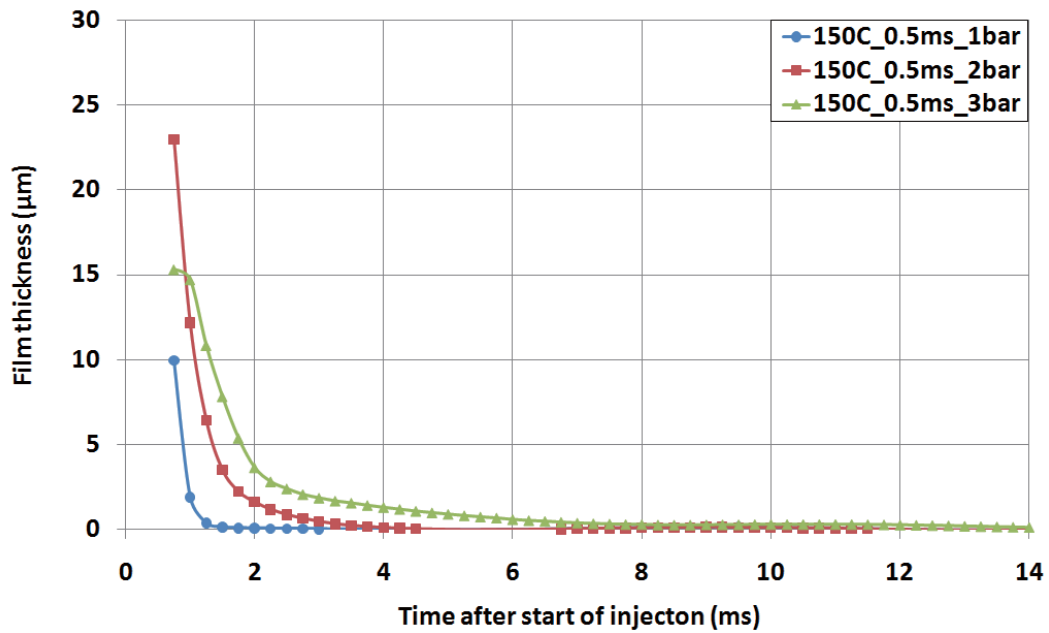


$T_{ch} = 150^{\circ}\text{C}$, $P_{ch} = 3\text{bar}$,
Injection duration = 0.5ms

Figure 4.36 Instantaneous images of the fuel film thickness. PDI injector, $T_{ch} = 150^{\circ}\text{C}$.



(a)



(b)

Figure 4.37 Averaged film thickness of PDI injection, (a) $T_{ch} = 150^{\circ}\text{C}$, Injection duration = 0.2ms, (b) $T_{ch} = 150^{\circ}\text{C}$, Injection duration = 0.5ms.

4.2.4 Wall Impingement and RIM test for multi-hole injectors

In homogeneous-charge direct-injection engines, a side-mounted or center-mounted high-pressure fuel injector delivers fuel directly into the combustion chamber early enough in the cycle to provide homogeneous fuel–air mixture formation and minimize wall wetting. In wall guide stratified-charge DI engines, the centrally located PDI injector or multi-hole injector injects through the cylinder axis to a near mounted spark plug with electrodes placed at the edge of the spray plume. For wall guide stratified-charge DI engines, side-mounted high-pressure multi-hole injectors are being used currently. The spray-wall interaction and wall wetting measurement are discussed in this section.

Fig. 4.38 shows the spray evolution at impinging conditions for GDI side-mounted multi-hole injector C. The experiment was carried out using a constant volume vessel and test results were used to support the CFD simulations. The distance between the piston surface and injector nozzle tip was set at 15 mm with an angle of 23 deg from the horizontal axis. The yellow line on the piston represents the bottom edge of the piston bowl. The impingement starts after 0.25 ms and the predicted 3D parcel cloud shows good agreement with the Schlieren spray visualization results. At 2 ms and 3 ms after start of injection, the droplets with bigger size can be seen on the tip of impinged spray from both experimental and numerical results. The 2-dimensions computed velocity field and equivalence ratio show that a bigger vortex formed after spray impinged the piston surface, moved along the piston bowl and then lifted when it reached the edge of the bowl.

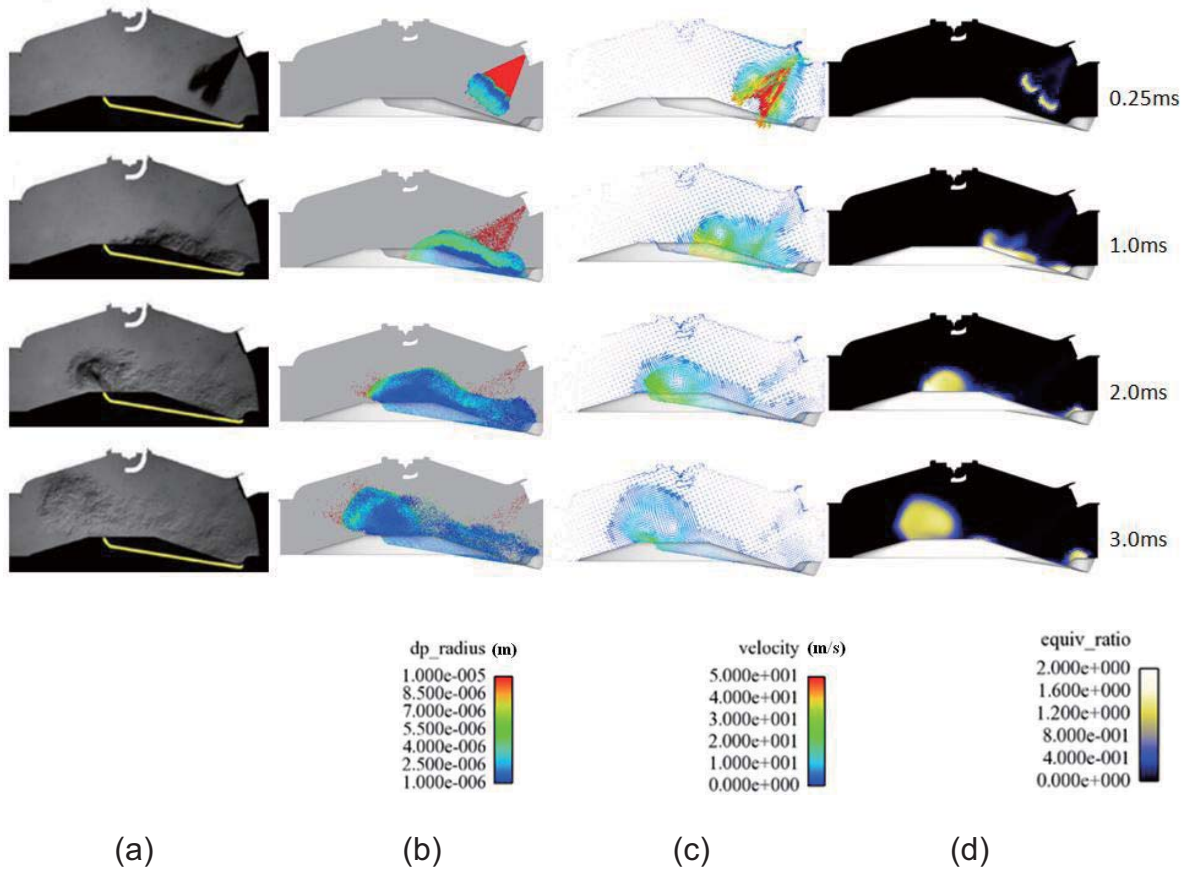
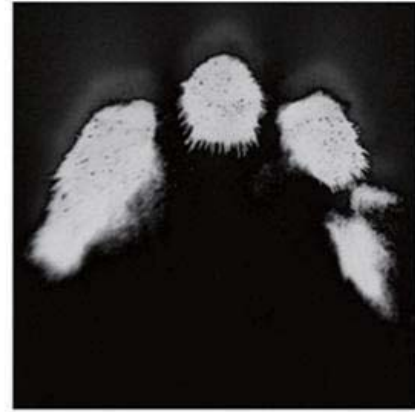
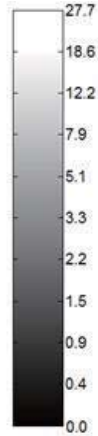


Figure 4.38 Comparison of experimental spray evolution and CFD-simulation for multi-hole injector (a) Schlieren images; (b) 3D parcel representation; (c) 2D velocity vector field; (d) 2D equivalence ratio ($T_{ch} = 150^{\circ}\text{C}$, $P_{ch} = 1\text{bar}$, Injection duration = 0.5ms)



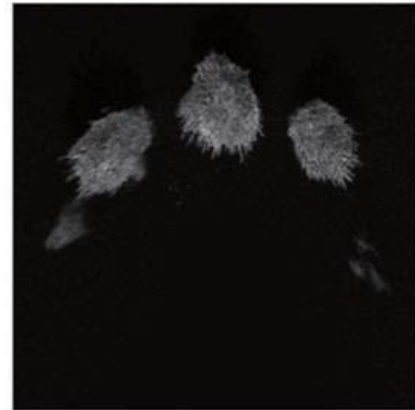
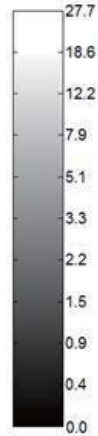
$T_{ch} = 100^\circ\text{C}$, $P_{ch} = 1\text{bar}$,
Injection duration = 0.5ms



$T_{ch} = 100^\circ\text{C}$, $P_{ch} = 3\text{bar}$,
Injection duration = 0.5ms

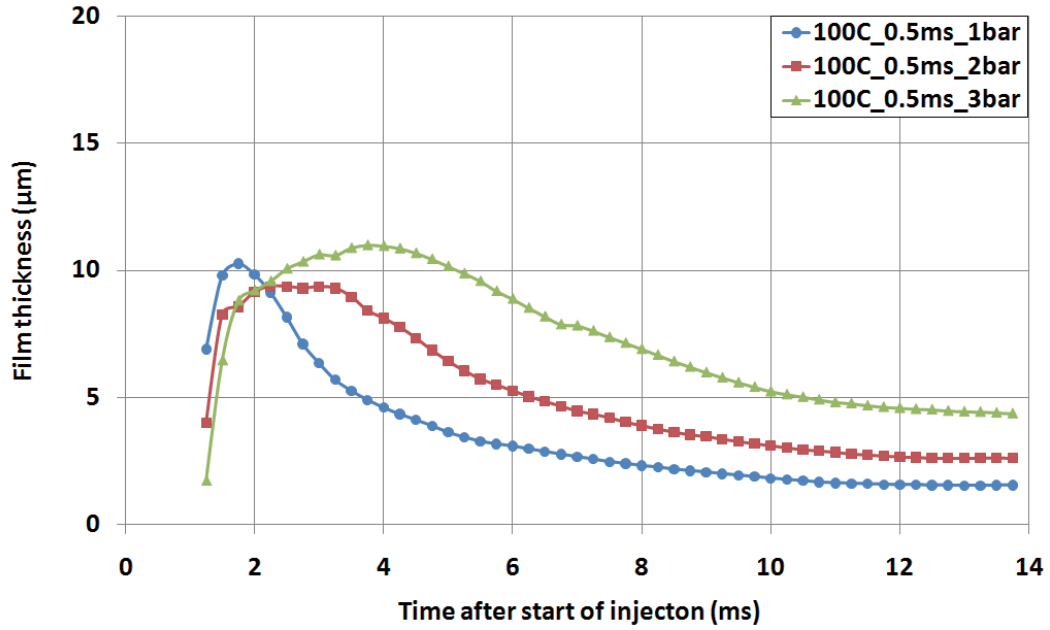


$T_{ch} = 150^\circ\text{C}$, $P_{ch} = 1\text{bar}$,
Injection duration = 0.5ms

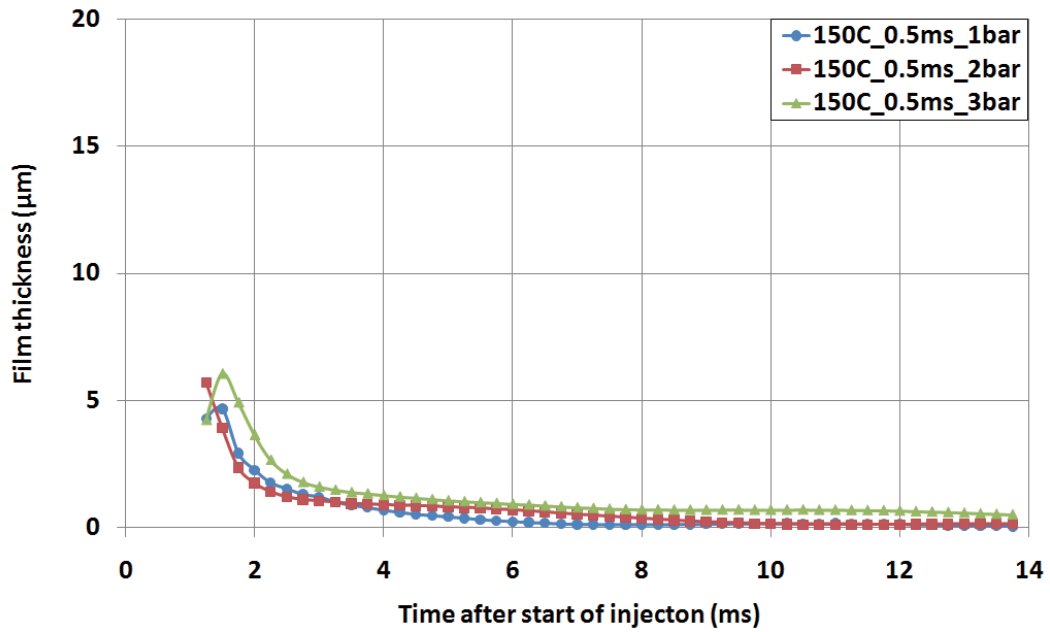


$T_{ch} = 150^\circ\text{C}$, $P_{ch} = 3\text{bar}$,
Injection duration = 0.5ms

Figure 4.39 Instantaneous images of the fuel film thickness. Multi-hole injector, Injection duration = 0.5ms.



(a)



(b)

Figure 4.40 Averaged film thickness of multi-hole injection, and injection duration = 0.5ms, (a) $T_{ch} = 100^\circ\text{C}$, (b) $T_{ch} = 150^\circ\text{C}$.

The film thick is also depended on the chamber pressure: the annular area of higher pressure is slightly larger and film thickness is also higher. Same situations can be seen in Fig. 4.39 and Fig. 4.40, which shows the instantaneous images and time evolution of liquid film thickness of the spray of multi-hole injector C. From the instantaneous images, only three spray plumes hit the window surface at $T_{ch}=150\text{ }^{\circ}\text{C}$, $P_{ch}=1\text{ bar}$ and Injection duration = 0.2 ms. Other cases have 5 plumes hit on the surface.

The computed evolution of liquid film thickness and equivalence ratio iso-surface was presented in Fig. 4.41. The wall surface is flat for both injectors. The liquid fuel film structure of outwardly opening PDI injector and multi-hole injector are in good agreement with experiment results as shown in Fig. 4.34 and Fig. 4.39. The values of liquid film thickness for both injectors when the fuel film deposit on surface are close to the results from RIM experiment as shown in Figure 4.35 and 4.40. For a further validation of film vaporization, more numerical calculations are required to verify the time evolution of liquid film thickness.

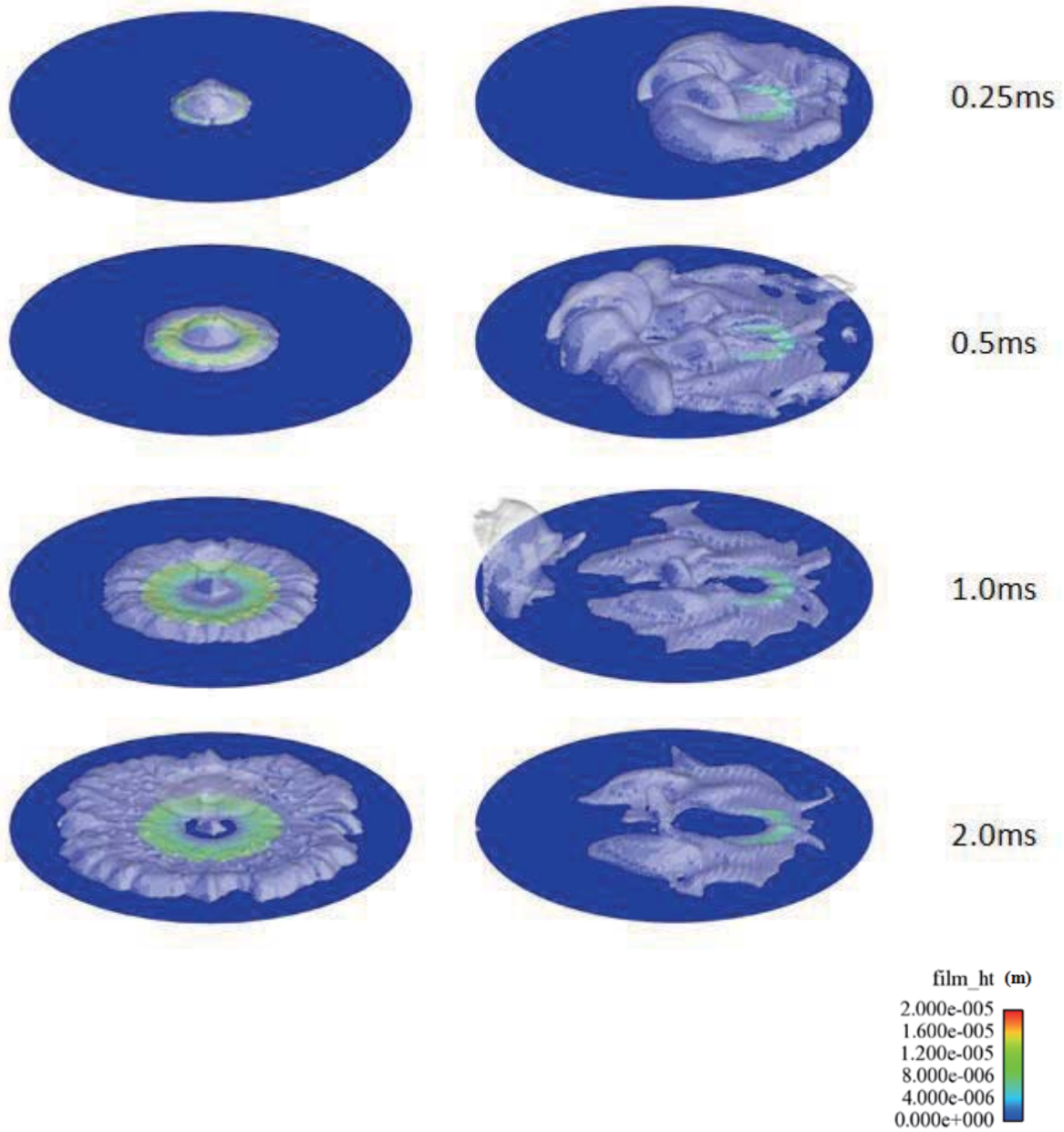


Figure 4.41 Computed evolution of liquid film thickness and iso-surfaces (equivalence ratio = 1, opaqueness = 30%) for PDI injector (left) and multi-hole injector (right) ($T_{ch} = 100^{\circ}\text{C}$, $P_{ch} = 1\text{bar}$, Injection duration = 0.5ms)

Refractive Index Matching (RIM) technique is used measure the liquid fuel film thickness for multi-hole GDI Injector D. Table 4.1 shows the reference conditions for a direct injection engine. Multi-hole injector was mounted with 25 deg to simulate a side-mounted DI engine configuration. Iso-octane was used as reference fuel. Different chamber pressure and temperature, injection pressure and duration, and distance between the injector tip and window were investigated. Fig. 4.2 and Fig. 4.3 show the wall wetting images.

Table 4.1 Operating conditions

Case #	Distance (mm)	Air press. (bar)	Air temp. (°C)	Injection press. (bar)	Fuel temp. (°C)	Pulse width (ms)
1	30	1	50	35	40	2.83
2	30	1	50	140	40	1.41
3	40	1	50	35	40	2.83
4	40	1	50	140	40	1.41
5	30	1	50	70	40	2
6	30	2	50	70	40	2
7	30	1	75	70	55	2
8	30	2	75	70	55	2
9	30	1	100	70	70	2
10	30	2	100	70	70	2

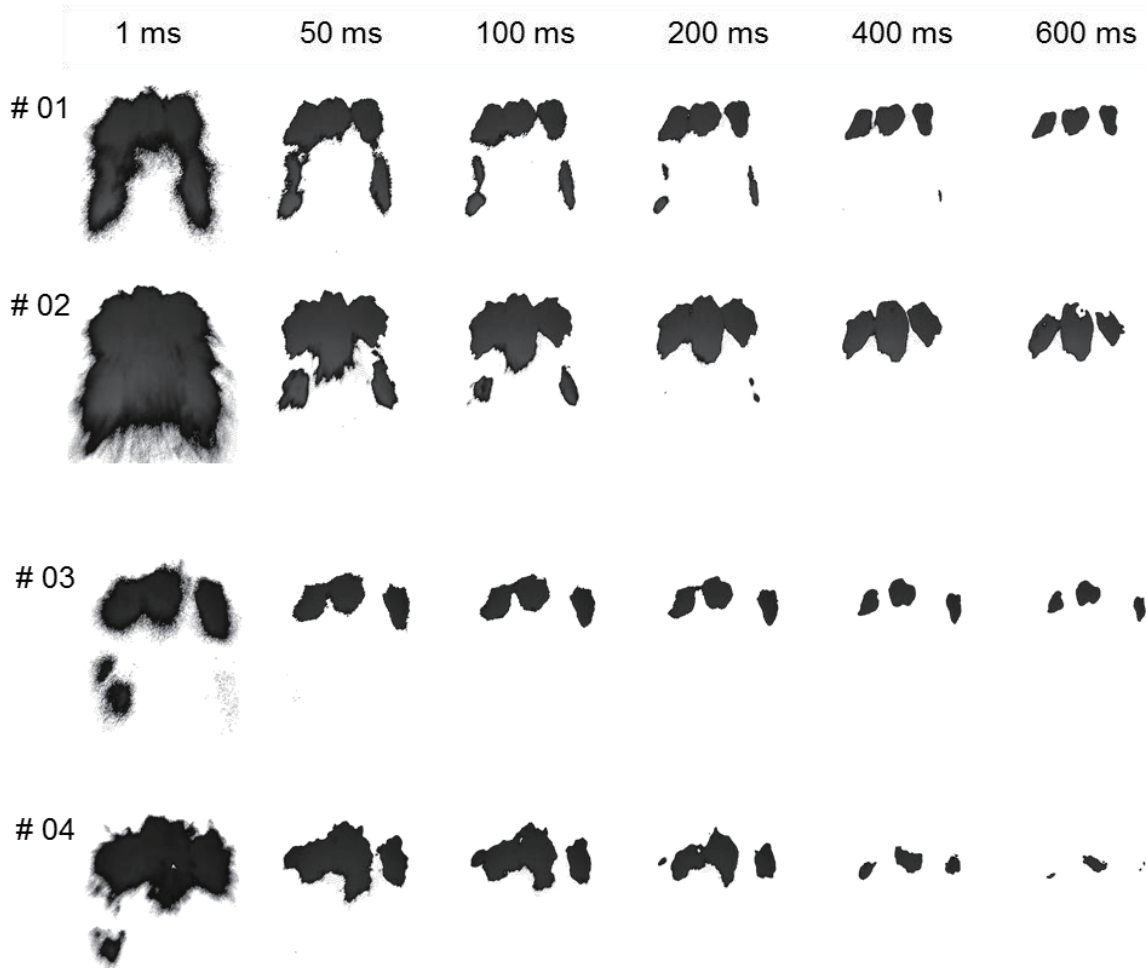


Figure 4.42 Wall wetting images (Case#1~4) after fuel droplet deposit on window surface.



Figure 4.43 Wall wetting images (Case#5~10) after fuel droplet deposit on window surface.

Liquid fuel film thickness, spatial distribution and adhered puddle mass for a side-mounted multi-hole injector under different operating conditions were studied using RIM method. Evolution of the fuel film thickness, mass and spatial distribution after fuel deposit on the window is presented in Fig. 4.44 for cases 1, 2, 3 and 4 to illustrate the effect of injection pressure (35bar and 140bar), injection duration (1.41 ms and 2.83 ms) and distance between the injector tip and window (30 mm and 40 mm). For injection emerging from the side-mounted multi-hole GDI injector, mean film thickness results from spray plumes were investigated. The mean film thickness is an instantaneous average over the entire area of deposit film. As the spray targeting scheme shown in Table 3.4, three lower spray plumes first impinge the window and then the two middle plumes (4th and 5th) land later. The last plume (6th) does not meet the window for all cases in this study. Therefore, up to five wetted spray footprints could be measured.

The dynamic evaporation can be found from the film thickness spatial distribution in Fig. 4.44, thinner film (blue) evaporates fast and thicker film (red) has slower evaporation. The wetted areas of cases 2 and 4 are much larger than the areas of cases 1 and 3 respectively due to the high injection pressure. The camera speed is 1000 fps for RIM test, which is not fast enough to record the process of spray impinging, so that the curves of averaged film thickness and mass in Fig. 4.45 could be roughly extended to initial deposit time though the line slope, which presents the rate of evaporation. Also, the gently sloping curves of cases 1 and 3 are result of saturation of the rough surface of the window. Therefore, the maximum film thickness of the RIM measurement in this study is underestimated. For the high

injection pressure cases 2 and 4, the film evaporates much faster after deposition on window, compared with cases with 35 bar injection pressure. The reason of the larger film area and faster evaporation for the high injection pressure cases is that the velocity at which droplet impacts is higher and the atomization of spray is better. For case 3 and 4, the distance between injector tip and window is 40mm, as shown in Fig. 4.44, the film thickness and deposit area of the 4th and 5th spray plumes were much thinner and smaller compared with 30mm distance cases.

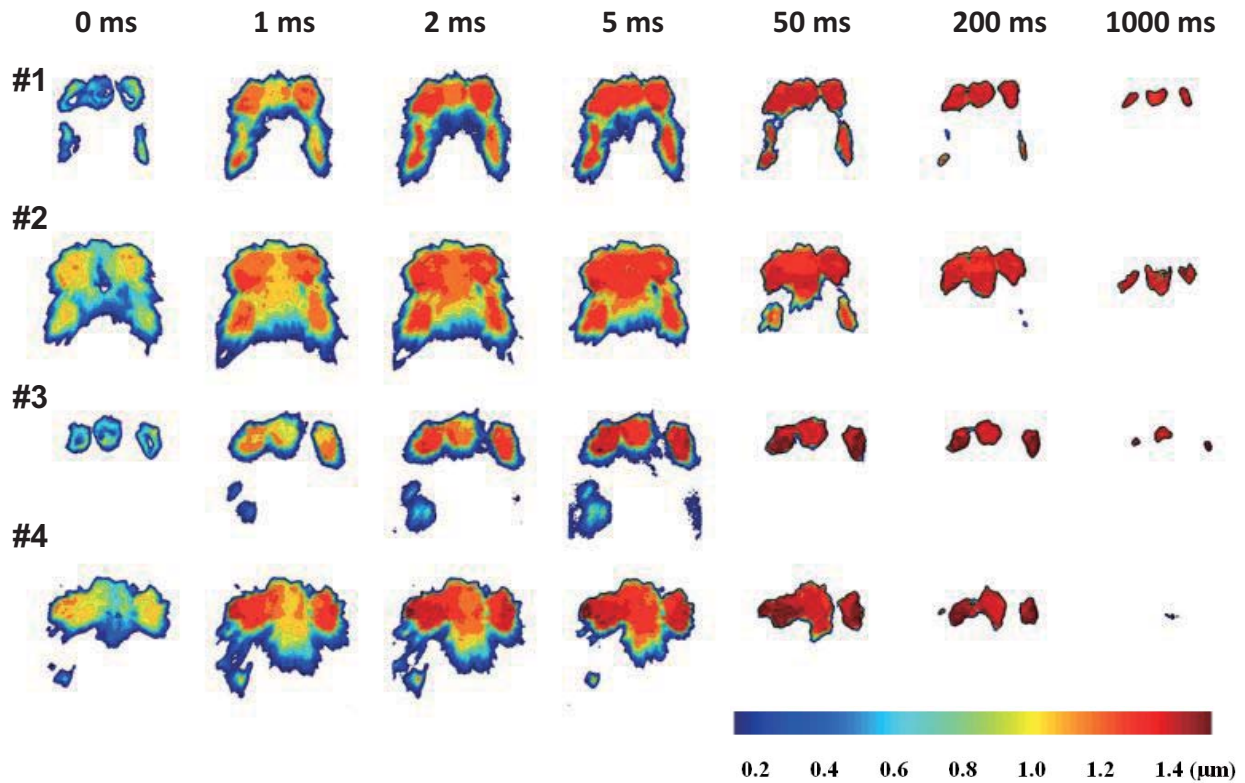


Figure 4.44 Evolution of fuel film thickness and spatial distribution (Case#1~4) after fuel droplet deposit on window

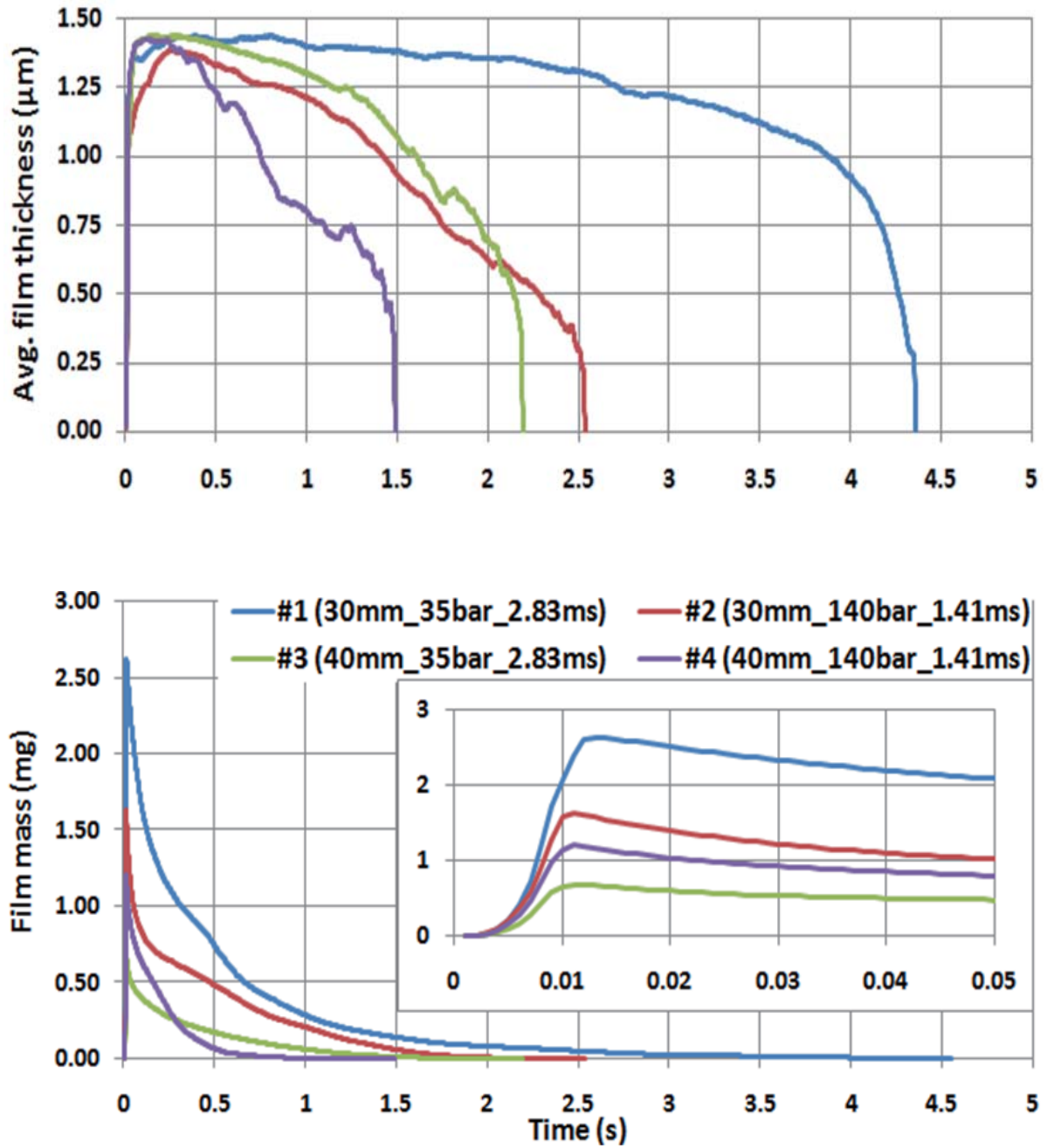


Figure 4.45 Averaged film thickness and film mass after fuel droplet deposit on window (Case#1~4).

The film mass in Fig. 4.45 was calculated from the averaged film thickness and the corresponding film deposit area. Case 1 has the longest evaporation time due to its low injection pressure and long injection duration. The maximum film mass of case 1 is around 3 mg at time zero (by extrapolation) and takes over 4 seconds to completely evaporate. Case 2 has a higher injection pressure than case 1, but both cases have the same injection mass (24.5mg); therefore case 2 has a shorter injection duration. The higher injection pressure resulted in lower film thickness and mass and consequently faster film evaporation. For cases 3 and 4, which have significantly different wetted footprints due to greater impact distance, the effects of injection pressure on film thickness and mass are similar, at least in the beginning.

The effects of ambient pressure (1bar and 2bar), ambient temperature (50°C, 75°C, and 100°C), and fuel temperature (40°C, 55°C, and 70°C) were investigated and shown in Fig. 4.46 and Fig. 4.47. Ambient temperature, which includes the impinging place, and fuel temperature were increased together to represent the warm up of an engine. For cases with 1bar air pressure (5, 7 and 9), the film thickness decreases faster with increasing temperature as shown in Fig. 4.47. For the cases of 2bar air pressure (6, 8, and 10), the maximum film thickness are higher than the ones with 1bar ambient pressure, at corresponding temperatures. The rate of evaporation is much slower for the 2bar air pressure cases, especially at low temperature. Comparing the results in Fig. 4.46 and Fig. 4.47, it is obvious that the temperature has the most dominant effects on fuel film thickness and mass. Ambient pressure has a secondary role on the film mass, but has stronger effects on the rate of film mass evaporation.

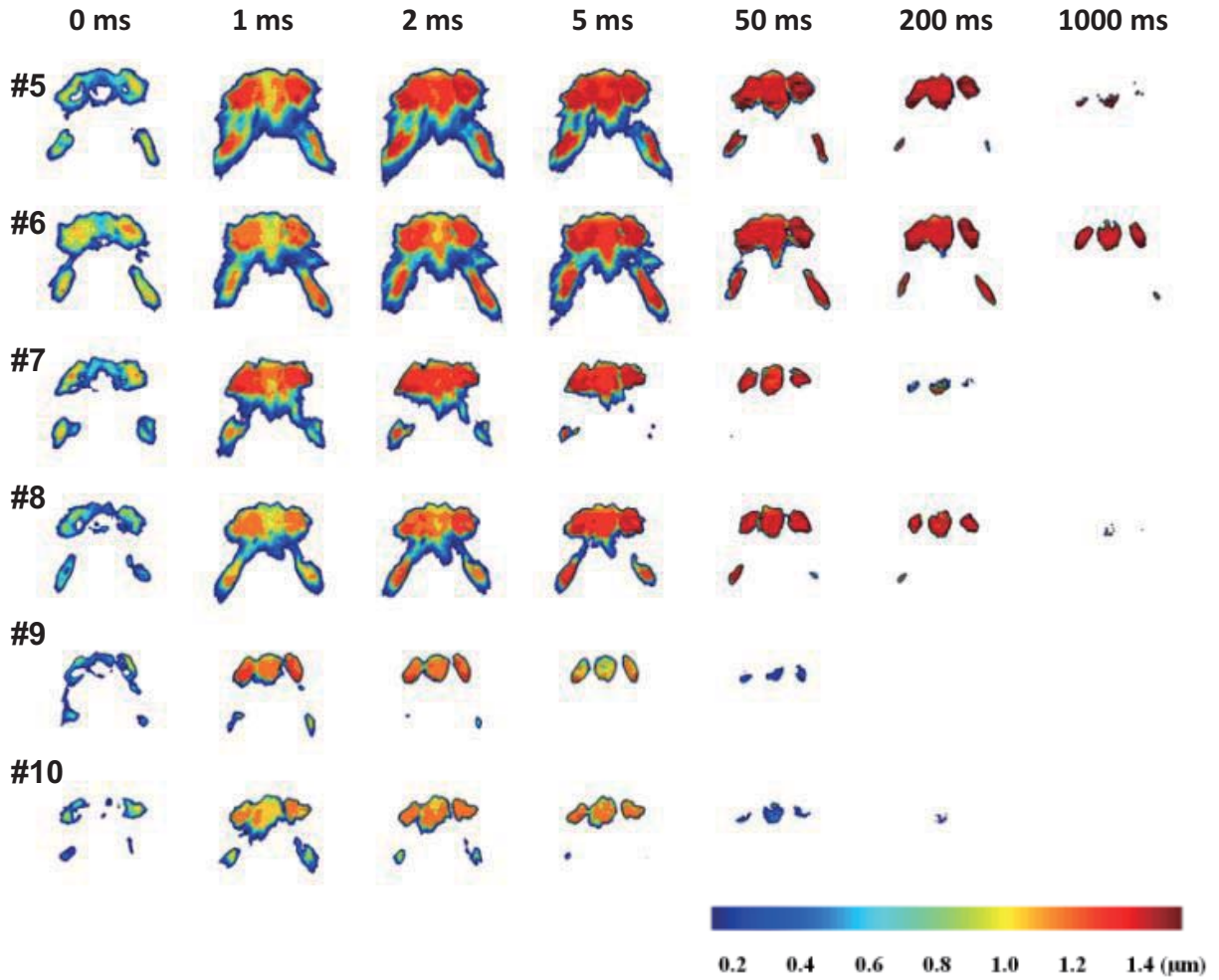


Figure 4.46 Evolution of fuel film thickness and spatial distribution (Case#5~10) after fuel droplet deposit on window.

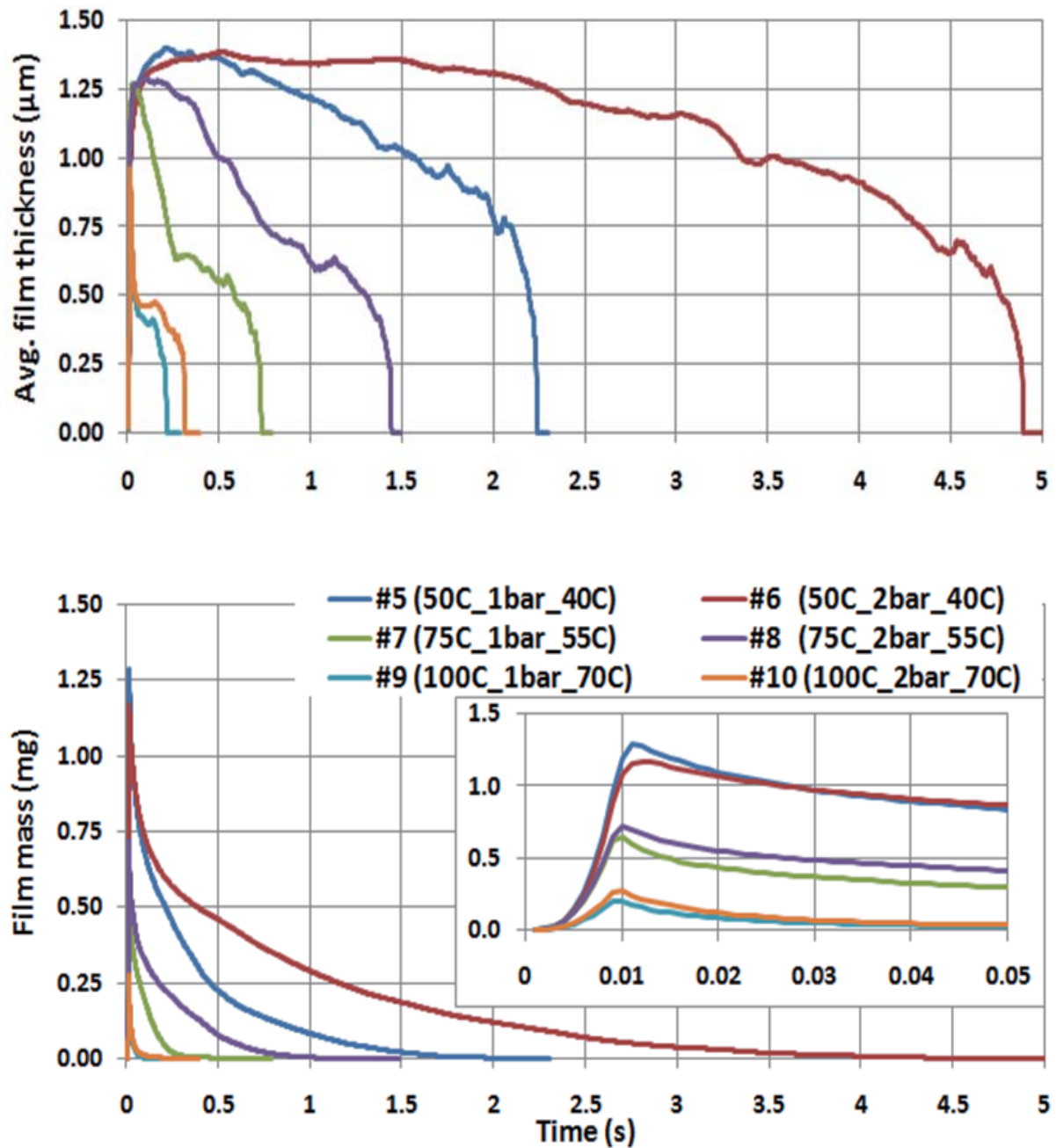
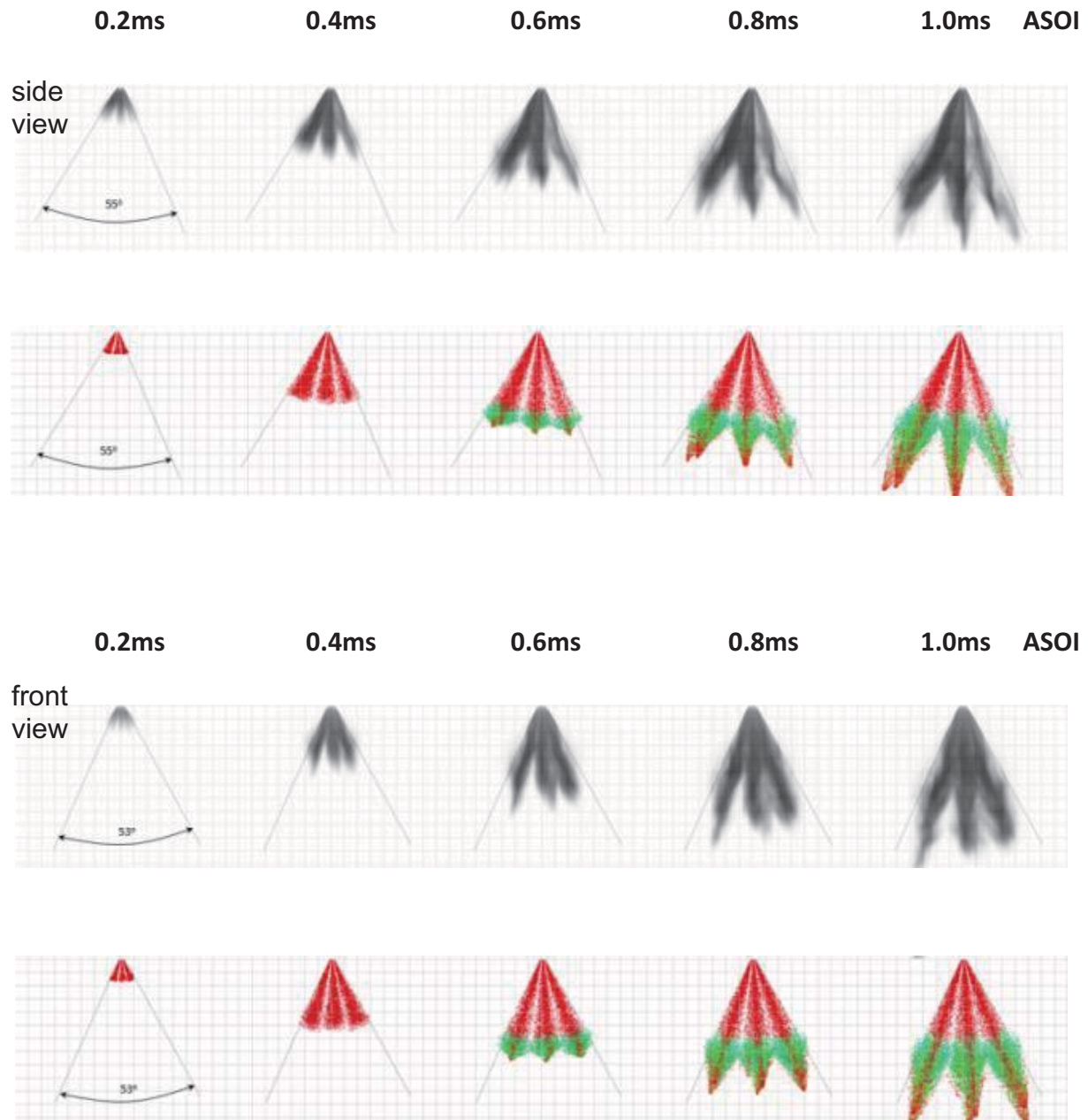


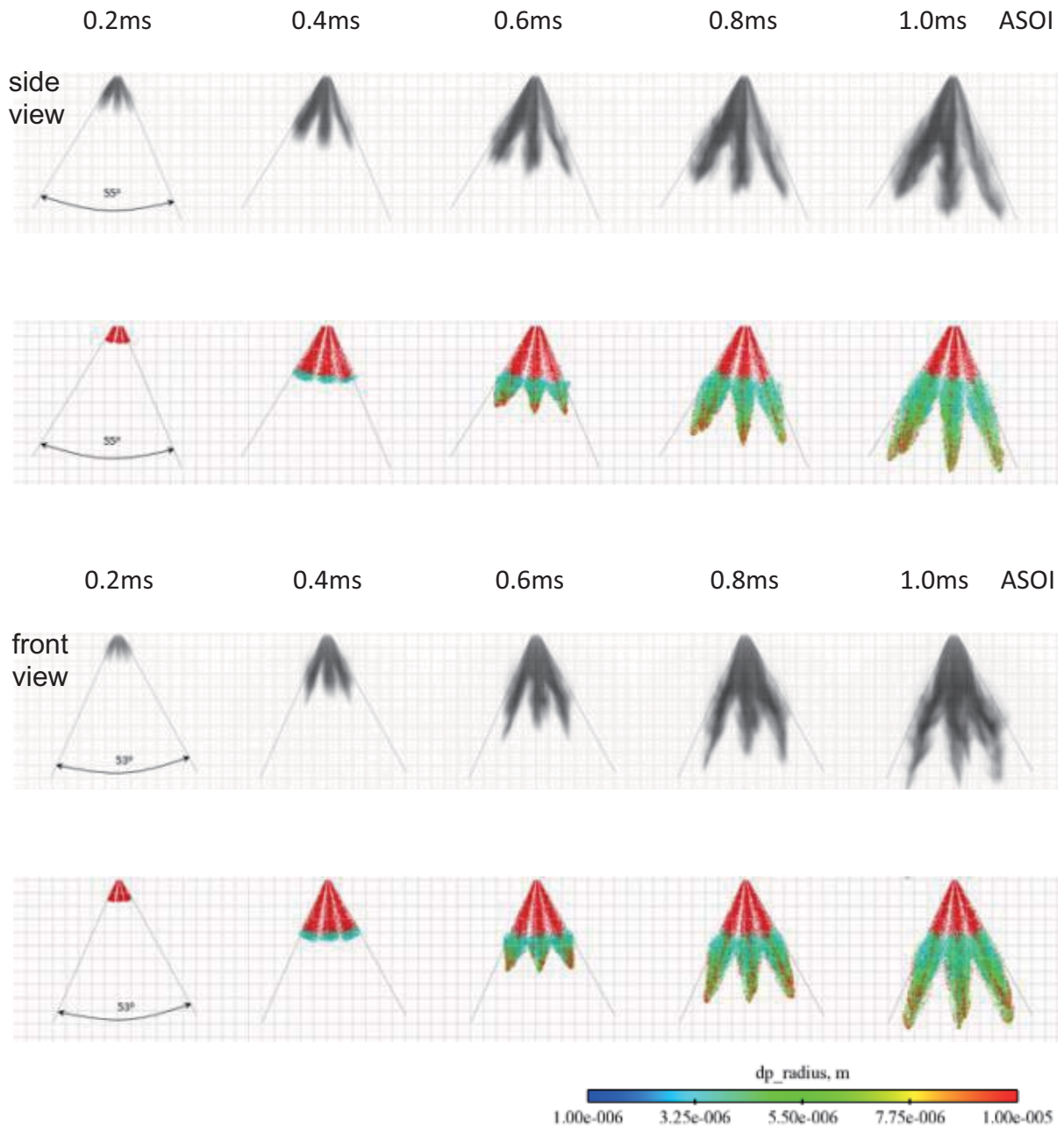
Figure 4.47 Averaged film thickness and film mass after fuel droplet deposit on window (Case#5~10).

In this study, numerical simulation of the multi-hole spray injection was carried out using multi-dimensional CONVERGE CFD codes. In each case, around 60,000 parcels of fuel spray were tracked for sufficiently precise statistical resolution. In order to obtain a better agreement of the spray impingement and wall fuel film of the multi-hole injector, back-lighting visualization technique was chosen to illuminate the free spray transport process first and then the spray impinging process. Fig. 4.48 shows the comparison of free spray development for case 5 and 6. The simulated spray behavior is also shown in this figure and good agreement between back-lighting visualization and calculations is obtained with respect to spray cone angle, tip penetration and general shapes under different ambient pressure. The size of background grids is 5 mm × 5 mm.

Experimental evolution of the impinging spray was compared with simulation results in Fig. 4.49. Fuel droplets deposited on a flat window surface around 0.6 ms after the start of injection. For the side-mounted multi-hole injector in this study, one spray plume will not reach the window surface as shown in the figure. Higher ambient pressure (Fig. 4.49, case 6) suppressed the spray shape propagation narrower and shorter. The spray cone angle and tip penetration of the experimental spray were compared with computational results and also show very good agreement.



(a) Case 5: side view and front view



(b) Case 6: side view and front view.

Figure 4.48 Comparison of experimental free spray evolution and CFD-simulation (3D parcel representation).

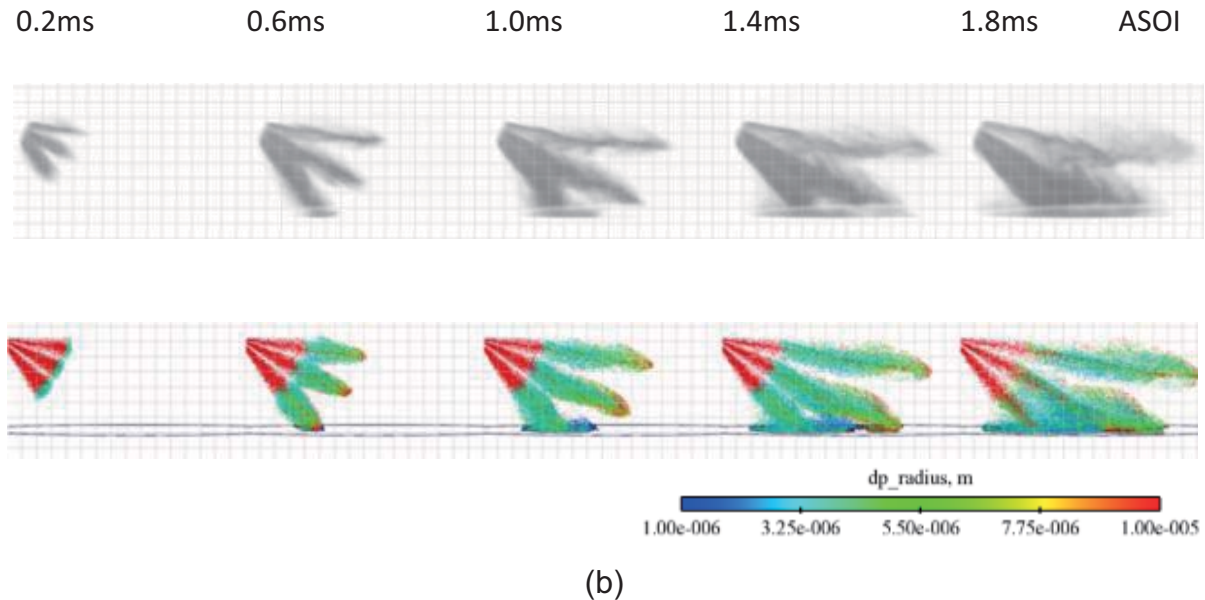
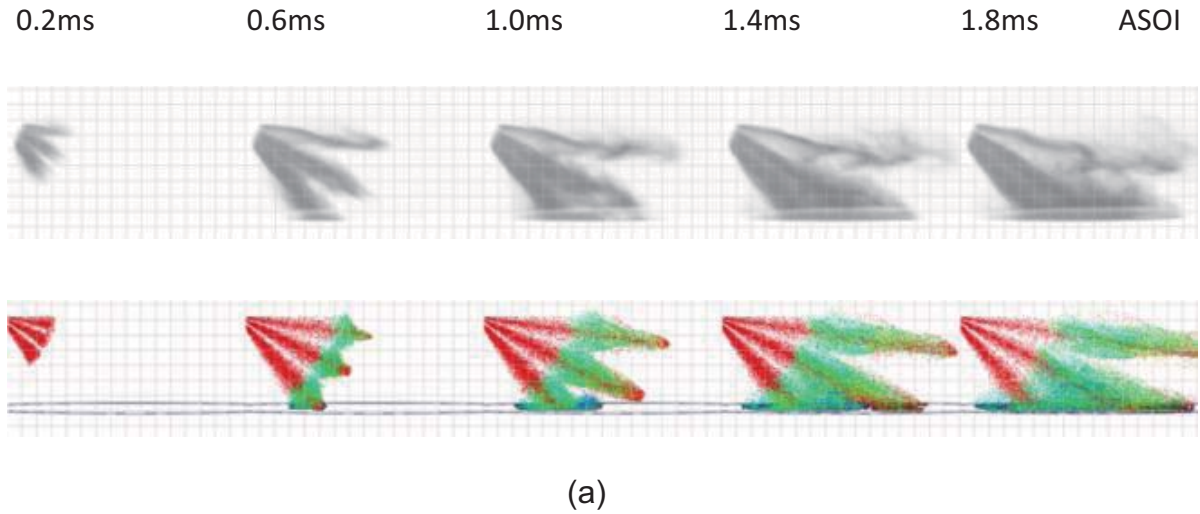
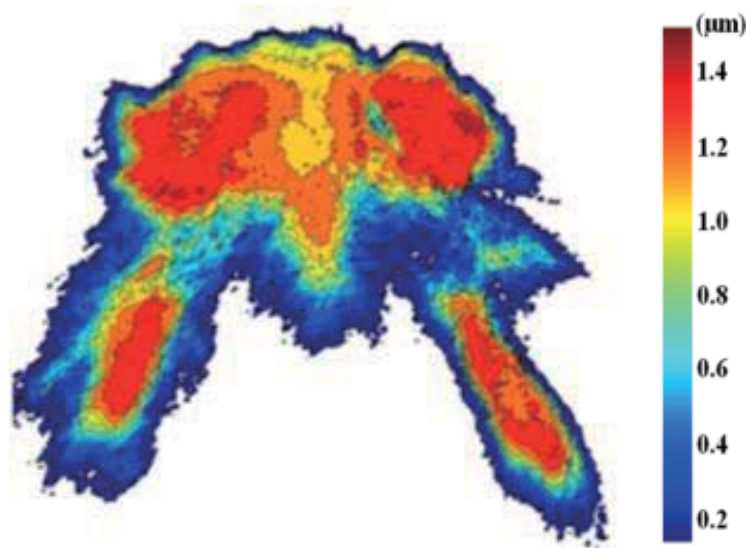


Figure 4.49 Comparison of experimental impinging spray and CFD-simulation (3D parcel representation). (a) case 5, (b) case 6.

Comparison of the experimental liquid film measurement and simulation is shown in Fig. 4.50 and Fig. 4.51. Injection mass in this work keeps 24.5 mg. The spray deposit area and shape have reasonable agreement as shown in Fig. 4.50. The simulation result of film spatial distribution shows higher film thickness around

the center of each puddle. The computational value of maximum film thickness is about 1.2 μm , which is very close to the experimental result of 1.4 μm . The numerical grid size of the impinging surface is 1mm, and the experiment image processing is based on 1 pixel (0.15 mm). This may be the main reason that why the simulation contours profile of film distribution is not as smooth as the experimental contour plot. Although the evolution of film mass evaporation shows similar trends, the calculated maximum film mass is consistently higher than the experimental values. As shown in Fig. 4.51, the simulated film mass is higher than the corresponding RIM experimental results. The reason for this discrepancy may have to do with the surface roughness of the ground glass diffuser and/or the modeling of spray impingement processes, and will be the subject of further investigation.



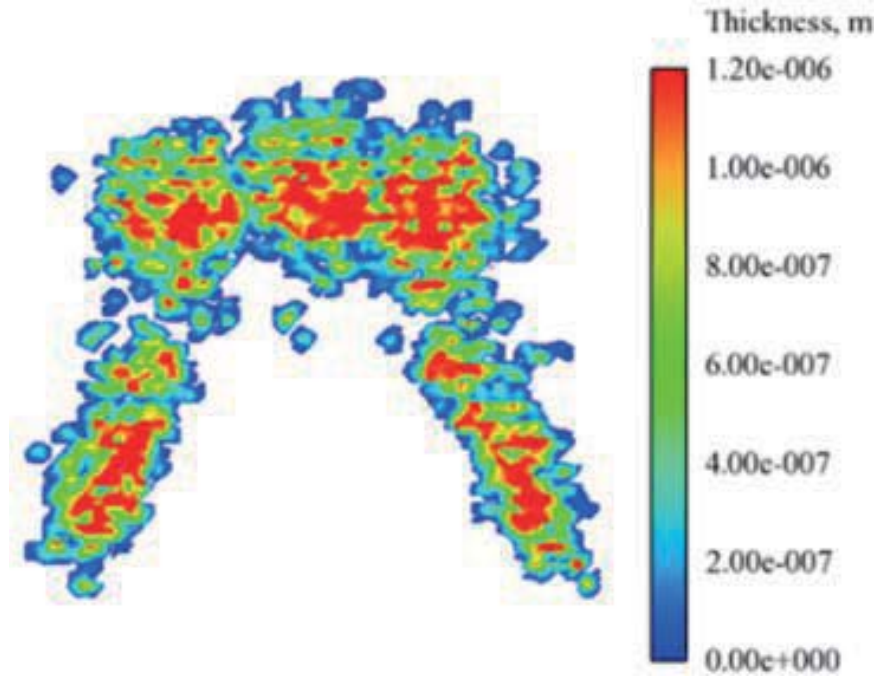
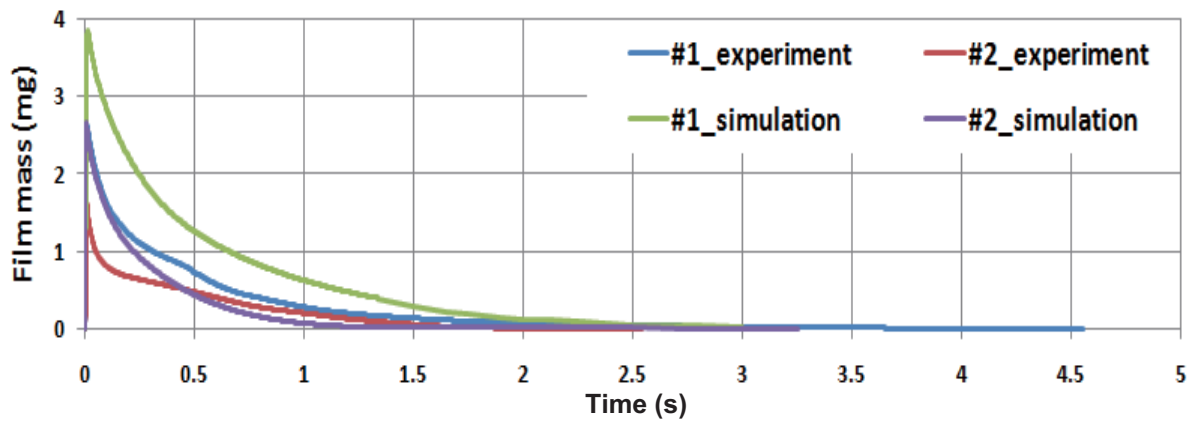
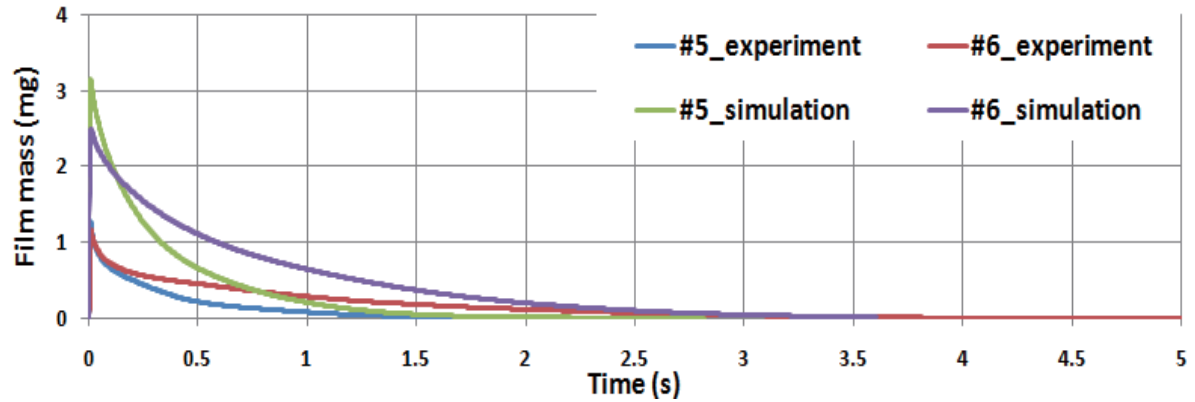


Figure 4.50 Comparison of experimental fuel film thickness and spatial distribution (left) and CFD-simulation (right), 2.6ms after start of injection (Case#6).



(a)



(b)

Figure 4.51 Comparison of experimental fuel film mass and CFD-simulation. Top: case1 and 2, Bottom: case 5 and 6.

4.3 Interaction between Spray and Charge Motion

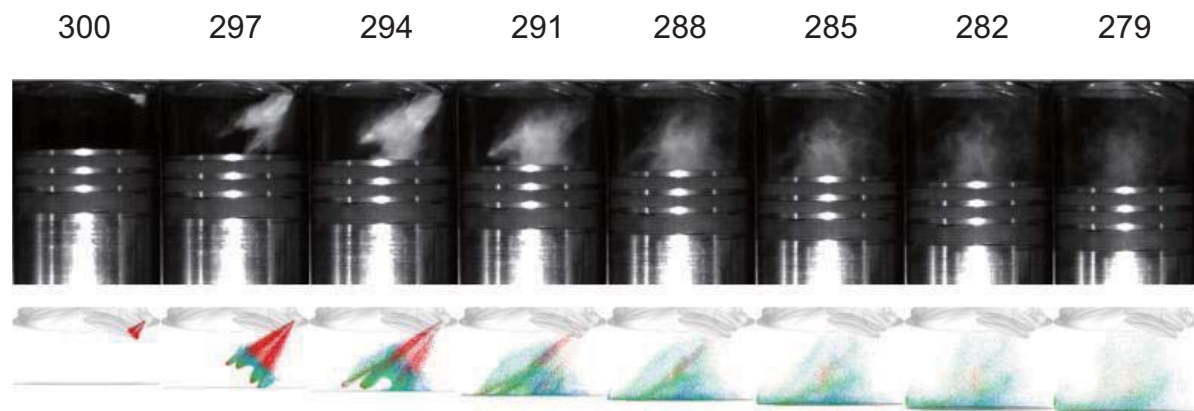
In GDI engines, detailed investigations of both spray-charge motion interaction and spray-wall interaction are necessary and challenging. The complete evolution of the fuel-spray, including the liquid film formation has been described in previous sections. Advanced flexible valve-train, with valve-deactivation and variable valve-lift, produces very dynamic charge flow motions, with varying tumble and swirl ratios. The resultant turbulent flow interact with off-axis multiple-hole DI injections, has important implications for the engine mixing and resultant combustion performance. In this section, the effect of fuel-spray and valve actuation on air-fuel mixing, in-cylinder flow development, surface wetting, and turbulence intensity is discussed. The resultant turbulent flow interacts with off-axis multiple-hole DI

injections, and effects on the engine mixing and resultant combustion performance are also presented.

4.3.1 Effects of Spray pattern and Injection Timing for Baseline case

Fig. 4.52 shows the comparison of spray visualization and the simulated spray particle clouds, color-coded with drop size down to 1 micron. The simulated spray distributions cover a larger area than the Mie scattering visualization, which may have problem resolving smaller drops. In general, the agreement is good for this case.

The air flow at the intake valve is very strong and is the dominant turbulence generation mechanism for ICE engines. The interactions with multi-hole spray is very complicated both spatially and temporally, especially for the deactivated cases, and will have a significant influence on the spray impingement and mixing.



(a)

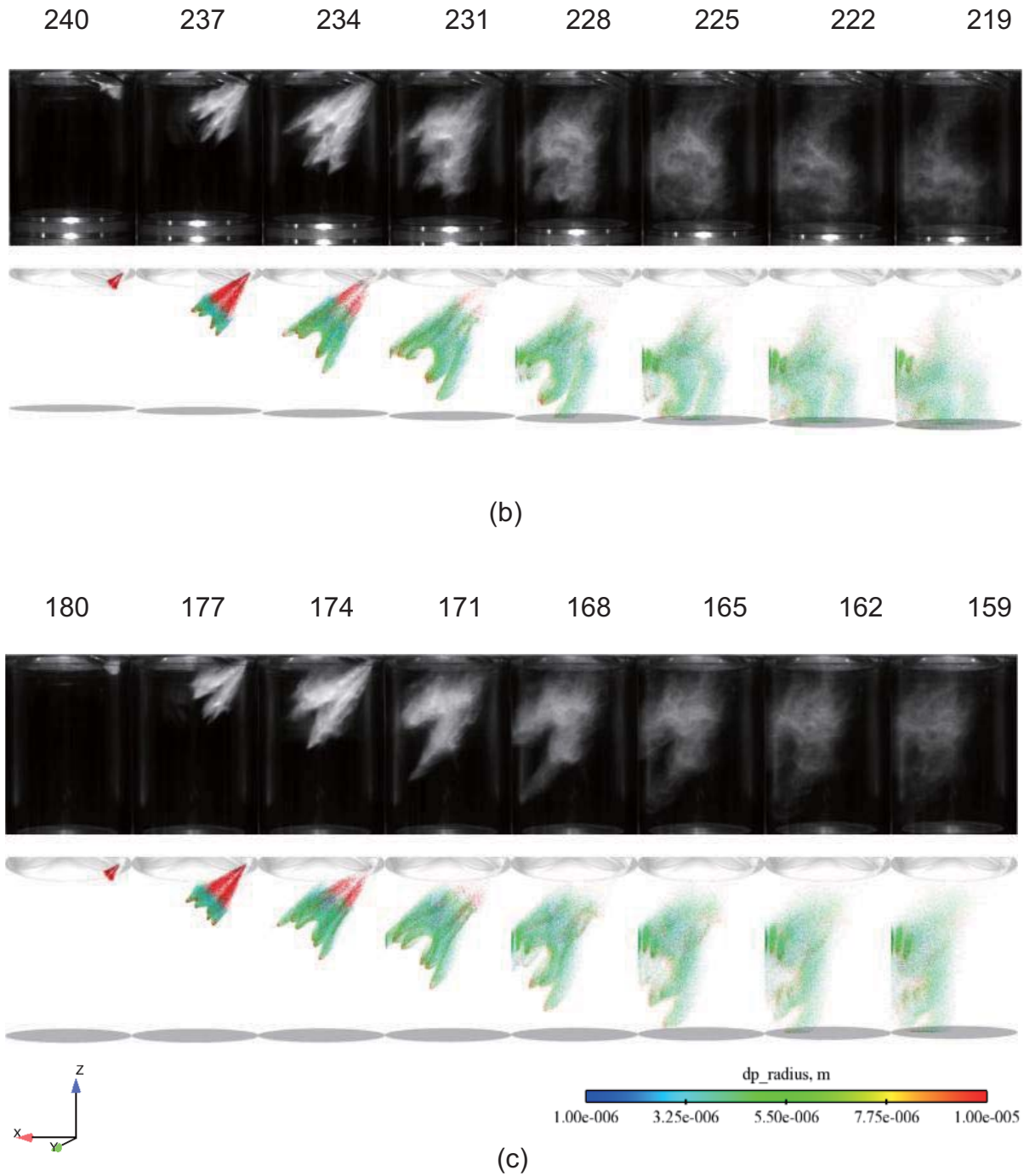
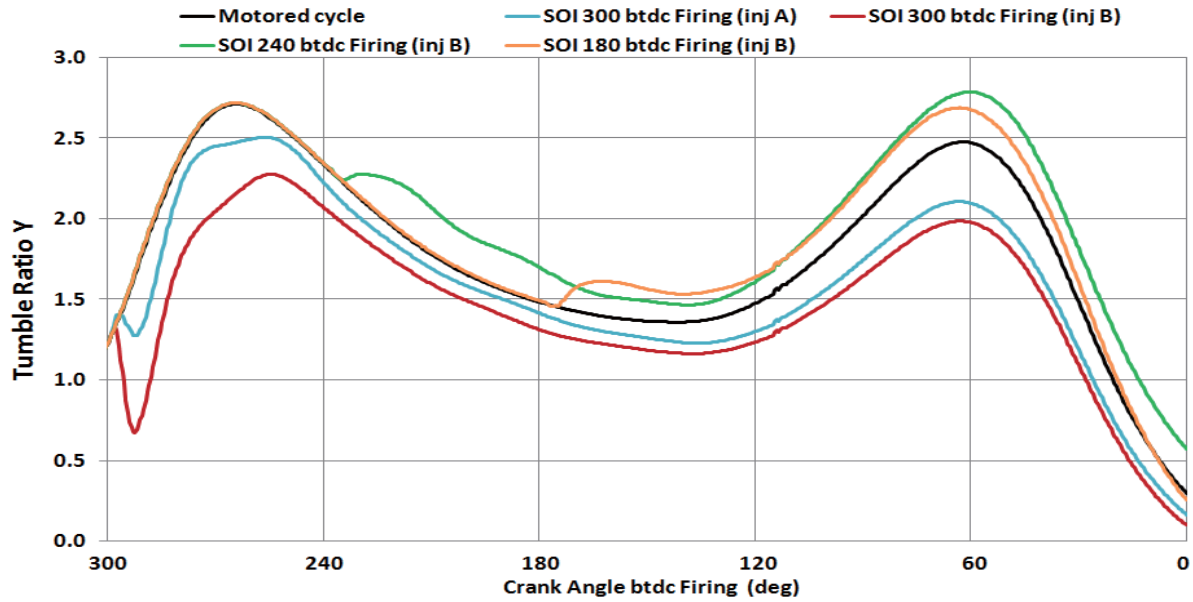
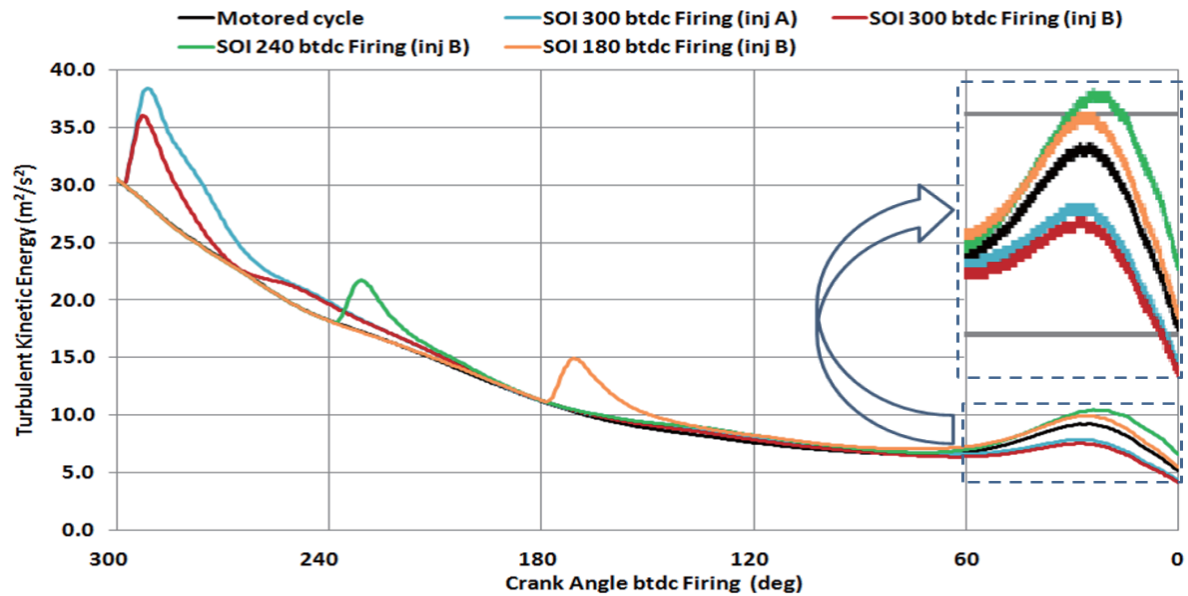


Figure 4.52 Comparison between CFD and OAE results of the in-cylinder spray processes, 1000 rpm, Injector B, 100MPa, 16mg (0.88ms duration). (a) SOI = 60 deg CA aTDC, (b) SOI = 120 deg CA aTDC, (c) SOI = 180 deg CA aTDC,

The charge motion is a combination of both swirl and tumble motions which is very dynamic and would require 3-D post-processing or CFD to resolve the mixture formation processes and interactions. However, the interactions of the fuel injections and the charge motions are bettered illustrated by the integral analyses. The predicted effects of injection timing on the tumble and swirl ratios of the charge motion and the total turbulent kinetic energy are shown in Fig. 4.53. The swirl, which is defined as the ratio of the angular speed of the flow about the center of mass in the z-direction to the angular speed of the crankshaft, is mostly negligible for the two inlet port geometry used in this engine. The tumble ratio Y is defined as the ratio of the angular speed of the flow about the center of mass in the y-direction to the angular speed of the crankshaft. Similarly, the tumble ratio in X-direction is calculated by evaluating the ratio of the angular speed of the flow about the center of mass in the x-direction. Depending on the injection timing and phasing of the tumble dynamics, the fuel injection could inhibit or enhance the tumble motion. Injecting too early actually decreases the tumble ratios; later injections at 240° and 180° crank angle degree (deg CA) before the fire TDC, the tumble flow was enhanced by the fuel injection. In these cases, enhanced turbulent kinetic energy (TKE) due to the eddy breakdown of the tumble motion is also observed at the end of compression stroke, where faster flame computed by CFD of a few injection timings is shown in Fig. 4.53.

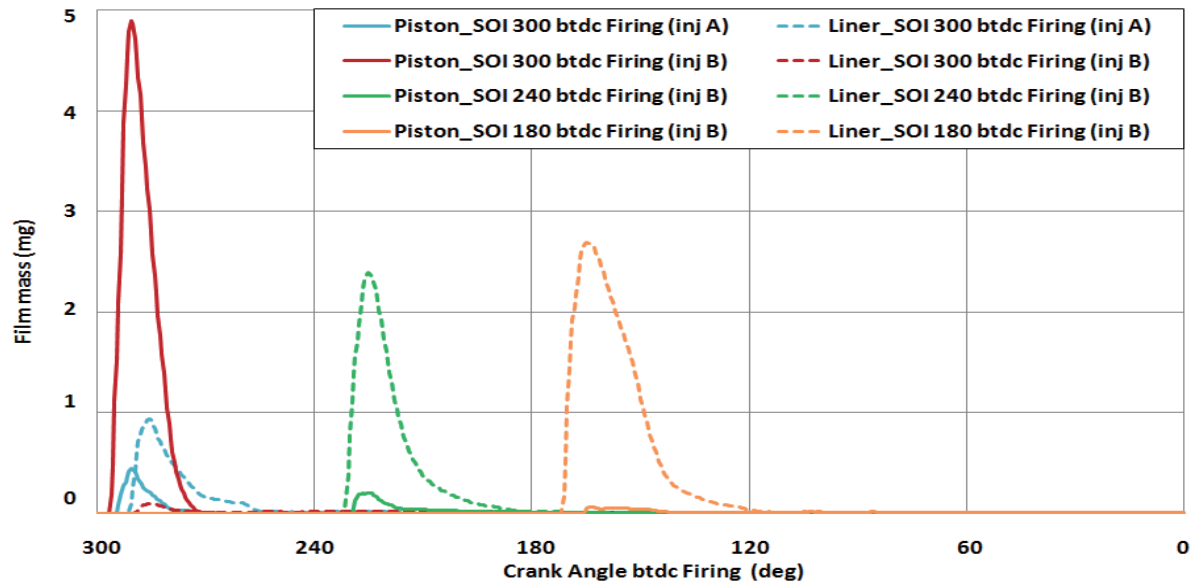


(a)



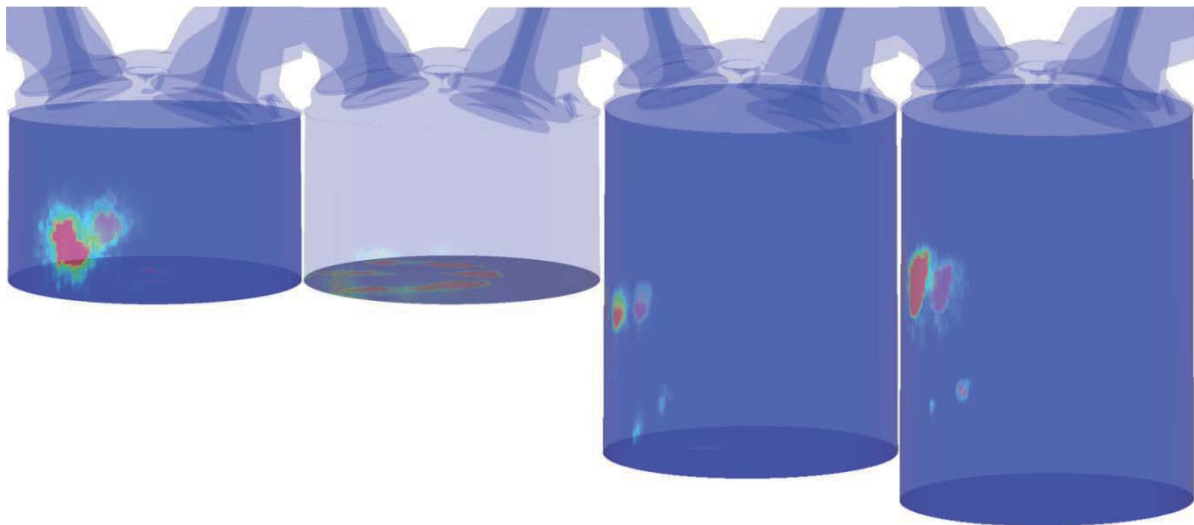
(b)

Figure 4.53 The effects of SOI on the (a) Tumble and Swirl ratios and (b) integrated turbulent kinetic energy, Late Intake Valve Closing (LIVC), injector B, optical engine.



(a)

SOI: 300 btdec (Inj A) 300 btdec (Inj B) 240 btdec (Inj B) 180 btdec (Inj B)



(b)

Figure 4.54 (a) Total liquid film mass evolution, and (b) wall wetting footprints at 12 deg CA ASOI (Right), Late Intake Valve Closing (LIVC), injector B, optical engine.

With the early start of injection (SOI) at 300 deg CA, a large amount of liquid impinges on the surface due to the relatively shorter injector-piston distance. For this case, the side- and bottom-view of the wetted footprints on the piston are also shown in Fig. 4.54. At this timing, the maximum wall film amount for Injector B is almost twice as much as Injector A, in spite of less liner wetting because of its spray targeting. This piston wetting can be avoided by retarding the injection timing. If the injection timing is set to be later than 240 deg CA, the maximum film mass is predicted to reduce by 62%. Since the spray injected at 240 deg CA and later was not found to touch the piston, the film mass could be located on the side wall.

A 4-cylinder 2.0-liter metal engine which has the same configuration of cylinder head, injector, cams, and bore size as the optical engine, was used to carry out the combustion and emission tests [112]. This present paper focuses only on the low-speed and naturally aspiration conditions, primarily because using Early Intake Valve Closing (EIVC) at higher speeds with one valve inactive limits the peak load of the engine. The engine has a compression ratio of 11.9, to enable flex-fuel (E0~E85) operation. A typical metal engine test results in Fig. 4.55 show the effects of start of injection (SOI) timing on soot (Filtered Soot Number or FSN, measured with an AVL 415 smoke meter), coefficient of variability (%COV) of BMEP, and the burning speed in deg CA (10 to 75% mass fraction burnt, or CA10-CA75). The injection window is constrained by the soot measurement which strongly depends on wall wetting, and Coefficients of Variability (COV) of IMEP which depends on the uniformity of the mixture. As a result, the injection window is around 120 deg CA to 200 deg CA after the intake TDC. During this window the burning speed and COV are observed to

increase and decrease respectively, consistent with the enhanced turbulent mixing of the DI sprays as indicated by the computed tumble flow and turbulent kinetic energy characteristics.

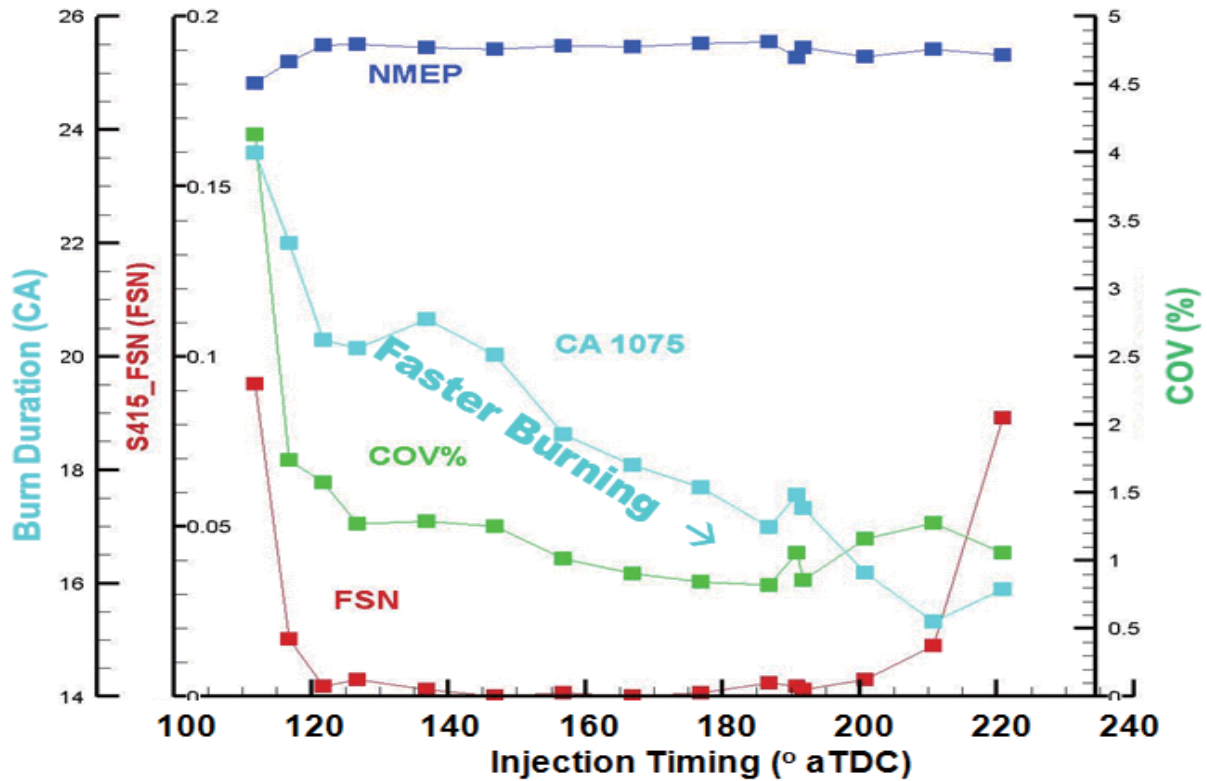


Figure 4.55 Effect of injection timing on engine combustion: 1500 rpm, 4.7 BMEP, Low-Lift EIVC, Injector B, E85 [112].

The results are consistent with the CFD in terms of the injection window, where the injection timing is constrained by wall impingement which is correlated to soot (FSN), and incomplete mixing which is correlated to combustion instability (COV). Injection too early or too late result into wall impingement; similarly injection too early or too late usually results into insufficient mixing due to the interaction of

spray injection with the tumble flow. Higher turbulence enhances mixing before ignition and enhances combustion after ignition; therefore, there is optimal injection timing for faster mixing and combustion speed within the injection window.

4.3.2 Effects of Valve Actuation for Low-Speed Low-Load Case

Naturally aspirated DISI engines usually has poor charge motion at low speeds with EIVC, and high particulate levels when operating at high loads on gasoline and intermediate ethanol blends. Use of valve deactivation has been shown to improve stability and reduce particulate emissions at low loads and very low (2~3 mm) lift valves [90, 91].

In order to evaluate the effects of flexible valvetrain, the engine is modified with a dual-independent cam-phaser (DICP) as shown in Fig. 3.12. The 2-Step variable valve lift system was installed to provide compression ratio management using Late- and Early- Intake Valve Closing (LIVC and EIVC). These strategies allowed change of effective compression ratio and load control by use of cam phasing.

Simulation was also carried out to compare and validate with experimental result for valve deactivation. For example, Fig. 4.56 shows images at 7.5 and 12.5 deg CA ASOI with injection at 270 deg CA with LIVC deactivation configuration. Only the bottom right intake valve was active in the bottom view for the one-valve case. The simulation results show the distribution of the particles with radius information in color. Even though CFD sprays overshoot for some extent, agreement of overall spray shape is in fair agreements for more asymmetric fuel distributions. Because of

the higher lift, there is spray impingement on the intake valve which should be avoided. High lift is also not necessary at low load cases.

The effects on valve deactivation of EIVC cases can be visualized by false coloring the spray images and superimpose them. For example, Fig. 4.57 shows the effects of valve-deactivation on the in-cylinder sprays, with the two-valve case colored red, and the one-valve case, green; therefore the overlapped spray regime is yellow. The effect of injection timing is also shown in 310 deg CA and 290 deg CA before fire TDC.

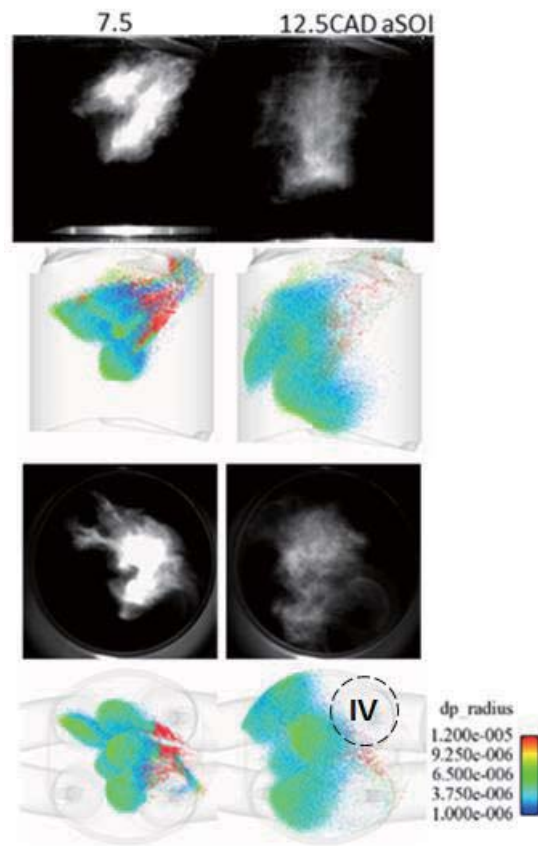
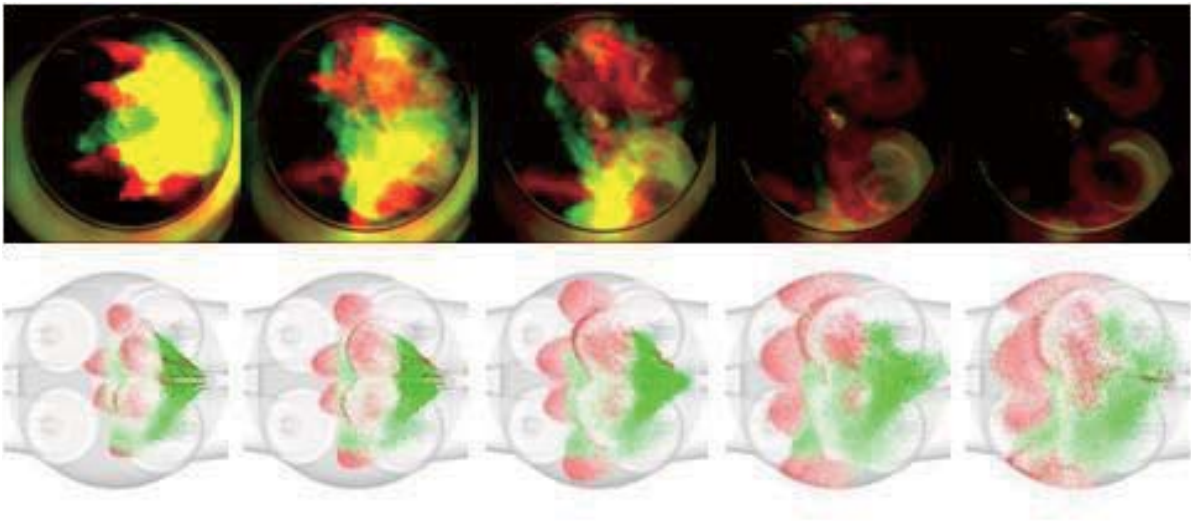
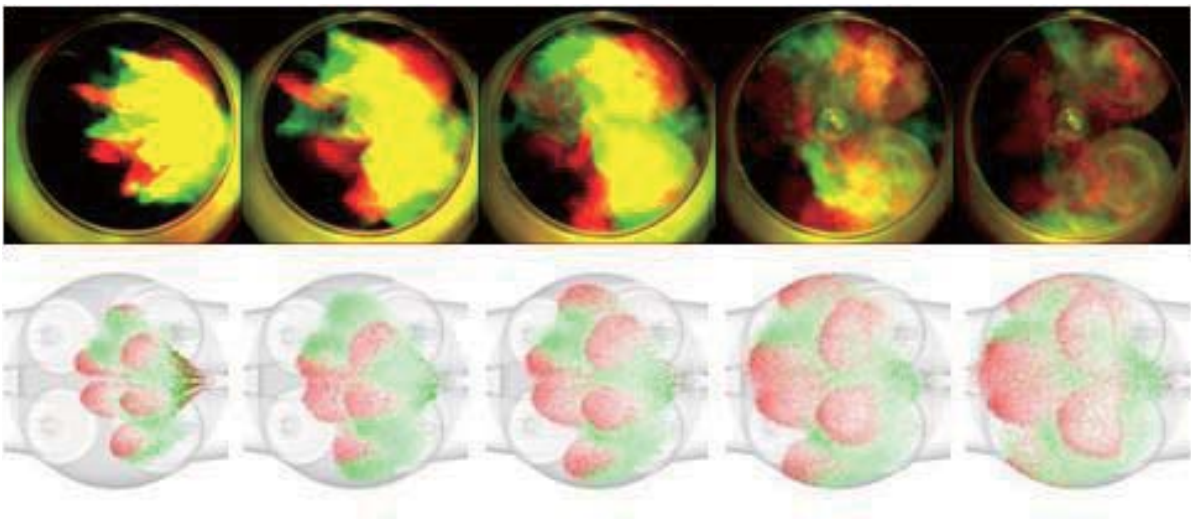


Figure 4.56 CFD validation with injection at 270 deg CA with LIVC deactivation configuration, 1000 rpm, Injector A.



(a)



(b)

Figure 4.57 Superimposed false-color in-cylinder spray image sequences showing the effects of valve deactivation on mixing, various SOI (vertical) from (a) 310 deg CA and (b) 290 deg CA bTDC: 2-Valve (Red) vs. 1-Valve (Green), EIVC, 1000 rpm, 1 bar BMEP equivalent.

The optical engine data show that valve deactivation deflects the spray and entrain it into the higher velocity intake flow. Visualization of sprays with valve deactivation appears to show faster impingement on the piston surface for early SOI at conditions that soot was also observed for the fired engine. The increased turbulent mixing due to the stronger bulk motion increases the rate of vaporization as the green spray of the deactivated-valve case is shown to disappear faster than the red baseline case. The acceptable injection timing window is limited in the engine data by soot (>0.1 FSN) for early timings, and poor combustion stability ($>1.5\%$ COV) for later timings. Valve deactivation is shown to increase the injection window by stronger turbulent mixing due to the reduced intake opening and therefore higher intake velocity. Vaporization of the spray is faster with valve deactivation according to the simulation as shown in Fig. 4.58.

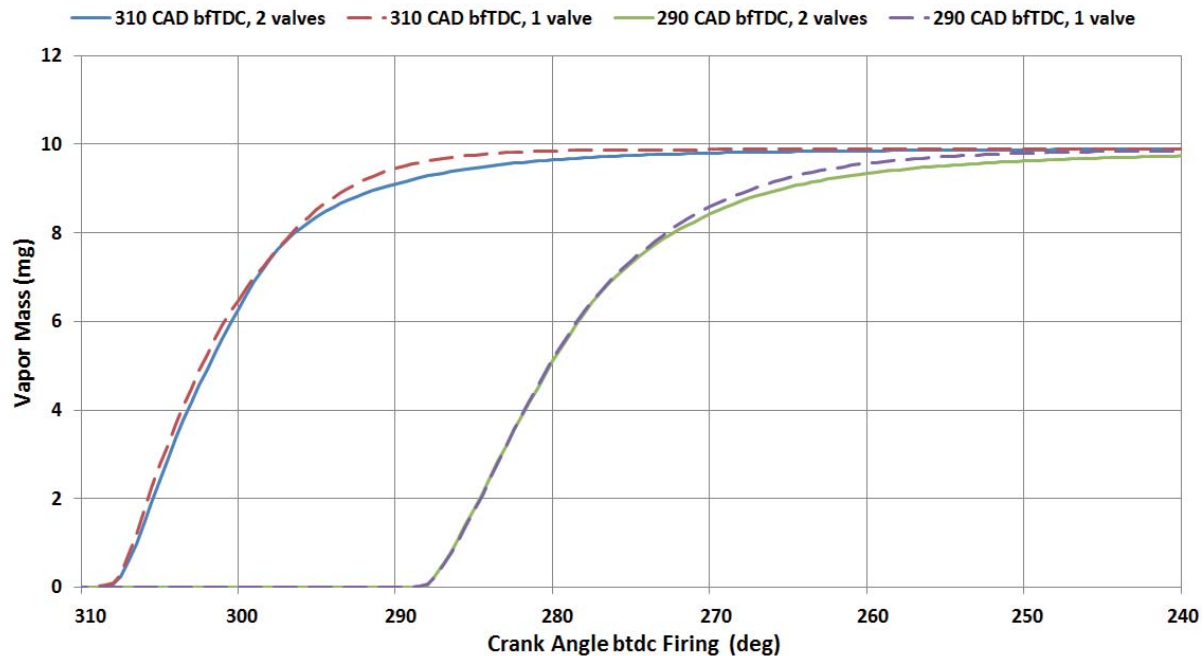
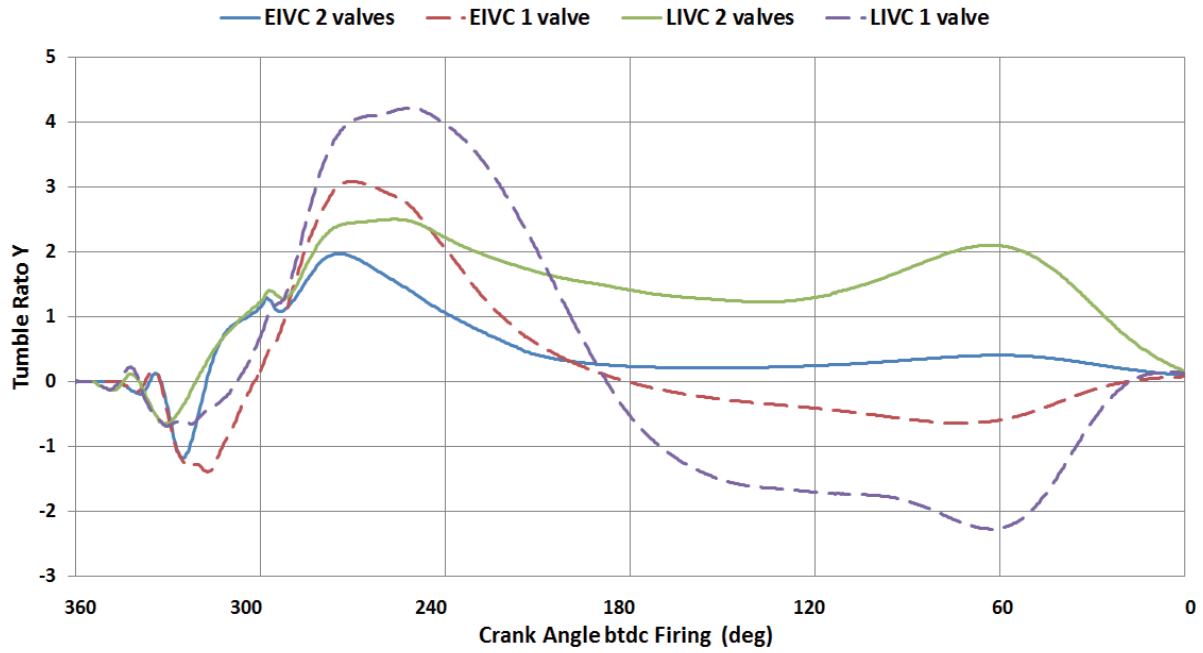
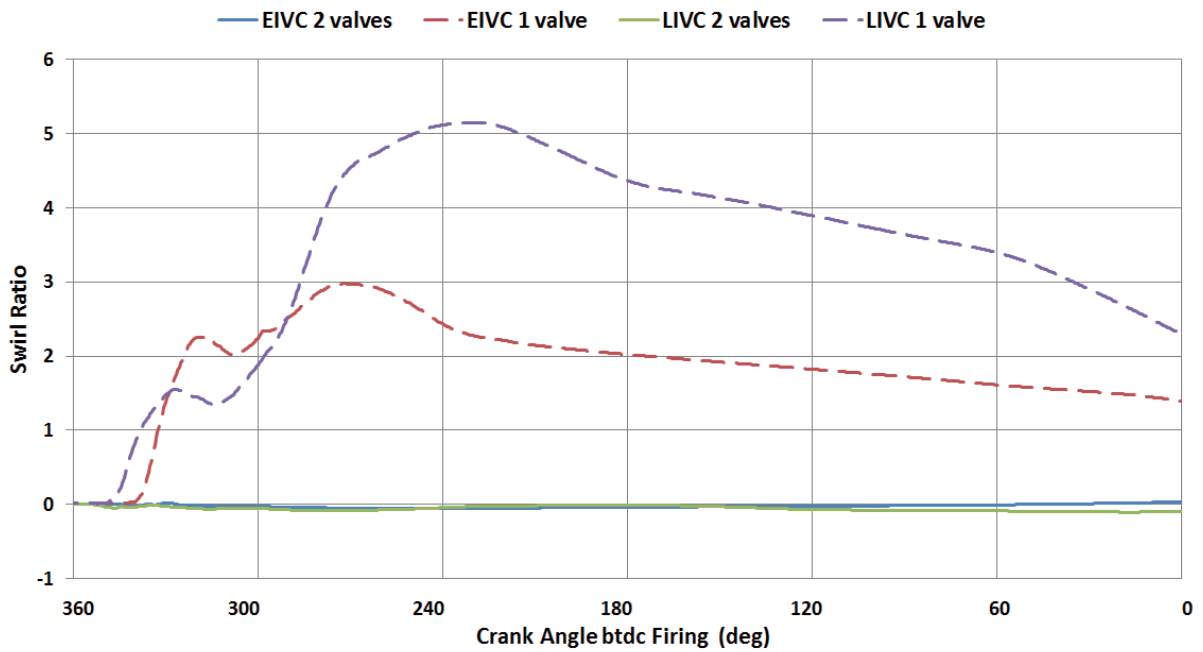


Figure 4.58 The effects of valve deactivation on spray vaporization.

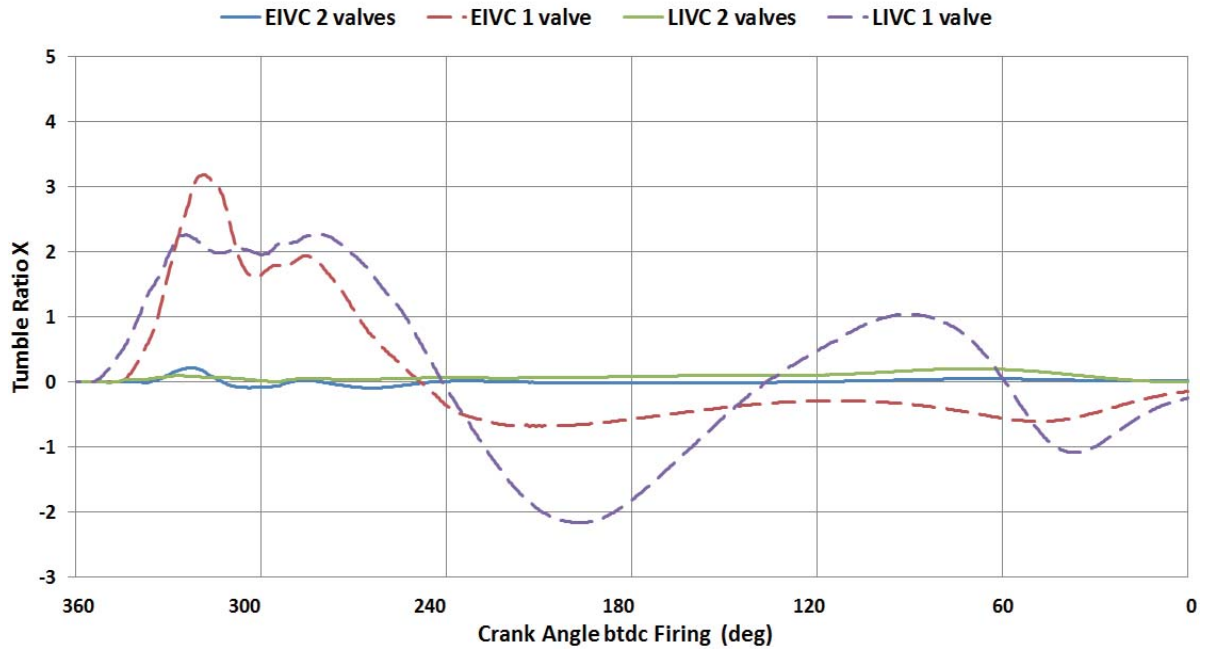
The computed integral analysis of the bulk flow dynamic ratios, which consists of a swirl ratio and two (X and Y) tumble ratios, are plotted in Fig. 4.59. The baseline 2-valve charge motions were dominated by the in-plane (or Y direction) counter-clockwise tumble motion, similar to Fig. 4.53, with the HLC case greater than LLC one. When one valve was deactivated, both the swirl and the out-of-plane (or X) tumble motions significantly appear, with the tumble changing directions or signs during the mixture preparation cycle, sometimes more than once. Even though HLC produces overall stronger and more coherent charge motion, the dynamic ratios of LLC develops faster at the beginning, due to the faster inlet air velocity coming through the reduced inlet valve open area. Consequently, the mass-averaged turbulent kinetic energy (TKE) during the mixture formation period is much higher; more than double that of the HLC cases. Similarly, the TKE of the deactivated cases more than double that of the two-valve cases, as shown in Fig. 4.60. However, the higher TKE dissipates quickly and does not sustain well into the flame initiation phase, but fall below that of the two-valve cases. The enhancement of TKE by the fuel injection depends on the phasing of valve opening and is shown to favor the HLC cases for the engine and injector configurations.



(a)



(b)



(c)

Figure 4.59 Computed Charge motion Dynamic ratios of VVA, SOI=60° aTDC, 1000 rpm, 1 bar BMEP equivalent. (a) Tumble ratio Y, (b) Tumble ratio X, (c) Swirl ratio.

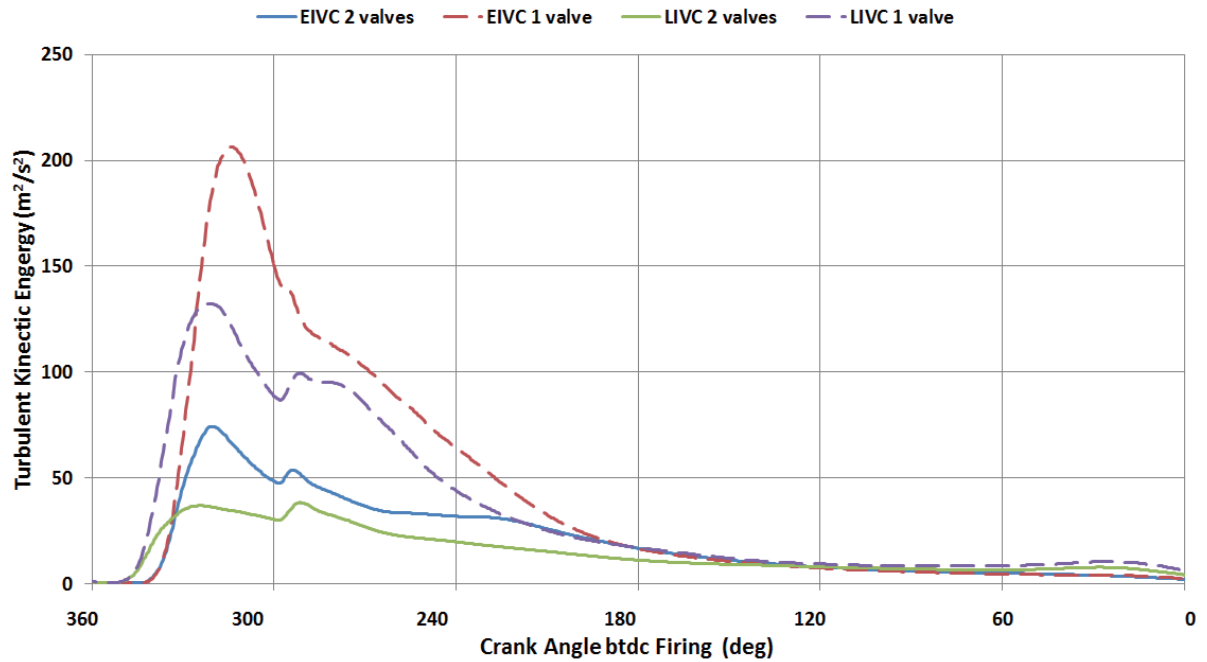


Figure 4.60 Averaged turbulent kinetic energy, SOI= 60° aTDC, 1000 rpm, 1 bar BMEP equivalent.

However, this TKE enhancement advantages is countered by the stronger bulk motion which sends more fuel sprays toward the combustion chamber walls. The deactivated 1-valve cases have not only stronger turbulent mixing but stronger 3-D rotational flows, which produce an insular effect on the spray plumes and keep the bulk spray plumes from the walls. Fig. 4.61 shows the cumulative combustion chamber wall film mass.

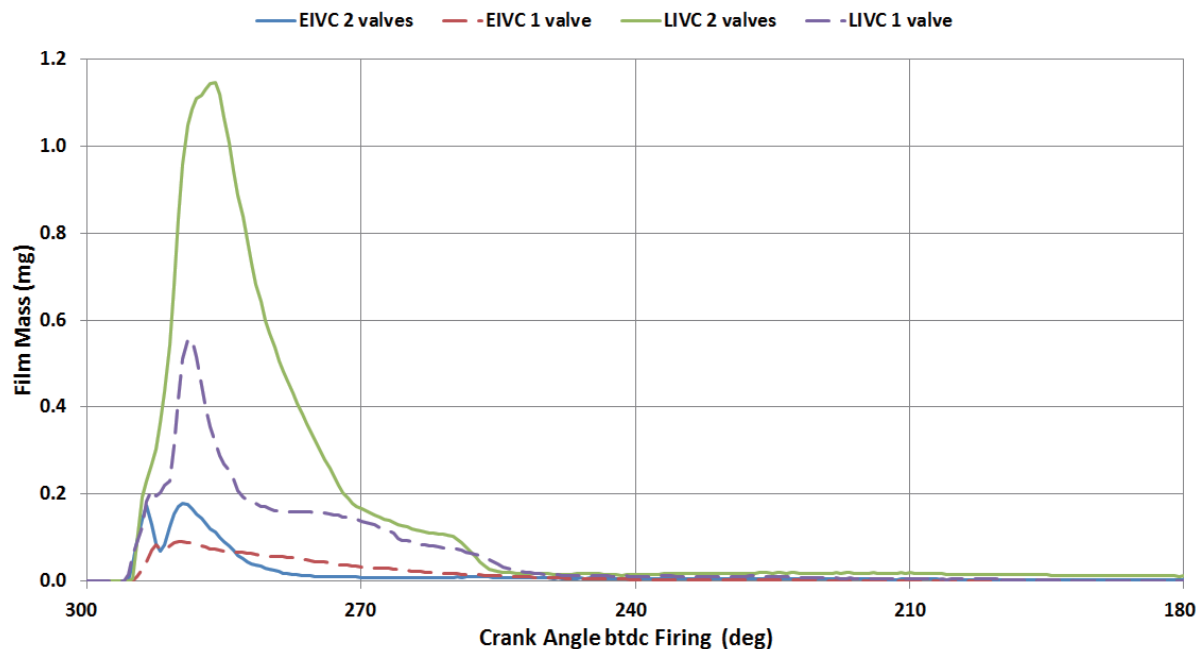
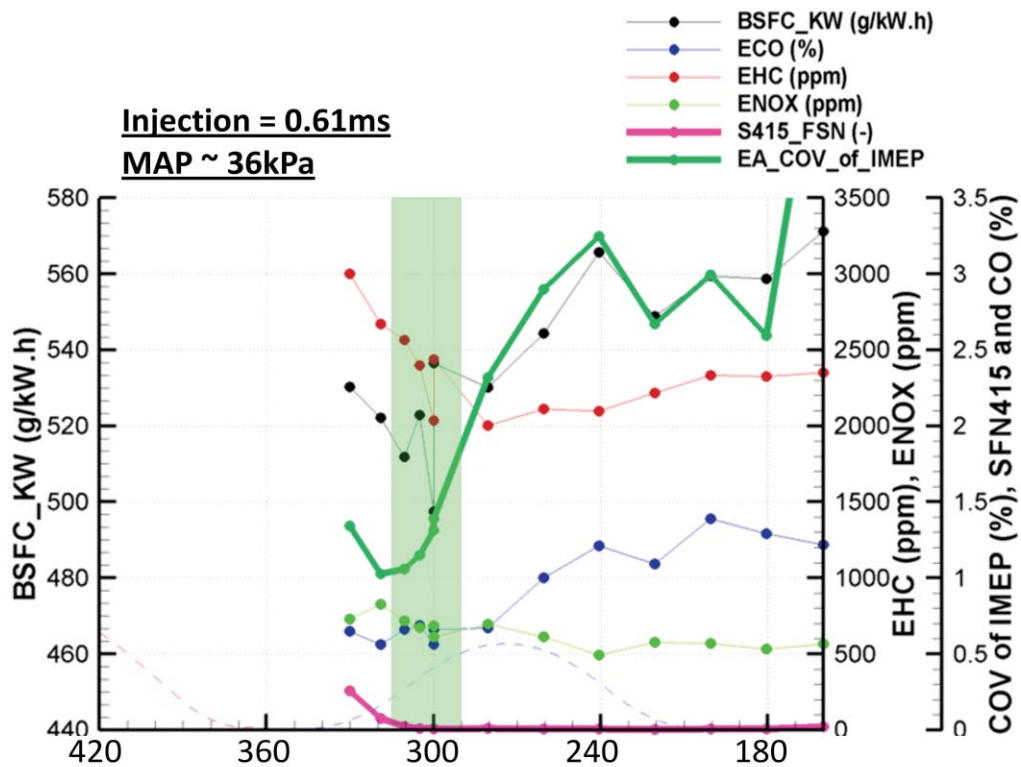


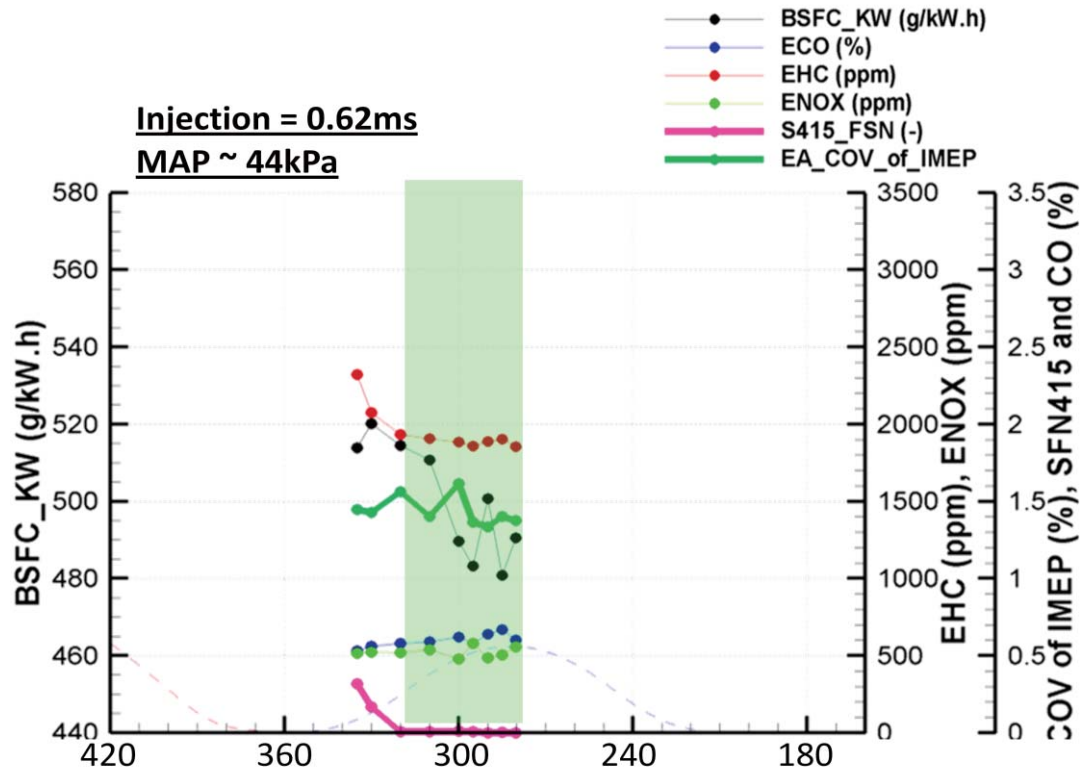
Figure 4.61 Total liquid film mass, SOI= 60° aTDC, 1000 rpm, 1 bar BMEP equivalent.

The mixing CFD calculations confirm the metal engine data (Fig. 4.62) that more turbulent resulted in more uniform mixing, less liquid film, more stable combustion and wider injection window. Injection too early at 30 deg CA aTDC cause wall impingements and incomplete mixing, as a result, the engine combustion

results is expected to have high soot and COV. For this engine test, cam timing optimization was carried out at each operation point to maximize engine efficiency for both the conventional 2 valve and the 1 valve (valve deactivation) modes. The cam timing optimization was conducted independently for the different strategies to allow comparison at an optimal performance point. During testing, two fundamental issues at low speed operations were identified with the conventional 2-valve configuration and that valve deactivation was able to address. At low loads with EIVC, combustion stability was poor under un-throttled conditions. To improve combustion stability and efficiency the engine had to run under throttle with minimal valve overlap to limit residual.



(a) Two intake valves



(b) One intake valve (Deactivation)

Figure 4.62 Metal engine test results at 1000RPM, 1bar BMEP with EIVC

4.3.3 Effect of Variable Valve Actuation for Medium and High-Load Case

Higher valve lift is usually beneficially at higher load due to better breathing. The effects of flexible valvetrain on engine combustion at higher speed and load are shown in Fig. 4.63 and Fig. 4.64 for 2000rpm, 2bar BMEP case, and 1500rpm, 8bar

BMEP case respectively. Fig. 4.63 shows a very small acceptable injection window, highlighted in yellow, for this condition with 2 valves. This narrow window was typical of the EIVC strategy. A comparable injection timing sweep with valve deactivation is shown in Fig. 4.63b. The use of valve deactivation at this condition allowed a wide degree of cam phasing with good stability. Un-throttled conditions could be achieved, although optimal efficiency was under slightly throttled conditions. This allowed a significant reduction in pumping losses resulting from reduced throttling from 53kPa MAP with 2 valves to 95kPa MAP with 1 valve deactivated. The lower pumping work resulted in a reduction of fuel consumption (Brake Specific Fuel Consumption, or BSFC).

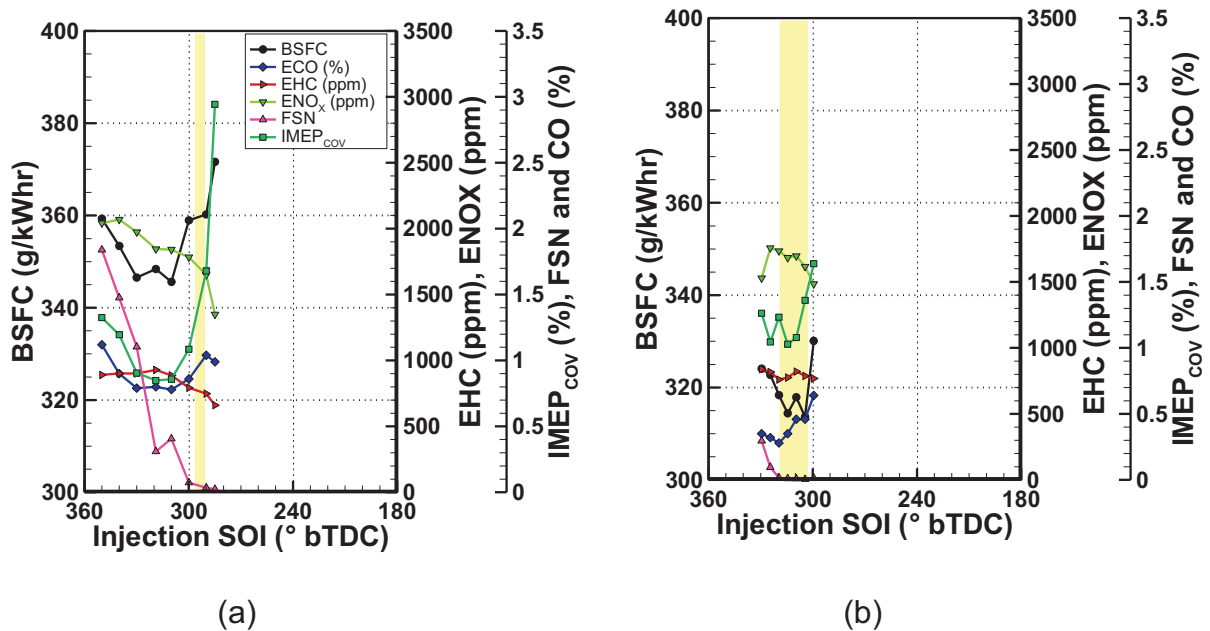


Figure 4.63 EIVC @2000 RPM, 2 Bar BMEP, LLC. (a) 2-valve vs. (b) 1-valve.

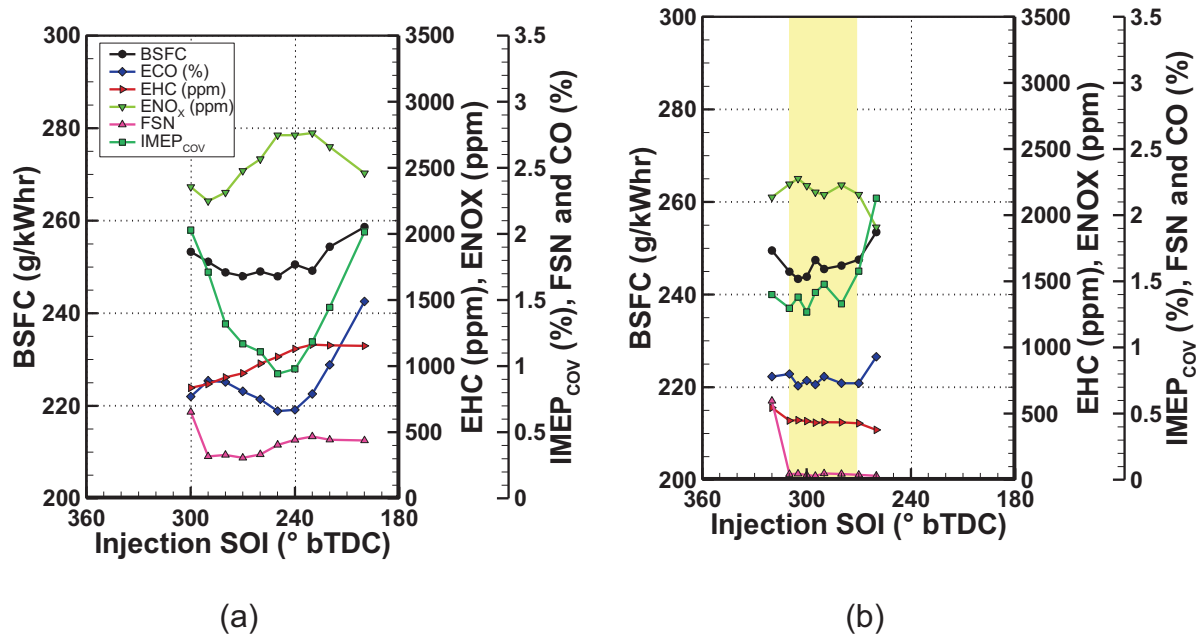
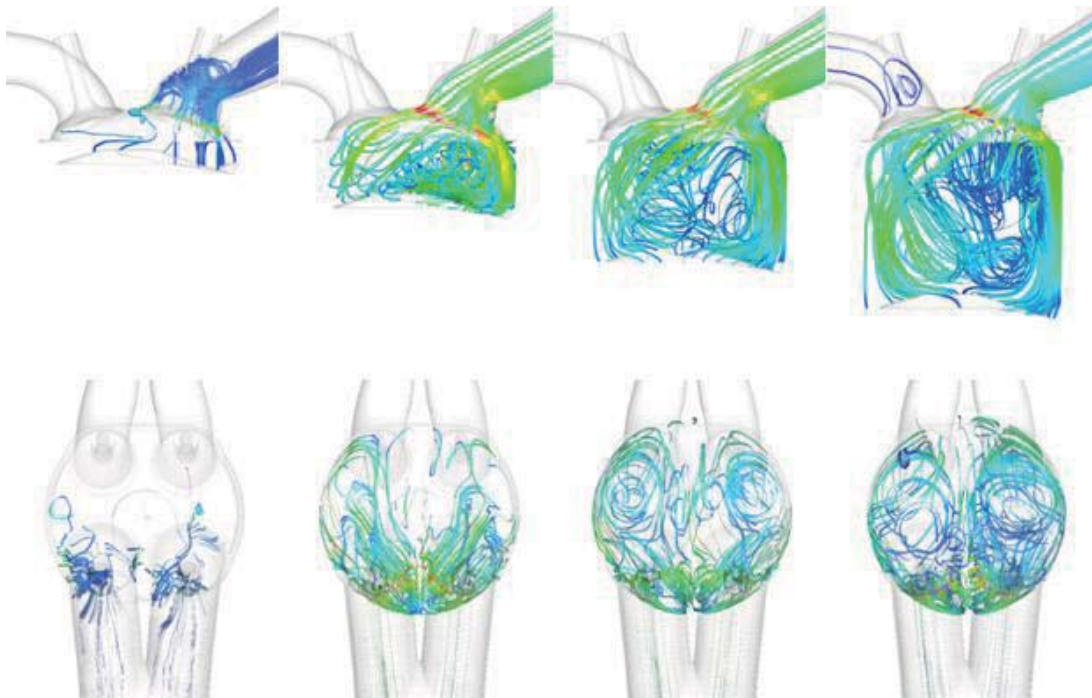


Figure 4.64 LIVC @1500 RPM, 8 Bar BMEP, HLC. (a) 2-valve vs. (b) 1-valve.

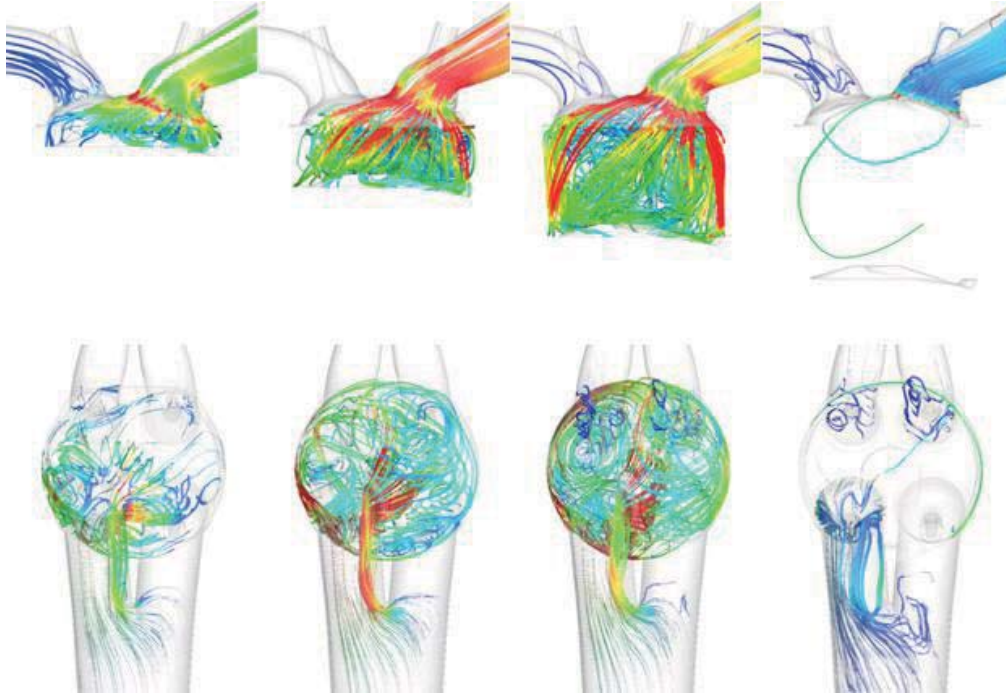
Another problem identified was the undesirably high soot emissions at low-speed high-load conditions with the LIVC strategy. Even though combustion stability was improved with wider timing authority, the soot could not be reduced by retarding injection timing. A typical operation point is at 1500 rpm 8 Bar BMEP, as shown in Fig. 4.64 for the LIVC timing sweep for the 2 valve configuration. A review of the soot and the hydrocarbons emissions shows increased levels with injection retard. This indicates that fuel impinging on the combustion chamber wall is not adequately vaporized and mixed prior to combustion, which may be in the mode of pool fire. Operating the engine with one valve deactivated increases swirl and tumble and provides a significant advantage in soot emissions, as shown in Fig. 4.64b. Injection Timing is still limited at early timings by impingement on the piston but later timing allows a significant reduction in soot and hydrocarbons. It is noteworthy that in Fig.

4.63 and 4.64, the CO emission, which is indicative of the level of uniformity of the combustible mixture, tracks the trends of COV and BSFC quite closely.

In the CFD simulation, four cases pertaining to operation of the Early Intake Valve Closing (EIVC) and Late Intake Valve Closing (LIVC) at 2000rpm 2Bar BMEP, and 1500rpm 8Bar BMEP, to illustrate the interactions of multi-hole DI sprays with VVA charge motions. The computed flow fields are highly dynamic and three-dimensional as shown by the instantaneous streamlines which is color-coded by the velocity magnitude in Fig. 4.65 for these four cases.



(a)



(b)



(c)

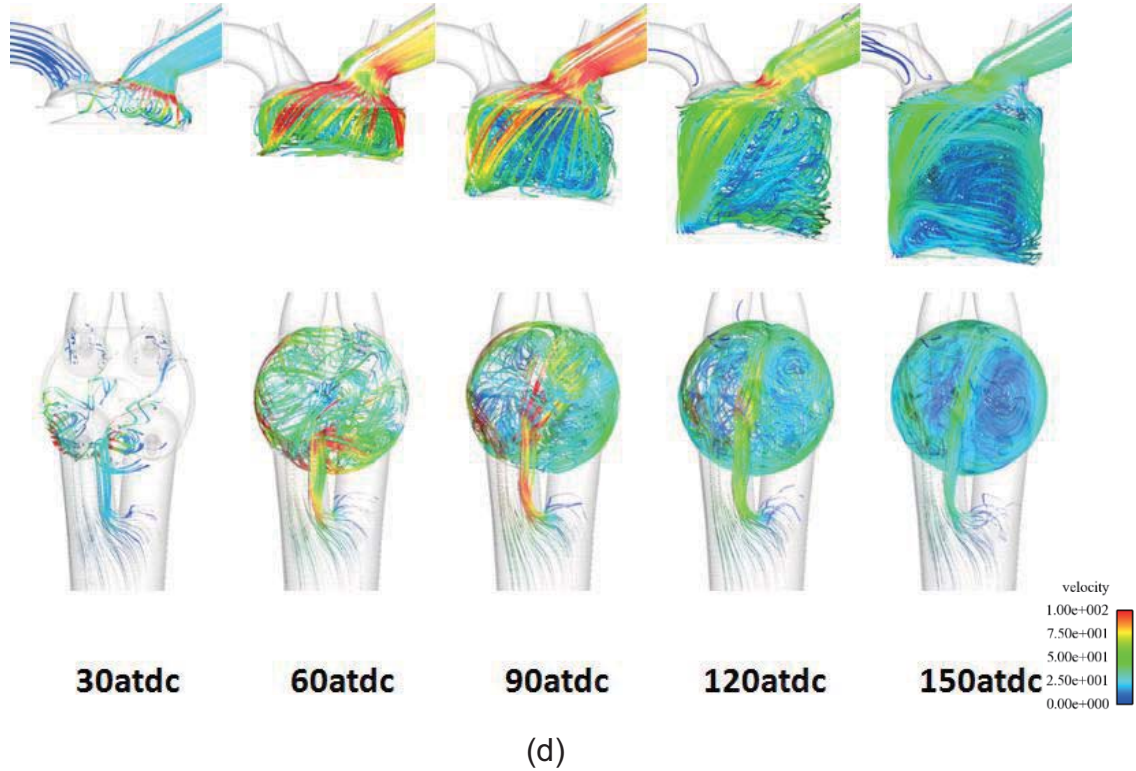
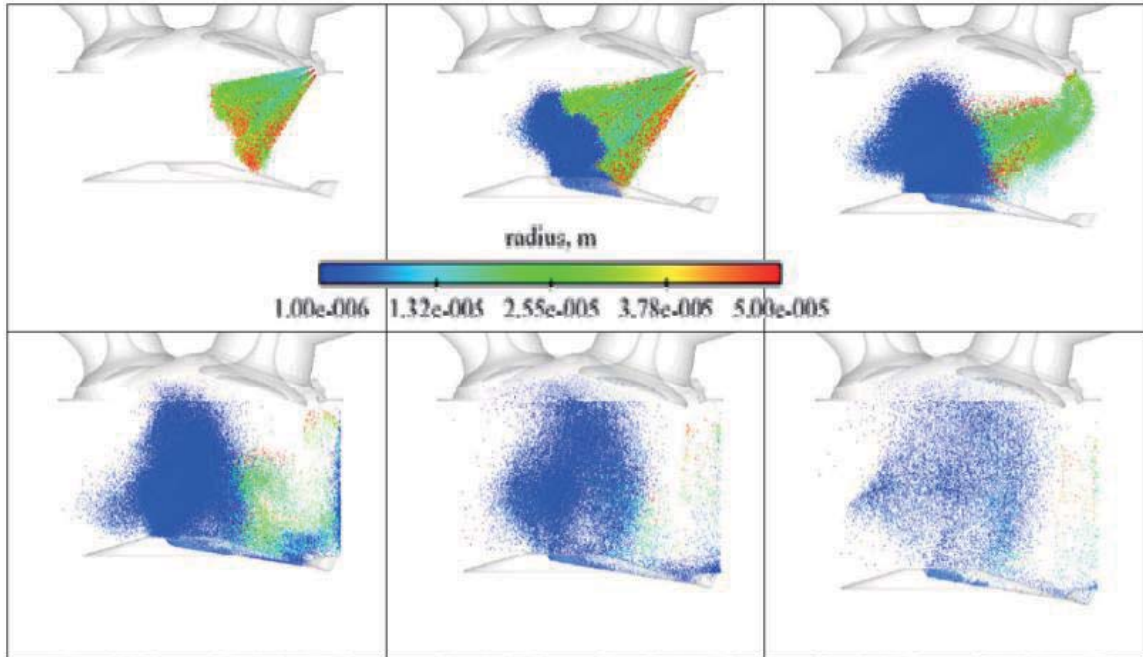
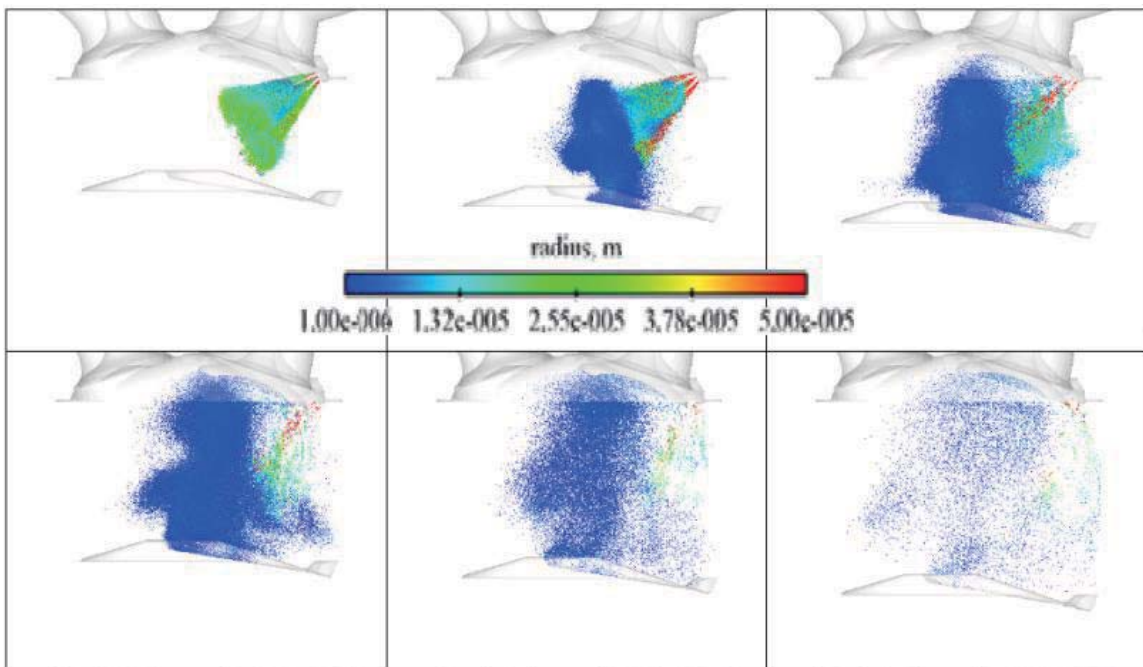


Figure 4.65 The Streamlines of EIVC cases at 2000 rpm: (a) 2-valve vs. (b) 1-valve; LIVC cases at 1500 rpm: (c) 2-valve (d) vs. 1-valve.

It is clearly visible that valve deactivation promotes more vigorous charge motion through the intake stroke, and directs the high speed flow advantageously to the center of the cylinder for mixing although larger pumping loss may be the trade-off.

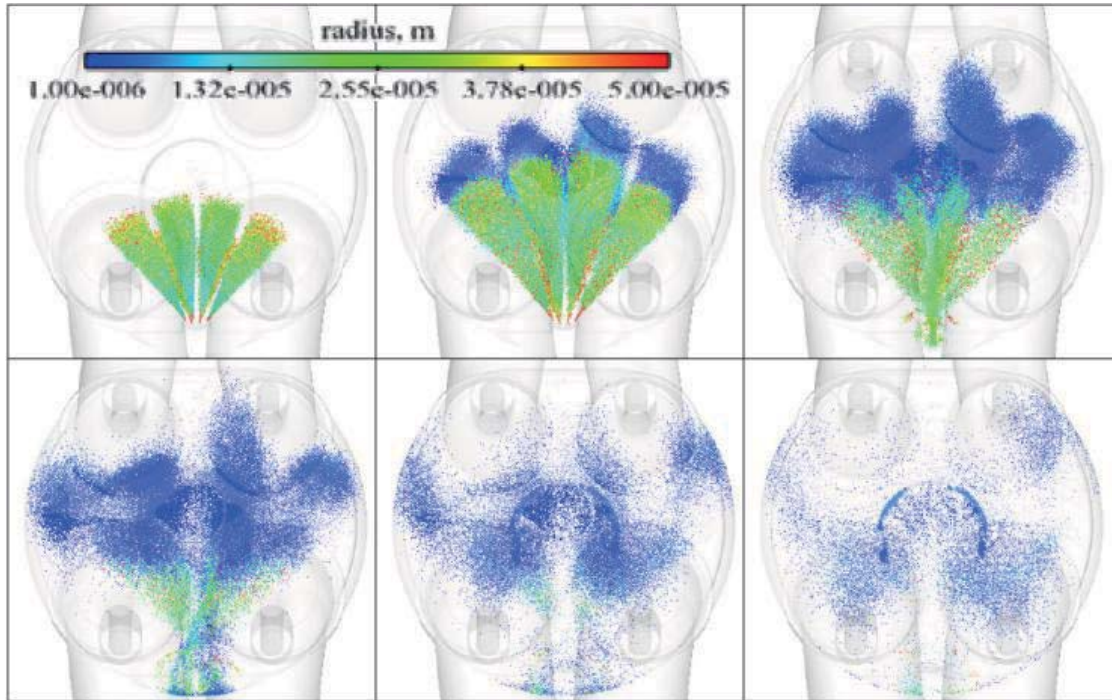


(a)

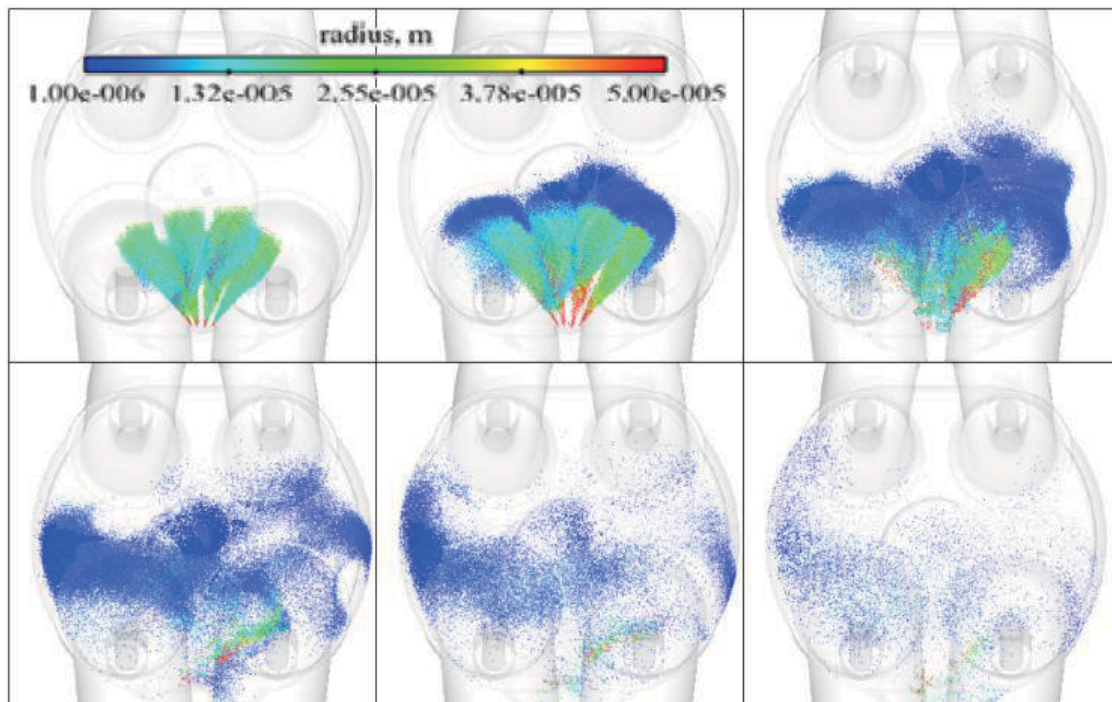


(b)

Figure 4.66 The side view of fuel droplet distributions of EIVC cases at 2000 rpm, 2 Bar BMEP:(a) 2-valve vs. (b) 1-valve.



(a)



(b)

Figure 4.67 The bottom view of fuel droplet distributions of EIVC cases at 2000 rpm, 2 Bar BMEP: (a) 2-valve vs. (b) 1-valve.

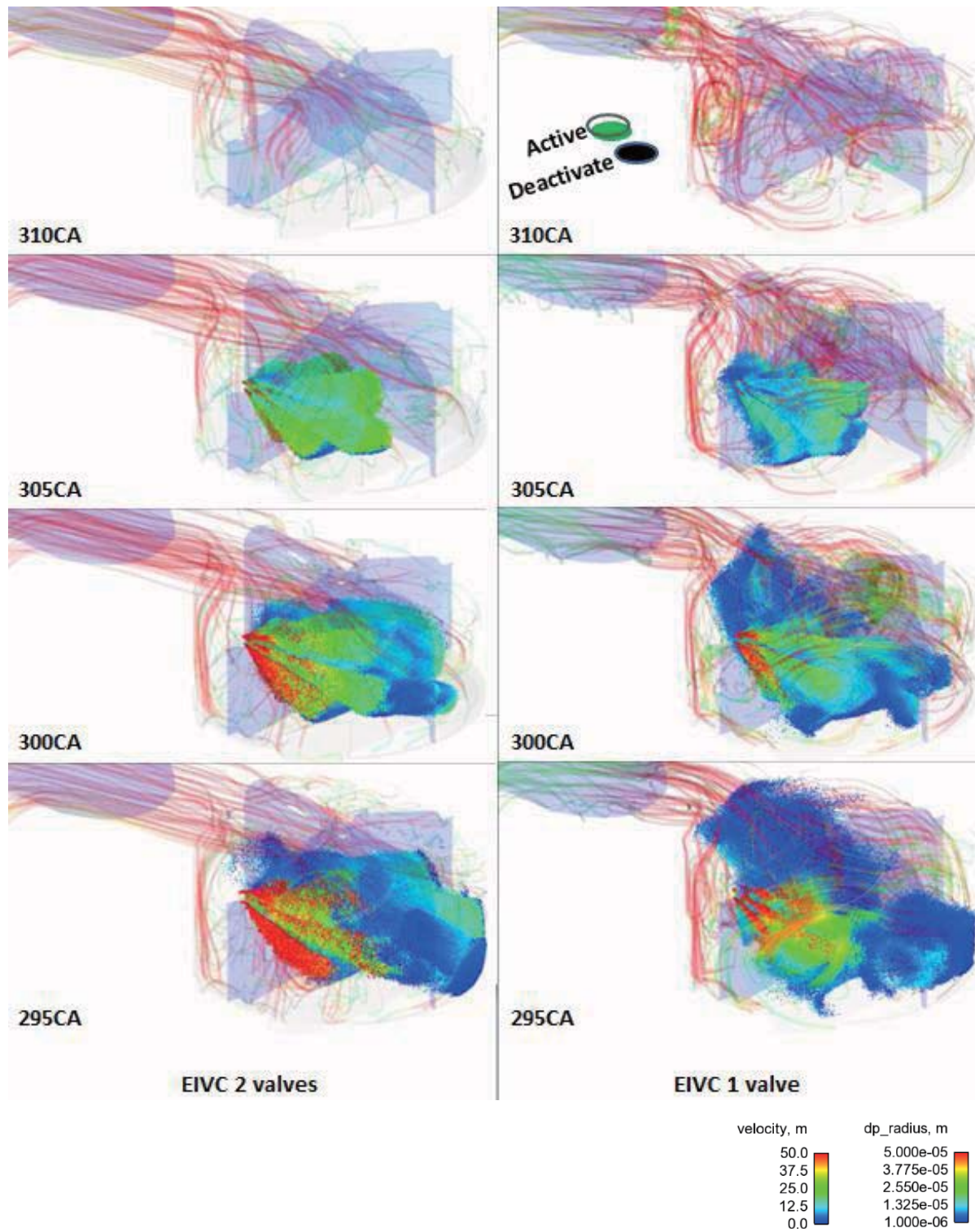
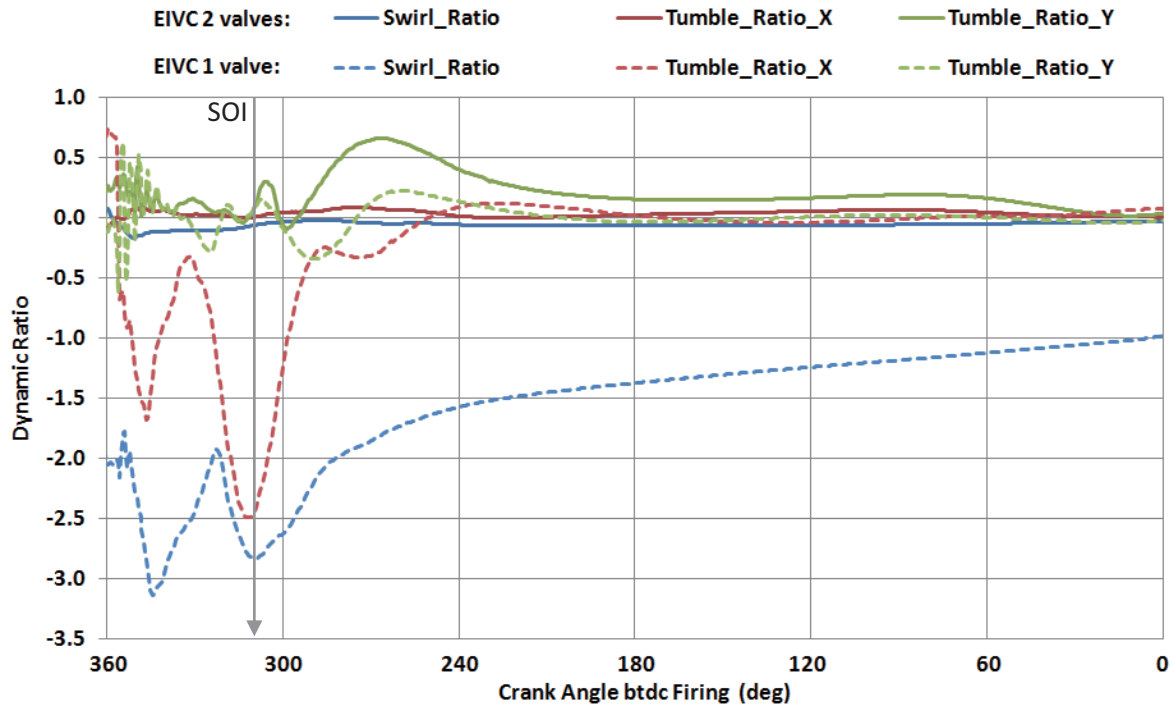


Figure 4.68 Interaction between spray and intake charge motion.

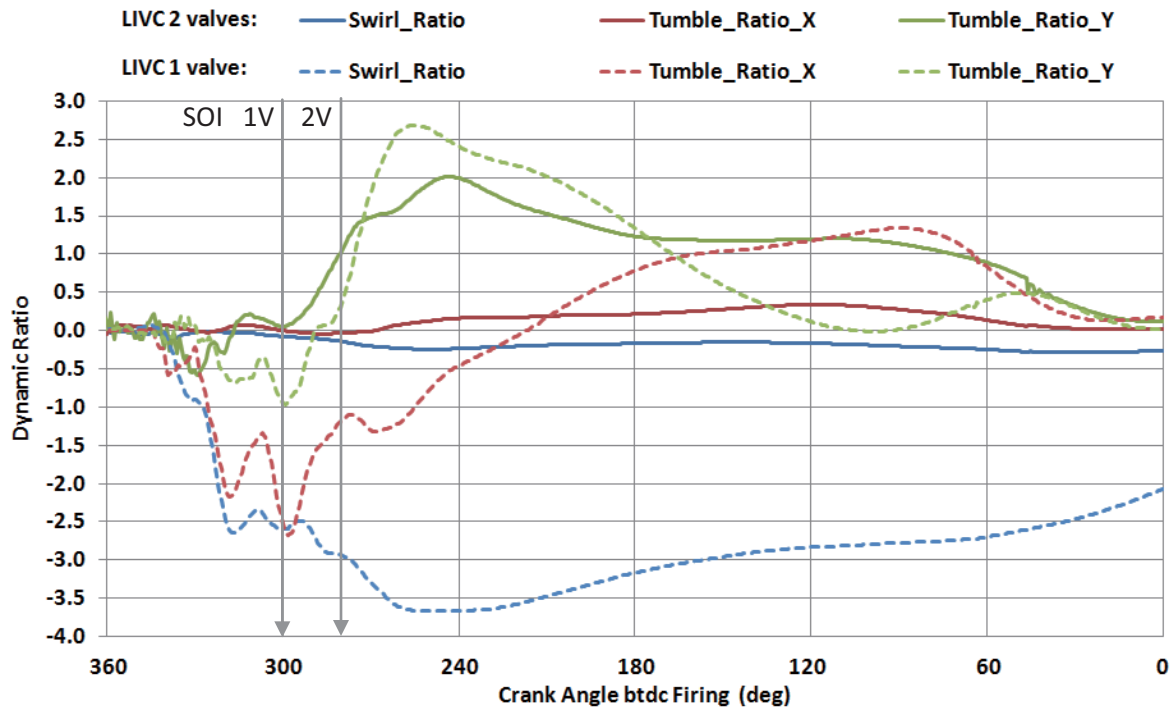
The simulated spray pattern and droplet distribution are shown for the EIVC 2000 RPM, 2 Bar BMEP cases are presented in Fig. 4.66 for side view and Fig. 4.67 for bottom view respectively, with (a) and without (b) valve deactivation. Injection timing is at 60 deg CA aTDC. Valve deactivation shows behavior similar to the optical engine visualization where the spray clouds are entrained toward the active intake valve into the inlet jet. Vaporization of the spray is faster with valve deactivation. The interaction between fuel injection and intake charge motion is also shown in Fig. 4.68.

The in-cylinder dynamic ratios were analyzed and the results are compared with and without valve deactivation in Fig. 4.69. The results show the swirl and two components of tumble around the x and y axis of Fig. 4.69a. When both valves are active the flow is tumble dominated, initially with a reverse tumble followed by a forward tumble around the y-axis. When a valve is deactivated swirl and a cross tumble around the x-axis become significant and the initial reverse tumble is reduced. The location of the SOI timing is shown for reference.

The dynamic ratios for the LIVC condition are presented in Fig. 4.69b. The results with 2 valves show the tumble dominated condition similar to EIVC. The use of valve deactivation promotes more vigorous charge motion through the intake stroke since the valve closes significantly after BDC. The absolute magnitude of the swirl and tumble increases and swirl persists up through TDC. Fig. 4.70 shows the velocity streamlines. Deactivation of one of the intake valves for both EIVC and LIVC produces swirl charge motion. The strong swirl in the cylinder significantly reduces the wall wetting (droplet particles in Fig. 4.70) which is also shown in Fig. 4.71.

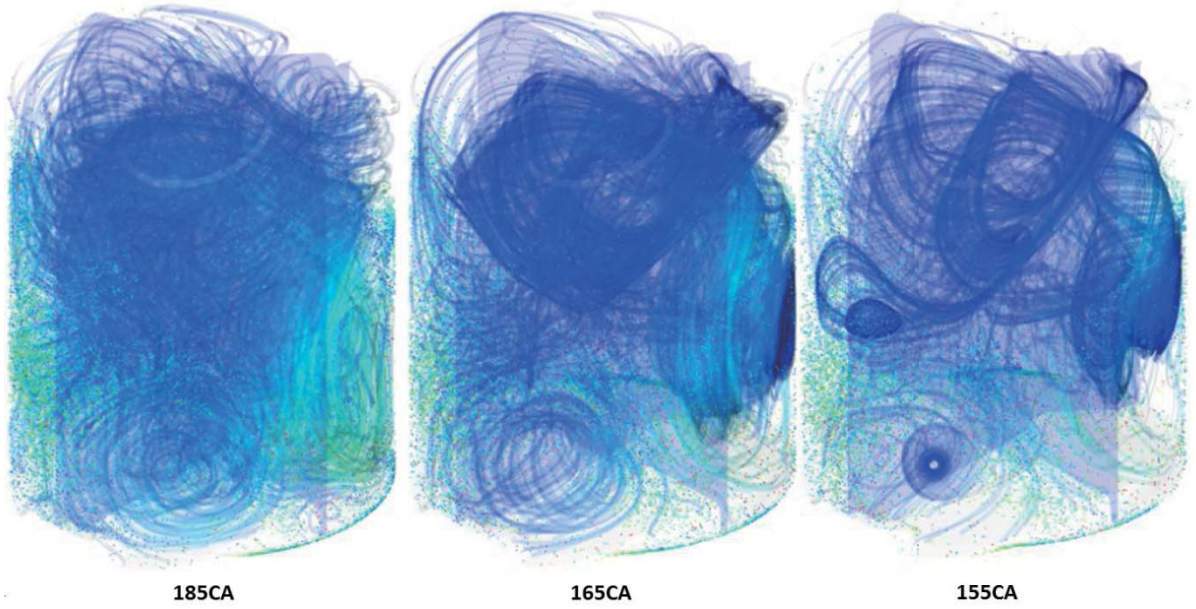


(a)

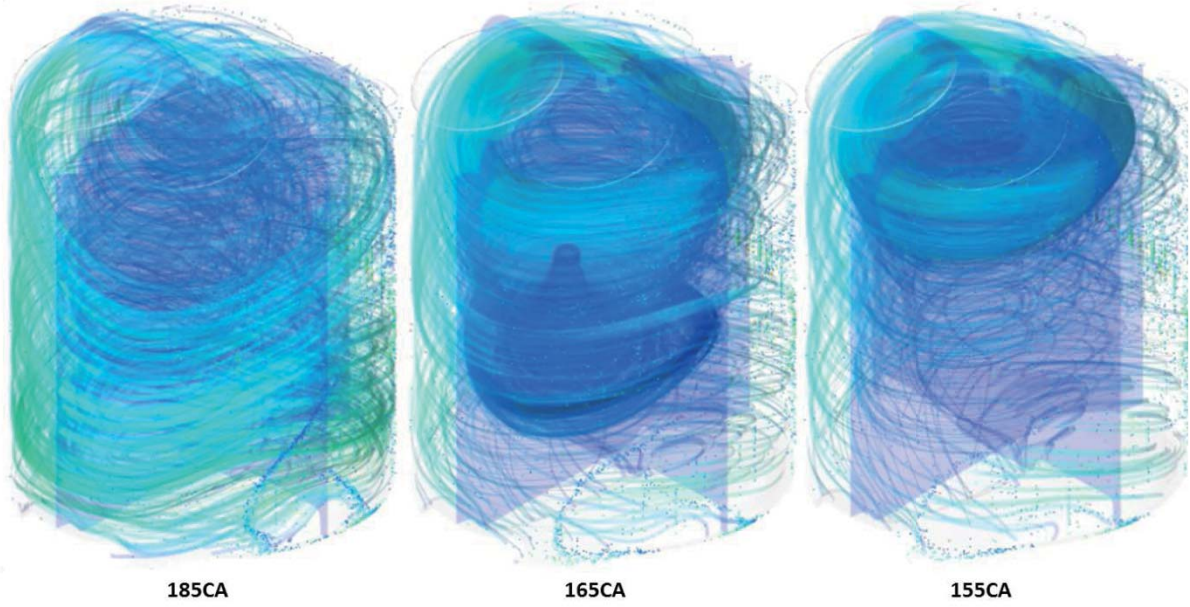


(b)

Figure 4.69 The effects of valve deactivations on computed charge motions dynamic ratios. (a) EIVC case:2000 rpm 2 bar BMEP, (b) LIVC case:1500 rpm 8 Bar BMEP.



EIVC 2 valves



EIVC 1 valve

(a)

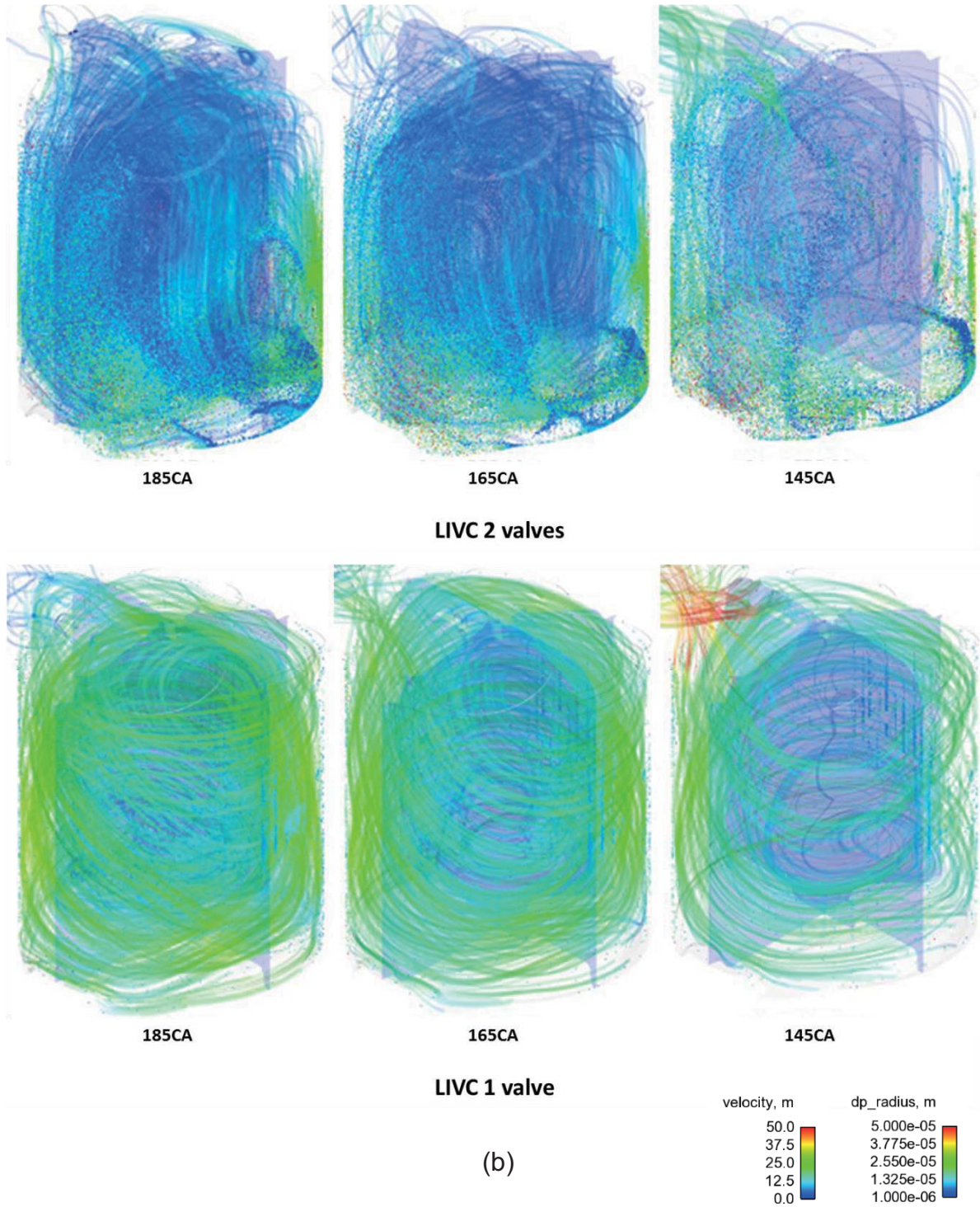


Figure 4.70 In-cylinder flow streamlines and wall wetting. (a) EIVC case:2000 rpm 2 bar BMEP, (b) LIVC case:1500 rpm 8 Bar BMEP.

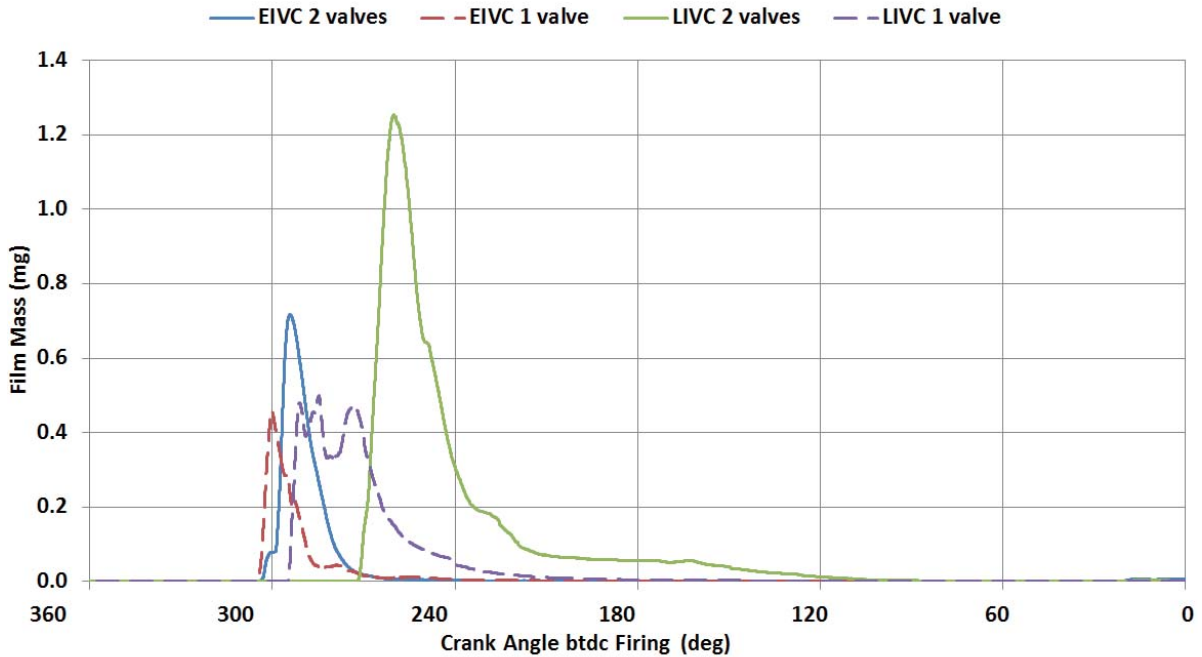


Figure 4.71 Total liquid film mass.

To evaluate the effectiveness of valve deactivation on fuel-air mixing, the homogeneous distribution in-cylinder was displayed by equivalence ratio contours and mass fraction plot in Fig. 4.72 and Fig. 4.73. Data is presented for both EIVC and LIVC operation conditions. Valve deactivation reduces the variation of air fuel ratio for both strategies. The LIVC has more variation earlier in the injection stroke as wall films and rich regions are mixed in at the higher load condition. At the time appropriate for ignition and combustion the more vigorous charge motion from the LIVC strategy has provided a more uniform mixture. Valve deactivation improve the spray vaporization and hence the air-fuel mixture homogeneity.

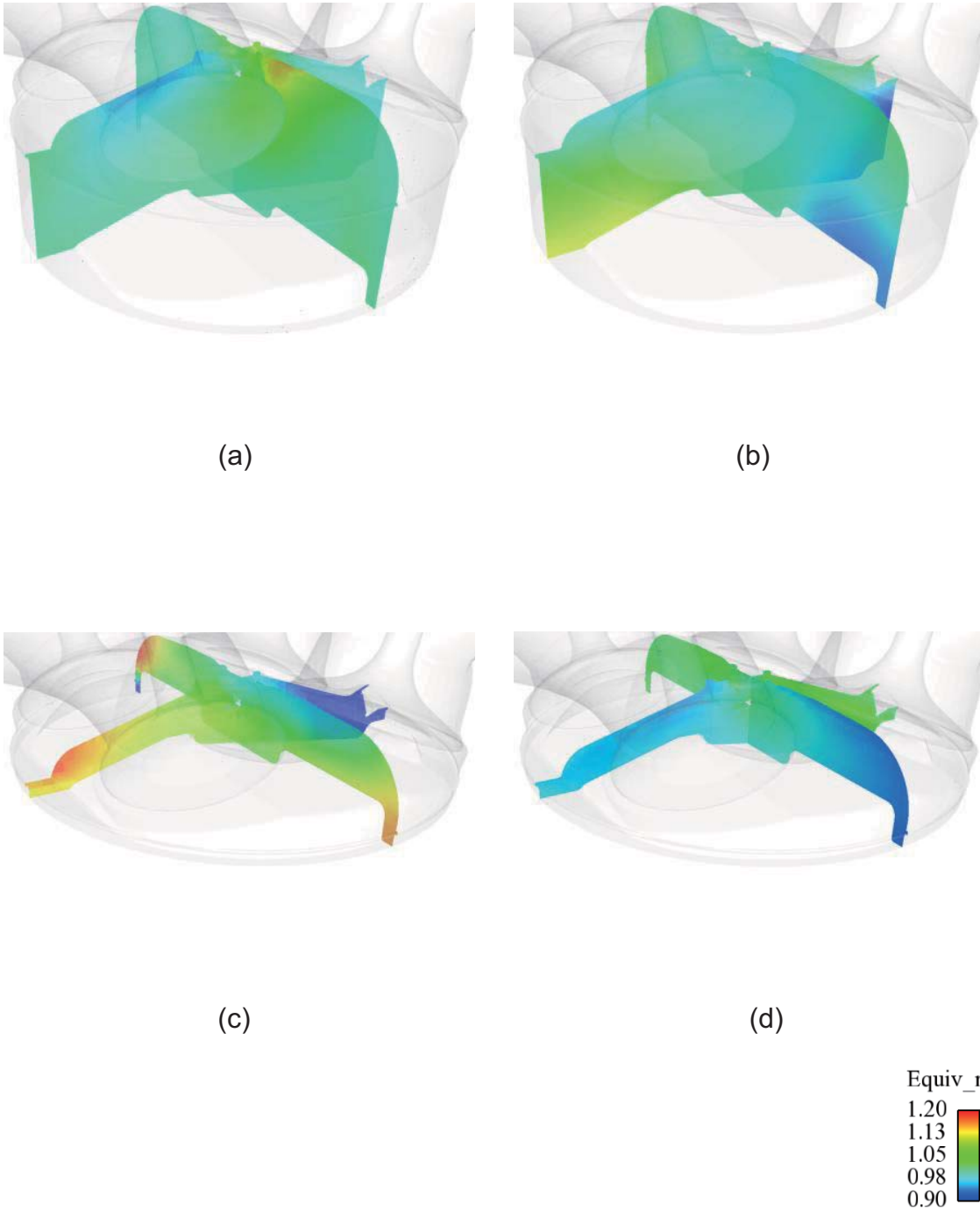


Figure 4.72 In-cylinder air-fuel distributions before combustion. (a) 2-valve, (b) 1-valve (EIVC, 2000 rpm), (c) 2-valve, (d) 1-valve (LIVC, 1500 rpm).

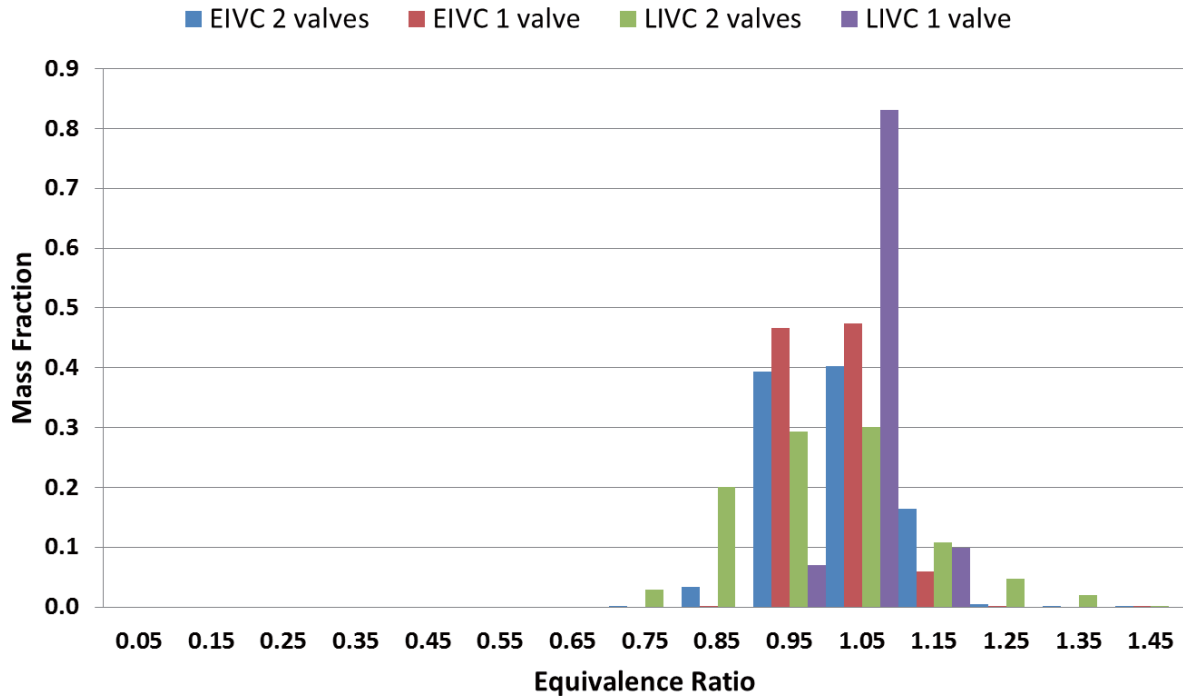


Figure 4.73 Equivalence ratio distributions at spark timing.

3D CONVERGE code was used to investigate the combustion process of GDI metal engine. With the capability of local mesh refinement, adaptive mesh refinement (AMR) and the detailed chemical kinetics combustion model, the spark ignition can be simulated by generating a fine mesh around the spark plug. Fluid motion in the spark region is not quiescent. On the ns time scale of the breakdown spark discharging phase (less than 0.5 degree CA), this fluid motion is not important. In the arc/glow spark discharging phase, the arc between the electrodes gets advected with the flow and stretches out in length [54]. Fig. 4.74 shows the spark energy source in EIVC valve deactivation case moving with the air flow. Each point in the spark source has different velocity due to the spatial variation of fluid velocity.

The energy source represented by temperature contour (2000 K) is moving with the clockwise in-cylinder swirl flow.

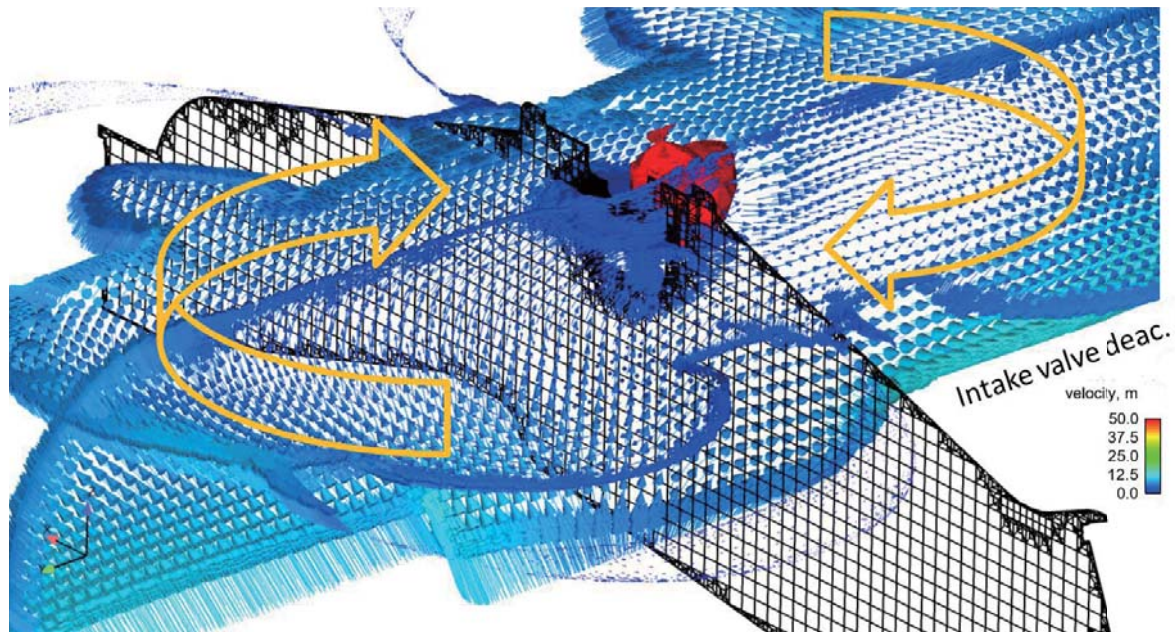


Figure 4.74 In-cylinder velocity vector field and temperature iso-surface (2000 K). 1-valve (EIVC, 2000 rpm).

The reaction mechanism involves iso-octane and n-heptane. It contained 48 species and 80 reactions. Predictions of NO_x emissions are made using an extended zeldovich NO_x model. The Comparison between computed and experimental profiles of in-cylinder pressure is shown in Fig. 4.75. The test result is the cylinder pressure averaged by 50 cycles. The operating condition is 2000 RPM, 2 Bar BMEP, throttling 53 kPa MAP. The initial and boundary conditions of this 3-D simulation are generated using 1-D GT-Power calculated results. A rather

satisfactory agreement is achieved. Fig. 4.76 shows the integrated heat release (summed over time) and the evolution of the ignition kernel and flame front of EIVC 2 valves and 1 valve case.

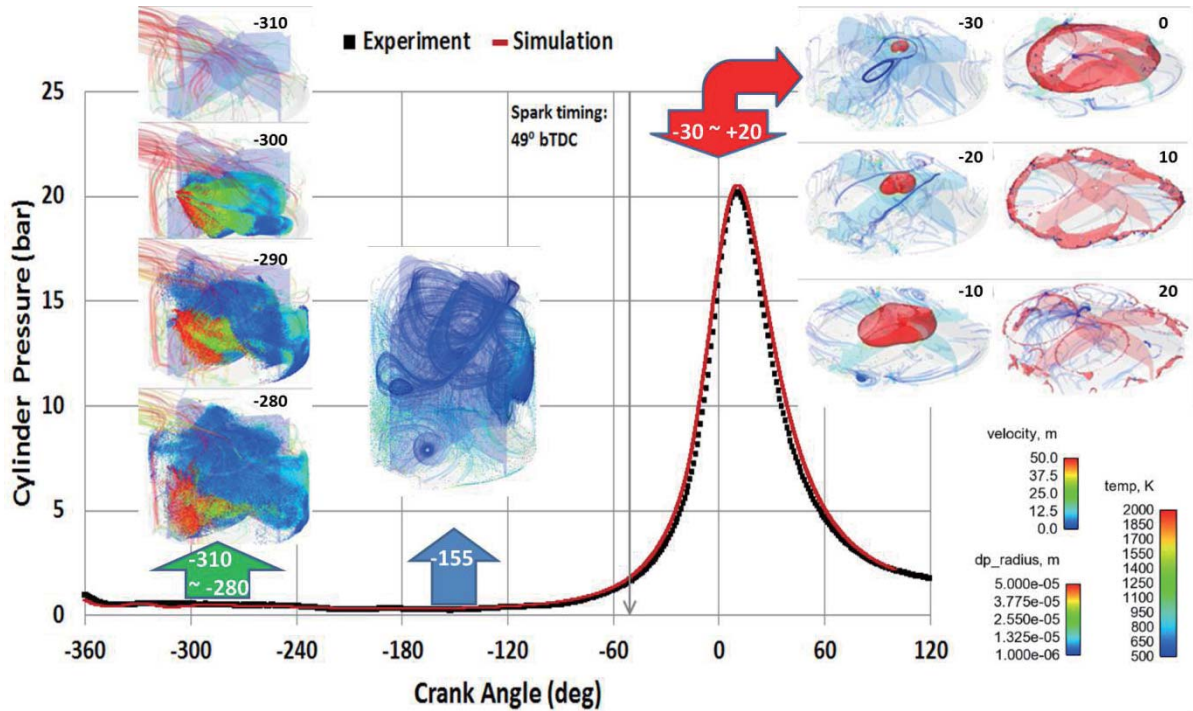


Figure 4.75 Comparison between computed and experimental profiles of in-cylinder pressure. EIVC Metal Engine 2000 rpm, 2 bar BMEP (2 valves).

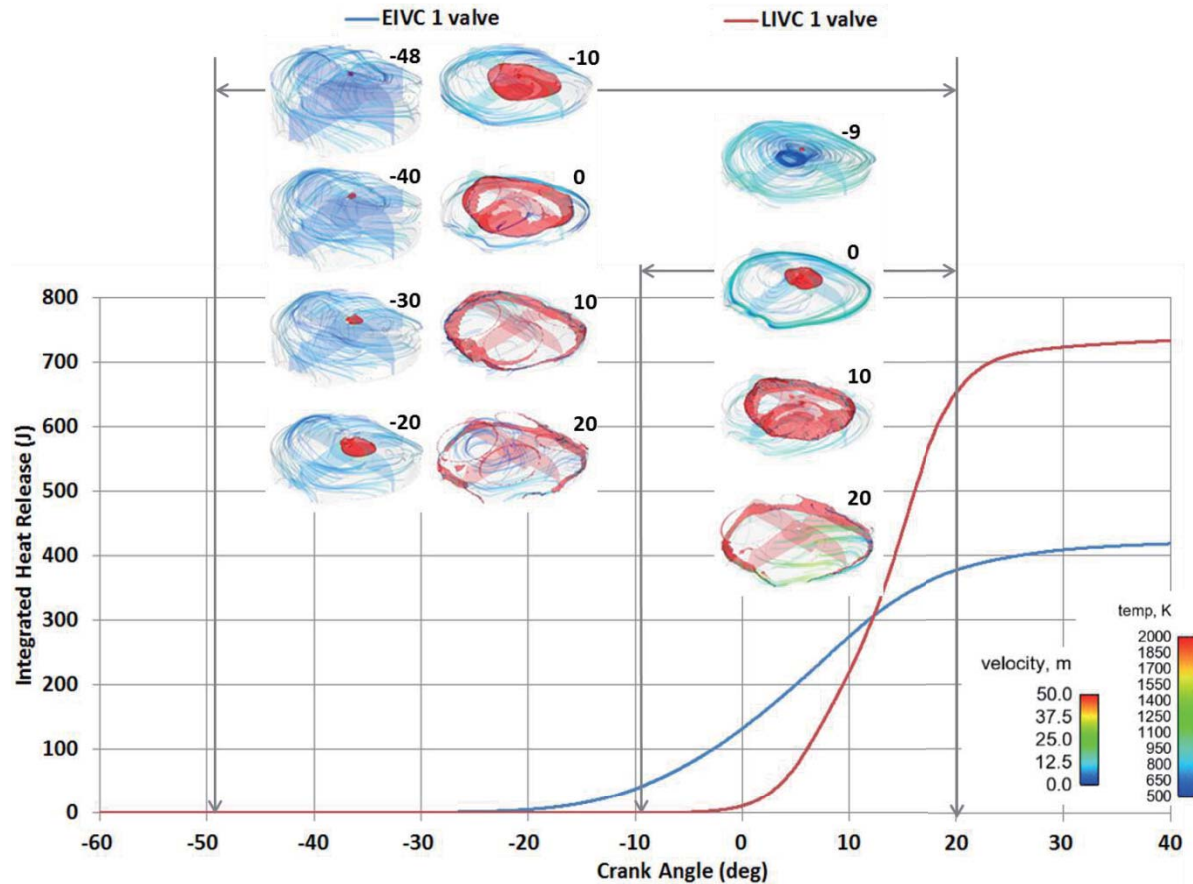


Figure 4.76 Evolution of ignition kernel and flame front. (a) EIVC Metal Engine 2000 rpm, 2 bar BMEP, (b) LIVC Metal Engine 1500 rpm, 8 bar BMEP. Temperature iso-surface (2000 K).

To analyze the turbulence and combustion interaction, local flame front structure is commonly observed by PLIF (planar laser-induced fluorescence) imaging of CH, OH, and CH₂O. Formaldehyde (CH₂O or HCHO) is an important combustion intermediate and formed primarily in the preheat zone. Fig. 4.77 shows the evolution of the CH₂O mass and concentration (40, 30, 20, 10 and 0 CA deg before TDC), which is correlated to the position of peak heat release within the flame front. Further study of optical visualization and numerical simulation of combustion should be conducted because it is very critical for GDI engines.

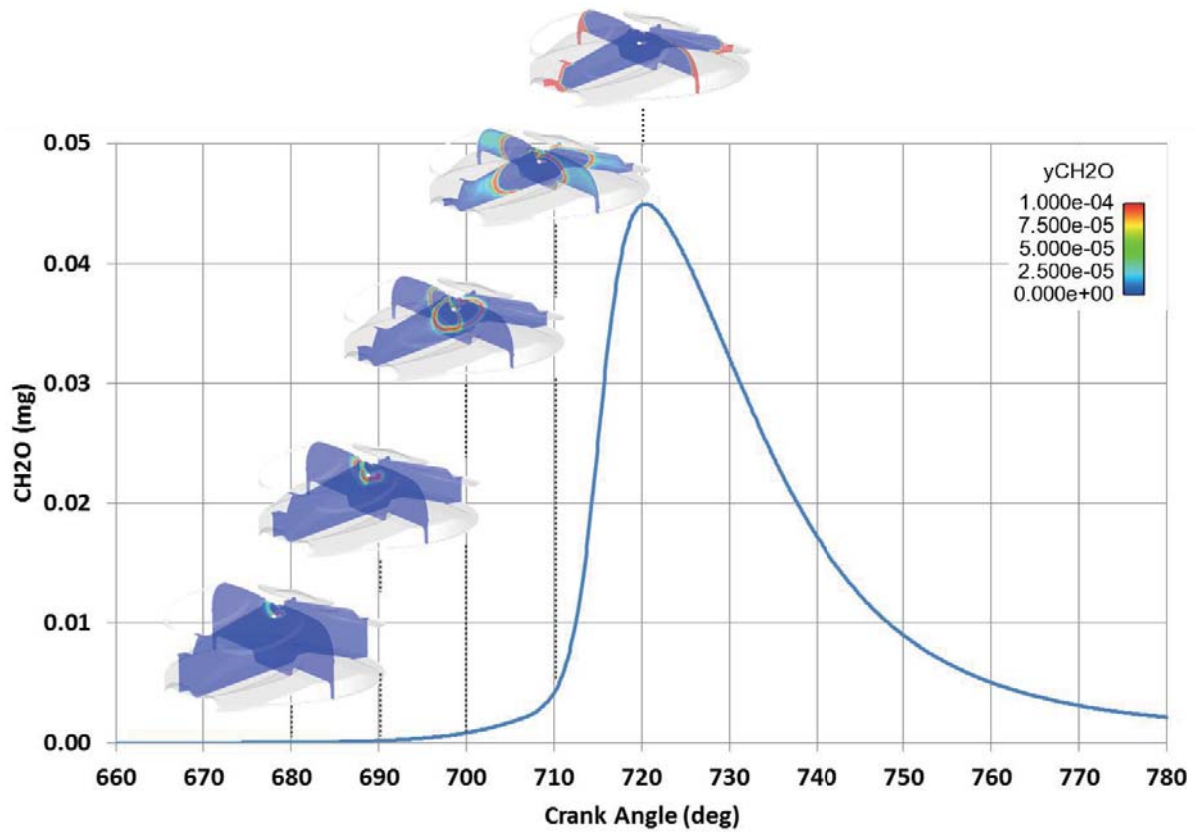


Figure 4.77 Evolution of CH₂O mass and concentration. EIVC Metal Engine 2000 rpm, 2 bar BMEP (2 valves).

CHAPTER 5 CONCLUSION

5.1 Summary of the Work

Internal nozzle flow

Nozzle exit flow conditions are critical to predictive spray modeling. Characteristics of the internal flow structure near a fundamental single-hole research diesel nozzle, a symmetric two-hole diesel nozzle, and a three-hole DI gasoline research injector exit were investigated using multi-dimensional multi-phase CFD simulations in an attempt to better understand the primary breakup mechanisms of DI injectors, and to better correlate to the near-nozzle jet morphology using ultrafast x-ray phase-contrast imaging technique during quasi-steady injection process.

- Sprays from the two-hole nozzle are dominated by vortex flow inside the nozzle. Vortical wavy structure of the emerging spray verifies the existence of rotational flows inside the nozzle. CFD simulations of the single-hole and two-hole fundamental flow configurations also show that the three-dimensional fluid flow entering the two-hole nozzle creates stronger streamline curvature, and streamwise vorticity which are by default absent in the axisymmetric single-hole nozzle.
- The overlapped wavy structures inside the two-hole nozzle spray indicate that the counter-rotating vortices formed inside the nozzle affects the two-hole nozzle spray development. Unstable flow characteristic of the two-hole nozzle caused higher shot-to-shot variation in spray morphology, larger spray angle and faster break-up of the spray compared to the single-hole nozzle spray which has laminar-like flow characteristics. Numerical results show that the

two-hole nozzle also produces thicker shear layer and higher turbulence level and wider initial divergence angle. The streamwise counter-rotating vortices are actually bound by a thin shear layer near the wall within the orifice which will be relaxed immediately upon exiting the orifice.

- More turbulent jet morphology was observed inside the two-hole nozzle spray upon increase in injection pressure. Wavelength of the wavy structure was decreased at high injection pressure and it caused faster break-up of the emerging spray. The shot-to-shot deviation in spray angle and wavelength was decreased upon increase in injection pressure supposedly due to break-up of the larger-scale unstable vortex flow into the finer-scale turbulences. CFD simulation also shows high strength of rotation with high injection pressure.
- The interactions of the streamwise vortices with the downwash and turbulent flows will enhance the interfacial instability and produce wider spray cone angles observed in the phase-contrast X-Ray images.
- The vorticity strength of the multi-hole nozzle is strong. Increase in the hole number were shown to have an intensifying effects in general for rotational and turbulent flow structure.
- The lower vortex pair turns out to have stronger intensity than the upper one at the nozzle exit. This is consistent to the observation in the spray that the lower waves have consistently shorter length scales than the upper ones mentioned above.

- The oscillation frequency of the URANS simulation is on the order of 5 to 10 MHz depending on the injection pressure is consistent to the wavelength observed experimentally.
- The results show that strong interactions of the vortex streaks, cavitation, and transitional turbulence in the nozzle and sac volume. These complicated unsteady flow features dominate the near-nozzle breakup mechanisms which are quite unlike those of diesel. The interfacial structure inside the spray is characterized by 3-D ligaments and membranes, indicative of turbulence/vorticities and cavitation breakup mechanisms. The results also show that the cavitation become stronger at lower needle lift.

Wall Impingement

In this work experimental and computational investigation was implemented for the spray vaporization and spray-wall interaction of the outward opening piezo-driven injector and side-mounted DI gasoline multi-hole injector. The Refractive Index Matching technique was performed to measure the fuel film resulting from spray impingement for the PDI injector and multi-hole injector in a conditioned pressure chamber.

- The effect of ambient temperature on fuel film thickness was very significant.
- The film evaporation rate was also strongly affected by the ambient pressure especially at lower temperature.
- The deposit area and shape of each spray plume was affected by the injection pressure and the distance between injector tip and window.

- Higher pressure at the same fuel amount tends to reduce film thickness.
- The computed results show close maximum peak film thicknesses with the experimental data, and need perform further work to verify the liquid film evolution.
- CFD simulation was also conducted, validated first with spray visualization on the free spray transport and then compared with the RIM test results. The numerical investigation of spray behavior and film characteristics agrees in general with the experimental observations in terms of overall spray shape, tip penetration and wall impingement pattern, and the maximum fuel film thickness. However, the predicted fuel mass is greater than the RIM results possibly due to the surface roughness and the modeling of spray impingement.

OAE Testing

This paper describes a combination of spray visualization and CFD simulation to investigate the interactions of side-mounted GDI multiple-hole sprays with the mixture formation processes. The major findings are listed as follows:

- Valve-deactivation and variable valve-lift, produces very dynamic charge flow motions, resulting in various tumble, swirl, and turbulent flows, which interacts with off-axis multiple-hole DI sprays, has important implications for the engine mixing and resultant combustion performance.
- Injection timing is constrained by wall impingement which is correlated to soot (FSN), and incomplete mixing which is correlated to combustion instability (COV).

Injection too early or too late result into wall impingement; similarly injection too early or too late usually results in insufficient mixing.

- Higher turbulence enhances mixing before ignition and enhances combustion after ignition; therefore, there is optimal injection timing for faster mixing and faster combustion.
- At low-speed low- and medium-load cases, valve deactivation promotes more vigorous charge motion through the intake stroke, and therefore better mixing and less wall impingement for a wider injection window.
- Combination of optical diagnostics and CFD simulations provides key tools for its continuous development and optimization, although more validations are needed. The integral analyses of CFD results are shown to correlate well to the combustion and emissions metal engine data.
- Ignition and flame propagation is complicated by chemistry and turbulence interactions, and need more future research.

5.2 Recommendation and Future Work

Turbulence and cavitation (flash boiling) modeling are crucial to internal nozzle flow and spray atomization, more research is needed in both the experiment and simulation sides to improve and validate the accuracy of the numerical schemes, and physical sub-models.

The surface conditions and heat transfer of the impingement window in RIM measurement should be considered and required more study. The predicted fuel

mass is greater than the RIM results possibly due to the surface roughness and the modeling of spray impingement.

The numerical and experimental studied of the in-cylinder spray/mixing in GDI engines have been summarized and reconsidered when the GDI engine is fired. The simulation study is recommended use 3-D commercial codes coupling with 1-D cycle simulation software. The detailed chemistry combustion model with primary reference fuel (PRF) reduced chemistry mechanism for 3-D combustion need more research.

REFERENCES

1. John Sousanis (2011-08-15). World Vehicle Population Tops 1 Billion Units. Ward AutoWorld. http://wardsauto.com/ar/world_vehicle_population_110815. Retrieved 2011-08-18.
2. Sperling, Daniel and Deborah Gordon (2009). Two billion cars: driving toward sustainability. Oxford University Press, New York. pp. 4 and 13. ISBN 978-0-19-537664-7. See Chapter 1, Note 1, pp. 261.
3. U.S. Environmental Protection Agency, National Emission Inventory Air Pollutant Emission Trends Web site www.epa.gov/ttn/chief/trends. (Additional resources: www.epa.gov/ttn/chief)
4. Zhao, F.-Q., Harrington, D. L., and Lai, M.-C., Automotive Gasoline Direct Injection Engines, Pittsburgh: Society of Automotive Engineers, 2002, R-315.
5. Moreira, A.L.N., Moita, A.S., and Pano, M.R., Prog. Energy Combust. Sci., 2010, 36, 544-580.
6. F. Zhao, T.W. Asmus, D.N. Assanis, J.E. Dec, J.A. Eng, and P.M. Najt (Eds.). Homogeneous Charge Compression Ignition (HCCI) Engines: Key Research and Development Issues. SAE International, Warrendale, PA, 2003.
7. Stanglmaier, R. H., Hall, M. J., and Matthews, R. D., Fuel-Spray/Charge-Motion Interaction within the Cylinder of a Direct-Injected, 4-Valve, SI Engine. SAE Paper 980155, SAE International, 1998.

8. W. Visnic, Wards Auto World, September 1 2005. Available at <http://www.wardsauto.com>.
9. M.C. Drake, D.C. Haworth., Advanced gasoline engine development using optical diagnostics and numerical modeling. Proceedings of the Combustion Institute, 2007. 31 : p. 99-124.
10. A.C. Alkidas, S.H. El Tahry, Contributors to the Fuel Economy Advantage of DISI Engines Over PFI Engines. SAE Paper 2003-01- 3101, 2003.
11. F. Zhao, D.L. Harrington, M.-C.D. Lai, Automotive Gasoline Direct-Injection Engines. SAE International, 2002.
12. Bergstrand, P. and Denbratt, I., "Diesel Combustion with Reduced Nozzle Orifice Diameter," SAE Technical Paper 2001-01-2010, 2001.
13. Noyori, T. and Inoue, H., Effects of Fuel Spray Characteristics on Smoke Emissions in a Small Displacement Spark-Ignition Direct Injection. SAE 2007-01-3492, 2007.
14. Shi, J., Baecher, H., Tichy, M., Bauer, W. "Numerical and Experimental Investigation of Fuel Injection and Droplet Evaporation in A Pressure Chamber for The Development of Gasoline Direct Injection," ILASS08-6-2.
15. Sellnau, M., Sinnamon, J., Hoyer, K., and Husted, H., Gasoline Direct Injection Compression Ignition (GDICI) - Diesel-like Efficiency with Low CO2 Emissions. SAE Int. J. Engines 4(1):2010-2022, 2011.
16. Befrui, B., Corbinelli, G., D'Onofrio M., Varble D., GDI Multi-hole Injector Internal Flow and Spray Analysis. SAE Technical Paper 2011-01-1211, (2011).

17. Andriotis, A. , Gavaises, M., and Arcoumanis, C., (2008) "Vortex Flow and Cavitation in Diesel Injector Nozzles," *Journal of Fluid Mechanics*, 610:195-215.
18. Andriotis, A., and Gavaises, M., (2009) "Influence of Vortex Flow and Cavitation on Near-Nozzle Diesel Spray Dispersion Angle," *Atomization and Sprays*, 19:247-261.
19. Qin, J., Dan, T., Lai, M.-C., Savonen, C., Schwartz, E., and Bryzik, W., (2000) "Correlating the Diesel Spray Behavior to Nozzle Design," *J. Fuels & Lubricants*, SAE Transc. 108(4), pp. 1726-1738, SAE 1999-01-3555.
20. Han, J.-S., Lu, P.-H., Lai, M.-C., and Henein, N. A (2003), "Investigation of Diesel Spray Primary Break-up for Different Nozzle Geometries," *J. Engine*, SAE Transc. 111(3), pp. 2528~2548, SAE 2002-01-2775.
21. Badock, C., Wirth, R., Fath, A., and Leipertz, A., (1999) "Investigation of Cavitation in Real Size Diesel Injection Nozzles," *Int'l Journal of Heat and Fluid Flow*, 20:538-544.
22. Sou, A., Tomiyama, A., Hosokawa, S., Nigorikawa, S., and Maeda, T. (2006) "Cavitation in a Two-Dimensional Nozzle and Liquid Jet Atomization," *JSME International Journal; Series B*, 49:1253-1259.
23. Lai, M.-C., Wang, T.-C., Xie, X., Han, J., Henein, N. A., Schwarz, E., and Bryzik, W., "Microscopic characterization of Diesel Sprays at VCO Nozzle Exit" *J. Fuels & Lubricants*, SAE Transc. 107(4), pp. 1283-1293, SAE 982542.

24. Liu, Z., Im, K., Xie, X., Wang, Y., Fezzaa, K., Lai, M.-C., and Wang, J. (2009) "Single-Shot Ultra-Fast Phase-Contrast X-ray Imaging of High-Pressure Diesel Fuel Sprays," 11th International Conference on Liquid Atomization and Spray Systems (ICLASS 2009), Vail, Colorado, August 2009.
25. Liu, Z., Im, K.-S., Xie, X., Wang, Y., Fezzaa, K., Lai, M.-C., and Wang, J., (2010) "Near-nozzle Structure of Diesel Sprays Affected by Internal Geometry of Injector Nozzle: Visualized by Single-shot X-ray Imaging," SAE Congress, Detroit, April 13~15, 2010. SAE 2010-01-0877.
26. Powell, C. F., Yue, Y., Poola, R., Wang, J., and Lai, M.-C., (2002) "A Quantitative Measurement of High-Pressure Dense Diesel Spray Core using Synchrotron X-Rays," J. Engine, SAE Transc. 110(3), pp. 422-429, SAE 2001-01-0531.
27. Wilkins, S. W., Gureyev, T. E., Gao, D., Pogany, A., and Stevenson, A. W.,(1996), "Phase-Contrast Imaging using Polychromatic Hard X-rays," Letters to Nature, 384:335-338, 1996.
28. Giannadakis, E. Papoulias, D., Gavaises, M., and Arcoumanis, C., (2007)"Evaluation of the Predictive Capability of Diesel Nozzle Cavitation Models," SAE 2007-01-0245.
29. Gavaises, M., Andriotis, A., Papoulias, D., Mitroglou, N., and Theodorakakos, A. (2009) "Characterization of String Cavitation in Large-Scale Diesel Nozzles," Physics of Fluids, 21:052107.

30. Dumouchel, C., On the Experimental Investigation on Primary Atomization of Liquid Streams. *Exp Fluids* 45:371-422, 2008.
31. Gorokhovski, M. and Herrmann, M., Modeling Primary Atomization. *Annu. Rev. Fluid Mech.*, 40:343-366, 2008.
32. Reitz R. D., (1978) "Atomization and other Breakup Regimes of a Liquid Jet," PhD thesis, Princeton Univ., Princeton, NJ.
33. Reitz R. D., Bracco, F.V., (1982) "Mechanism of atomization of a liquid jet," *Phys. Fluids*. 25:1730–42.
34. Wu, P. K., Miranda, R. F. and Faeth, G. M., (1995) "Effects of Initial Flow Conditions on Primary Breakup of Nonturbulent and Turbulent Round Liquid Jets," *Atomiz. Sprays*, 5(2).
35. Lin, S. P., and Reitz, R. D. (1998) "Drop and Spray Formation from a Liquid Jet," *Annu. Rev. Fluid Mech.*30:85–105.
36. Arai, M., Shimizu, M., and Hiroyasu, H. (1985) "Break-up length and spray angle of high speed jet." *Proceedings of ICLASS '85*, London, UK, 8–10 July 1985, paper IB/4.
37. Soteriou C. C. E., and Andrews, R. J. (1993) "Cavitation Hydraulic Flip and Atomization in Direct Injection Diesel Sprays," *Proc IMechE*, C465/051/93 45-65.
38. Chaves, H., Knapp, M., Kubitzek, A. and Obermeier, F., (1995) "Experimental Study of Cavitation in the Nozzle Hole of Diesel Injectors using Transparent Nozzles." *SAE Paper* 950290.

39. Hiroyasu, H., (2000) "Spray breakup mechanism from the hole-type nozzle and its applications," *Atomiz. Sprays* 10:511–527.
40. Arcoumanis, C., Badami, M., Flora, H. and Gavaises, M., (2000) "Cavitation in real-size multi-hole diesel injector nozzles." *SAE Trans. J. Engines* 109-3, 2000-01-1249.
41. Gavaises, M., Arcoumanis, C., Roth, H., Choi, Y.S., and Theodorakakos, A., Nozzle flow and spray development from VCO diesel injector nozzles. in *Selected Papers from THIESEL 2002 Conference on Thermo- and Fluid-Dynamic Processes in Diesel Engines*, Whitelaw, Arcoumanis, and Payri, Editors. Springer Verlag. pp. 31-48, 2004.
42. Andriotis, A. and Gavaises, M., Influence of Vortex Flow and Cavitation on Near-nozzle Diesel Spray Dispersion Angle. *Atomiz. Sprays*, 19(3), 2009.
43. Shi, J.-M., Wenzlawski, K., Helie, J., Nuglisch, H. and Cousin, J., URANS & SAS analysis of Flow Dynamics in a GDI nozzle. 23rd Annual European Conference on Liquid Atomization and Spray Systems, ILASS-Europe, Brno, 2010.
44. Park, S.W., Lee, C.S., Atomization Characteristics of Fuel Injected Through the Injector of a SI Engine with a Direct Injection System. *Atomization and Sprays* 13:517-534 (2003).
45. Schmidt, D. P., Nouar, I., Senecal, P. K., Hoffman, J., Rutland, C. J., Martin, J., and Reitz, R. D., Pressure-Swirl Atomization in the Near Field. *SAE Technical Paper* 1999-01-0496.

46. O'Rourke, P. J. and Amsden, A. A., The TAB Method for Numerical Calculation of Spray Droplet Breakup. SAE Technical Paper 872089.
47. Apte S.V., Gorokhovski M., Moin P., LES of Atomizing Spray with Stochastic Modeling of Secondary Breakup. Int. J. Multiphase Flow 29, 1503-1522, 2003.
48. De Villiers E., Gosman A., Weller H., Large Eddy Simulation of Primary Diesel Spray Atomization. SAE international, SAE paper 2004-01-0100.
49. Lebas R., Menard T., Beau P., Berlemont A., Demoulin F., Numerical simulation of primary break-up and atomization: DNS and modelling study. Int. J. Multiphase Flow 35, 247-260, 2009.
50. Menard T., Beau P., Tanguy S., Demoulin F., Berlemont A., Primary break-up: DNS of liquid jet to improve atomization modelling. WIT transactions on Engineering Sciences 55, 343-352, 2005.
51. Liu, A. B., Mather, D. K. and Reitz, R. D., Modeling the Effects of Drop Drag and Breakup on Fuel Sprays. SAE Paper No. 930072, 1993.
52. Schmidt, D. P. and Rutland, C. J., A New Droplet Collision Algorithm. Journal of Computational Physics, Vol. 164, p. 62, 2000.
53. O'Rourke, P. J., Collective Drop Effects on Vaporizing Liquid Sprays. Ph.D. Thesis, Princeton University, 1981.
54. Richards, K. J., Senecal, P. K., and Pomraning, E., CONVERGE (Version 1.4.1), Convergent Science, Inc., Middleton, WI (2012).

55. Amsden, A. A., O'Rourke, P. J. and Butler, T. D., KIVA-II: A Computer Program for Chemically Reactive Flows with Sprays. Los Alamos National Laboratory Report No. LA-11560-MS, 1989.
56. Pickett, L.M., S. Kook, and T.C. Williams, Visualization of Diesel Spray Penetration, Cool-Flame, Ignition, High-Temperature Combustion, and Soot Formation Using High-Speed Imaging. SAE Technical Paper 2009-01-0658, 2009.
57. Adam, A., et al., Analysis of Droplets Evaporation Process of Diesel Spray at Ignition Delay Period using Dual Nano-sprark Shadowgraph Photography Method. SAE Technical Paper 2009-32-0017, 2009.
58. Kalantari D, Tropea C, Spray impact onto flat and rigid walls: Empirical characterization and modelling. International Journal of Multiphase Flow 33:525– 544. 12, 2007.
59. Kolpakov, A. V. et al., Calculation of the Rebound Condition for Colliding Drops of Sharply Different Size. Kollodn. Zh. (47), 1985.
60. Moreira, A.L.N., Moita, A.S., and Panao, M.R., Advances and challenges in explaining fuel spray impingement: how much of single droplet impact research is useful? Prog. Energy Combust. Sci., 2 36, 544-580, 2010.
61. Drake, M., Fansler, D. Solomon, A.S., and Rosalik, M.E., SAE Technical Paper 2003-01-0547, (2003).
62. Iyer, C. and Yi, J., Spray Pattern Optimization for the Duratec 3.5L EcoBoost Engine. SAE Int. J. Engines 2(1):1679-1689, 2009.

63. Yoo, J., Zhao, F.-Q., Lai, M.-C., and Lee, K.-S. "Characterization of Direct Injection Gasoline Sprays in Different Ambient and Wall Impingement Conditions," SAE Technical Paper 982702.
64. Park, J., Xie, X., Im, K.-S., Kim, H., Lai, M.-C., Yang, J., Han, Z., and Anderson, R. "Characteristics of Direct injection Gasoline Spray Wall Impingement at Elevated Temperature Conditions," SAE Technical Paper 1999-01-3662.
65. Stanglmaier, R. H., Li, J., and Matthews, R. D., "The Effect of In-Cylinder Wall Wetting Location on the HC Emissions from SI Engines," SAE Paper 1999-01-0502, SAE International, 1999
66. Park, J., Xie, X., Im, K.-S., Kim, H., Lai, M.-C. "Visualization and Analysis of the Direct Injection Gasoline Spray Impingement," J. Fuels & Lubricants, SAE Transc. 110(4), pp. 1517-1536.
67. Park, J., Im, K.-S., Kim, H., and Lai, M.-C. "Visualization and Measurement of a Narrow-Cone DI Gasoline Spray for the Impingement Analysis," Int. J. Automotive Technology, 5(4), pp. 221-238.
68. Mathews, W.S., Lee, C.F., Peters, J.E. "Experimental Investigations of Spray/Wall Impingement," Atomization and Sprays 13:223-242 (2003).
69. Borthwick, R.P., Farrell, P.V. "Fuel Injection Spray and Combustion Chamber Wall Impingement in Large Bore Diesel Engines," SAE Technical Paper 2002-01-0496.
70. Fan, Q., Deng, J., Hu, Z. and Li, L. "An experimental study on spray characteristics after impingement on a piston surface through an

asymmetrical multi-hole injector of a direct-injection spark ignition gasoline engine", Journal of Automobile Engineering, 21 September 2011

71. Zhao, F., M.-C. Lai, and D.L. Harrington, Progress in Energy and Combustion Science, 1999. 25: p. 437-562.
72. Drake, M., Fansler, D. and Rosalik, M.E., 15th Annual Conference on Liquid Atomization and Spray Systems, Madison,WI, May 2002.
73. Yang, B., Ghandhi, J., SAE Technical Paper 2010-01-0485, (2010).
74. Maligne, D., Bruneaux, G., SAE Technical Paper 2011-01-1215, (2011).
75. Lindgren, R., and Denbratt, I., SAE Technical Paper 2004-01-1951, (2004).
76. Montorsi, L., Magnusson, A., and Andersson, S., SAE Technical Paper 2007-01-0486, (2007).
77. Montanaro, A., Malaguti, S., Alfuso, S., SAE Technical Paper 2012-01-1266, (2012).
78. Karlsson, R. B. and Heywood, J. B., SAE Technical Paper 2001-01-2022, (2001).
79. Rivera, E., Mastro, N., Zizelman, J., Kirwan, J., Development of Injector for the Direct Injection Homogeneous Market using Design for Six Sigma. SAE Technical Paper, 2010-01-0594, 2010.
80. Lucchini, T., D'Errico, G., Onorati, A., Bonandrini, G. et al., Development of a CFD Approach to Model Fuel-Air Mixing in Gasoline Direct-Injection Engines. SAE Technical Paper 2012-01-0146, 2012.
81. Velji, A., Yeom, K., Wagner, U., Spicher, U. et al., Investigations of the Formation and Oxidation of Soot Inside a Direct Injection Spark Ignition

- Engine Using Advanced Laser-Techniques. SAE Technical Paper 2010-01-0352, 2010.
82. Zhan, R., Eakle, S., and Weber, P., Simultaneous Reduction of PM, HC, CO and NOx Emissions from a GDI Engine. SAE Technical Paper 2010-01-0365, 2010.
83. Koyanagi, K., et al., Optimizing Common Rail-Injection by Optical Diagnostics in a Transparent Production Type Diesel Engine. SAE Technical Paper 1999-01-3646, 1999.
84. Senda, J., et al., Experimental Analysis on Soot Formation Process in DI Diesel Combustion Chamber by Use of Optical Diagnostics. SAE Technical Paper 2002-01-0893, 2002.
85. Li, J.W., Huang, Y., Alger, T.F., Matthews, R.D; Hall, M.J., Stanglmaier, R.H., Roberts, C.E., Dai, W. and Anderson, R.W. Liquid fuel impingement on in-cylinder surfaces as a source of hydrocarbon emissions from direct injection gasoline engines [J]. J. Eng. Gas Turbines Power, 2001, 123: 659-668.
86. Ra, Y. and Reitz, R.D., A Model for Droplet Vaporization for Use in Gasoline and HCCI Engine Applications. Proceedings of ICEC'02, ASME Spring Technical Conference, Rockford, Ill., April 14-17, 2002.
87. Joh, M., Huh K. Y., Yoo, J.-H., and Lai, M.-C. Numerical Prediction and Validation of Fuel Spray Behavior in a Gasoline Direct-Injection Engine [J]. J. Fuels & Lubricants, 2002, 110(4): 2387-2404.

88. Schmitz, I., Ipp, W., and Leipertz, A., Flash Boiling Effects on the Development of Gasoline Direct Injection Sprays [J]. SAE 2002-01-2661, 2002.
89. Horie, K., Kohda, Y., Ogawa, K., and Goto, H. Development of a High Fuel Economy and Low Emission Four-Valve Direct Injection Engine with a Center-Injection System [J]. SAE 2004-01-2941, 2004.
90. Stansfield, P., Wigley, G., Garner, C., Patel, R., Ladommatos, N., Pitcher, G., Turner, J., Nuglisch, H., and Helie, J. Un-throttled Engine Operation using Variable Valve Actuation: The Impact on the Flow Field, Mixing and Combustion [J]. SAE 2007-01-1414, 2007.
91. Patel, R., Ladommatos, N., Stansfield, P., Wigley, G., Garner, C., Pitcher, P., Turner, J., and Nuglisch, H. Comparison between Un-throttled, Single and Two-valve Induction Strategies Utilizing Direct Gasoline Injection: Emissions, Heat-release and Fuel Consumption Analysis [J]. SAE 2008-01-1626, 2008.
92. Xue, Q., and Kong, S.-C. Simulation of Direct Injection Gasoline Sprays Using Multi-Level Dynamic Mesh Refinement. ASME International Mechanical Engineering Congress and Exposition (IMECE2008), Oct. 31–Nov. 6, 2008, Boston.
93. Wang, Z., Wang, J-X., Shuai, S-J., Wang, Y-J., Tian, G-H., and An, X-L. Study of Multimode Combustion System With Gasoline Direct Injection [J]. J. Eng. Gas Turbines Power, 2007, 129(4): 1079.

94. Battistoni, M., Grimaldi, C., and Mariani, F., Coupled Simulation of Nozzle Flow and Spray Formation Using Diesel and Biodiesel for CI Engine Applications [J]. SAE Technical Paper 2012-01-1267, 2012.
95. Montanaro, A., Allocca, L., Ettore, D., Lucchini, T. et al., Experimental Characterization of High-Pressure Impinging Sprays for CFD Modeling of GDI Engines [J]. SAE Int. J. Engines 4(1):747-763, 2011.
96. Gao, J., Trujillo, M., and Deshpande, S., Numerical Simulation of Hollow-Cone Sprays Interacting with Uniform Crossflow for Gasoline Direct Injection Engines [J]. SAE Int. J. Engines 4(2):2207-2221, 2011.
97. Renberg, U., Westin, F., Angstrom, H., and Fuchs, L., Study of Junctions in 1-D & 3-D Simulation for Steady and Unsteady Flow [J] SAE Technical Paper 2010-01-1050, 2010.
98. Dempsey, A., Wang, B., Reitz, R., Petersen, B. et al., Comparison of Quantitative In-Cylinder Equivalence Ratio Measurements with CFD Predictions for a Light Duty Low Temperature Combustion Diesel Engine [J]. SAE Int. J. Engines 5(2):162-184, 2012.
99. Yang, X., Solomon, A., and Kuo, T., Ignition and Combustion Simulations of Spray-Guided SIDI Engine using Arrhenius Combustion with Spark-Energy Deposition Model [J]. SAE Technical Paper 2012-01-0147, 2012.
100. Gembicky, M., Oss, D., Fuchs, R., and Coppensa, P., A Fast Mechanical Shutter for Submicrosecond Time-Resolved Synchrotron Experiments. Journal of Synchrotron Radiation, 12:665-669, 2005.

101. Mulemane, A., Subramaniyam, S., Lu, P.-H., Han, J., Lai, M.-C., and Poola, R., (2004) "Comparing Cavitation in Diesel Injectors Based on Different Modeling Approaches," SAE 2004-01-0027, SAE Int'l Congress and Exposition, March 1-4, 2004, Detroit, MI. Diesel Injection and Spray (SP-1824): 101~116.
102. Miranda, R., Chaves, H., and Obermeier, F. (2002), "Imaging of Cavitation, Hollow Jets and Jet Branching at Low Lift in a Real-size VCO Nozzle," ILASS-Europe 2002, Zaragoza, Spain, Sept. 9 –11, 2002.
103. Collicott, S. and Li, H. (2006), "True-scale True-pressure Internal Flow Visualization for Diesel Injectors ," SAE 2006-01-0890.
104. Lai, M.-C., Zhao, F.-Q., Amer, A. and Chue, T.-H. (1995) "An Experimental and Analytical Study of Fuel Sprays from Automotive Port Injectors," J. Fuels & Lubricants, SAE Transc. 103(4):833-852.
105. Menter, F.R., (1993) "Zonal Two Equation $k-\omega$ Turbulence Models for Aerodynamic Flows," AIAA Paper 93-2906.
106. F.R. Menter and Y. Egorov (2005), "A Scale-Adaptive Simulation Model using Two-Equation Models", AIAA 2005-1095.
107. M. Lesieur, P. Begou, E. Briand, A. Danet, F. Delcayre & J.L. Aider, "Coherent-vortex dynamics in large-eddy simulations of turbulence", Journal of turbulence, 4, 016 (2003). <http://soldjournals.iop.org/article/1468-5248/4/1/016/jt3116.html>
108. Y. Dubief & F. Delcayre, "On coherent vortex identification in turbulence", Journal of turbulence, 1, 011 (2000).

109. Marriott, C., Wiles W., Gwidt, J., and Parrish, S. (2008) "Development of a Naturally Aspirated Spark Ignition Direct-Injection Flex-Fuel Engine," SAE 2008-01-0319.
110. Senecal, P. K., Pomraning, E., and Richards, K. J., "Multi-Dimensional Modeling of Direct-Injection Diesel Spray Liquid Length and Flame Lift-off Length using CFD and Parallel Detailed Chemistry," SAE Paper No. 2003-01-1043, 2003.
111. Babajimopoulos A., Assanis D.N., Flowers D.L., Aceves S.M., Hessel R.P., A fully coupled computational fluid dynamics and multi-zone model with detailed chemical kinetics for the simulation of premixed charge compression ignition engines. International Journal of Engine Research, Vol. 6, 5: p. 497, 2005.
112. Moore, W., et al. Charge Motion Benefits of Valve Deactivation to Reduce Fuel Consumption and Emissions in an SIDI, VVA engine [J]. SAE 2011-01-1221.

ABSTRACT**SIMULATIONS AND EXPERIMENTS OF FUEL INJECTION, MIXING AND COMBUSTION IN DI GASOLINE ENGINES**

by

YI ZHENG**May 2013****Advisor:** Dr. Ming-Chia Lai**Major:** Mechanical Engineering**Degree:** Doctor of Philosophy

Direct Injection (DI) has been known for its improved performance and efficiency in gasoline spark-ignition engines. In order to take all the advantages of the GDI technology, it is important to investigate in detail the interactions of fuel spray and combustion system, such as air-fuel mixing, in-cylinder flow development, surface wetting, and turbulence intensity. The characterizations of the internal nozzle flow of DI injector are first studied using the multidimensional computational fluid dynamic (CFD) simulation. In the meanwhile the numerical and experimental studies are carried out to observe the external spray and wall impingements in an optical constant volume vessel. The fuel film deposit characteristics were derived using the Refractive Index Matching (RIM) technique. Finally, the interactions of sprays with the charge motion are investigated in an optical accessible engine using CFD simulation and high-speed imaging of sprays inside engines.

The numerical results DI injector nozzle show that the complicated unsteady flow features dominate the near-nozzle breakup mechanisms which are quite unlike those of diesel. The spray impingement, wetted area, fuel film thickness, and the

resultant footprint mass were investigated experimentally. The CFD simulation with selected models of spray validated first for its transport in the air is used to compare the impingement models with the experimental measurements. The spray cone, tip penetration and fuel film shapes were in very good agreement. The effects of spray patterns, injection timing and flexible valve-train on the bulk flow motion and fuel-air mixing in an optical accessible engine, in terms of tumble and swirl ratios, turbulence level, and fuel wall film behaviors are discussed. Using integral analyses of the simulation results, the mechanisms in reducing fuel consumption and emissions in a variable valve-actuation engine, fueled by side-mounted multi-hole DI injectors are illustrated. The implications to the engine mixing and the resultant combustion in a metal engine are also demonstrated.

AUTOBIOGRAPHICAL STATEMENT

Yi Zheng was born in 1981 in Beijing, China. He obtained his Bachelor's degree in Aeronautical Science and Engineering from Beijing University of Aeronautics and Astronautics in 2003. When he was a senior, he joined the Heat and mass transfer Lab and worked for the development of software of dynamic environmental control. In this lab, he received Master's degree in 2006. Yi Zheng joined the Ph.D. program in Mechanical Engineering at Wayne State University in 2008. His research interest includes spray and wall impingement, gasoline/diesel injector analysis, and in-cylinder charge and combustion diagnostics and simulation.

Major Publications:

1. Characterization of Di Spray and Wall Impingements. ILASS-America, Ventura, CA, May 15~19, 2011.
2. Measurement and Simulation of DI Spray Impingements and Film Characteristics. ICLASS 2012-1253, Heidelberg, Sept. 2012.
3. CFD Simulation and Optical Engine Diagnostics of Mixture Formation Processes in Di Gasoline Engine with Flexible Valvetrain. F2012- A05-011, FISITA Conference, Beijing China. Nov. 26~29, 2012.
4. Spray Characterization of Ethanol Gasoline Blends and Comparison to a CFD Model for a Gasoline Direct Injector. SAE International Journal of Engines, 3(1), 2010:402-425 SAE 2010-01-0601.
5. Characterization of the Near-Field Spray and Internal Flow of Single-Hole and Multi-Hole Sac Nozzles using Phase Contrast X-Ray Imaging and CFD. SAE Int. J. Engines, 4(1):703-719. SAE 2011-01-0681.